uOttawa

L'Université canadienne
Canada's university

FACULTÉ DES ÉTUDES SUPÉRIEURES ET POSTDOCTORALES

uOttawa

L'Université canadienne
Canada's university

FACULTY OF GRADUATE AND POSTDOCTORAL STUDIES

Jean-Paul Prévost
AUTEUR DE LA THÈSE / AUTHOR OF THESIS

Ph.D. (Physics)
GRADE / DEGREE

Department of Physics
FACULTÉ, ÉCOLE, DÉPARTEMENT / FACULTY, SCHOOL, DEPARTMENT

Theoretical Studies of the First-row Transition Metals: Ground State and Thermal Properties
TITRE DE LA THÈSE / TITLE OF THESIS

Pierre Berini (acting supervisor)
DIRECTEUR (DIRECTRICE) DE LA THÈSE / THESIS SUPERVISOR

CO-DIRECTEUR (CO-DIRECTRICE) DE LA THÈSE / THESIS CO-SUPERVISOR

EXAMINATEURS (EXAMINATRICES) DE LA THÈSE / THESIS EXAMINERS

K. Chen

I. L'Heureux

M. Stott

P. Watson

Gary W. Slater
Le Doyen de la Faculté des études supérieures et postdoctorales / Dean of the Faculty of Graduate and Postdoctoral Studies

Theoretical Studies of the First-Row Transition Metals: Ground State and Thermal Properties

by Jean-Paul L. Prévost

Thesis submitted to the
Faculty of Graduate and Postdoctoral Studies
in partial fulfillment of the requirements
for the Ph.D. degree in physics.

Department of Physics
Faculty of Science
University of Ottawa

Your file Votre référence
ISBN: 978-0-494-61227-9
Our file Notre référence
ISBN: 978-0-494-61227-9

Abstract

Theoretical studies of the ground state properties of the first-row transition metals (Sc to Zn) are conducted using the Stuttgart TB-LMTO ESC program. The standard deviation of the calculation precision errors (CPE's) and the magnitude of the systematic calculation errors (SCE's) in the output of the TB-LMTO ESC program are estimated. The ground state lattice parameters, local atomic magnetic moment magnitudes and bulk moduli of the first-row transition metals are calculated. Lattice parameters are found to be within 5% to 10% of experimental values, and magnetic moment magnitudes are found to be within 10% to 20% of experimental values. Bulk moduli are found to be within 60% of experimental values. Lattice parameter and magnetic moment magnitude calculations are most accurate when the non-local exchange-correlation functional of Hu and Langreth is used. Bulk modulus calculations are most accurate when conducted using the exchange-correlation functional of Perdew and Yue. The TB-LMTO ESC program is also used to study the volume-controlled low-moment to high-moment (LM-HM) transition of the first-row transition metals (Sc to Ni) when they are constrained to take the FCC crystal structure. A LM-HM transition is predicted to occur in all FCC first-row transition metals if their lattice parameter is sufficiently increased. FCC Fe is found to occupy a unique position in the first-row transition metal series, as its LM-HM transition occurs when its lattice parameter is less than 2.5% larger than its ground state value. The LM-HM transition of the other FCC first-row transition metals occur when their lattice parameters are much larger or much smaller than their ground state values. It is argued that when the lattice parameters of the FCC first-row transition metals are too small, the energy bands of their valence electrons are too wide to allow magnetic moments to form within these metals. A method is proposed for calculating the Helmholtz' free energy of non-magnetic, bulk, crystalline solids consisting of a single chemical species. The method assumes only that an inter-atomic interaction potential can be derived from the minimum total energy versus lattice parameter curve of a solid using results published by Chen, Chen and Wei, and that this potential can accurately reproduce the energy increase that occurs when the atomic nuclei of the solid move away from their equilibrium positions as they undergo small amplitude thermal oscillations. The method is entirely theoretical as the minimum total energy versus lattice parameter curve of a solid can be calculated entirely from first principles using an ESC program. Within the method, the atomic nuclei of a solid are treated in a quasi-harmonic approximation, either as independent harmonic oscillators, or as coupled harmonic oscillators. The thermal expansion of metallic Cu is studied using the proposed method for calculating the Helmholtz' free energy of solids in conjunction with the TB-LMTO ESC program. The lattice parameter versus temperature curve of metallic Cu can be accurately calculated using the method, but its accuracy is sensitive to the functional form of the calculated minimum total energy versus lattice parameter curve of FCC Cu and to the range of the inter-atomic interaction potential. The results of these calculations suggest that the range of the inter-atomic interaction potential extends only

to first nearest neighbour atomic nuclei in the metallic Cu solid. These results also suggest that the curvature of the minimum total energy versus lattice parameter curve of FCC Cu is most accurate when the curve is calculated using the exchange-correlation functional of Perdew and Yue even though the ground state lattice parameter of metallic Cu is most accurately predicted using the exchange-correlation functional of Hu and Langreth. However, it may be that imposing a short range to the inter-atomic interaction potential and that using the minimum total energy versus lattice parameter curve obtained with the exchange-correlation functional of Perdew and Yue simply better cancels the errors introduced in the calculation as a result of the quasi-harmonic approximation, as a result of not knowing the correct range of the inter-atomic interaction potential, and as a result of inaccuracies in the calculated minimum total energy versus lattice parameter curve of FCC Cu. Future research efforts should be focussed on the evaluation of the effect of these three factors on the accuracy of the method. We also recommend a direct evaluation of the accuracy of the energy increase that occurs when the atomic nuclei of the solid are displaced slightly from their equilibrium positions, as reproduced using the inter-atomic interaction potential constructed using the results of Chen, Chen and Wei.

Merci à tous et à toutes qui m'avez donné quoi que ce soit.
Sans vous, je n'aurais jamais pu.

Subí al infinito, y observé que tiene textura.

Pude ver algunas de sus partes con mis propios ojos,

Deduje la forma de otras de sus partes,

Y otras más, pude las imaginar.

En fin, comprendí que habrá partes de él que siempre quedarán en secreto.

Acknowledgements

This work would not have been possible without the scientific advice of Dr. Denis Rancourt. Additional scientific and technical support was provided by a number of professors from the Department of Physics of the University of Ottawa. Dr. Ivan L'Heureux, Dr. Liang Chen, Dr. Peter Piercy and Dr. Thomas Brabec come to mind. Additional scientific and technical support was provided by Dr. R. James Evans, Dr. Mei Zhen Dang, Dr. Brad Sim, Severin Stojanovic and other present and former students of the Department of Physics and the Department of Earth Sciences of the University of Ottawa. Finally, the evaluation committee of this thesis provided much useful feedback.

Importantly, Dr. Shyamal Bose of Brock University provided me with the TB-LMTO ESC program that I use in this study, and helped me understand its operation.

Financial support for this work was provided by:

The Natural Sciences and Engineering Research Council of Canada

The Province of Ontario

The University of Ottawa

La Fondation Baxter et Alma Ricard

Dr. Denis Rancourt

and members of the Prévost and Proulx families.

Contents

1 Introduction **1**

2 The TB-LMTO ESC Program **6**

2.1 Physical and Mathematical Basis of DFT 7

2.1.1 The Total Energy of a Solid 7

2.1.2 The Hartree-Fock ESC Method 9

2.1.3 Density Functional Theory 13

2.2 Implementation of DFT in the TB-LMTO ESC Program 18

2.2.1 The Single-Electron Wave Functions and Energy Values 18

2.2.2 Calculation of $E_{e_{tot}}$ and E_{tot} 24

2.2.3 Implementation of DFT in the TB-LMTO ESC Program : Additional Considerations 28

2.3 Applicability of the TB-LMTO ESC Program to the Study of the 3d Metals . 31

3 Numerical Precision of the TB-LMTO ESC Program **34**

3.1 Numerical Precision of the TB-LMTO ESC Program : Definition 35

3.2 Numerical Precision of the TB-LMTO ESC Program : Evaluation 39

3.2.1 The Initial Conditions of a TB-LMTO Calculation 39

3.2.2 Convergence Tolerances and the Precision of the Minimum E_{tot} . . . 42

3.2.3 Discretization of the First BZ and the Precision of the Minimum E_{tot} 51

3.3 Numerical Precision of the TB-LMTO ESC Program : Summary 61

3.4 Appendix : Initial Conditions INIT1 and INIT2 63

4 Accuracy of the TB-LMTO ESC Program - Calculation of Some Zero-Kelvin Properties of the First-Row Transition Metals **68**

4.1 Accuracy of the TB-LMTO ESC Program : Definition 70

4.2 Accuracy of the TB-LMTO ESC Program : Evaluation 73

4.2.1 Zero-Kelvin Properties of the First-Row Transition Metals : Calculation Details 74

4.2.2 Accuracy of the Calculated Zero-Kelvin Crystal Structure and Magnetic Structure of the First-Row Transition Metals 77

4.2.3 Accuracy of the Calculated Zero-Kelvin Lattice Parameters of the First-Row Transition Metals 82

4.2.4 Accuracy of the Calculated Bulk Modulus of the First-Row Transition Metals 88

4.2.5 Accuracy of Calculated Magnitude of the Magnetic Moments of Fe, Co and Ni at Zero-Kelvin 93

4.3 Accuracy of the TB-LMTO ESC Program : Summary 97

5 The LM-HM Transition in the FCC 3d Transition Metals **101**

5.1 Calculation of the $\mu(a)$ and $E_{tot}(a)$ Curves of the FCC 3d Metals 104

5.2 Identification of the LM-HM Transition in the FCC 3d Metals 105

5.3 General Aspects of the LM-HM Transition in the FCC 3d Metals 115

5.4 Electronic Aspects of the LM-HM Transition in the FCC 3d Metals 124

5.5 Summary and Future Work 143

5.6 Calculated $E_{tot}(a)$ and $\mu(a)$ Curves of FCC Sc to Ni 145

6 A Theoretical Method for Calculating the Helmholtz' Free Energy of Crystalline Solids **158**

6.1 Calculating the Thermal Properties of a Solid - General Considerations . . . 159

6.2 Calculating the Helmholtz' Free Energy of a Crystalline Solid 162

6.2.1 The Microstates of a Solid and Their Energy 162

6.2.2 $F(v,T)$ Curve of a Solid - Mean-Field Potential Method 168

6.2.3 $F(v,T)$ Curve of a Solid - Phonon Spectrum Method 169

6.3 Major Assumptions of and Novelty of the Method 171

6.4 Validation of the Method 177

6.5 Appendix: Taylor Expansion of the Potential $U_{vib}\left((\ldots), \left\langle \vec{R}_I \right\rangle + \Delta\vec{R}_I, (\ldots)\right)$ 178

7 Calculation of the Thermal Expansion of Metallic Copper **181**

7.1 The $E_{tot}(a)$ Curve and the Potential $E_{a-a}(x)$ of FCC Cu 182

7.2 Calculation of the $F(a,T)$ Curve of Metallic Cu 193

7.2.1 $F(a,T)$ Curve Using the Mean-Field Potential Method 193

7.2.2 $F(a,T)$ Curve Using the Phonon Spectrum Method 196

7.2.3 A Typical Calculated $F(a,T)$ Curve 200

7.3 Calculation of the $a(T)$ Curve of Metallic Cu 205

7.3.1 $a(T)$ Curve of Metallic Cu Using the Mean-Field Potential Method . 205

7.3.2 $a(T)$ Curve of Metallic Cu Using the Phonon Spectrum Method . . . 211

7.4 Calculated $a(T)$ Curve of Metallic Cu - Summary and Discussion 216

7.4.1 Implications of the Assumptions Made in Deriving the Method of Chapter 6 216

7.4.2 Accuracy of the Calculated $a(T)$ and $F(a,T)$ Curve of Metallic Cu . 220

7.4.3 Conclusions Concerning the Potential $E_{a-a}(x)$ 223

8 Conclusion **227**

A Literature Review: Studies of the First-Row Transition Metals Using ESC Programs **231**

A.1 Pre-1980 Studies of the First-Row Transition Metals Using ESC Programs . . 232

A.2 Post-1980 Studies of the First-Row Transition Metals Using ESC Programs . 235

A.3 Summary of Studies of the First-Row Transition Metals Using ESC Programs 238

B Parametrization of the Calculated E_{tot} (a) Curve of FCC Cu **241**

B.1 Parametrization of and Evaluation of the Numerical Precision of the Calculated $E_{tot}(a)$ Curves 242

B.1.1 Parametrization of the Calculated $E_{tot}(a)$ Curves - General Considerations 242

B.1.2 Parametrization of and Estimation of the Numerical Precision of the 1NN Section of the EXC2 $E_{tot}(a)$ Curve 245

B.1.3 Parametrization of and Estimation of the Numerical Precision of All Sections of the EXC2 and EXC4 $E_{tot}(a)$ Curves 252

B.2 Evaluation of the Numerical Precision of the Derivatives of the EXC2 and EXC4 $E_{tot}(a)$ Curves 273

B.2.1 Evaluation of the Numerical Precision of the Derivatives of the 1NN Section of the $E_{tot}(a)$ Curve 273

B.2.2 Evaluation of the Numerical Precision of the Derivatives of All Sections of the EXC2 and EXC4 $E_{tot}(a)$ Curve 278

List of Figures

3.1 INIT1 E_{tot} - INIT2 E_{tot} obtained using different convergence tolerances . . . 46

3.2 E_{tot} versus convergence tolerance 50

3.3 INIT1 E_{tot} - INIT2 E_{tot} obtained using different first-BZ discretization integers 54

3.4 E_{tot} versus first-BZ discretization integers 56

3.5 $E_{tot}(a)$ curve of FCC Cu obtained using different first-BZ discretization integers 59

3.6 Comparison of $E_{tot}(a)$ curves of FCC Cu obtained using different first-BZ discretization integers 60

4.1 $E_{tot}(a)$ curve of NM BCC Fe, AFM BCC Fe and FM BCC Fe 81

4.2 Comparison of calculated and measured lattice parameters of the first-row transition metals 87

4.3 Comparison of calculated and measured bulk modulus of the first-row transition metals 92

4.4 Comparison of calculated and measured magnetic moment magnitudes of the first-row transition metals 96

5.1 $E_{tot}(a)$ curve of NM FCC Co, AFM FCC Co and FM FCC Co 110

5.2 $\mu(a)$ curve of NM FCC Co, AFM FCC Co and FM FCC Co 111

5.3 $E_{tot}(a)$ curve of NM FCC Fe, AFM FCC Fe and FM FCC Fe 112

5.4 Detail of $E_{tot}(a)$ curve of NM FCC Fe, AFM FCC Fe and FM FCC Fe 113

5.5 $\mu(a)$ curve of NM FCC Fe, AFM FCC Fe and FM FCC Fe 114

5.6 $\Delta\mu$ at a_{tx} for FCC Sc to FCC Ni 119

5.7 a_{tx} and a_0 for FCC Sc to FCC Ni 120

5.8 $v_{tx} = a_{tx}^3$ and $v_0 = a_0^3$ for FCC Sc to FCC Ni 121

5.9 $(a_{tx} - a_0)/a_0$ for FCC Sc to FCC Ni 122

5.10 $W = E_{tot}(a_{tx}) - E_{tot}(a_0)$ and p_{tx} for FCC Sc to FCC Ni 123

5.11 $\Delta E_{e_{kin}}$ and $\Delta U_{e_{tot}}$ for FCC Sc to FCC Ni 126

5.12 Calculated and measured $n_v(\epsilon)$ function of FCC Cu 131

5.13 Calculated $n_v(\epsilon)$ functions of the NM and HM FCC 3d metals at a_{tx} (part a). 133

5.13 Calculated $n_v(\epsilon)$ functions of the NM and HM FCC 3d metals at a_{tx} (part b). 134

5.14 Calculated $\rho_v(\vec{r})$ functions of the NM and HM FCC 3d metals at a_{tx}. 135

5.15 Calculated $n_v(\epsilon)$ functions of the FCC 3d metals at a_0 and a_{tx} (part a). 139

5.15 Calculated $n_v(\epsilon)$ functions of the FCC 3d metals at a_0 and a_{tx} (part b). 140

5.16 Calculated valence electron distributions $\rho_v(|\vec{r}|)$ of the NM FCC 3d metals at a_0 and a_{tx}. 141

5.17 Calculated d-orbital components of the electron distributions of the FCC 3d metals at a_0 and a_{tx}. 142

5.18 $E_{tot}(a)$ curve of NM FCC Sc, AFM FCC Sc and FM FCC Sc 146

5.19 $\mu(a)$ curve of NM FCC Sc, AFM FCC Sc and FM FCC Sc 147

5.20 $E_{tot}(a)$ curve of NM FCC Ti, AFM FCC Ti and FM FCC Ti 148

5.21 $\mu(a)$ curve of NM FCC Ti, AFM FCC Ti and FM FCC Ti 149

5.22 $E_{tot}(a)$ curve of NM FCC V, AFM FCC V and FM FCC V 150

5.23 $\mu(a)$ curve of NM FCC V, AFM FCC V and FM FCC V 151

5.24 $E_{tot}(a)$ curve of NM FCC Cr, AFM FCC Cr and FM FCC Cr 152

5.25 $\mu(a)$ curve of NM FCC Cr, AFM FCC Cr and FM FCC Cr 153

5.26 $E_{tot}(a)$ curve of NM FCC Mn, AFM FCC Mn and FM FCC Mn 154

5.27 $\mu(a)$ curve of NM FCC Mn, AFM FCC Mn and FM FCC Mn 155

5.28 $E_{tot}(a)$ curve of NM FCC Ni, AFM FCC Ni and FM FCC Ni 156

5.29 $\mu(a)$ curve of NM FCC Ni, AFM FCC Ni and FM FCC Ni 157

7.1 Calculated EXC2 and EXC4 $E_{tot}(a)$ curves of FCC Cu 187

7.2 Calculated EXC2, EXC4 and EXC4′ $E_{tot}(a)$ curves of FCC Cu in the vicinity of their global minimum values 188

7.3 Calculated EXC2 and EXC4 $E_{a-a}(x)$ potentials of FCC Cu 192

7.4 1NN EXC2 $F(a,T)$ curve of metallic Cu at $T = 293$ Kelvin 202

7.5 1NN EXC2 $F(a,T)$ curve of metallic Cu at $T = 1300$ Kelvin 203

7.6 1NN, 3NN, 7NN and 15NN EXC2 $F(a,T)$ curve of metallic Cu at $T = 293$ Kelvin 204

7.7 EXC2 and EXC4 $a(T)$ curves of metallic Cu, calculated using the mean-field potential method 209

7.8 1NN and 7NN EXC2 and EXC4′ $a\,(T)$ curves of metallic Cu, calculated using the mean-field potential method 210

7.9 EXC2 and EXC4 $a\,(T)$ curves of metallic Cu, calculated using the phonon spectrum method 213

7.10 Comparison of the 1NN and 7NN EXC2 $a\,(T)$ curves obtained using the mean-field potential method and using the phonon spectrum method 214

7.11 Comparison of the 1NN and 7NN EXC4′ $a\,(T)$ curves obtained using the mean-field potential method and using the phonon spectrum method 215

B.1 $\log_{10}(\chi^2)$ versus polynomial order for the 1NN section of the EXC2 $E_{tot}\,(a)$ curve of FCC Cu 250

B.2 1NN section of the EXC2 $E_{tot}\,(a)$ curve of FCC Cu 251

B.3 1NN section of the EXC2 $E_{tot}\,(a)$ curve of FCC Cu (repeated) 259

B.4 2NN section of the EXC2 $E_{tot}\,(a)$ curve of FCC Cu 260

B.5 3NNto5NN section of the EXC2 $E_{tot}\,(a)$ curve of FCC Cu 261

B.6 6NNto8NN section of the EXC2 $E_{tot}\,(a)$ curve of FCC Cu 262

B.7 9NNto11NN section of the EXC2 $E_{tot}\,(a)$ curve of FCC Cu 263

B.8 12NNto14NN section of the EXC2 $E_{tot}\,(a)$ curve of FCC Cu 264

B.9 15NNandmore section of the EXC2 $E_{tot}\,(a)$ curve of FCC Cu 265

B.10 1NN section of the EXC4 $E_{tot}\,(a)$ curve of FCC Cu 266

B.11 2NN section of the EXC4 $E_{tot}\,(a)$ curve of FCC Cu 267

B.12 3NNto5NN section of the EXC4 $E_{tot}\,(a)$ curve of FCC Cu 268

B.13 6NNto8NN section of the EXC4 $E_{tot}\,(a)$ curve of FCC Cu 269

B.14 9NNto11NN section of the EXC4 $E_{tot}\,(a)$ curve of FCC Cu 270

B.15 12NNto14NN section of the EXC4 $E_{tot}\,(a)$ curve of FCC Cu 271

B.16 15NNandmore section of the EXC4 $E_{tot}\,(a)$ curve of FCC Cu 272

List of Tables

2.1 Exchange-correlation functionals available in the TB-LMTO ESC program . 29

3.1 Lattice parameters used in convergence tolerance calculations 44

3.2 Value of $\int^{E_F} n_{v,l}(\epsilon)d\epsilon$ in initial conditions for HCP Sc 64

3.3 Value of $\int^{E_F} n_{v,l}(\epsilon)d\epsilon$ in initial conditions for BCC Fe 65

3.4 Value of $\int^{E_F} n_{v,l}(\epsilon)d\epsilon$ in initial conditions for FCC Cu 67

4.1 Predicted zero-Kelvin crystal structure and magnetic structure of the first-row transition metals 80

4.2 Assumed magnetic and crystal structure of the first-row transition metals when calculating their zero-Kelvin lattice parameters 84

4.3 Zero-Kelvin lattice parameters of the first-row transition metals predicted using the TB-LMTO ESC program. 85

4.4 Measured lattice parameters of the first-row transition metals 86

4.5 Zero-Kelvin bulk modulus of the first-row transition metals predicted using the TB-LMTO ESC program. 90

4.6 Measured bulk moduli of the first-row transition metals 91

4.7 Magnitude of the magnetic moments of BCC Fe, HCP Co and FCC Ni at zero Kelvin, predicted using the TB-LMTO ESC program. 95

4.8 Measured magnitude of the magnetic moments of BCC Fe, HCP Co and FCC Ni at zero Kelvin 95

5.1 SCE's in the $E_{tot}\,(a)$ curves of the AFM FCC 3d metals relative to the SCE's in the $E_{tot}\,(a)$ curves of the NM FCC 3d metals 107

5.2 Details of the LM-HM transition in the FCC 3d metals 109

7.1 Convergence tolerances for calculating the $E_{tot}\,(a)$ curve of FCC Cu 184

7.2 Notable features of the calculated $E_{tot}\,(a)$ curves of FCC Cu 185

7.3 Constants $r\,[n]$, $b\,[n]$ and $I\,[n]$ for the FCC crystal structure 190

7.4 Temperatures at which values of the $F\,(a,T)$ curve of FCC Cu are calculated 196

7.5 Calculated and measured bulk modulus of metallic Cu 225

A.1 Number of papers discussing the use of ESC programs to study the first-row transition metals cited in the review of A. P. Cracknell 233

A.2 Number of papers discussing the electronic structure of the first-row transition metals published after 1980 236

B.1 Parametrization sections of the EXC2 and EXC4 $E_{tot}\,(a)$ curves 244

B.2 Coefficients of the optimal polynomial description of the 1NN section of the EXC2 $E_{tot}\,(a)$ curve 247

B.3 Average, standard deviation, root-mean-squared, and absolute maximum value of the function $\Delta E(a)$ shown in figure B.2 248

B.4 One-σ confidence intervals of the coefficients of the optimal polynomial description of the 1NN section of the EXC2 $E_{tot}(a)$ curve 249

B.5 Numerical precision of all sections of the EXC2 and EXC4 $E_{tot}(a)$ curves . . 254

B.6 Parameters describing the EXC2 $E_{tot}(a)$ curve 255

B.7 One-σ confidence intervals for the parameters describing all sections of the EXC2 $E_{tot}(a)$ curve 256

B.8 Parameters describing the EXC4 $E_{tot}(a)$ curve 257

B.9 One-σ confidence intervals for the parameters describing all sections of the EXC4 $E_{tot}(a)$ curve 258

B.10 Mean, standard deviation, and maximum absolute value of the functions $\Delta E^{(1)}(a)$ and $\Delta E^{(2)}(a)$ obtained using approach 1 275

B.11 Mean, standard deviation, and maximum absolute value of the functions $\Delta E^{(1)}(a)$ and $\Delta E^{(2)}(a)$ obtained using approach 2 277

B.12 Comparison of the standard deviation and absolute maximum value of the functions $\Delta E^{(1)}(a)$ and $\Delta E^{(2)}(a)$ obtained using approach 1 and approach 2 278

B.13 Numerical precision of the first-derivative of the EXC2 and EXC4 $E_{tot}(a)$ curves 279

B.14 Numerical precision of the second-derivative of the EXC2 and EXC4 $E_{tot}(a)$ curves 279

Acronyms and Symbols

3d	- short for "third-row transition", as in "third-row transition metal"
a	- lattice parameter
$a\,(T)$	- equilibrium lattice parameter as a function of temperature
AFM	- anti-ferromagnetic
ASA	- atomic sphere approximation
BCC	- body-centered cubic
BZ	- Brillouin zone
c	- c-axis lattice parameter of a HCP solid
CPE	- calculation precision error
DFT	- density functional theory
$E_{a-a}\,(x)$	- inter-atomic interaction potential
E_{tot}	- minimum total energy of a solid
$E_{tot}\,(a)$	- minimum total energy versus as a function of lattice parameter
EAM	- embedded atom method
ESC	- electronic structure calculation
EXC	- exchange-correlation functional
EXC1	- exchange-correlation functional of von Barth and Hedin
EXC2	- exchange-correlation functional of Hu and Langreth
EXC3	- exchange-correlation functional of Vosko, Wilk and Nusair
EXC4	- exchange-correlation functional of Perdew and Yue
$F\,(a,T)$	- Helmholtz' free energy per atom as a function of lattice parameter and temperature

FCC	- face-centered cubic
FM	- ferromagnetic
HCP	- hexagonal close-packed
INIT1	- initial condition set number 1
INIT2	- initial condition set number 2
LMTO	- linear muffin-tin orbitals
μ	- magnetic moment
$\mu(a)$	- magnetic moment as a function of lattice parameter
$n_v(\epsilon)$	- density of states function of a solid's valence electrons
$\rho_c(\vec{r})$	- spatial distribution of a solid's core electrons
$\rho_v(\vec{r})$	- spatial distribution of a solid's valence electrons
SCE	- systematic calculation error
T	- temperature
TB	- tight binding
TB-LMTO	- tight-binding linear muffin-tin orbitals
WS	- Wigner Seitz

Chapter 1

Introduction

The metals of the first-row transition series (Sc to Zn) are fascinating. A number of these elements undergo structural phase transitions as they are heated [1]. Metallic iron undergoes the well-studied martensitic phase transition at approximately 1183 Kelvin [1]. In addition, the lighter of these elements (Sc, Ti, V) are non-magnetic at ambient pressures and temperatures [2]. In contrast, Cr, Mn, Fe, Co and Ni all exhibit interesting magnetic properties. More specifically, Cr and Mn exhibit complex anti-ferromagnetism while Fe, Co and Ni are ferromagnets [2]. Alloys of these metals also exhibit intriguing thermal properties. For instance, the Invar alloy, consisting of approximately 65 atomic % Fe, exhibits little to no thermal expansion over a broad range of temperatures near room temperature [3].

The first-row transition metals are also very useful. Metals like Cu and Fe are among the first metals used by human beings for tool-making and aesthetic purposes [4]. These metals continue to be used in a wide variety of practical applications, especially iron, as it is an important constituent of steel and other useful alloys [5]. Iron is also believed to be an important constituent of the Earth's inner core [6, p. 421]. A recent experimental study of typical Earth mantle minerals at high pressures and temperatures has also revealed that the Earth's lower mantle may contain small particles of metallic Fe [7]. In addition, the presence of iron in the deep interiors of planetary bodies is substantiated by the existence

of a class of iron-bearing meteorites believed to have originated in the depths of asteroidal or planetary bodies [8].

As a result of its interesting magnetic and structural properties, of its practical usefulness, and of its importance in the field of geophysics, metallic iron has been the object of considerable experimental and theoretical study in recent years. One recent experimental study of Fe-rich Fe-Ni alloys has resulted in a new understanding of the magnetic properties of metallic Fe [9, 10]. These studies have revealed that FCC Fe-Ni alloys consisting of more than 70 atomic % Fe have no magnetic moments at zero Kelvin, but that magnetic moments appear in these alloys as their temperature is increased. This is likely to be occurring in pure metallic Fe when it takes the FCC crystal structure [11]. Also, these studies have revealed that the anomalously low thermal expansion exhibited by the Invar alloys [3] is the result of an unusual volume dependence of their ferromagnetism. This dependence is itself the result of a composition controlled low-moment to high-moment transition that occurs in the FCC Fe-Ni alloy system.

These results have important implications. First of all, this new understanding of the Invar and anti-Invar property of Fe-rich alloys could lead to the design of new materials with novel thermal properties. In addition, even though a number of studies of metallic Fe under the pressure and temperature conditions characteristic of planetary interiors have been conducted [11–27], these studies are of non-magnetic phases of metallic Fe. The observed unconventional magnetic properties of metallic Fe may affect the properties of this metal as it exists in planetary or asteroidal bodies, or as it exists in meteoritic fragments of such bodies.

In light of this, we wish to develop a theoretical method for calculating the thermal properties of metallic Fe that incorporates the microscopic phenomena at the root of the Invar and anti-Invar behaviours. This method should be sufficiently precise and sufficiently accurate to allow for the theoretical prediction of the properties of metallic Fe under the conditions of high pressure and temperature that are characteristic of planetary interiors.

This thesis consists of a pair of related studies. The first is a first-principles study of the magnetic properties of the first-row transition metals (Sc to Ni) when they adopt the FCC crystal structure. The second is a theoretical study of the thermal expansion of metallic Cu. In order to conduct this study, we derive a theoretical method for calculating the Helmholtz' free energy of bulk, non-magnetic, crystalline solids consisting of a single chemical species. We intend that this be the first step in the development of a method for calculating the Helmholtz' free energy of metallic Fe that incorporates the microscopic phenomena at the root of the Invar and anti-Invar behaviours.

We thus begin, in chapter 2, with a description of an ESC program [28] based on the TB-LMTO theory of Andersen et al. [29–32]. This TB-LMTO ESC program [28] can be used to calculate the zero-Kelvin properties of bulk, crystalline solids. In chapter 3, we discuss some aspects of the program that affect its numerical precision. We also evaluate the numerical precision of the total energy of solids, as calculated using the program. In chapter 4, we study the accuracy of the TB-LMTO ESC program [28] by using it to calculate some zero-Kelvin properties of the first-row transition metals. We focus on these metals because metallic Fe is among them. We study the accuracy of the TB-LMTO ESC program when it is used in conjunction with all four exchange-correlation functionals that are available within it. Chapters 3 and 4 are in effect an evaluation of the numerical precision and of the accuracy of the TB-LMTO ESC program [28] prior to using it in our study of the magnetism of the FCC first-row transition metals and in our study of the thermal expansion of metallic Cu.

We then study in chapter 5 the magnetic properties of the first-row transition metals (Sc to Ni) when they take the FCC crystal structure. We conduct this study using the TB-LMTO ESC program [28], and specifically study the volume controlled low-moment to high-moment magnetic transition that occurs in all of these metals. This study reveals that metallic Fe occupies a unique position within the first-row transition metal series. The study also provides insights into the magnetic moment formation process in the first-row transition metals.

In chapter 6, we present a theoretical method for calculating the Helmholtz' free energy of bulk, crystalline solids consisting of a single chemical species. The method assumes only that an inter-atomic interaction potential can be derived from the minimum total energy versus lattice parameter curve of a solid, and that this potential can accurately reproduce the energy increase that occurs when the atomic nuclei of the solid move away from their equilibrium positions as they undergo small amplitude thermal oscillations. We argue that the method is entirely theoretical, as the minimum total energy versus lattice parameter curve of a solid can be calculated using an ESC program. When using the method, we can choose to treat the atomic nuclei of solids as independent harmonic oscillators or as coupled harmonic oscillators.

Then, in chapter 7, we use the theoretical method of chapter 6 to study the thermal expansion of metallic Cu. We specifically study metallic Cu as it is a first-row transition metal like metallic Fe, and because it possesses the FCC crystal structure, as does metallic Fe at high temperatures [1]. Also, metallic Cu has no magnetic moments at all temperatures (it is a diamagnetic metal). We use the TB-LMTO ESC program [28] to calculate the minimum total energy versus lattice parameter curve of FCC Cu. We then use this curve to define an inter-atomic interaction potential, and then to calculate the Helmholtz' free energy of metallic Cu as a function of its lattice parameter and temperature. Using the calculated Helmholtz' free energy of metallic Cu, we then calculate the equilibrium lattice parameter of metallic Cu as a function of its temperature. By evaluating the accuracy of the equilibrium lattice parameter of metallic Cu, as calculated using the theoretical method of chapter 6, we evaluate indirectly the accuracy of the Helmholtz' free energy of metallic Cu, also as calculated using the method of chapter 6.

Finally, in chapter 8, we summarise the main conclusions and accomplishments of the previous chapters, and recommend areas of focus for future research efforts.

This thesis also contains two appendices. Appendix A contains a review of the literature discussing the use of ESC programs to calculate the zero-Kelvin properties of the first-row transition metals. In addition, appendix B discusses a parametrization of the minimum

total energy versus lattice parameter curve of FCC Cu, as calculated using the TB-LMTO ESC program [28], for the purpose of using it in the calculation of the Helmholtz' free energy of metallic Cu as per the theoretical method of chapter 6.

The main scientific contributions of this thesis are:

- a novel treatment of the numerical errors in the results of electronic structure calculations, inspired from a standard treatment of experimental measurement errors.
- original calculations of the ground state properties of the first-row transition metals using the TB-LMTO ESC program [28].
- an original study of the volume-controlled LM-HM transition occurring in the FCC 3d metals.
- a novel method for calculating the Helmholtz' free energy of bulk, crystalline, non-magnetic solids consisting of a single chemical species.
- original calculations of the Helmholtz' free energy and lattice parameter versus temperature curve of metallic Cu.

We expect that the results of this thesis will be of interest to all who are interested in the theoretical calculation of the ground state and thermal properties of solids, in particular those of bulk, crystalline solids. Researchers interested in the magnetic properties of solids will also find this research relevant, as will researchers seeking to understand the properties of materials under conditions of high temperature and pressure.

Chapter 2

The TB-LMTO ESC Program

In this thesis, we conduct a number of theoretical studies of the properties of the first-row transition metals (Sc to Zn). In chapters 4 and 5, we study the properties of these metals at zero Kelvin, and in chapters 6 and 7, we study the thermal expansion of metallic Cu. In conducting these studies, we use an electronic structure calculation (ESC) program to calculate the minimum total energy versus lattice parameter curve $E_{tot}\,(a)$ of these metals, as well as the spatial distribution of the electrons within these metals.

The particular ESC program that we use is based on the tight-binding linear muffin-tin orbitals (TB-LMTO) ESC method [29–32]. This ESC method is itself based on density functional theory (DFT) [33,34]. We specifically use version 4.7 of the TB-LMTO ESC program [28], developed by G. Krier, M. van Schilfgaarde, A. T. Paxton, O. Jepsen and O. K. Andersen at the Max Planck Institute for Solid State Research. This program is sometimes termed the "Stuttgart TB-LMTO program". From this point onwards, we shall use the term "TB-LMTO ESC program" to designate specifically this particular ESC program.

The purpose of this chapter is to provide a basic summary of the physical and mathematical basis of the TB-LMTO ESC program in order to facilitate the understanding of the research presented in the later chapters of this thesis. In section 2.1, we provide a description of DFT. Then, in section 2.2, we describe what we consider to be the most important

aspects of the implementation of DFT within the TB-LMTO ESC program. This chapter is not meant to be a complete description of the TB-LMTO ESC program. Readers interested in a more complete description of the TB-LMTO ESC program should refer to the work of Andersen and Skriver [29–32], and to the program's user manual [35].

2.1 Physical and Mathematical Basis of DFT

We here provide a description of the physical and mathematical basis of density functional theory (DFT), a theory that can be used to calculate the lowest-energy electron distribution and the minimum total energy of a solid. As previously indicated, the TB-LMTO ESC program [28] is based on DFT.

2.1.1 The Total Energy of a Solid

The total energy of a solid consists of the kinetic energy and electrostatic potential energy of the solid's constituent atomic nuclei and electrons. The Hamiltonian operator giving the total energy of a solid can be written as:

$$\begin{aligned} H_{tot} &= \sum_I \frac{\vec{P_I}^2}{2M_I} + \sum_i \frac{\vec{p_i}^2}{2m} - \sum_I \sum_i \frac{qQ_I}{|\vec{R_I} - \vec{r_i}|} \\ &+ \frac{1}{2}\sum_i \sum_{j \neq i} \frac{q^2}{|\vec{r_i} - \vec{r_j}|} + \frac{1}{2}\sum_I \sum_{J \neq I} \frac{Q_I Q_J}{|\vec{R_I} - \vec{R_J}|}, \end{aligned} \tag{2.1}$$

where q, m, $\vec{r_i}$ and $\vec{p_i}$ are the charge, mass, position and momentum of the i^{th} electron in the solid while Q_I, M_I, $\vec{R_I}$ and $\vec{P_I}$ are the charge, mass, position and momentum of the I^{th} atomic nucleus in the solid. In equation 2.1, the operators $\vec{P_I}^2$ and $\vec{p_i}^2$ must be understood as $\vec{P_I}^2 = \vec{P_I} \cdot \vec{P_I} = -\hbar^2 \nabla_I^2$ and $\vec{p_i}^2 = \vec{p_i} \cdot \vec{p_i} = -\hbar^2 \nabla_i^2$. Additionally, the summations over i and I are respectively summations over all electrons and all atomic nuclei in a specific solid. The total energy of a solid is $< \Psi_{tot}|H_{tot}|\Psi_{tot} >$ when $|\Psi_{tot} >$ is the quantum state of the solid's constituent atomic nuclei and electrons. The first two terms in equation 2.1

are operators giving the total kinetic energy of the solid's atomic nuclei and of the solid's electrons respectively. The third term in the equation is the operator giving the energy that is due to the electrostatic interaction between each atomic nucleus and each electron in the solid. The fourth term gives the energy due to the electrostatic interaction between each pair of electrons in the solid. Finally, the fifth term gives the energy due to the electrostatic interaction between each pair of atomic nuclei in the solid.

The calculation of the eigenstates of the Hamiltonian H_{tot} represents a formidable mathematical problem. Without approximations, this problem is mathematically intractable because of the difficulty inherent in applying quantum mechanics in treating a large number of interacting bodies. However, the calculation of the eigenstates of H_{tot} can be simplified by separating the Hamiltonian into an atomic and an electronic component. This is physically justified by an argument first reported by Born and Oppenheimer [36]. Specifically, Born and Oppenheimer argued that the kinetic energy of a solid's electrons is much higher than that of the solid's atomic nuclei. As a result, the electrons of the solid adjust very rapidly to any changes in the position of its atomic nuclei. Thus, it is reasonable to calculate the eigenstate of the electrons of a solid assuming that its atomic nuclei remain stationary at well-defined positions in space. The complete eigenstate of the solid can then be calculated by treating its atomic nuclei as particles moving in an effective field produced by its electrons.

If the atomic nuclei of a solid are assumed to be stationary, then the vectors $\vec{R}_I$ in the expression for H_{tot} are constants and the kinetic energy of the solid's atomic nuclei is null. This transforms equation 2.1 to the following expression:

$$H_{tot} = H_{e_{tot}} + \frac{1}{2}\sum_{I}\sum_{J\neq I}\frac{Q_I Q_J}{|\vec{R}_I - \vec{R}_J|}, \tag{2.2}$$

where:

$$H_{e_{tot}} = \sum_{i}\frac{\vec{p_i}^2}{2m} - \sum_{I}\sum_{i}\frac{qQ_I}{|\vec{R}_I - \vec{r_i}|} + \frac{1}{2}\sum_{i}\sum_{j\neq i}\frac{q^2}{|\vec{r_i} - \vec{r_j}|}. \tag{2.3}$$

The Hamiltonian $H_{e_{tot}}$, given in equation 2.3, describes the total energy of the electrons in a solid when this solid's atomic nuclei remain stationary at positions specified by the vectors $\vec{R}_I$.

The TB-LMTO ESC program [28] is designed expressly to find the lowest-energy eigenstate of the Hamiltonian H_{tot} as expressed in equation 2.2. The energy of this eigenstate, which we label E_{tot}, is the minimum total energy of the solid assuming that its constituent atomic nuclei remain stationary at well-defined positions in space. It is argued that E_{tot} is the total energy of a real solid at zero Kelvin, but this is not quite the case. The atomic nuclei of a real solid are always in motion, even at zero Kelvin, as a result of the quantum-mechanical phenomenon of zero point motion [37, p. 416]. However, the energy of the atomic nuclei of a solid at zero Kelvin, typically of the order of 10^{-3} Rydberg units, is much smaller than E_{tot}, which is typically of the order of 10^{3} Rydberg units. Thus, E_{tot} is a good approximation of the minimum total energy of a real solid.

2.1.2 The Hartree-Fock ESC Method

One of the earliest ESC methods is termed the Hartree-Fock method [38]. The mathematical basis of this ESC method is neatly summarised in the text of Ashcroft and Mermin [37]. It is repeated here since understanding the derivation of the main equations of the Hartree-Fock method facilitates one's understanding of the derivation of the main equations of density functional theory.

The Hartree-Fock method begins with the expression for the total energy of the electrons in a solid, $E_{e_{tot}} =< \Psi|H_{e_{tot}}|\Psi >$, where $|\Psi >$ is the quantum state of the electrons in the solid, and $H_{e_{tot}}$ is as given in equation 2.3. To evaluate $E_{e_{tot}}$, the wave function $\Psi(\vec{r_1}, s_1; \vec{r_2}, s_2; ...; \vec{r_N}, s_N)$ of all electrons in the solid must be known. Hartree proposed that $\Psi(\vec{r_1}, s_1; \vec{r_2}, s_2; ...; \vec{r_N}, s_N)$ can be expressed as the following Slater determinant [37,38]:

$$\Psi\left(\vec{r_1}, s_1; \vec{r_2}, s_2; \cdots; \vec{r_N}, s_N\right) = \frac{1}{\sqrt{N!}} \begin{vmatrix} \psi_1(\vec{r_1}, s_1) & \psi_1(\vec{r_2}, s_2) & \cdots & \psi_1(\vec{r_N}, s_N) \\ \psi_2(\vec{r_1}, s_1) & \psi_2(\vec{r_2}, s_2) & \cdots & \psi_2(\vec{r_N}, s_N) \\ \vdots & \vdots & \ddots & \vdots \\ \psi_N(\vec{r_1}, s_1) & \psi_N(\vec{r_2}, s_2) & \cdots & \psi_N(\vec{r_N}, s_N) \end{vmatrix}, \qquad (2.4)$$

where N is the total number of electrons in the solid, while $\vec{r_i}$ and s_i represent respectively the position and the spin quantum number of the i^{th} electron in the solid. Also, the wave

functions $\psi_i(\vec{r}, s_i)$ are wave functions associated to quantum states that are available to the individual electrons within the solid. If the single-electron wave functions $\psi_i(\vec{r}, s_i)$ are spatially orthonormal, then the total energy of the electrons in the solid is [37,38]:

$$\begin{aligned} E_{e_{tot}} &= \sum_i \int \vec{dr} \psi_i^*(\vec{r}, s_i) \frac{\vec{p}^2}{2m} \psi_i(\vec{r}, s_i) \\ &- \sum_i \int \vec{dr} \psi_i^*(\vec{r}, s_i) \left\{ \sum_I \frac{Q_I q}{|\vec{R}_I - \vec{r}|} \right\} \psi_i(\vec{r}, s_i) \\ &+ \frac{1}{2} \sum_{i,j} \int \int \vec{dr} \vec{dr'} \frac{q^2}{|\vec{r} - \vec{r'}|} |\psi_i(\vec{r}, s_i)|^2 |\psi_j(\vec{r'}, s_j)|^2 \\ &- \frac{1}{2} \sum_{i,j} \int \int \vec{dr} \vec{dr'} \frac{q^2}{|\vec{r} - \vec{r'}|} \delta_{s_i s_j} \psi_i^*(\vec{r}, s_i) \psi_i(\vec{r'}, s_i) \psi_j^*(\vec{r'}, s_j) \psi_j(\vec{r}, s_j), \end{aligned} \tag{2.5}$$

where the summations over i and j are summations over each electron in the solid, while the summation over I is a summation over each atomic nucleus in the solid. The first term in equation 2.5 is the total kinetic energy of the solid's electrons. The second term is the energy that is due to the electrostatic interaction between each of the solid's electrons and each of the solid's atomic nuclei. Finally, the last two terms give the energy that is due to the electrostatic interaction between each pair of the solid's electrons. The third term in equation 2.5 is termed the "direct electrostatic energy" of the solid's electrons, while the fourth term is termed the "exchange energy" of the solid's electrons. The exchange energy term is a correction of the direct electrostatic energy term in order to take into account that electrons do not interact with themselves (self-interaction correction) and must obey Pauli's exclusion principle [39]. The delta function $\delta_{s_i s_j}$ in the exchange energy term indicates that only electron pairs possessing the same spin quantum number are considered in the calculation of the exchange energy.

Using equation 2.5, it is possible to find the single-electron wave functions $\psi_i(\vec{r}, s_i)$ that minimise the total energy $E_{e_{tot}}$. An equation for a specific wave function $\psi_x(\vec{r}, s_x)$ can be constructed by minimising $E_{e_{tot}}$ with respect to the function $\psi_x^*(\vec{r}, s_x)$ (namely the complex conjugate of $\psi_x(\vec{r}, s_x)$), all the while respecting the constraint that $\int \vec{dr} |\psi_x(\vec{r}, s_x)|^2 = 1$. This is accomplished by simultaneously minimising with respect to the function $\psi_x^*(\vec{r}, s_x)$

and with respect to the Lagrange multiplier ϵ_x the function $Y(\psi_x^*(\vec{r}, s_x), \epsilon_x) = E_{e_{tot}} - \epsilon_x\{\int \vec{dr}|\psi_x(\vec{r}, s_x)|^2 - 1\}$. Setting equal to zero the functional derivative of $Y(\psi_x^*(\vec{r}, s_x), \epsilon_x)$ with respect to $\psi_x^*(\vec{r}, s_x)$ gives [37,38]:

$$\begin{aligned}\frac{\vec{p}^2}{2m}\psi_x(\vec{r}, s_x) \;&-\; \sum_I \frac{Q_I q}{|\vec{R}_I - \vec{r}|}\psi_x(\vec{r}, s_x) + \sum_i \int \vec{dr'} \frac{q^2}{|\vec{r} - \vec{r'}|}|\psi_i(\vec{r'}, s_i)|^2\psi_x(\vec{r}, s_x) \\ &-\; \sum_i \int \vec{dr'} \frac{q^2}{|\vec{r} - \vec{r'}|}\delta_{s_x s_i}\psi_x(\vec{r'}, s_x)\psi_i^*(\vec{r'}, s_i)\psi_i(\vec{r}, s_i) = \epsilon_x\psi_x(\vec{r}, s_x). \quad (2.6)\end{aligned}$$

Equation 2.6 is clearly very similar to Schrödinger's equation [40]. It can be used to find the wave function $\psi_x(\vec{r}, s_x)$, which is the wave function of one of the solid's electrons *in the field of all other electrons and atomic nuclei in the solid*, when all other electrons in the solid have known wave functions $\psi_i(\vec{r}, s_i)$. The Lagrange multiplier ϵ_x is simply the energy of the electron that has the wave function $\psi_x(\vec{r}, s_x)$. Equation 2.6 can be used to calculate the single-electron wave functions $\psi_i(\vec{r}, s_i)$ that minimise $E_{e_{tot}}$ (one wave function for each electron in the solid), as well as the corresponding single-electron energy values ϵ_i.

Once the single-electron wave functions $\psi_i(\vec{r}, s_i)$ are known, they can be used in conjunction with equation 2.5 to calculate the minimum value of $E_{e_{tot}}$. However, this requires evaluating the kinetic energy of the electrons in the solid as follows:

$$E_{e_{kin}} = \sum_i \int \vec{dr}\psi_i^*(\vec{r}, s_i)\frac{\vec{p}^2}{2m}\psi_i(\vec{r}, s_i). \quad (2.7)$$

There is a simpler way of evaluating the minimum value of $E_{e_{tot}}$ using the energy values ϵ_i and the single-electron wave functions $\psi_i(\vec{r}, s_i)$. Specifically, using equations 2.6 and 2.7, one can show that the total kinetic energy of the electrons in the solid is:

$$\begin{aligned}E_{e_{kin}} \;&=\; \sum_i \epsilon_i + \sum_i \int \vec{dr} \sum_I \frac{Q_I q}{|\vec{R}_I - \vec{r}|}|\psi_i(\vec{r}, s_i)|^2 \\ &-\; \sum_{i,j} \int\int \vec{dr}\vec{dr'} \frac{q^2}{|\vec{r} - \vec{r'}|}|\psi_i(\vec{r}, s_i)|^2|\psi_j(\vec{r'}, s_j)|^2 \\ &+\; \sum_{i,j} \int\int \vec{dr}\vec{dr'} \frac{q^2}{|\vec{r} - \vec{r'}|}\delta_{s_i s_j}\psi_i^*(\vec{r}, s_i)\psi_i(\vec{r'}, s_i)\psi_j^*(\vec{r'}, s_j)\psi_j(\vec{r}, s_j). \quad (2.8)\end{aligned}$$

The expression for the minimum value of $E_{e_{tot}}$ can be simplified by substituting equation 2.8 into equation 2.5 as follows:

$$\begin{aligned} E_{e_{tot}} &= \sum_i \epsilon_i \\ &- \frac{1}{2}\sum_{i,j}\int\int \vec{dr}\vec{dr'}\frac{q^2}{|\vec{r}-\vec{r'}|}|\psi_i(\vec{r},s_i)|^2|\psi_j(\vec{r'},s_j)|^2 \\ &+ \frac{1}{2}\sum_{i,j}\int\int \vec{dr}\vec{dr'}\frac{q^2}{|\vec{r}-\vec{r'}|}\delta_{s_i s_j}\psi_i^*(\vec{r},s_i)\psi_i(\vec{r'},s_i)\psi_j^*(\vec{r'},s_j)\psi_j(\vec{r},s_j). \end{aligned} \tag{2.9}$$

It is simpler to calculate the minimum value of $E_{e_{tot}}$ using equation 2.9 than equation 2.5 because the first two terms of equation 2.5 are replaced by a simple summation in equation 2.9. Nonetheless, the calculation of the minimum value of $E_{e_{tot}}$ using equation 2.9 remains very cumbersome, for it requires the evaluation of many integrals involving the single-electron wave functions $\psi_i(\vec{r},s_i)$. Density functional theory (DFT), which we discuss in the next section, provides an even simpler procedure for calculating the minimum value of $E_{e_{tot}}$.

Before beginning our discussion of DFT, we emphasize that the Hartree-Fock method is based on an independent electron approximation. Specifically, equation 2.6 allows for the calculation of the wave function of one electron assuming that all other electrons have wave functions that are independent of the first's. In reality, the electrons in a solid are not independent, as electrons interact via the electrostatic interaction. The deviation from physical reality that this approximation entails is partially eliminated by requiring that the single-electron wave functions $\psi_i(\vec{r},s_i)$ be calculated using a self-consistent procedure. However, because the Hartree-Fock ESC method is derived using an independent electron approximation, the method fails to account for any correlations that can exist between the electrons in a solid due to their Coulomb repulsion. Electron correlations are important in modelling super-conductivity (which results from Cooper pair formation) and in modelling the propagation of the exchange-correlation hole along with an electron as it moves through the solid (see section 2.1.3).

2.1.3 Density Functional Theory

Developed in the mid 1960's [33,34], density functional theory (DFT) is the theoretical basis of many of the modern ESC programs, including the TB-LMTO ESC program [28]. ESC methods based on DFT are simpler and less computationally intensive than the Hartree-Fock ESC method.

The derivation of DFT begins with the Hamiltonian $H_{e_{tot}}$ (equation 2.3). In 1964, Hohenberg and Kohn published a landmark paper proving that $E_{e_{tot}}$, the smallest eigenvalue of $H_{e_{tot}}$, can be expressed as a functional of $\rho(\vec{r})$, the spatial distribution or density of a solid's electrons [33]. Additionally, they proved that the functional $E_{e_{tot}}[\rho(\vec{r})]$ has a single global minimum value which corresponds to a unique electron density $\rho(\vec{r})$ [33]. Thus, $E_{e_{tot}}[\rho(\vec{r})]$ can be expressed as follows [33,34]:

$$E_{e_{tot}}[\rho(\vec{r})] = T[\rho(\vec{r})] + V_{ext}[\rho(\vec{r})] + U[\rho(\vec{r})], \tag{2.10}$$

where $T[\rho(\vec{r})]$ is the kinetic energy of the electrons of the solid (see the first term of equation 2.3), $V_{ext}[\rho(\vec{r})]$ is the energy resulting from the electrostatic interaction between the solid's electrons and atomic nuclei (and from any other field externally applied to the solid's electrons), and $U[\rho(\vec{r})]$ is the energy resulting from the electrostatic interaction of the electrons of the solid. If $V_{ext}[\rho(\vec{r})]$ is due only to the electrostatic interaction of the solid's electrons with the solid's atomic nuclei, it can be expressed as a functional of $\rho(\vec{r})$ as follows:

$$V_{ext}[\rho(\vec{r})] = -\int \vec{dr} \sum_I \frac{Q_I q}{|\vec{R}_I - \vec{r}|}\rho(\vec{r}). \tag{2.11}$$

In contrast, the functionals $T[\rho(\vec{r})]$ and $U[\rho(\vec{r})]$ are more difficult to construct.

Perhaps inspired by the Hartree-Fock ESC method, Kohn and Sham proposed that $T[\rho(\vec{r})]$

and $U[\rho(\vec{r})]$ can be expressed together as [34]:[1]

$$T[\rho(\vec{r})] + U[\rho(\vec{r})] = T_s[\rho(\vec{r})] + \frac{1}{2}\int\int \vec{dr}\vec{dr'}\frac{q^2}{|\vec{r}-\vec{r'}|}\rho(\vec{r})\rho(\vec{r'}) - E_{xc}[\rho(\vec{r})], \tag{2.12}$$

and that $E_{e_{tot}}$ can be expressed as [34]:

$$\begin{aligned} E_{e_{tot}} &= T_s[\rho(\vec{r})] - \int \vec{dr}\sum_I \frac{Q_I q}{|\vec{R}_I - \vec{r}|}\rho(\vec{r}) \\ &+ \frac{1}{2}\int\int \vec{dr}\vec{dr'}\frac{q^2}{|\vec{r}-\vec{r'}|}\rho(\vec{r})\rho(\vec{r'}) - E_{xc}[\rho(\vec{r})], \end{aligned} \tag{2.13}$$

where $E_{xc}[\rho(\vec{r})]$ is termed an "exchange-correlation functional" and $T_s[\rho(\vec{r})]$ is the kinetic energy of the electrons in the solid obtained via a single-electron approximation similar to that made in deriving the Hartree-Fock equations. More specifically [34]:

$$\begin{aligned} T_s[\rho(\vec{r})] &= \sum_i \epsilon_i + \int \vec{dr}\sum_I \frac{Q_I q}{|\vec{R}_I - \vec{r}|}\rho(\vec{r}) \\ &- \int\int \vec{dr}\vec{dr'}\frac{q^2}{|\vec{r}-\vec{r'}|}\rho(\vec{r})\rho(\vec{r'}) + \sum_s \int \vec{dr} V_{xc}(\vec{r}, s)\,\rho_s(\vec{r}), \end{aligned} \tag{2.14}$$

where the "exchange-correlation potential" $V_{xc}(\vec{r}, s)$ is the functional derivative of $E_{xc}[\rho(\vec{r})]$ with respect to $\rho_s(\vec{r})$, and $\rho_s(\vec{r})$ is the spatial distribution of the electrons within the solid that have spin eigenstate s. Furthermore, the single-electron energy values ϵ_i appearing in equation 2.14 are the eigenvalues of the Hamiltonian [34]:

$$H = \frac{\vec{p}^2}{2m} - \sum_I \frac{Q_I q}{|\vec{R}_I - \vec{r}|} + \int \vec{dr'}\frac{q^2}{|\vec{r}-\vec{r'}|}\rho(\vec{r'}) - V_{xc}(\vec{r}, s_x). \tag{2.15}$$

Equations 2.13, 2.14 and 2.15 are respectively analogous to equations 2.5, 2.8 and 2.6, and can be used in a variational procedure, originally proposed by Kohn and Sham [34], for finding the lowest-energy electron distribution and minimum total energy of a solid. The Kohn-Sham procedure begins with an initial estimate of the solid's lowest-energy electron

[1] In the paper of Kohn and Sham [34], $E_{xc}[\rho(\vec{r})]$ is added to $T_s[\rho(\vec{r})] + \frac{1}{2}\int\int \vec{dr}\vec{dr'}\frac{q^2}{|\vec{r}-\vec{r'}|}\rho(\vec{r})\rho(\vec{r'})$ to make $T[\rho(\vec{r})] + U[\rho(\vec{r})]$. In the TB-LMTO ESC program [28], $T[\rho(\vec{r})] + U[\rho(\vec{r})]$ is implemented by subtracting $E_{xc}[\rho(\vec{r})]$ from $T_s[\rho(\vec{r})] + \frac{1}{2}\int\int \vec{dr}\vec{dr'}\frac{q^2}{|\vec{r}-\vec{r'}|}\rho(\vec{r})\rho(\vec{r'})$. This is why we express $T[\rho(\vec{r})] + U[\rho(\vec{r})]$ as per equation 2.12.

distribution $\rho(\vec{r})$. Single-electron energy values ϵ_i are calculated using equation 2.15, and the energy of the electrons when they take the initial electron distribution is calculated using equations 2.13 and 2.14. The electron density is then varied. Using the new electron distribution, equation 2.15 is again used to calculate single-electron energy values ϵ_i, and the energy of the electrons when they take the new electron distribution is calculated using equations 2.13 and 2.14. If this latter energy is smaller than the first calculated value of $E_{e_{tot}}$, the new electron distribution is adopted as an improved estimate of the lowest-energy electron distribution of the solid. The electron distribution is varied again and the process continues until the lowest-energy electron distribution is found.

The only remaining difficulty in applying the variational procedure of Kohn and Sham is the construction of the exchange-correlation functional $E_{xc}[\rho(\vec{r})]$ and the exchange-correlation potential $V_{xc}(\vec{r}, s)$ appearing in equations 2.13, 2.14 and 2.15. We have already stated that $V_{xc}(\vec{r}, s)$ is the functional derivative of $E_{xc}[\rho(\vec{r})]$ with respect to the density of electrons with spin s, $\rho_s(\vec{r})$. $E_{xc}[\rho(\vec{r})]$, on the other hand, is defined from equation 2.12 as follows:

$$E_{xc}[\rho(\vec{r})] = T_s[\rho(\vec{r})] - T[\rho(\vec{r})] + \frac{1}{2}\int\int \vec{dr}\vec{dr'}\frac{q^2}{|\vec{r}-\vec{r'}|}\rho(\vec{r})\rho(\vec{r'}) - U[\rho(\vec{r})], \tag{2.16}$$

where $E_c[\rho(\vec{r})] = T_s[\rho(\vec{r})] - T[\rho(\vec{r})]$ is termed a "correlation functional", and $E_x[\rho(\vec{r})] = \frac{1}{2}\int\int \vec{dr}\vec{dr'}\frac{q^2}{|\vec{r}-\vec{r'}|}\rho(\vec{r})\rho(\vec{r'}) - U[\rho(\vec{r})]$ is termed an "exchange functional".

To understand the construction of the exchange component $E_x[\rho(\vec{r})]$, it is necessary to understand how the total electrostatic energy of a solid's electrons should be correctly calculated. This energy, which we have labelled $U[\rho(\vec{r})]$, is the result of the electrostatic interaction of all pairs of electrons within the solid. The correct expression for this energy is:

$$U[\rho(\vec{r})] = \frac{1}{2}\int\int \frac{q^2}{\left|\vec{r}-\vec{R}\right|}\rho(\vec{R})\rho_{\vec{R}}(\vec{r})\,\vec{dr}\vec{dR}, \tag{2.17}$$

where $\rho(\vec{r})$ is the average spatial distribution of the electrons in the solid, and $\rho_{\vec{R}}(\vec{r})$ is the distribution of the remaining electrons in the solid when one of them is located at $\vec{r} = \vec{R}$. The distribution $\rho(\vec{r})$ satisfies $\int \vec{dr}\rho(\vec{r}) = N$, where N is the total number of electrons in the solid. In addition, all distributions $\rho_{\vec{R}}(\vec{r})$ satisfy $\int \vec{dr}\rho_{\vec{R}}(\vec{r}) = (N-1)$.

These latter distributions are analogous to conditional probability distributions. They take into account that, due to Pauli's exclusion principle, the average distribution of a solid's electrons is not the same as the distribution of the solid's electrons when it is known that one of these electrons is located at $\vec{r} = \vec{R}$.

An elegant and physically insightful expression for $E_x[\rho(\vec{r})]$ was proposed in 1951, well before the development of DFT, by J. C. Slater. In an effort to simplify the Hartree-Fock method, Slater proposed that the presence of an electron at $\vec{r} = \vec{R}$ produces an "exchange hole" around it, within which no other electrons possessing the same spin can be located [39]. Thus, when an electron with spin s is located at $\vec{r} = \vec{R}$, one can define a distribution $\rho_{s,\vec{R}}(\vec{r})$ as follows:

$$\rho_{s,\vec{R}}(\vec{r}) = \begin{cases} 0 & \text{if } \left|\vec{R} - \vec{r}\right| \leq r_x \\ \rho_s(\vec{r}) & \text{if } \left|\vec{R} - \vec{r}\right| > r_x \end{cases}, \tag{2.18}$$

where r_x is the radius of the exchange hole (assumed to be spherical) surrounding the electron at $\vec{r} = \vec{R}$. To define r_x, Slater assumed that the electron density in the vicinity of $\vec{r} = \vec{R}$ is constant. This is termed a "local density approximation" (LDA), and leads to the following expression for r_x:

$$r_x = \left(\frac{3}{4\pi\rho_s\left(\vec{R}\right)}\right)^{\frac{1}{3}}. \tag{2.19}$$

Having defined the distributions $\rho_{s,\vec{R}}(\vec{r})$ in the LDA, Slater arrived at an elegant functional expression for $E_x[\rho(\vec{r})]$, namely:

$$E_x[\rho(\vec{r})] = 3^{\frac{2}{3}}\{4\pi\}^{\frac{1}{3}}\frac{q^2}{2}\sum_s \int d\vec{r}\rho_s(\vec{r})^{\frac{4}{3}}. \tag{2.20}$$

In reporting their development of DFT, Kohn and Sham proposed that an exchange-correlation functional can be defined as [34]:

$$E_{xc}[\rho(\vec{r})] = \int d\vec{r}\rho(\vec{r})\,\epsilon_{xc}(\rho(\vec{r})), \tag{2.21}$$

where $\epsilon_{xc}(\rho(\vec{r}))$ is the exchange and correlation energy per electron of a homogeneous electron gas of density $\rho(\vec{r})$. This description is valid only for slowly varying electron

densities $\rho(\vec{r})$, and so can be considered a "local exchange-correlation functional" (ie. derived using a LDA). A number of researchers proposed means of calculating the exchange-correlation energy per electron of the uniform electron gas, $\epsilon_{xc}(\rho(\vec{r}))$, sometimes using theoretical models of such a gas (e.g. [41–43]), and sometimes using computer simulations of such a gas (e. g. [44–46]).

Kohn and Sham had also recognized, in their original development of DFT, that exchange-correlation functionals derived in the LDA would fail if the electron density $\rho(\vec{r})$ varies rapidly [34]. In such cases, they proposed that the exchange-correlation energy of a solid can be expressed as:

$$E_{xc}[\rho(\vec{r})] = \int d\vec{r}\rho(\vec{r})\,\epsilon_{xc}(\rho(\vec{r})) + \int d\vec{r}\left|\vec{\nabla}\rho(\vec{r})\right|^2 \epsilon_{xc}^{(2)}(\rho(\vec{r}))\,. \tag{2.22}$$

Equation 2.22, like equation 2.21, is only an approximate expression for $E_{xc}[\rho(\vec{r})]$. However, equation 2.22 is a more complete expression for $E_{xc}[\rho(\vec{r})]$ than equation 2.21 as it accounts for the spatial variation of $\rho(\vec{r})$ by including a term proportional to the gradient $\vec{\nabla}\rho(\vec{r})$. Exchange-correlation functionals constructed in this manner are said to be derived in the "generalized gradient approximation" (GGA). They are also termed "non-local functionals" to distinguish them from local functionals derived in the LDA (for a good review of non-local exchange-correlations functionals, see the work of Langreth and Mehl [47]). Non-local functionals are often implemented as extensions of a local functional (e.g. [48,49]).

The development of exchange-correlation functionals remains an active area of research in DFT. Some recently published exchange-correlation functionals attempt to go beyond the LDA and the GGA by taking into account the full spatial variation of the electron distribution in solids [50].

2.2 Implementation of DFT in the TB-LMTO ESC Program

We now discuss some details of the implementation of DFT in the TB-LMTO ESC program [28]. As its name implies, this ESC program is based on the tight-binding linear muffin-tin orbitals (TB-LMTO) electronic structure calculation scheme [29–32]. We explain, in section 2.2.1, how the TB-LMTO ESC program calculates the single-electron wave functions $\psi_i(\vec{r}, s_i)$ and the single-electron energy values ϵ_i of the electrons in solids. We then explain, in section 2.2.2, how the TB-LMTO ESC program uses these single-electron wave functions and energy values to calculate the lowest-energy spatial distribution and minimum total energy of the electrons in a solid, and then the minimum total energy of the solid. Finally, in section 2.2.3, we provide information about three other aspects of the TB-LMTO ESC program, namely the combined correction terms, the relativistic treatment of the kinetic energy of electrons, and the exchange-correlation functionals that are available within the program. We repeat that this is not intended to be a complete description of the TB-LMTO ESC program. For more information, readers may refer to the text of H. L. Skriver [32], the TB-LMTO ESC program's user manual [35], as well as the papers of O. K. Andersen et al. [29–31].

2.2.1 The Single-Electron Wave Functions and Energy Values

The TB-LMTO ESC program uses equation 2.15 to calculate the single-electron wave functions $\psi_i(\vec{r}, s_i)$ and the single-electron energy values ϵ_i of the electrons in solids. We here explain these calculations.

First of all, it must be noted that the TB-LMTO ESC program is specifically designed to provide information about infinite solids possessing a periodic, crystalline atomic structure. The atoms of an infinite, chemically ordered, crystalline solid possess translational symmetry [37]. When a solid is in its lowest-energy state, the single-electron wave functions of the solid's electrons usually possess the same (or a similar) translational symmetry as the solid's atoms. Thus, it is not necessary to calculate these wave functions everywhere

within the solid. Rather, it is sufficient to calculate them within the solid's Wigner-Seitz (WS) unit cell only. (For a definition of the Wigner-Seitz unit cell of a solid, see the text of Ashcroft and Mermin [37, p. 73].)

A solid's WS unit cell is usually a complex polyhedron. Within the TB-LMTO ESC program, a solid's WS unit cell is modelled using a collection of spheres (one sphere per atom in the WS unit cell) possessing a total volume that is equal to that of the solid's WS unit cell [32, p. 82]. Each sphere is centered on one of the atoms of the solid's WS unit cell. The use of spheres to approximate the WS unit cell of a solid is termed the "atomic sphere approximation" (ASA) [32, p. 82]. The TB-LMTO ESC program calculates the single-electron wave functions of a solid's electrons within the volume of space defined by the atomic spheres, and not in the true WS unit cell of the solid. It should be noted that the use of the atomic sphere approximation (ASA) introduces errors in the calculated values of the total energy of a solid. The so-called "combined correction terms" can be used to offset the errors introduced by the ASA in the energy values calculated by the TB-LMTO ESC program [32, p. 95]. Users of the TB-LMTO ESC program must specify whether or not the combined correction terms are to be used in any given calculation. (The combined correction terms are explained in greater detail in section 2.2.3.)

The TB-LMTO ESC program calculates, within each atomic sphere defining a solid's WS unit cell, the single-electron wave functions and single-electron energy values of two groups of electrons, labelled "core electrons" and "valence electrons". We now explain the treatment of both groups of electrons within the TB-LMTO ESC program.

Core Electrons

The first group of electrons, the "core electrons", are not engaged in the formation of the solid's chemical bonds. Thus, these electrons remain within one atomic sphere at all times. Each core electron in a particular atomic sphere is associated with a single-electron wave function termed an "atomic orbital", which is like the wave function of an electron bound to a free atom. Specifically, the single-electron wave function of a core electron is

expressed as:

$$\psi_i(\vec{r}, s_i) = Y_{l_i}^{m_i}(\theta, \phi)\, \phi_{l_i}(\epsilon_i, |\vec{r}|, s_i), \tag{2.23}$$

where l_i, m_i and s_i are the orbital angular momentum and spin quantum numbers of the electron, $Y_{l_i}^{m_i}(\theta, \phi)$ is a spherical harmonic function [40], and $\phi_{l_i}(\epsilon_i, |\vec{r}|, s_i)$ is the radial component of the electron's wave function. The vector $\vec{r}$ and the spherical harmonic function $Y_{l_i}^{m_i}(\theta, \phi)$ are both defined with respect to the center of the atomic sphere. Only a finite number of core electrons are located within each atomic sphere. Equation 2.15 is used to calculate the single-electron energy value ϵ_i and the radial component of the wave function of all core electrons in each atomic sphere in the solid's WS unit cell.

Valence Electrons

The TB-LMTO ESC program also calculates, within each atomic sphere defining a solid's WS unit cell, the single-electron wave functions of electrons that are engaged in the formation of the solid's chemical bonds. These electrons, termed "valence electrons", are not confined to a single atomic sphere and may travel throughout the solid. Within the TB-LMTO ESC program, the valence electrons of a solid are each associated with a single-electron wave function termed a "Bloch wave" (see [37, p. 133]). Such a Bloch wave extends throughout the solid, and is expressed as follows [32, p. 18]:[2]

$$\psi_i(\vec{r}, s_i) = \sum_I e^{j\vec{k_i}\cdot\vec{R}_I} \sum_{l,m} a_{l,m}^i \chi_{l,m}(\epsilon_i, \vec{r} - \vec{R}_I, s_i), \tag{2.24}$$

where s_i is the spin quantum number of the valence electron, $\vec{k_i}$ is a vector in reciprocal space, $\vec{R}_I$ is a vector defining the position of the I^{th} atom in the solid, and $j = \sqrt{-1}$. Importantly, each Bloch wave can be associated to a reciprocal space vector $\vec{k_i}$ in the solid's first Brillouin zone (BZ) [37, p. 133]. (The text of Ashcroft and Mermin should be consulted for a definition of a solid's first Brillouin zone [37].) The summation over I in equation 2.24 is

[2]Equation 2.24 is the wave function of a valence electron in a solid possessing only one atom per WS unit cell. The wave function of a valence electron in a solid possessing more than one atom per WS unit cell is given in the text of Skriver [32].

a summation over all atoms in the solid. Also, the summation over the angular momentum quantum numbers l and m is termed a "linear combination of muffin-tin orbitals". The user of the TB-LMTO ESC program must specify the angular momentum quantum numbers l and m that are considered in the summation of equation 2.24. The constants $a^i_{l,m}$ are the coefficients of the linear combination, and the functions $\chi_{l,m}(\epsilon_i, \vec{r} - \vec{R}_I, s_i)$ are "muffin-tin orbitals" associated with the atomic sphere centered at $\vec{R}_I$. A single muffin-tin orbital associated with an atomic sphere centered at the origin is defined as [32, p. 17]:

$$\chi_{l,m}(\epsilon, \vec{r}, s) = Y_l^m(\theta, \phi) \begin{cases} \phi_l(\epsilon, |\vec{r}|, s) + p_l(\epsilon, s) T_0(|\vec{r}|), & |\vec{r}| \leq S \\ T_\infty(|\vec{r}|), & |\vec{r}| > S \end{cases}, \tag{2.25}$$

where l, m and s are the angular momentum and spin quantum numbers of the muffin-tin orbital, $Y_l^m(\theta, \phi)$ is a spherical harmonic function, and $\phi_l(\epsilon, |\vec{r}|, s)$ is the radial component of an atomic orbital located in the atomic sphere that is centered at the origin. Additionally, S is the radius of the atomic sphere centered at the origin, $p_l(\epsilon, s)$ is termed a "potential function", and both $T_0(|\vec{r}|)$ and $T_\infty(|\vec{r}|)$ are functions appropriate for describing the radial component of the wave function of a travelling free electron. The function $T_0(|\vec{r}|)$ must be bounded at $|\vec{r}| = 0$, while $T_\infty(|\vec{r}|)$ must be bounded at $|\vec{r}| \to \infty$. Obviously, the muffin-tin orbital of equation 2.25 is defined differently inside and outside the atomic sphere with which it is associated. Inside the atomic sphere, the muffin-tin orbital consists of an atomic orbital, $Y_l^m(\theta, \phi)\, \phi_l(\epsilon, |\vec{r}|, s)$, plus a term that includes the potential function, $p_l(\epsilon, s) Y_l^m(\theta, \phi)\, T_0(|\vec{r}|)$. Outside the atomic sphere, the muffin-tin orbital is described using a "tail function", $Y_l^m(\theta, \phi)\, T_\infty(|\vec{r}|)$. The potential function $p_l(\epsilon, s)$ is defined to ensure that the muffin-tin orbital is continuous and differentiable at the boundary of the atomic sphere with which it is associated [32, p.18]. When the functions $T_0(|\vec{r}|)$ and $T_\infty(|\vec{r}|)$ are chosen appropriately, $p_l(\epsilon, s)$ is a known function of l, s and ϵ. In the TB-LMTO ESC program, $T_0(|\vec{r}|)$ is a spherical Bessel function while $T_\infty(|\vec{r}|)$ is a spherical Neumann function [32, p. 69].

To calculate the single-electron energy values of a solid's valence electrons, the TB-LMTO ESC program begins with the expression for the Bloch wave function of equation 2.24 in

the atomic sphere centered at the origin (ie. the sphere centered at $\vec{R}_I = \vec{R}_{I_0} = \vec{0}$). Within this atomic sphere (ie. for $|\vec{r}| \leq S$), the Bloch wave function $\psi_i(\vec{r}, s_i)$ can be expressed as:

$$\begin{aligned}\psi_i(\vec{r}, s_i) &= \sum_{l,m} a^i_{l,m} Y^m_l\left(\theta, \phi; \vec{R}_{I_0}\right) \left\{\phi_l(\epsilon_i, |\vec{r}|, s_i) + p_l(\epsilon_i, s_i) T_0(|\vec{r}|)\right\} \\ &+ \sum_{l,m} a^i_{l,m} \sum_{I \neq I_0} e^{j\vec{k}_i \cdot \vec{R}_I} Y^m_l\left(\theta, \phi; \vec{R}_I\right) T_\infty\left(\left|\vec{r} - \vec{R}_I\right|\right), \end{aligned} \tag{2.26}$$

where $Y^m_l(\theta, \phi; \vec{R}_I)$ is a spherical harmonic function with origin at $\vec{R}_I$, and all other symbols are as defined in equations 2.24 and 2.25. Importantly, the summations over the angular momentum quantum numbers l and m in equation 2.26 are identical to the summation in equation 2.24. Equation 2.26 can be viewed as a linear combination of functions [32, p. 75]:

$$\begin{aligned}\Omega^i_{l,m}(\vec{r}, s_i) &= Y^m_l\left(\theta, \phi; \vec{R}_{I_0}\right) \left\{\phi_l(\epsilon_i, |\vec{r}|, s_i) + p_l(\epsilon_i, s_i) T_0(|\vec{r}|)\right\} \\ &+ \sum_{I \neq I_0} e^{j\vec{k}_i \cdot \vec{R}_I} Y^m_l\left(\theta, \phi; \vec{R}_I\right) T_\infty\left(\left|\vec{r} - \vec{R}_I\right|\right), \end{aligned} \tag{2.27}$$

with each function $\Omega^i_{l,m}(\vec{r}, s_i)$ weighted by a coefficient $a^i_{l,m}$. In the TB-LMTO ESC program, the functions $\Omega^i_{l,m}(\vec{r}, s_i)$ are used as a basis to express the single-electron Hamiltonian of equation 2.15 in matrix form. This matrix is labelled $\bar{\bar{H}}$, and its elements are defined as $H_{i,j} = \int d\vec{r} \Omega^{j*}_{l,m}(\vec{r}, s_j) H \Omega^i_{l,m}(\vec{r}, s_i)$. An "overlap matrix" $\bar{\bar{O}}$ is also defined, the elements of which are defined as $O_{i,j} = \int d\vec{r} \Omega^{j*}_{l,m}(\vec{r}, s_j) \Omega^i_{l,m}(\vec{r}, s_i)$. In both the definition of $H_{i,j}$ and $O_{i,j}$, the integral is over the volume of the atomic sphere located at $\vec{R}_I = \vec{0}$. The single-electron energies ϵ_i and the coefficients $a^i_{l,m}$ are found by solving the eigenvalue problem [32, p. 9]:

$$\left\{\bar{\bar{H}} - \epsilon_i \bar{\bar{O}}\right\} \cdot \vec{a_i} = 0, \tag{2.28}$$

where $\vec{a_i}$ is the vector of coefficients $a^i_{l,m}$.

Equation 2.28 is used to calculate the energies ϵ_i of valence electrons associated with all vectors $\vec{k}$ in the first Brillouin zone of the solid. Once the energy values ϵ_i are known, the TB-LMTO ESC program defines a function $\epsilon\left(\vec{k}\right)$. This function gives, for all vectors

$\vec{k}$ in the solid's first BZ, the single-electron energy value ϵ_i of the valence electron that possesses the wave function associated to the reciprocal lattice vector $\vec{k}_i = \vec{k}$. The function $\epsilon\left(\vec{k}\right)$ is termed the "dispersion relation" of the solid's valence electrons. Its range defines a number of energy bands within which the single-electron energy values ϵ_i of the solid's valence electrons must lie. It is thus said that $\epsilon\left(\vec{k}\right)$ provides information about the "band structure" of the solid's valence electrons.

In addition, equation 2.28 permits the calculation of the coefficients $a^i_{l,m}$ that define the Bloch wave functions as per equation 2.24. Once these coefficients are known, the single-electron wave functions of the solid's valence electrons can be expressed, within any atomic sphere, as [32, p. 90]:

$$\psi_i\left(\vec{r}, s_i\right) = \sum_{l,m} a^i_{l,m} Y^m_l\left(\theta, \phi\right) \phi_l(\epsilon_i, \left|\vec{r}\right|, s_i), \tag{2.29}$$

where the vector $\vec{r}$ and the spherical harmonic function $Y^m_l\left(\theta, \phi\right)$ are both defined with respect to the center of the atomic sphere. The summation over the angular momentum quantum numbers l and m in the latter equation is identical to the summation of equation 2.24. Equation 2.29 is a linear combination of atomic orbitals. In each atomic sphere in the solid's WS unit cell, equation 2.15 is used to calculate the radial components $\phi_l(\epsilon_i, \left|\vec{r}\right|, s_i)$ of the atomic orbitals describing the wave functions of the solid's valence electrons. However, an infinite number of valence electrons pass through each atomic sphere. Thus, the TB-LMTO ESC program must calculate, in theory, an infinite number of radial functions $\phi_l(\epsilon_i, \left|\vec{r}\right|, s_i)$. In practice, the TB-LMTO ESC program calculates only a small number of functions $\phi_l(\epsilon_{\mu,l}, \left|\vec{r}\right|, s_i)$ associated with specific values of energy $\epsilon_i = \epsilon_{\mu,l}$. The TB-LMTO ESC program also calculates functions $\phi'_l(\epsilon_{\mu,l}, \left|\vec{r}\right|, s_i)$ and $\phi''_l(\epsilon_{\mu,l}, \left|\vec{r}\right|, s_i)$ as follows [32, p.38]:

$$\phi'_l(\epsilon_{\mu,l}, \left|\vec{r}\right|, s_i) = \left.\frac{d}{d\epsilon_i}\phi_l(\epsilon_i, \left|\vec{r}\right|, s_i)\right|_{\epsilon_i=\epsilon_{\mu,l}} \tag{2.30}$$

$$\phi''_l(\epsilon_{\mu,l}, \left|\vec{r}\right|, s_i) = \left.\frac{d^2}{d\epsilon_i^2}\phi_l(\epsilon_i, \left|\vec{r}\right|, s_i)\right|_{\epsilon_i=\epsilon_{\mu,l}}. \tag{2.31}$$

Using the functions $\phi'_l(\epsilon_{\mu,l}, \left|\vec{r}\right|, s_i)$ and $\phi''_l(\epsilon_{\mu,l}, \left|\vec{r}\right|, s_i)$, the functions $\phi_l(\epsilon_i, \left|\vec{r}\right|, s_i)$ are ex-

pressed as a second-order Taylor expansion as follows [32, p. 39]:

$$\begin{aligned}\phi_l(\epsilon_i, |\vec{r}|, s_i) &= \phi_l(\epsilon_{\mu,l}, |\vec{r}|, s_i) + (\epsilon_i - \epsilon_{\mu,l})\,\phi_l'(\epsilon_{\mu,l}, |\vec{r}|, s_i) \\ &+ \frac{1}{2}(\epsilon_i - \epsilon_{\mu,l})^2\,\phi_l''(\epsilon_{\mu,l}, |\vec{r}|, s_i). \end{aligned} \tag{2.32}$$

Thus, the TB-LMTO ESC program uses equation 2.15 to calculate four important properties of a solid's electrons, namely the single-electron wave functions of the solid's core electrons, the single-electron energy values of the solid's core electrons, the dispersion relation $\epsilon\left(\vec{k}\right)$ of the solid's valence electrons, and the single-electron wave functions of the solid's valence electrons, including the coefficients $a^i_{l,m}$.

2.2.2 Calculation of $E_{e_{tot}}$ and E_{tot}

Having calculated the single-electron wave functions $\psi_i(\vec{r}, s_i)$ and the single-electron energy values ϵ_i of all electrons in a solid using equation 2.15, the TB-LMTO ESC program then uses equations 2.13 and 2.14 to calculate the total energy of the solid's electrons. This requires the evaluation of the sum of all the single-electron energy values of the solid's electrons, as well as the evaluation of integrals involving the spatial density of the solid's electrons, $\rho(\vec{r})$.

The TB-LMTO ESC program evaluates the sum of the single-electron energy values of a solid's electrons as follows:

$$\sum_i \epsilon_i = \sum_{i,core} \epsilon_i + \sum_{i,valence} \epsilon_i, \tag{2.33}$$

where the terms on the right-hand side are respectively the sum of the single-electron energy values of the solid's core electrons and the sum of the single-electron energy values of the solid's valence electrons.

In the solid's WS unit cell, there is a finite number of core electrons. Thus, the single-electron energy values of these electrons can be summed directly. The sum of the single-electron energy values of the solid's valence electrons, on the other hand, is more difficult

to evaluate. The TB-LMTO ESC program evaluates this sum as follows:

$$\sum_{i,valence} \epsilon_i = \int^{E_F} \epsilon n_v(\epsilon)\, d\epsilon, \tag{2.34}$$

where the function $n_v(\epsilon)$ is termed the "density of states" of the solid's valence electrons, and E_F is the solid's Fermi energy. (The text of Ashcroft and Mermin should be consulted for a definition of the Fermi energy of a solid [37, p. 142]). The density of states of the solid's valence electrons is defined as follows:

$$n_v(\epsilon) = \frac{V_{WS}}{(2\pi)^3} \int_{BZ} \delta\left(\epsilon\left(\vec{k}\right) - \epsilon\right) d\vec{k}, \tag{2.35}$$

where V_{WS} is the volume of the solid's WS unit cell, $\epsilon\left(\vec{k}\right)$ is the solid's dispersion relation, and $\delta\left(\epsilon\left(\vec{k}\right) - \epsilon\right)$ is a delta function. The integral in equation 2.35 is restricted to the solid's first BZ.

The TB-LMTO ESC program constructs the spatial distribution of a solid's electrons as follows:

$$\rho(\vec{r}) = \rho_c(\vec{r}) + \rho_v(\vec{r}), \tag{2.36}$$

where $\rho_c(\vec{r})$ and $\rho_v(\vec{r})$ are respectively the spatial distribution of the solid's core and valence electrons.

In each atomic sphere in the solid's WS unit cell, there is a finite number of core electrons. Thus, in each atomic sphere, $\rho_c(\vec{r})$ is defined as:

$$\rho_c(\vec{r}) = \frac{1}{4\pi} \sum_{i,core} \left|\phi_{l_i}(\epsilon_i, |\vec{r}|, s_i)\right|^2, \tag{2.37}$$

where the functions $\phi_{l_i}(\epsilon_i, |\vec{r}|, s_i)$ are the radial components of the single-electron wave functions of the solid's core electrons, as given in equation 2.23, and the vector $\vec{r}$ is defined with respect to the center of the atomic sphere. It should be noted that, in each atomic sphere, $\rho_c(\vec{r})$ is spherically symmetric (ie. a function of $|\vec{r}|$ only) as the core electrons occupy complete orbital shells.

The construction of $\rho_v(\vec{r})$ is more complex. In each atomic sphere in the solid's WS unit

cell, the spatial distribution of the solid's valence electrons is defined as follows [32, p. 94]:

$$\begin{aligned}\rho_v(\vec{r}) &= \frac{1}{4\pi}\sum_l \left|\phi_l(\epsilon_{\mu,l},|\vec{r}|,s_i)\right|^2 \int^{E_F} n_{v,l}(\epsilon)d\epsilon \\ &+ \frac{1}{4\pi}\sum_l 2\phi_l(\epsilon_{\mu,l},|\vec{r}|,s_i)\phi_l'(\epsilon_{\mu,l},|\vec{r}|,s_i)\int^{E_F}(\epsilon-\epsilon_{\mu,l})\,n_{v,l}(\epsilon)d\epsilon \\ &+ \frac{1}{4\pi}\sum_l \left\{\left|\phi_l'(\epsilon_{\mu,l},|\vec{r}|,s_i)\right|^2+\phi_l''(\epsilon_{\mu,l},|\vec{r}|,s_i)\phi_l(\epsilon_{\mu,l},|\vec{r}|,s_i)\right\}\int^{E_F}(\epsilon-\epsilon_{\mu,l})^2\,n_{v,l}(\epsilon)d\epsilon,\end{aligned} \tag{2.38}$$

where the functions $\phi_l(\epsilon_{\mu,l},|\vec{r}|,s_i)$, $\phi_l'(\epsilon_{\mu,l},|\vec{r}|,s_i)$ and $\phi_l''(\epsilon_{\mu,l},|\vec{r}|,s_i)$ are as in equation 2.32. The valence electron density $\rho_v(\vec{r})$ is assumed to be spherically symmetric in each atomic sphere even though the distribution of the valence electrons of real solids is very rarely spherically symmetric (more on this in section 2.3). The functions $n_{v,l}(\epsilon)$ appearing in equation 2.38 are the so-called "l-projected density of states functions". These functions are defined using the solid's dispersion relation $\epsilon\left(\vec{k}\right)$ and a function $a_{l,m}\left(\vec{k}\right)$. This function $a_{l,m}\left(\vec{k}\right)$ gives, for every vector $\vec{k}$ in the solid's first BZ, the coefficients $a_{l,m}^i$ that are required to define the Bloch wave function associated to the reciprocal lattice vector $\vec{k_i}=\vec{k}$. Specifically, the l-projected density of states functions are defined as follows [32, p. 94]:

$$n_{v,l}(\epsilon) = \frac{V_{WS}}{(2\pi)^3}\sum_m \int_{BZ}\left|a_{l,m}\left(\vec{k}\right)\right|^2\delta\left(\epsilon\left(\vec{k}\right)-\epsilon\right)d\vec{k}. \tag{2.39}$$

Having calculated $\rho(\vec{r})$, and having evaluated the sum of the single-electron energy values of all electrons in the solid, the TB-LMTO ESC program then calculates the total energy of the electrons in the solid, $E_{e_{tot}}$. The TB-LMTO ESC program expresses $E_{e_{tot}}$ as the sum of the kinetic energy $E_{e_{kin}}$ and the potential energy $U_{e_{tot}}$ of the electrons in the solid. Specifically, $E_{e_{kin}}$ is expressed as a sum of three terms, as follows:

$$\begin{aligned}E_{e_{kin}} &= \sum_{i,core}\epsilon_i + \sum_{i,valence}\epsilon_i \\ &- \left\{-\int d\vec{r}\sum_I \frac{Q_I q}{\left|\vec{R}_I-\vec{r}\right|}\rho(\vec{r}) + \int\int d\vec{r}\,d\vec{r'}\frac{q^2}{|\vec{r}-\vec{r'}|}\rho(\vec{r})\rho(\vec{r'}) - \sum_s \int d\vec{r}V_{xc}(\vec{r},s)\rho_s(\vec{r})\right\},\end{aligned} \tag{2.40}$$

where $\rho_s(\vec{r})$ is the density of electrons possessing spin quantum number s only. Similarly, $U_{e_{tot}}$ is also expressed as a sum of three terms, as follows:

$$U_{e_{tot}} = -\int d\vec{r} \sum_I \frac{Q_I q}{\left|\vec{R}_I - \vec{r}\right|} \rho(\vec{r}) + \frac{1}{2} \int\int d\vec{r} d\vec{r}' \frac{q^2}{|\vec{r} - \vec{r}'|} \rho(\vec{r})\rho(\vec{r}') - E_{xc}[\rho(\vec{r})]. \tag{2.41}$$

It should be noted that all integrals over real space in equations 2.40 and 2.41 should be evaluated over the solid's WS unit cell, but are evaluated instead over the atomic spheres. Additionally, the summations over i appearing in equation 2.40, are restricted to electrons located in one of the solid's WS unit cells only. Also, the summations over I in both the latter equations are restricted to the atoms in one of the solid's WS unit cells.

The TB-LMTO ESC program then uses $E_{e_{kin}}$ and $U_{e_{tot}}$ to calculate the total energy of the solid, E_{tot}. Because the integrals over real space in equations 2.40 and 2.41 are restricted to the solid's WS unit cell, the sum of $E_{e_{kin}}$ and $U_{e_{tot}}$ is not quite equal to the total energy of the electrons in the solid, $E_{e_{tot}}$. Specifically, the sum of $E_{e_{kin}}$ and $U_{e_{tot}}$ neglects to take into account the Coulomb interaction between the electrons located in different WS unit cells. In the TB-LMTO ESC program, this problem is addressed by defining the total energy of the solid as follows:

$$\begin{aligned} E_{tot} &= E_{e_{tot}} + \frac{1}{2} \sum_I \sum_{J \neq I} \frac{Q_I Q_J}{\left|\vec{R}_I - \vec{R}_J\right|} \\ &= E_{e_{kin}} + U_{e_{tot}} + E_{Mad}, \end{aligned} \tag{2.42}$$

where E_{Mad} is called a "Madelung term". The Madelung term corrects for the fact that $E_{e_{kin}}$ and $U_{e_{tot}}$, as defined in equations 2.40 and 2.41, do not take into account the Coulomb interaction between electrons located in different WS unit cells of the solid. It also includes the Coulomb interaction between the atomic nuclei in the solid, which must be added to $E_{e_{tot}}$ to obtain E_{tot}.

2.2.3 Implementation of DFT in the TB-LMTO ESC Program : Additional Considerations

Having described the treatment of the single-electron wave functions and single-electron energy values within the TB-LMTO ESC program, and having described how the program calculates the minimum total energy of a solid using DFT, we now clarify a few details of these calculations. Specifically, we describe the exchange-correlation functionals that are used to conduct the calculations, the combined correction terms and their impact on the calculations, and the relativistic treatment of the kinetic energy of electrons in solids.

Exchange-Correlation Functionals

The calculation of $E_{e_{tot}}$ as per equations 2.13 and 2.14, and the calculation of the single-electron wave functions and energy values using equation 2.15, requires knowledge of the exchange-correlation functional $E_{xc}[\rho(\vec{r})]$ and of the exchange-correlation potential $V_{xc}(\vec{r}, s)$. Within the TB-LMTO ESC program, four exchange-correlation functionals are available. Information about these functionals is summarized in table 2.1.

The first two of these exchange-correlation functionals are local functionals, meaning that they are derived in the LDA [43, 46]. These two functionals are different in that the first is derived using a mathematical model of the exchange and correlation energy of a free electron gas [43], while the second is a constructed by parametrizing the results of computer simulations of a free electron gas [46]. As indicated in table 2.1, we label the first functional "EXC1" and the second functional "EXC3".

Two additional exchange-correlation functionals are available within the TB-LMTO ESC program, both of which are non-local functionals derived in the GGA [48, 49]. The first is an extension of functional EXC1 [48], while the second is an extension of functional EXC3 [49]. As shown in table 2.1, we label these functionals "EXC2" and "EXC4" respectively.

We expect that calculations performed with the non-local functionals will be more ac-

curate than those performed with the local functionals. The user of the TB-LMTO ESC program must specify which of the four exchange-correlation functionals must be used in a given calculation.

Table 2.1: Exchange-correlation functionals available in the TB-LMTO ESC program

Functional name	Type of functional	Authors
EXC1	local	von Barth and Hedin [43]
EXC2	non-local	Hu and Langreth [48]
EXC3	local	Vosko, Wilk and Nusair [46]
EXC4	non-local	Perdew and Yue [49]

Combined Correction Terms

The user of the TB-LMTO ESC program must also specify whether or not the so-called "combined correction terms" are to be used when conducting calculations. These terms are described by Andersen [29] and by Skriver [32, p. 95].

The purpose of the combined correction terms is to increase the accuracy with which the TB-LMTO ESC program calculates the dispersion relation $\epsilon\left(\vec{k}\right)$ of the valence electrons of a solid. As explained in section 2.2.1, the dispersion relation is calculated using the Hamiltonian of equation 2.15 by expressing it in the matrix form of equation 2.28. Calculating the elements of the matrices $\bar{\bar{H}}$ and $\bar{\bar{O}}$ appearing in equation 2.28 requires the evaluation of integrals of the form:

$$H_{i,j} = \int \vec{dr} \Omega^{j*}_{l,m}\left(\vec{r}, s_j\right) H \Omega^{i}_{l,m}\left(\vec{r}, s_i\right). \tag{2.43}$$

and of the form:

$$O_{i,j} = \int \vec{dr} \Omega^{j*}_{l,m}\left(\vec{r}, s_j\right) \Omega^{i}_{l,m}\left(\vec{r}, s_i\right). \tag{2.44}$$

These integrals should be evaluated over the volume of the WS unit cell of the solid, but are in fact evaluated over the volume of an atomic sphere.

The combined correction terms are corrections applied to the matrix elements $H_{i,j}$ and $O_{i,j}$. The correction applied to the elements $H_{i,j}$ is as follows:

$$\begin{aligned} H_{i,j} &= \int \vec{dr} \Omega^{j*}_{l,m}(\vec{r}, s_j)\, H\Omega^{i}_{l,m}(\vec{r}, s_i) \\ &+ \int_{WS} \vec{dr} T^{j*}_{l,m}(\vec{r}, s_j)\, HT^{i}_{l,m}(\vec{r}, s_i) - \int \vec{dr} T^{j*}_{l,m}(\vec{r}, s_j)\, HT^{i}_{l,m}(\vec{r}, s_i), \end{aligned} \tag{2.45}$$

and that applied to the elements $O_{i,j}$ is as follows:

$$\begin{aligned} O_{i,j} &= \int \vec{dr} \Omega^{j*}_{l,m}(\vec{r}, s_j)\, \Omega^{i}_{l,m}(\vec{r}, s_i) \\ &+ \int_{WS} \vec{dr} T^{j*}_{l,m}(\vec{r}, s_j)\, T^{i}_{l,m}(\vec{r}, s_i) - \int \vec{dr} T^{j*}_{l,m}(\vec{r}, s_j)\, T^{i}_{l,m}(\vec{r}, s_i). \end{aligned} \tag{2.46}$$

In equations 2.45 and 2.46, the second integral is over the volume of the WS unit cell of the solid while the first and third integrals are over the volume of an atomic sphere. Also, the function $T^{i}_{l,m}(\vec{r}, s_i)$ is a wave function appropriate for describing free electrons. Such a wave function is appropriate for modelling a solid's electrons in the so-called "interstitial regions", namely the regions of space that are in an atomic sphere but not in the WS unit cell, or vice versa. In the TB-LMTO ESC program, the functions $T^{i}_{l,m}(\vec{r}, s_i)$ are linear combinations of the functions $T_0(\vec{r}, s_i)$ and $T_\infty(\vec{r}, s_i)$ appearing in the definition of the muffin-tin orbitals (equation 2.25).

The combined correction terms will thus increase the accuracy of the calculated dispersion relation $\epsilon\left(\vec{k}\right)$ of the valence electrons of a solid, but only if an atomic sphere is a reasonable approximation of the solid's Wigner-Seitz unit cell (see [32, p. 83]). The combined correction terms do nothing to correct for the error introduced in the calculated minimum total energy of a solid E_{tot} as a result of the assumption that the solid's valence electron distribution $\rho(\vec{r})$ is spherically symmetric, or as a result of evaluating the integrals of equations 2.40 and 2.41 over the volume of an atomic sphere rather than the volume of the WS unit cell.

Relativistic Treatment of Electron Kinetic Energy

The TB-LMTO ESC program is also capable of treating the motion of the electrons in solids relativistically or non-relativistically. Users of the TB-LMTO ESC program have the option of including or neglecting relativistic effects in the calculation of the kinetic energy of a solid's electrons. Relativistic effects are taken into account by replacing the kinetic energy operator of equation 2.15 with a Dirac operator (for more information, see the text of Skriver [32, p. 219]). The Dirac operator is a kinetic energy operator that includes a mass-velocity correction and a Darwin correction.

To evaluate the order of magnitude of the relativistic component of the total energy of the electrons in the first-row transition metals, we calculated the total energy of a FCC Cu metal with and without the relativistic correction. We found that relativistic effects increase the total energy of FCC Cu by approximately 10^{-7} Rydberg units. This is, as we shall see in chapter 3, a numerically insignificant quantity. Nonetheless, we include relativistic effects in all calculations that we conduct using the TB-LMTO ESC program in order to ensure that these effects are taken into account should they be significant in any of the metals that we study.

2.3 Applicability of the TB-LMTO ESC Program to the Study of the 3d Metals

Having discussed the mathematical basis and the implementation of the TB-LMTO ESC program, it is appropriate that we discuss the applicability of the program to the study of the first-row transition metals that we wish to undertake.

One aspect of the TB-LMTO ESC program that may limit its accuracy in a study of the first-row transition metals is that it calculates the electron distribution in each WS unit cell of a solid assuming that this distribution is spherically symmetric. The electron distribution

of each first-row transition metal possesses a translation symmetry that is identical to that of the metal's crystal lattice. In addition, all first-row transition metals have partially filled orbital shells. These realities guarantee that the electron distribution of these metals is not spherically symmetric. Tests of the TB-LMTO ESC program have revealed that the assumption of spherical symmetry is reasonable in cubic or close-packed solid [51]. However, we expect that the TB-LMTO ESC program will be less accurate in calculating the properties of the HCP metals (Sc, Ti, Co and Zn) than in calculating the properties of the other metals which possess a cubic crystal structure. This is because the electron distribution of a cubic metal is more spherical than the electron distribution of a HCP metal. For instance, the electron distribution of a cubic metal satisfies $\rho(\vec{r}) = \rho(-\vec{r})$, as does a spherical electron distribution. In a HCP metal, $\rho(\vec{r}) \neq \rho(-\vec{r})$. In addition, we expect the TB-LMTO ESC program to be most accurate in calculating the properties of metallic Cu, as the orbital shells of this metal are all completely filled except for its highest-energy s-orbital.

Secondly, we expect the TB-LMTO ESC program to be most accurate when calculating the properties of metals with small-volume WS unit cells than of metals with large-volume WS unit cells. This is a result of the use of the ASA in deriving the TB-LMTO ESC method. It has been shown that the errors resulting from the use of the ASA is an integral over the interstitial region, which is the volume of space that is inside the WS unit cell of a solid but not in the atomic sphere modelling this unit cell, or vice-versa [32, p. 83]. The interstitial region is larger when the WS unit cell of a solid is larger. It can therefore be expected that the error due to the ASA will be larger when a solid's WS unit cell is larger [52]. This will have important implications when we study the thermal expansion of metallic Cu, in chapter 7, as our method for conducting this study requires knowledge of the minimum total energy versus lattice parameter curve of metallic Cu over a broad range of lattice parameters.

This concludes our explanation of the mathematical and physical basis of the TB-LMTO ESC program [28]. We now turn our attention to evaluating its numerical precision and accuracy.

Chapter 3

Numerical Precision of the TB-LMTO ESC Program

In this chapter, we examine the numerical precision of the TB-LMTO ESC program [28].

As indicated in chapter 2, we wish to use this program to calculate the minimum total energy versus lattice parameter curve $E_{tot}(a)$ and the lowest-energy electron distribution $\rho(\vec{r})$ of the first-row transition metals (Sc to Zn). We specifically evaluate, in this chapter, the numerical precision of the $E_{tot}(a)$ curves of the first-row transition metals, as calculated using the TB-LMTO ESC program. We focus our attention on these curves as their precision will determine that of the majority of the other first-row transition metal properties that we shall later calculate. For instance, we shall calculate, in chapter 4, the lattice parameters of the first-row transition metals at zero Kelvin. The numerical precision of these calculations will be entirely determined by the numerical precision of the calculated $E_{tot}(a)$ curves of the first-row transition metals. In addition, we shall calculate, in chapter 7, the lattice parameter versus temperature curve of metallic Cu. The numerical precision of this calculation will be determined by appropriately propagating the numerical errors in the calculated $E_{tot}(a)$ curve of FCC Cu. The discussion presented here is also intended to serve as a model for the evaluation of the numerical precision of other quantities that will be calculated using the TB-LMTO ESC program, like the magnitude of the magnetic

moments of the first-row transition metals, the density of states function of these metals, and the single-electron wave functions of the valence electrons of these metals (see chapters 4 and 5).

We thus begin, in section 3.1, with a definition of the numerical precision of the TB-LMTO ESC program. We also highlight a number of factors affecting the numerical precision of the program, and explain that the result of any calculation conducted using the program is analogous to an experimental measurement. As a result any value calculated using the TB-LMTO ESC program contains a random calculation precision error (CPE) and a systematic calculation error (SCE). In section 3.2, we evaluate the magnitude of the CPE and the SCE in the calculated minimum total energy of some first-row transition metals. Finally, in section 3.3, we summarise the results of section 3.2 and compare them to the results of other studies of the numerical precision of ESC programs

To our knowledge, an evaluation of the numerical precision of an ESC program (any ESC program), as presented in this chapter, has never previously been published. In some published papers discussing the use of an ESC program to study materials, the numerical precision of the ESC program is not discussed at all (e.g. [53]). In others, the numerical precision of an ESC program is discussed, but not quantified (e.g. [54–63]). Even among those papers in which the numerical precision of an ESC program is quantified (e.g. [64–72]), we found no papers treating the calculated minimum total energy of a solid as a theoretical measurement of this energy containing a CPE and a SCE. We therefore consider that the analysis presented here is novel.

3.1 Numerical Precision of the TB-LMTO ESC Program : Definition

The minimum total energy of any solid, as computed using the TB-LMTO ESC program [28], is not exact. This is so because a number of physical assumptions and mathemati-

cal approximations were made in implementing the program. For instance, the program can be used in conjunction with one of four exchange-correlation functionals (see table 2.1), each derived using different physical models and mathematical descriptions of the interaction of electrons. These assumptions and approximations affect the accuracy of the minimum total energy values computed by the TB-LMTO ESC program, accuracy being understood as the degree of correspondence between the minimum total energy of the solid as computed by the program and the real-world value of this energy.[1]

In addition, the output of the TB-LMTO ESC program is affected by parameters controlling some of the algorithmic processes that are implemented within it. As indicated in chapter 2, the TB-LMTO ESC program uses an iterative procedure to find the lowest-energy electron distribution of a solid, beginning with an initial estimate of this electron distribution and then gradually refining it until a good estimate of the lowest-energy electron distribution has been found. In conjunction with this good estimate of a solid's lowest-energy electron distribution, the program also calculates a good estimate of the solid's minimum total energy. The program concludes that it has found "good estimates" of the minimum total energy and lowest-energy electron distribution of a solid when both of two conditions are met. The first is that successive estimates of the solid's lowest-energy electron distribution differ by no more than a quantity termed the "electron density convergence tolerance" at all points in the solid's WS unit cell. The second is that successive estimates of the minimum total energy of a solid differ by no more than a quantity termed the "energy convergence tolerance". When conducting a calculation, the user of the TB-LMTO ESC program must set the value of both convergence tolerances.

The minimum total energy of a solid, as computed beginning with one initial estimate of the solid's lowest-energy electron distribution, differs slightly from the same energy as computed beginning with different initial conditions. This is because the minimum total energy of a solid, as obtained in a single calculation, can be seen as a theoretical measure-

[1]This definition of the "accuracy" of the TB-LMTO ESC program was inspired by the definitions of the French terms "exactitude" and "justesse" given in the "Grand dictionnaire terminologique" of the "Office québécois de la langue française" [73].

ment of the energy in question. Like an experimental measurement, this theoretical measurement contains a random error, which we term a "calculation precision error" (CPE). As a consequence, when conducting a single calculation of the minimum total energy of a solid using the TB-LMTO ESC program, we cannot be certain that the good estimate of the minimum total energy of the solid produced by the program is the best estimate of this energy that the program can produce. We define the numerical precision of the TB-LMTO ESC program as the degree to which we are certain that the minimum total energy of a solid, as obtained in a given calculation, is the best estimate of this energy that the TB-LMTO ESC program can produce.[2] It should be noted that this best estimate of the solid's minimum total energy can be very different from the real-world value of this energy (ie. it may not be very accurate).

This definition of the numerical precision of the TB-LMTO ESC program requires a definition of the "best estimate" of the minimum total energy of a solid that the program can produce. Because the program is designed to find the *minimum* total energy of a solid, it is tempting to define the best estimate of this energy as the smallest energy value that the program can calculate. If this definition is chosen, then it must be that the CPE's in the output of the TB-LMTO ESC program are always positive. Because these CPE's are at least in part due to computational truncation and roundoff errors [74], they can, in reality, be either positive or negative. Thus, the best estimate of the minimum total energy of a solid should not be defined as the smallest value of this energy that the TB-LMTO ESC program can calculate.

A better definition of the best estimate of the minimum total energy of a solid is the value that is most likely to be obtained when running a single calculation of this energy using the TB-LMTO ESC program. If the minimum total energy of a solid is calculated a large number of times, each time beginning with a different set of initial conditions, a distribution of energy values is obtained. Using this distribution, the energy value that is most

[2]This definition of the "numerical precision" of the TB-LMTO ESC program was inspired by the definition of the French term "précision" given in the "Grand dictionnaire terminologique" of the "Office québécois de la langue française" [73].

likely to be obtained when running a single calculation of the minimum total energy of the solid can be identified.

Once the best estimate of the minimum total energy of the solid is known, the distribution of the calculated minimum total energy values can be transformed into a distribution which has a most likely value of zero [75]. This new distribution can be viewed as the distribution of the CPE's that arose in the process of calculating the minimum total energy values described above. The numerical precision of the minimum total energy values computed using the TB-LMTO ESC program can be quantified meaningfully as $\pm 1\sigma$, where σ is the standard deviation of the distribution of CPE's. This effectively gives a range of energy values within which must lie the best estimate of the minimum total energy of a solid. Also, the probability that the best estimate of the minimum total energy of the solid lies within this range can be evaluated using the known distribution of CPE's. It is of note that the numerical precision of the TB-LMTO ESC program is dependent upon the value of its convergence tolerances.

The output of the TB-LMTO ESC program is also affected by parameters relating to the numerical evaluation of integrals. As indicated in chapter 2, a number of integrals must be evaluated in order to calculate the minimum total energy of a solid using the TB-LMTO ESC program. The value of these integrals can only be estimated using numerical integration techniques [74]. If the numerical evaluation of an integral is not performed with care, the value of the integral, as evaluated numerically, will be significantly different from the true value of the integral. The error in a numerical integral, namely the difference between the numerical estimate of the value of an integral and the correct value of the integral, is not a random variable. Rather, it is systematic, in the sense that it will be the same every time a given integral is numerically evaluated. We term these errors "systematic calculation errors" (SCE's). The output of the TB-LMTO ESC program contains SCE's that are dependent on parameters controlling the numerical evaluation of integrals.

3.2 Numerical Precision of the TB-LMTO ESC Program : Evaluation

We now evaluate the numerical precision of the minimum total energy values calculated using the TB-LMTO ESC program. We first evaluate, in section 3.2.2, the magnitude of the CPE's in these calculated values. In section 3.2.3, we evaluate the magnitude of their SCE's. Prior to doing so, we describe in section 3.2.1 the definition of the initial conditions of a calculation to be performed using the TB-LMTO ESC program.

3.2.1 The Initial Conditions of a TB-LMTO Calculation

As we indicated previously, a calculation of the minimum total energy of a solid conducted using the TB-LMTO ESC program [28] requires that an initial estimate of the lowest-energy electron distribution of the solid be constructed. This requires an initial estimate of the core electron distribution $\rho_c(\vec{r})$ and of the valence electron distribution $\rho_v(\vec{r})$ of the TB-LMTO ESC program.

As indicated in section 2.2.2, the distribution of the core electrons $\rho_c(\vec{r})$ is spherically symmetric. Thus, to construct an initial estimate of this function, we require only an initial estimate of its radial component $\rho_c(|\vec{r}|)$. The definition of the valence electron distribution is more complex. As indicated in section 2.2.2, $\rho_v(\vec{r})$ is defined as follows within the TB-LMTO ESC program:

$$\begin{aligned}
\rho_v(\vec{r}) &= \frac{1}{4\pi}\sum_l |\phi_l(\epsilon_{\mu,l},|\vec{r}|,s_i)|^2 \int^{E_F} n_{v,l}(\epsilon)d\epsilon \\
&+ \frac{1}{4\pi}\sum_l 2\phi_l(\epsilon_{\mu,l},|\vec{r}|,s_i)\phi_l'(\epsilon_{\mu,l},|\vec{r}|,s_i) \int^{E_F} (\epsilon-\epsilon_{\mu,l})\, n_{v,l}(\epsilon)d\epsilon \\
&+ \frac{1}{4\pi}\sum_l \left\{|\phi_l'(\epsilon_{\mu,l},|\vec{r}|,s_i)|^2 + \phi_l''(\epsilon_{\mu,l},|\vec{r}|,s_i)\phi_l(\epsilon_{\mu,l},|\vec{r}|,s_i)\right\} \int^{E_F} (\epsilon-\epsilon_{\mu,l})^2\, n_{v,l}(\epsilon)d\epsilon.
\end{aligned} \tag{3.1}$$

To specify an initial estimate of $\rho_v(\vec{r})$, we must specify an initial estimate of the energy values $\epsilon_{\mu,l}$ and an initial estimate of the integrals $\int^{E_F} n_{v,l}(\epsilon)d\epsilon$, $\int^{E_F} (\epsilon - \epsilon_{\mu,l}) n_{v,l}(\epsilon)d\epsilon$ and $\int^{E_F} (\epsilon - \epsilon_{\mu,l})^2 n_{v,l}(\epsilon)d\epsilon$. It is also necessary that we specify an initial estimate of the functions $\phi_l(\epsilon_{\mu,l}, |\vec{r}|, s_i)$, $\phi_l'(\epsilon_{\mu,l}, |\vec{r}|, s_i)$ and $\phi_l''(\epsilon_{\mu,l}, |\vec{r}|, s_i)$.

The TB-LMTO ESC program is equipped with routines, namely the "lminit.run" and "lmhart.run" routines, for automatically generating an initial estimate of these parameters and functions [35, p. 6]. These routines set the value of the integrals $\int^{E_F} (\epsilon - \epsilon_{\mu,l}) n_{v,l}(\epsilon)d\epsilon$ and $\int^{E_F} (\epsilon - \epsilon_{\mu,l})^2 n_{v,l}(\epsilon)d\epsilon$ to zero. They also define an initial estimate of the integral $\int^{E_F} n_{v,l}(\epsilon)d\epsilon$ and an initial estimate of the function $\phi_l(\epsilon_{\mu,l}, |\vec{r}|, s_i)$. This latter function is simply taken to be a function appropriate for describing the radial component of the spatial distribution of an electron in an orbital of type l and energy $\epsilon_{\mu,l}$. (The functions $\phi_l'(\epsilon_{\mu,l}, |\vec{r}|, s_i)$ and $\phi_l''(\epsilon_{\mu,l}, |\vec{r}|, s_i)$ are irrelevant in defining the initial estimate of $\rho_v(\vec{r})$ because the initial value of the integrals $\int^{E_F} (\epsilon - \epsilon_{\mu,l}) n_{v,l}(\epsilon)d\epsilon$ and $\int^{E_F} (\epsilon - \epsilon_{\mu,l})^2 n_{v,l}(\epsilon)d\epsilon$ is zero.) The "lminit.run" and "lmhart.run" routines also define an initial estimate of three "p-parameters", labelled $p_{\mu,l}$. There is one p-parameter per orbital in the linear combination of atomic orbitals describing the valence electrons of the solid (see equation 2.29). These p-parameters are essentially values of the potential functions $p_l(\epsilon)$ (see equation 2.25), defined at $\epsilon = \epsilon_{\mu,l}$. The energy values $\epsilon_{\mu,l}$ can be obtained from the p-parameters $p_{\mu,l}$, as the potential function $p_l(\epsilon)$ is a known function of ϵ. The p-parameters also define an initial estimate of the dispersion relation $\epsilon\left(\vec{k}\right)$ of the solid. This is done using the "canonical bands" (for a description of these bands, see Skriver [32, p. 20-25]).

The p-parameters $p_{\mu,l}$ in conjunction with the integrals $\int^{E_F} n_{v,l}(\epsilon)d\epsilon$, $\int^{E_F} (\epsilon - \epsilon_{\mu,l}) n_{v,l}(\epsilon)d\epsilon$ and $\int^{E_F} (\epsilon - \epsilon_{\mu,l})^2 n_{v,l}(\epsilon)d\epsilon$ are the variational parameters of the TB-LMTO ESC program. Thus, there are four variational parameters per orbital in the linear combination of atomic orbitals describing the valence electrons of the solid (see equation 2.29). Changing the p-parameters varies the estimate of the dispersion relation of the solid's electrons. Varying the other integrals varies the estimate of the lowest-energy valence electron distribution of the solid. Given that the TB-LMTO ESC program is designed to find the global minimum of the minimum total energy functional $E_{tot}[\rho(\vec{r})]$, it is tempting to expect that the

TB-LMTO ESC program will always find this global minimum regardless of the initial estimate of $\rho(\vec{r})$ that the program begins with. However, this is not the case. As a result of instabilities of the algorithm for finding the lowest-energy electron distribution of solids implemented within the TB-LMTO ESC program, and also as a result of the presence of local minima in the functional $E_{tot}[\rho(\vec{r})]$, the initial conditions of calculations conducted using the program must be selected carefully. Within the "lminit.run" and the "lmhart.run" routine, the results of more basic physical models of the electronic structure of solids are used in order to construct physically reasonable initial conditions for the calculations to be performed using the TB-LMTO ESC program.

Though the user of the TB-LMTO ESC program is not free to begin calculations using any initial conditions, there is a certain degree of flexibility in the construction of the initial conditions of TB-LMTO ESC program calculations. The sensitivity of the calculations performed with the program to the initial conditions of the calculations defines the magnitude of the CPE's and SCE's in the output of the program. Thus, in order to estimate the magnitude of these CPE's and SCE's, we must study the initial condition sensitivity of the results of calculations conducted using the TB-LMTO ESC program. This requires that we define a few sets of initial conditions. We define two such sets of initial conditions, which we label INIT1 and INIT2.

To understand how we construct initial conditions for our TB-LMTO calculations, consider the construction of initial condition sets INIT1 and INIT2 to be used in a study of HCP Sc. To generate INIT1 and INIT2, we first use the TB-LMTO ESC program to automatically generate the initial conditions of the calculation using the "lminit.run" and "lmhart.run" programs [35, p. 6]. We then run the program to identify a good estimate of the lowest-energy electron distribution and minimum total energy of HCP Sc. Having obtained a good estimate of the lowest-energy valence electron distribution of HCP Sc, we now possess values of the energies $\epsilon_{\mu,l}$ and of the three integrals $\int^{E_F} n_{v,l}(\epsilon)d\epsilon$, $\int^{E_F} (\epsilon - \epsilon_{\mu,l}) n_{v,l}(\epsilon)d\epsilon$ and $\int^{E_F} (\epsilon - \epsilon_{\mu,l})^2 n_{v,l}(\epsilon)d\epsilon$, as well as definitions of the functions $\phi_l(\epsilon_{\mu,l}, |\vec{r}|, s_i)$, $\phi_l'(\epsilon_{\mu,l}, |\vec{r}|, s_i)$ and $\phi_l''(\epsilon_{\mu,l}, |\vec{r}|, s_i)$. These values and functions can be used to construct a good estimate of the valence electron distribution $\rho_v(\vec{r})$ of HCP Sc. We take

these values and functions to be a basis set of initial conditions, which we use to construct INIT1 and INIT2. To construct the initial condition sets INIT1 and INIT2, we change the basis set of initial conditions by modifying the value of the integral $\int^{E_F} n_{v,l}(\epsilon)d\epsilon$ only, leaving all other integrals and functions as they are in the basis set. The value of the integrals $\int^{E_F} n_{v,l}(\epsilon)d\epsilon$ in INIT1 and INIT2 are shown in table 3.2, in the appendix at the end of this chapter.

The construction of INIT1 and INIT2 may seem arbitrary, as we do not use physical arguments to justify our choice of values for the integrals $\int^{E_F} n_{v,l}(\epsilon)d\epsilon$ when defining INIT1 and INIT2. However, the TB-LMTO ESC program converges successfully when used to calculate the minimum total energy of HCP Sc beginning with INIT1 and INIT2. We take this to signify that our choice of values for the integrals $\int^{E_F} n_{v,l}(\epsilon)d\epsilon$ is physically appropriate. In addition, the value of these integrals in INIT1 and INIT2 is quite different of the value of these integrals obtained when running the "lminit.run" routine. For instance, in INIT1, $\int^{E_F} n_0(\epsilon)d\epsilon \approx 0.2$, while $\int^{E_F} n_0(\epsilon)d\epsilon \approx 1.2$ in INIT2. In contrast, the "lminit.run" routine sets $\int^{E_F} n_0(\epsilon)d\epsilon = 0.7$, which is approximately equal to the value of $\int^{E_F} n_0(\epsilon)d\epsilon$ in the basis set of initial conditions. Given that the integrals $\int^{E_F} n_{v,l}(\epsilon)d\epsilon$ in INIT1 and INIT2 are so different of the value of these integrals when they describe a good estimate of the lowest-energy electron distribution of HCP Sc, we believe that testing the initial condition sensitivity of the output of the TB-LMTO ESC program using INIT1 and INIT2 allows us to obtain a good estimate of the magnitude of the CPE's in the minimum total energy values computed using the program.

Initial condition sets INIT1 and INIT2 are reported for HCP Sc, BCC Fe and FCC Cu in section 3.4 of this chapter.

3.2.2 Convergence Tolerances and the Precision of the Minimum E_{tot}

As indicated in section 3.1, the CPE's in the energy values computed using the TB-LMTO ESC program are dependent on the value of the program's convergence tolerances. Given

the intended function of these convergence tolerances, we have certain expectations concerning the effect of these tolerances on the numerical precision of the program. First of all, we expect that the minimum total energy of a solid will be computed with greater precision (ie. with a smaller CPE) when the convergence tolerances are smaller. Secondly, we expect that the calculated minimum total energy values will be more sensitive to the initial conditions of the calculation, namely the initial estimate of a solid's lowest-energy electron distribution, when the convergence tolerances are set to larger values.

First of all, we wish to examine the relationship between the value of the convergence tolerances and the initial-condition sensitivity of the minimum total energy values calculated using the TB-LMTO ESC program. To do so, we use the program to calculate the minimum total energy E_{tot} of HCP Sc, BCC Fe and FCC Cu. (We specifically calculate the minimum total energy of non-magnetic HCP Sc and FCC Cu (NM HCP Sc and NM FCC Cu), and of ferromagnetic BCC Fe (FM BCC Fe) (see chapter 4 for more information).) The minimum total energy of these three metals is calculated four times, each time beginning the calculation with one of two sets of initial conditions, described in section 3.4 at the end of this chapter, and setting the convergence tolerances to a value of either 1.0×10^{-2} or 1.0×10^{-5} (Rydberg units for the total energy convergence tolerance, and electrons per cubic Bohr radii for the electron density convergence tolerance). These values are small relative to the expected value of the minimum total energy of the metals (of the order of thousands of Rydberg units per atom), and relative to the expected lowest-energy electron density of the metals (of the order of 1 to 10 electrons per cubic Bohr radii in those areas within the metals where the electron density is largest). Four such calculation sets are carried out, each using a different one of the four exchange-correlation functionals available in the TB-LMTO ESC program. Table 3.1 shows the lattice parameters of the metals during the calculations. In all calculations, the motion of the electrons is treated relativistically, and the combined correction terms are utilised (see chapter 2). Also, the single-electron wave functions of the metals' valence electrons are expressed as a linear combination of s-, p- and d-orbitals only. Finally, the first Brillouin zone (BZ) of each solid is discretised by defining the value of the first BZ discretisation integers as $L = M = N = 30$ (see section

3.2.3).

In all calculations described above, we set both convergence tolerances to equal values (ie. both equal to 1.0×10^{-2}, or both equal to 1.0×10^{-5}). As indicated in section 3.1, the convergence tolerances define two conditions that must both be satisfied in order for a calculation to terminate. Naturally, one would expect that one of these conditions will be more difficult to meet. We believe that the energy convergence tolerance defines the most stringent calculation termination condition. However, we focus here on the total effect of both convergence tolerances when they are kept equal.

Table 3.1: Lattice parameters used in convergence tolerance calculations

Metal	Exch.-correlation func. EXC1	Exch.-correlation func. EXC2	Exch.-correlation func. EXC3	Exch.-correlation func. EXC4
HCP Sc	6.24 Bohr radii c/a = 1.45	6.34 Bohr radii c/a = 1.46	6.26 Bohr radii c/a = 1.45	6.41 Bohr radii c/a = 1.47
BCC Fe	5.28 Bohr radii	5.36 Bohr radii	5.30 Bohr radii	5.54 Bohr radii
FCC Cu	6.69 Bohr radii	6.78 Bohr radii	6.71 Bohr radii	7.00 Bohr radii

The exchange-correlation functionals are described in table 2.1.

The $E_{tot}\,(a)$ curves of the metals listed above, as calculated using the different exchange-correlation functionals, possess a global minimum value at the indicated lattice parameters.

Figure 3.1 shows, for HCP Sc, BCC Fe and FCC Cu, the difference of the minimum total energy of a metal as obtained using initial conditions INIT1 and as obtained using initial conditions INIT2. Initial conditions INIT1 and INIT2 are described in sections 3.2.1 and 3.4 of this chapter. We repeat that these initial conditions are in fact initial estimates of the lowest-energy electron distribution of a solid. The information in figure 3.1 is reported as obtained using each of the four exchange-correlation functionals available in the TB-LMTO ESC program. However, no effort is made to distinguish results obtained with the different exchange-correlation functionals. This represents no loss of information, as

the numerical precision of the TB-LMTO ESC program is independent of the exchange-correlation functional used in the calculations.

Figure 3.1 shows that the difference between the minimum total energy values obtained using different initial conditions is larger when the convergence tolerances take the larger value, namely 1.0×10^{-2}. Thus, these results support the assertion that the minimum total energy values computed using the TB-LMTO ESC program are more precise when obtained using smaller convergence tolerances. Regardless of the exchange-correlation functional used, the minimum total energy values obtained for a given metal, beginning with initial conditions INIT1 and INIT2 described in sections 3.2.1 and 3.4 of this chapter, differ by no more than 2.0×10^{-7} Rydberg units per atom when the convergence tolerances are set to 1.0×10^{-5}. Given this result, we estimate that, when the convergence tolerances are set to 1.0×10^{-5}, the CPE in the minimum total energy value of a metal, as computed using the TB-LMTO ESC program, is of the order of $\pm 2.0 \times 10^{-7}$ Rydberg units per atom.

It is also evident, in figure 3.1, that the minimum total energy values obtained with initial conditions INIT2 are always smaller than those obtained with initial conditions INIT1. This is surprising because, if the initial conditions INIT1 and INIT2 are randomly defined, the difference of the minimum total energy values obtained using these initial conditions should as likely be positive or negative. We believe that our specific definitions of the initial conditions INIT1 and INIT2 are such that the minimum total energy values obtained with INIT2 are always smaller than those obtained with INIT1.

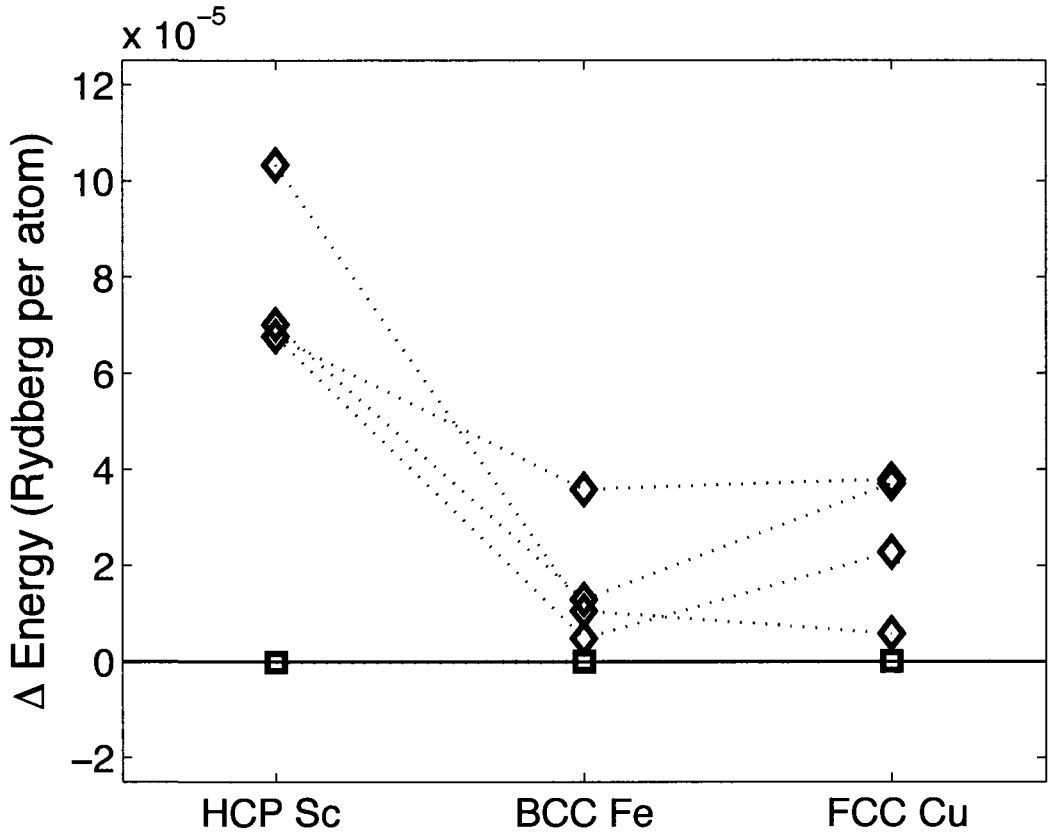

Figure 3.1: Difference between the calculated minimum total energy E_{tot} of a metal obtained with initial conditions INIT1, and the calculated minimum total energy of the metal obtained with initial conditions INIT2 ($E_{tot}\,(INIT1) - E_{tot}\,(INIT2)$). INIT1 and INIT2 are described in section 3.4 of this chapter. Results were obtained with convergence tolerances set to 1.0×10^{-2} (diamonds) and set to 1.0×10^{-5} (squares). Results are shown as obtained using each of the four exchange-correlation functionals available in the TB-LMTO ESC program. To maintain the clarity of the figure, results obtained with the different exchange-correlation functionals are not identified with unique symbols. However, the dotted lines guide the eye to data points obtained using the same exchange-correlation functional. The lattice parameters of the metals are specified in table 3.1.

We next compute the minimum total energy of HCP Sc, BCC Fe and FCC Cu as a function of the value of the convergence tolerances. Each of these energy values is calculated seven times, each time setting the convergence tolerances of the TB-LMTO ESC program to a different value between 1.0×10^{-1} to 1.0×10^{-7} (Rydberg units for the total energy convergence tolerance, and electrons per cubic Bohr radii for the electron density convergence tolerance). We repeat that these values are small relative to the expected minimum total energy of the metals (of the order of thousands of Rydberg units per atom), and relative to the expected lowest-energy electron density of the metals (of the order of 1 to 10 electrons per cubic Bohr radii in those areas within the metals where the electron density is largest). In all calculations, the electron density convergence tolerance and the total energy convergence tolerance are assigned identical values (e.g. both equal to 1.0×10^{-1}). Four such calculation sets are carried out, each using a different one of the four exchange-correlation functionals available in the TB-LMTO ESC program. Table 3.1 shows the lattice parameters of the metals. In all calculations, the motion of the electrons is treated relativistically, and the combined correction terms are utilised. Also, the single-electron wave functions of the metals' valence electrons are expressed as a linear combination of s-, p- and d-orbitals only. Finally, the first Brillouin zone (BZ) of each solid is discretised by setting the first BZ discretisation integers to $L = M = N = 30$ (see section 3.2.3).

Figure 3.2 shows the calculated minimum total energy E_{tot} of HCP Sc, BCC Fe and FCC Cu versus the value of the convergence tolerances. All minimum total energy values computed for a given metal using a given exchange-correlation functional are reported relative to the minimum total energy value obtained when the convergence tolerances were set to a value of 1.0×10^{-7}. Figure 3.2 shows this information as calculated using all four exchange-correlation functionals available in the TB-LMTO ESC program. To maintain the clarity of the figure, results obtained using the different exchange-correlation functionals are not distinguished. This represents no loss of information, as the numerical precision of the TB-LMTO ESC program is independent of the exchange-correlation functional used in the calculations.

Figure 3.2 shows that all values of the minimum total energy of a given metal, obtained us-

ing a given exchange-correlation functional, and computed with convergence tolerances between 1.0×10^{-7} and 1.0×10^{-5}, differ by no more than 2.5×10^{-7} Rydberg units per atom. Given this information, we estimate that the CPE's in the minimum total energy values obtained using the TB-LMTO ESC program are of the order of $\pm 2.5 \times 10^{-7}$ Rydberg units per atom. Also, figure 3.2 suggests that, when the convergence tolerances are no larger than 1.0×10^{-5}, the CPE's in the calculated minimum total energy of metals possessing different crystal structures and different lattice parameters are of comparable magnitude. However, figure 3.2 also shows that, when the convergence tolerances are between 1.0×10^{-5} and 1.0×10^{-2}, the calculated minimum total energy values can be up to 2.5×10^{-6} Rydberg per atom smaller than the values obtained when the convergence tolerances are between 1.0×10^{-7} and 1.0×10^{-5}.

That the calculated minimum total energy of a material can be significantly smaller when it is obtained using larger convergence tolerance values was, at first observation, surprising to us. We initially feared that the algorithm implemented within the TB-LMTO ESC program can fail to find the minimum total energy of a solid when the convergence tolerances are made too small. However, remembering that we defined the best estimate of a solid's minimum total energy as the energy value most likely to be obtained in a single calculation, we understood this matter differently. Given the definition of the best estimate of the minimum total energy of a solid that we presented in section 3.1, we understand the energy values that are obtained with large convergence tolerances, and that are smaller than those obtained with small convergence tolerances, as examples of calculation results where the roundoff effects of the computer conspire to produce exceptionally large and negative CPE's. Only when the convergence tolerances are very large can the TB-LMTO ESC program conclude that an energy value containing such an exceptionally large and negative CPE is a good estimate of the minimum total energy of a solid. (We use here the term "good estimate" of the minimum total energy of a solid as it is defined in section 3.1). This is because, when the convergence tolerances are smaller, the TB-LMTO ESC program cannot terminate a calculation when an exceptionally large CPE arises in a calculated minimum total energy value.

Two observations support our previously described understanding of the exceptionally small minimum total energy values that can be obtained when the convergence tolerances are large. First of all, such exceptionally small minimum total energy values are obtained only when calculations are conducted beginning with a restricted set of initial conditions. Calculations conducted with the same large convergence tolerances, but using different initial conditions, produce good estimates of the minimum total energy of the solid that are similar to those obtained when the convergence tolerances are small. Secondly, the lowest-energy electron distribution that corresponds to an exceptionally small estimate of the minimum total energy of a solid can be used as the initial condition of a calculation conducted using small convergence tolerances. When this is done, the TB-LMTO ESC program does not find that the exceptionally small minimum total energy value is a good estimate of the minimum total energy of the solid. Rather, the program finds, under these conditions, a good estimate of the minimum total energy of the solid that is typical of the good estimates of this energy that are obtained using small convergence tolerances.

Having now completed our study of the effect of the convergence tolerances on the output of the TB-LMTO ESC program, we estimate that the CPE's in the minimum total energy values computed using the TB-LMTO ESC program are of the order of $\pm 2.5 \times 10^{-7}$ Rydberg per atom when the convergence tolerances are no larger than 1.0×10^{-5}. We have not identified the statistical distribution of these CPE's. However, the information that we have obtained about these CPE's will allow us to conduct a good study of the accuracy of the TB-LMTO ESC program (chapter 4).

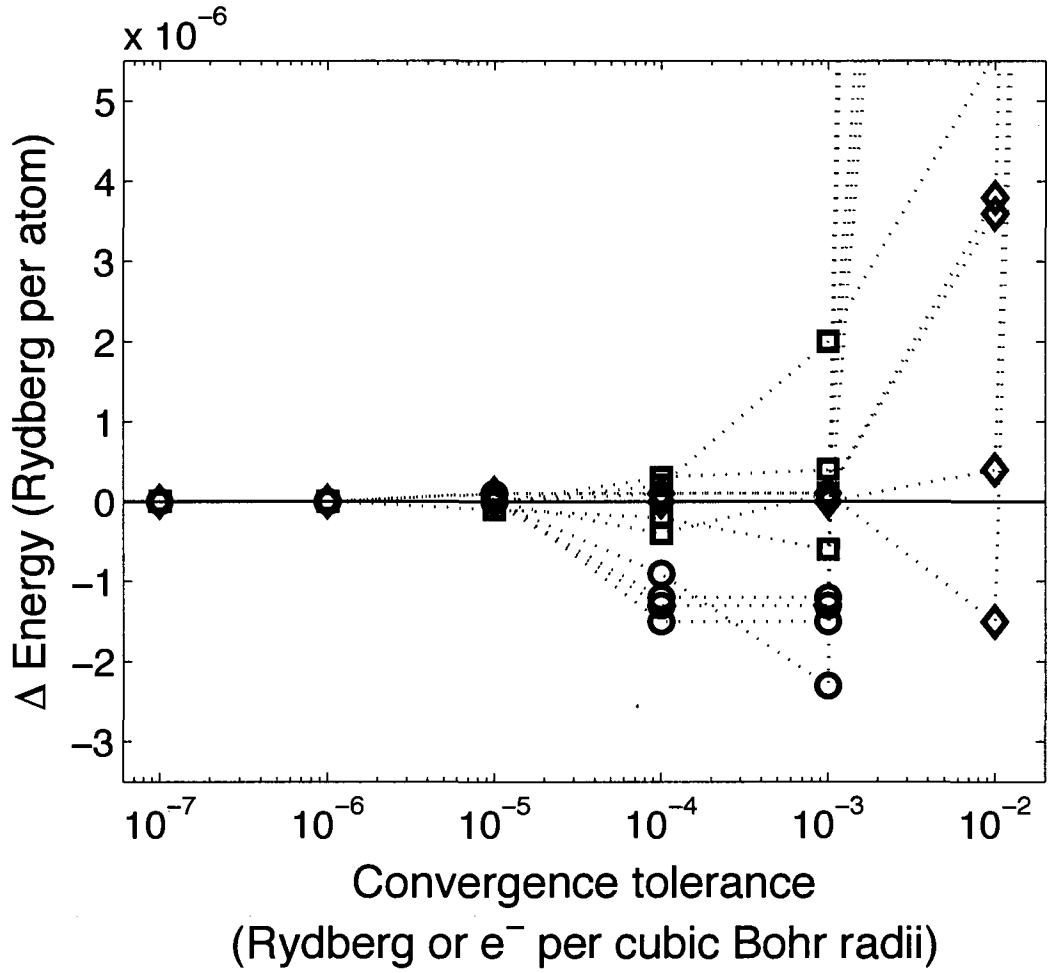

Figure 3.2: Calculated minimum total energy E_{tot} of HCP Sc (circles), BCC Fe (squares), and FCC Cu (diamonds), as calculated using each of the four exchange-correlation functionals available in the TB-LMTO ESC program, versus the value of the convergence tolerances. All energy values calculated for a particular metal using a particular exchange-correlation functional are given relative to the energy obtained with convergence tolerances equal to 1.0×10^{-7}. To maintain the clarity of the figure, energy values computed using the different exchange-correlation functionals are not distinguished. However, the dotted lines guide the eye to data points obtained for a given metal using a given exchange-correlation functional. The lattice parameters of the metals are specified in table 3.1.

3.2.3 Discretization of the First BZ and the Precision of the Minimum E_{tot}

As indicated in section 3.1, the calculation of the total energy of a solid requires that integrals be evaluated numerically. Some of these integrals are over one single variable (like energy or a one-dimensional distance), and the discretization of the range of these integrals does not pose any exceptional challenges. Within the TB-LMTO ESC program, default parameters defining the discretization of the range of these integrals are defined [35]. In all our calculations, we allow that the range of these integrals be discretized as per these default settings.

However, when calculating the total energy of a solid, it is also necessary to evaluate integrals over reciprocal space. The range of these integrals is the solid's first Brillouin zone (BZ), a three-dimensional range of integration. It is more difficult to appropriately discretize the range of these integrals in order to ensure that the numerical estimate of the integrals is not significantly different from the true value of the integrals. In conducting our calculations, we specify the discretization of this range of reciprocal space. This is accomplished by defining a collection of vectors in the solid's first BZ, which are expressed as follows [35]:

$$\vec{k}_{lmn} = \frac{l}{L}\vec{K}_1 + \frac{m}{M}\vec{K}_2 + \frac{n}{N}\vec{K}_3, \tag{3.2}$$

where l, L, m, M, n, and N are integers and the vectors $\vec{K}_i$ are the solid's reciprocal lattice vectors. We will henceforth refer to the integers L, M and N as the "first BZ discretization integers". The vectors $\vec{k}_{lmn}$, where $0 \leq l \leq L$, $0 \leq m \leq M$, and $0 \leq n \leq N$, are used in the numerical evaluation of the integrals over the solid's first BZ.

As indicated in section 3.1, the discretization integers control the magnitude of a systematic calculation error (SCE) in the output of the TB-LMTO ESC program. This is so because numerical integration techniques incorrectly estimate the value of an integral if the range of integration is discretized too coarsely [74]. The error in a numerical integral, namely the difference between the numerical estimate of the value of an integral and the correct value of the integral, is not a random variable. Thus, the SCE is a systematic error, in the

sense that, each time a calculation is performed using a given set of discretization integers, the result will contain the same SCE.

To verify this, we conduct a series of calculations to examine the effect of the discretization of the first BZ of a material on the initial-condition sensitivity of the calculated minimum total energy of the material. Specifically, we calculate the minimum total energy E_{tot} of HCP Sc, BCC Fe and FCC Cu, using the TB-LMTO ESC program. The minimum total energy of these three metals is calculated four times, each time beginning the calculation with one of the two sets of initial conditions, described in detail in section 3.4 at the end of this chapter, and setting the first BZ discretization integers to either $L = M = N = 10$ or $L = M = N = 30$. Four such calculation sets are carried out, each using a different one of the four exchange-correlation functionals available in the TB-LMTO ESC program. Table 3.1 shows the lattice parameters of the metals. In all calculations, the motion of the electrons is treated relativistically, and the combined correction terms are utilised. Also, the single-electron wave functions of the metals' valence electrons are expressed as a linear combination of s-, p- and d-orbitals only. Finally, the electron density convergence tolerance and the total energy convergence tolerance are both assigned a value of 1.0×10^{-5}.

Figure 3.3 shows, for HCP Sc, BCC Fe and FCC Cu, the difference between the calculated minimum total energy of a metal as obtained using the initial conditions INIT1, and the minimum total energy of the metal as obtained using initial conditions INIT2. This information is reported as obtained using each of the four exchange-correlation functionals available in the TB-LMTO ESC program. However, no effort is made to distinguish results obtained with the different exchange-correlation functionals. This represents no loss of information, as the main features of these results do not depend on the specific exchange-correlation functional used in the calculations.

Figure 3.3 shows that, for all three metals considered, and using all four exchange-correlation functionals available in the TB-LMTO ESC program, the difference between the total energy values obtained using INIT1 and INIT2 is not numerically significant, in the sense that it is no larger than the calculation precision errors (CPE's) that these energy values are

known to contain. It can thus be concluded that there is no relationship between the value of the first BZ discretization integers and the initial-condition sensitivity of the minimum total energy values calculated using the TB-LMTO ESC program. This is consistent with the view that the effect of the first-BZ discretization integers on the output of the TB-LMTO ESC program is systematic.

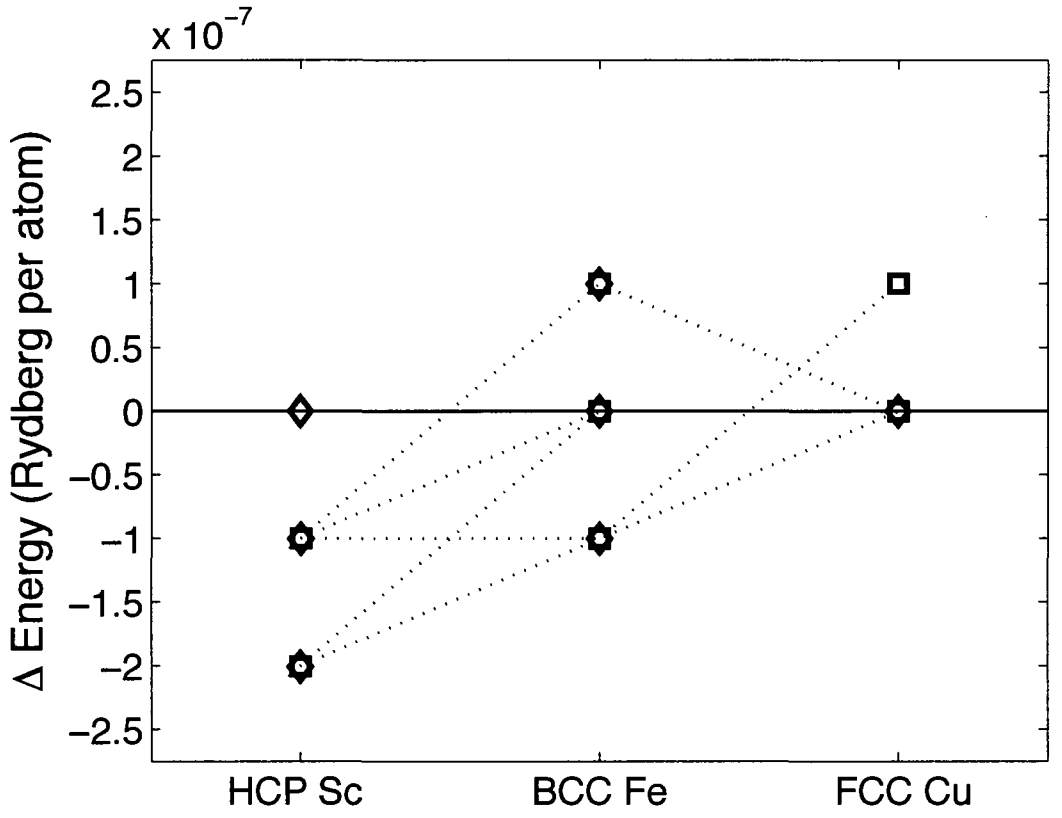

Figure 3.3: Difference between the calculated minimum total energy E_{tot} of a metal obtained with initial conditions INIT1, and the calculated minimum total energy of the metal obtained with initial conditions INIT2 ($E_{tot}\,(INIT1) - E_{tot}\,(INIT2)$). INIT1 and INIT2 are described in section 3.4 of this chapter. Results were obtained with discretization integers $L = M = N = 10$ (diamonds) and $L = M = N = 30$ (squares). Results are shown as obtained using each of the four exchange-correlation functionals available in the TB-LMTO ESC program. To maintain the clarity of the figure, results obtained with the different exchange-correlation functionals are not identified with unique symbols. However, the dotted lines guide the eye to data points obtained using the same exchange-correlation functional. The lattice parameters of the metals are specified in table 3.1.

In order to further clarify the effect of the discretization integers on the numerical precision of the TB-LMTO ESC program, we perform more calculations of the minimum total energy E_{tot} of HCP Sc, BCC Fe and FCC Cu. Specifically, we calculate ten times the minimum total energy of each of these three metals, each time setting the first BZ discretization integers L, M and N to a different value between 5 and 50. During all calculations, L, M and N are kept equal. Four such calculation sets are performed, each using a different one of the four exchange-correlation functionals available in the TB-LMTO ESC programs. The lattice parameters of the metals are as shown in table 3.1. In all calculations, the motion of the electrons is treated relativistically, and the combined correction terms are utilised. Also, the single-electron wave functions of the metals' valence electrons are expressed as a linear combination of s-, p- and d-orbitals only. Finally, the convergence tolerances of the program are set to a value of 1.0×10^{-5}.

Figure 3.4 shows the minimum total energy E_{tot} of HCP Sc, BCC Fe and FCC Cu versus the value of the discretization integers L, M, and N. All minimum total energy values computed for a given metal using a given exchange-correlation functional are reported relative to the minimum total energy value obtained when $L = M = N = 50$. Figure 3.4 shows this information as calculated using all four exchange-correlation functionals available in the TB-LMTO ESC program. To maintain the clarity of the figure, the energy values calculated using different exchange-correlation functionals are not distinguished. This represents no loss of information, as the numerical precision of the TB-LMTO ESC program is independent of the exchange-correlation functional used in the calculations.

Figure 3.4 shows that when the discretization integers are smaller than $L = M = N = 30$, the SCE in the calculated minimum total energy of a solid possessing a given crystal structure is very different of the SCE in the calculated minimum total energy of a solid possessing a different crystal structure. Thus, to compare the minimum total energy of solids possessing different crystal structures, the minimum total energy of the solids should be calculated with $L = M = N \geq 30$. However, even when $L = M = N = 30$, the minimum total energy of a material computed using the TB-LMTO ESC program can be as much as 5.0×10^{-5} Rydberg per atom smaller than that obtained with $L = M = N = 50$.

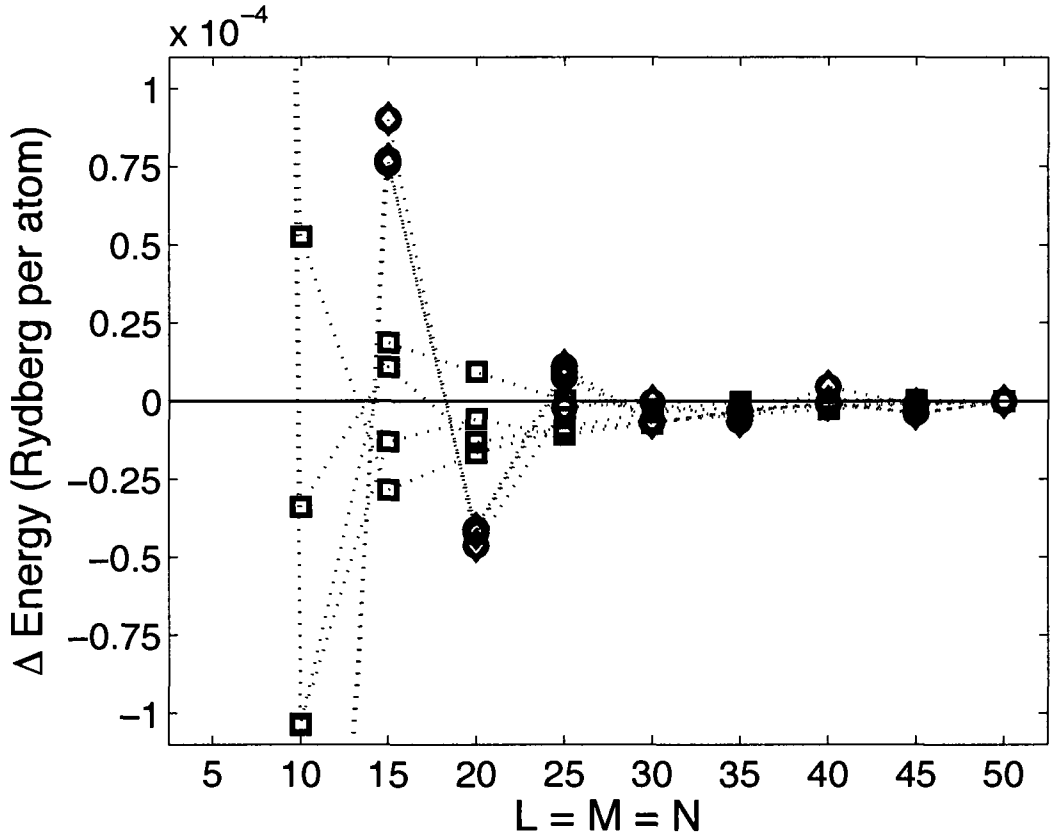

Figure 3.4: Calculated minimum total energy E_{tot} of HCP Sc (circles), BCC Fe (squares) and FCC Cu (diamonds), as calculated using each of the four exchange-correlation functionals available in the TB-LMTO ESC program, versus the value of the first BZ discretization integers L, M, and N. All energy values calculated for a particular metal using a particular exchange-correlation functional are given relative to the energy obtained with the first BZ discretization integers set to $L = M = N = 50$. To maintain the clarity of the figure, energy values computed using the different exchange-correlation functionals are not distinguished. However, the dotted lines guide the eye to data points obtained for a given metal using a given exchange-correlation functional. The lattice parameters of the metals are specified in table 3.1. (Note: the diamonds and circles strongly overlap in the figure.)

Having evaluated the magnitude of the SCE's in the output of the TB-LMTO ESC program, we now verify that these SCE's are not dependent upon the lattice parameter of the solid that is being studied. This is of importance to us, as we shall later be using the calculated $E_{tot}(a)$ curve of FCC Cu to calculate the $a(T)$ curve of metallic Cu using the theoretical method described in chapter 6. We shall see that the shape of this calculated $a(T)$ curve is sensitive to the shape of the calculated $E_{tot}(a)$ curve of FCC Cu. We thus calculate the minimum total energy versus lattice parameter curve $E_{tot}(a)$ of FCC Cu between 6.72 and 6.84 Bohr radii.[3] The curve is calculated three times, once with $L = M = N = 16$, once with $L = M = N = 30$, and once with $L = M = N = 50$. All calculations are performed with exchange-correlation functional EXC2 (see table 2.1), and with the convergence tolerances set to 1.0×10^{-5}. The single-electron wave functions of the metal's valence electrons are constructed using a linear combination of s-, p- and d-orbitals only. The motion of the metal's electrons is treated relativistically, and the combined correction terms are utilised in all calculations. The calculated $E_{tot}(a)$ curves of FCC Cu are shown in figure 3.5. It is clear that the curves that are calculated using $L = M = N = 30$ and $L = M = N = 50$ are very similar. Nonetheless, these curves are in fact significantly different, in the sense that they differ by more than the magnitude of the CPE's in the minimum total energy values computed using the TB-LMTO ESC program. However, the curve obtained using $L = M = N = 16$ is very different of those obtained using $L = M = N = 30$ and $L = M = N = 50$.

Figure 3.6 shows the calculated $E_{tot}(a)$ curve of FCC Cu obtained with discretization integers $L = M = N = 50$, shifted downward by $1.137 \times 10^{-4} \pm 5.0 \times 10^{-7}$ Rydberg per atom, minus the calculated $E_{tot}(a)$ curve of FCC Cu obtained with $L = M = N = 16$. The magnitude of the downward shift was chosen to make the smallest calculated value of the $E_{tot}(a)$ curve computed with $L = M = N = 50$ equal to the smallest calculated value of the $E_{tot}(a)$ curve computed with $L = M = N = 16$. The figure also shows the $E_{tot}(a)$ curve of FCC Cu obtained with discretization integers $L = M = N = 50$, shifted

[3]Specifically, we use the term "calculating the $E_{tot}(a)$ curve of a material" to refer to the process of calculating the value of a material's $E_{tot}(a)$ curve at a number of lattice parameter values in an effort to gain knowledge of some continuous portion of the material's $E_{tot}(a)$ curve.

downward by 6.3×10^{-6} Rydberg units, minus the calculated $E_{tot}(a)$ curve of FCC Cu obtained with $L = M = N = 30$. These results indicate that the $E_{tot}(a)$ curves of FCC Cu obtained with $L = M = N = 16$ and with $L = M = N = 30$ are, within $\pm 2.0 \times 10^{-6}$ Rydberg per atom, simply downward shifted versions of the same $E_{tot}(a)$ curve obtained with $L = M = N = 50$.

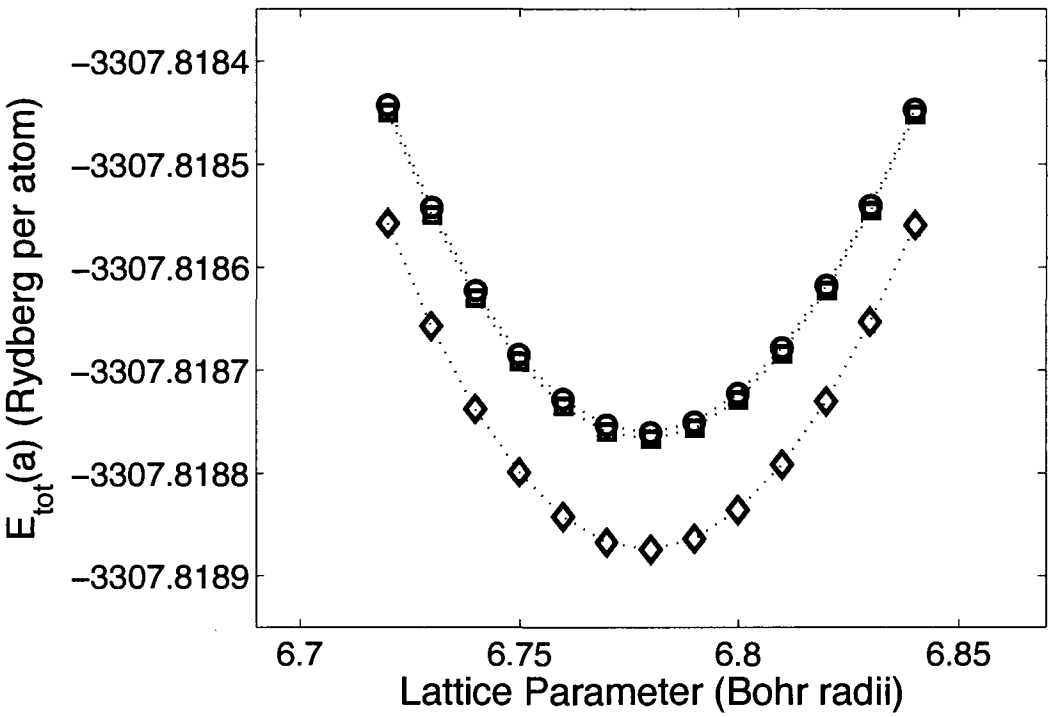

Figure 3.5: Calculated minimum total energy versus lattice parameter curve of FCC Cu obtained with discretization integers $L = M = N = 16$ (diamonds), $L = M = N = 30$ (squares), and $L = M = N = 50$ (circles). Each symbol indicates the calculated minimum total energy of a FCC Cu solid possessing a specific lattice parameter. Error bars indicating the magnitude of the CPE's in the calculated energy values are smaller than the data symbols. Dotted lines guide the eye to energy values computed using the same discretization integers. All curves were calculated using exchange-correlation functional EXC2.

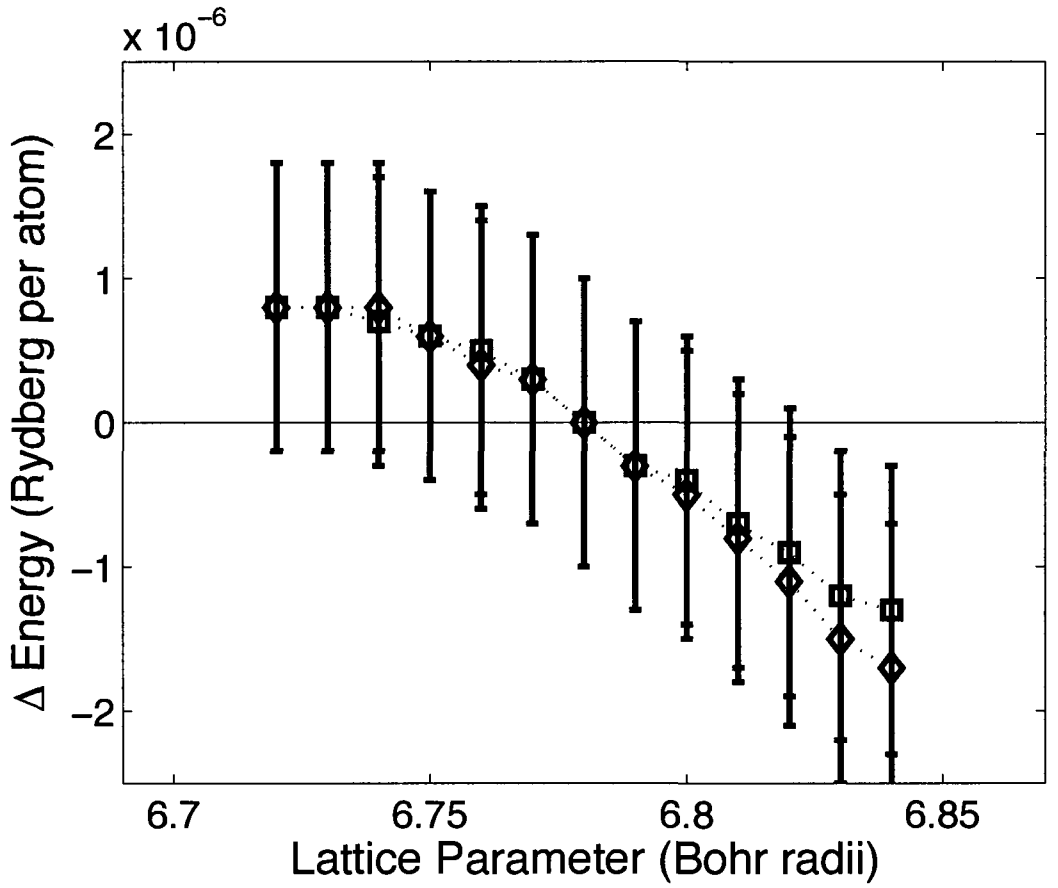

Figure 3.6: Graph shows the calculated minimum total energy versus lattice parameter curve $E_{tot}(a)$ of FCC Cu obtained with discretization integers $L = M = N = 50$, shifted downward by $1.137 \times 10^{-4} \pm 5.0 \times 10^{-7}$ Rydberg per atom, minus the calculated $E_{tot}(a)$ curve of FCC Cu obtained with $L = M = N = 16$ (diamonds). The graph also shows the calculated $E_{tot}(a)$ curve of FCC Cu obtained with discretization integers $L = M = N = 50$, shifted downward by $6.3 \times 10^{-6} \pm 5.0 \times 10^{-7}$ Rydberg per atom, minus the calculated $E_{tot}(a)$ curve of FCC Cu obtained with $L = M = N = 30$ (squares). The original $E_{tot}(a)$ curves are shown in figure 3.5. Error bars take into account that all calculated energy values are precise to $\pm 2.5 \times 10^{-7}$ Rydberg per atom, and that the shifting constants are precise only to $\pm 5.0 \times 10^{-7}$ Rydberg per atom. All $E_{tot}(a)$ curves were calculated using exchange-correlation functional EXC2.

3.3 Numerical Precision of the TB-LMTO ESC Program : Summary

We established, in section 3.1, a clear definition of the numerical precision of the TB-LMTO ESC program. We also indicated that the minimum total energy values computed using the program are affected by a number of parameters within the program. We indicated that some of these parameters, like the exchange-correlation functional that is used in conducting calculations, affect the accuracy of the calculated minimum total energy values. We also indicated that other parameters, like the program's convergence tolerances and first-BZ discretization integers, affect the precision of the TB-LMTO ESC program. We indicated that the minimum total energy of a solid, as calculated using the TB-LMTO ESC program, can be viewed as a theoretical measurement of this energy containing a random calculation precision error (CPE) and a systematic calculation error (SCE).

We have shown in section 3.2.2 that, during all calculations performed with the TB-LMTO ESC program [28], the program's convergence tolerances should be no larger than 1.0×10^{-5} (Rydberg units for the total energy convergence tolerance, and electrons per cubic Bohr radii for the electron density convergence tolerance). Making the magnitude of these convergence tolerances larger than 1.0×10^{-5} noticeably decreases the precision of the TB-LMTO ESC program. At the same time, making the magnitude of these convergence tolerances smaller than 1.0×10^{-5} produces no significant improvement of the precision of the program.

We have also illustrated that all calculated values of the minimum total energy of a solid contain a random calculation precision error (CPE). We have not identified the statistical distribution of the CPE's in the minimum total energy values obtained using the TB-LMTO ESC program. However, we have estimated that they are of the order of $\pm 2.5 \times 10^{-7}$ Rydberg per atom when the convergence tolerances are set to 1.0×10^{-5}. Thus, we argue that the minimum total energy values computed using the TB-LMTO ESC program are only precise to $\pm 2.5 \times 10^{-7}$ Rydberg per atom.

We have also shown in section 3.2.3 that the first-BZ discretization integers of the TB-LMTO ESC program control the magnitude of a systematic calculation error (SCE) in the minimum total energy values computed by the program. These SCE's are systematic, in the sense that they are not dependent on the initial conditions of the calculation. All calculated values of the minimum total energy of a given solid, obtained using the same first-BZ discretization integers, will contain the same SCE.

In addition, we have shown that, in conducting a calculation, a good choice of the value of the first BZ discretization integers is $L = M = N = 30$. Setting these integers to a larger value increases the time required to calculate the minimum total energy of a solid while not reducing very much the SCE's in the minimum total energy values computed using the TB-LMTO ESC program. However, when $L = M = N = 30$, the SCE in the calculated minimum total energy of a metal possessing one crystal structure can differ by as much as 5.0×10^{-5} Rydberg per atom from the SCE in the calculated minimum total energy of a metal possessing a different crystal structure. This knowledge is important, as we shall use the TB-LMTO ESC program to predict the crystal structure of the first-row transition metals in the next chapter.

We also observed that, when the first-BZ discretization integers are set to $L = M = N = 30$, the minimum total energy of FCC Cu, as computed using the TB-LMTO ESC program, contains a SCE of the order of -5.0×10^{-6} Rydberg per atom. In addition, when the first-BZ discretization integers are set to $L = M = N = 16$, the minimum total energy of FCC Cu, as computed using the TB-LMTO ESC program, contains a SCE of the order of -1.0×10^{-4} Rydberg per atom. Importantly, we also demonstrated that the $E_{tot}(a)$ curve of FCC Cu, as computed using $L = M = N = 16$, is essentially a downward shifted version of the same curve obtained using $L = M = N = 50$. This is important to us because, in chapter 7, we will use the calculated $E_{tot}(a)$ curve of FCC Cu to calculate the lattice parameter versus temperature curve $a(T)$ of metallic Cu using the theoretical method described in chapter 6. We shall see that this calculated $a(T)$ curve is sensitive to the shape of the calculated $E_{tot}(a)$ curve of FCC Cu.

This concludes our study of the numerical precision of the TB-LMTO ESC program. We now evaluate the program's accuracy by using it to calculate some of the zero-Kelvin properties of the first-row transition metals.

3.4 Appendix : Initial Conditions INIT1 and INIT2

In sections 3.2.2 and 3.2.3, we studied the sensitivity of the minimum total energy of a solid, as calculated using the TB-LMTO ESC program, to the initial conditions of the calculation of this energy. More specifically, we conducted calculations beginning with two sets of initial conditions, which we labelled INIT1 and INIT2. We described in section 3.2.1 the method we employed to construct these initial condition sets.

As we explained in section 3.2.1, initial conditions INIT1 and INIT2 are in effect initial estimates of the valence electron distribution $\rho_v(\vec{r})$ of HCP Sc, BCC Fe and FCC Cu. The initial estimates of $\rho_v(\vec{r})$ that are part of INIT1 and INIT2 are not good estimates of the lowest-energy distribution of the valence electrons of HCP Sc (as defined in section 3.1). However, they are sufficiently different of such a good estimate to allow for a meaningful study of the initial-condition sensitivity of the calculation of the minimum total energy of HCP Sc, BCC Fe and FCC Cu. The values of the integrals $\int^{E_F} n_{v,l}(\epsilon)d\epsilon$ in the basis set of initial conditions, and in the initial condition sets INIT1 and INIT2, are given in tables 3.2, 3.3 and 3.4 for HCP Sc, BCC Fe and FCC Cu respectively. It should be noted that not all figures reported in these tables are necessarily significant. We report, in tables 3.2, 3.3 and 3.4, all figures provided by the TB-LMTO ESC program for the integral $\int^{E_F} n_{v,l}(\epsilon)d\epsilon$ in the basis set of initial conditions. We also report as many figures for the values of the integrals $\int^{E_F} n_{v,l}(\epsilon)d\epsilon$ in initial condition sets INIT1 and INIT2. We report all these figures because we simply do not know how many of them are significant prior to studying the initial condition sensitivity of the output of the TB-LMTO ESC program.

Table 3.2: Value of $\int^{E_F} n_{v,l}(\epsilon)d\epsilon$ in initial conditions for HCP Sc

Initial values of $\int^{E_F} n_{v,l}(\epsilon)d\epsilon$ for calculations using EXC1.

Integral	Basis value	INIT1 value	INIT2 value
$\int^{E_F} n_0(\epsilon)d\epsilon$	0.69902182	1.19902182	0.19902182
$\int^{E_F} n_1(\epsilon)d\epsilon$	0.65010959	1.15010959	0.15010959
$\int^{E_F} n_2(\epsilon)d\epsilon$	1.65086857	0.65086857	2.15086857

Initial values of $\int^{E_F} n_{v,l}(\epsilon)d\epsilon$ for calculations using EXC2.

Integral	Basis value	INIT1 value	INIT2 value
$\int^{E_F} n_0(\epsilon)d\epsilon$	0.70689694	1.20689694	0.20689694
$\int^{E_F} n_1(\epsilon)d\epsilon$	0.68835006	1.18835006	0.18835006
$\int^{E_F} n_2(\epsilon)d\epsilon$	1.60475296	0.60475296	2.10475296

Initial values of $\int^{E_F} n_{v,l}(\epsilon)d\epsilon$ for calculations using EXC3.

Integral	Basis value	INIT1 value	INIT2 value
$\int^{E_F} n_0(\epsilon)d\epsilon$	0.70069240	1.20069240	0.20069240
$\int^{E_F} n_1(\epsilon)d\epsilon$	0.65308972	1.15308972	0.15308972
$\int^{E_F} n_2(\epsilon)d\epsilon$	1.64621785	0.64621785	2.14621785

Initial values of $\int^{E_F} n_{v,l}(\epsilon)d\epsilon$ for calculations using EXC4.

Integral	Basis value	INIT1 value	INIT2 value
$\int^{E_F} n_0(\epsilon)d\epsilon$	0.71273734	1.21273734	0.21273734
$\int^{E_F} n_1(\epsilon)d\epsilon$	0.67538902	1.17538902	0.17538902
$\int^{E_F} n_2(\epsilon)d\epsilon$	1.61187357	0.61187357	2.11187357

units of integrals: electrons

$n_0(\epsilon)$ = density of states of s-electrons

$n_1(\epsilon)$ = density of states of p-electrons

$n_2(\epsilon)$ = density of states of d-electrons

Table 3.3: Value of $\int^{E_F} n_{v,l}(\epsilon)d\epsilon$ in initial conditions for BCC Fe

Initial values of $\int^{E_F} n_{v,l}(\epsilon)d\epsilon$ for calculations using EXC1.

Integral	Basis value	INIT1 value	INIT2 value
$\int^{E_F} n_{0,s_1}(\epsilon)d\epsilon$	0.32228175	0.82228175	0.07228175
$\int^{E_F} n_{0,s_2}(\epsilon)d\epsilon$	0.31211326	0.81211326	0.06211326
$\int^{E_F} n_{1,s_1}(\epsilon)d\epsilon$	0.42561937	0.92561937	0.17561937
$\int^{E_F} n_{1,s_2}(\epsilon)d\epsilon$	0.37862646	0.87862646	0.12862646
$\int^{E_F} n_{2,s_1}(\epsilon)d\epsilon$	2.17871607	1.17871607	2.67871607
$\int^{E_F} n_{2,s_2}(\epsilon)d\epsilon$	4.38264308	3.38264308	4.88264308

Initial values of $\int^{E_F} n_{v,l}(\epsilon)d\epsilon$ for calculations using EXC2.

Integral	Basis value	INIT1 value	INIT2 value
$\int^{E_F} n_{0,s_1}(\epsilon)d\epsilon$	0.32672011	0.82672011	0.07672011
$\int^{E_F} n_{0,s_2}(\epsilon)d\epsilon$	0.31227108	0.81227108	0.06227108
$\int^{E_F} n_{1,s_1}(\epsilon)d\epsilon$	0.43701766	0.93701766	0.18701766
$\int^{E_F} n_{1,s_2}(\epsilon)d\epsilon$	0.37189844	0.87189844	0.12189844
$\int^{E_F} n_{2,s_1}(\epsilon)d\epsilon$	2.09296637	1.09296637	2.59296637
$\int^{E_F} n_{2,s_2}(\epsilon)d\epsilon$	4.45912635	3.45912635	4.95912635

Initial values of $\int^{E_F} n_{v,l}(\epsilon)d\epsilon$ for calculations using EXC3.

Integral	Basis value	INIT1 value	INIT2 value
$\int^{E_F} n_{0,s_1}(\epsilon)d\epsilon$	0.32497455	0.82497455	0.07497455
$\int^{E_F} n_{0,s_2}(\epsilon)d\epsilon$	0.30871714	0.80871714	0.05871714
$\int^{E_F} n_{1,s_1}(\epsilon)d\epsilon$	0.43677550	0.93677550	0.18677550
$\int^{E_F} n_{1,s_2}(\epsilon)d\epsilon$	0.35936750	0.85936750	0.10936750
$\int^{E_F} n_{2,s_1}(\epsilon)d\epsilon$	2.11337419	1.11337419	2.61337419
$\int^{E_F} n_{2,s_2}(\epsilon)d\epsilon$	4.45679112	3.45679112	4.95679112

Value of $\int^{E_F} n_{v,l}(\epsilon)d\epsilon$ in initial conditions for BCC Fe (continued)

Initial values of $\int^{E_F} n_{v,l}(\epsilon)d\epsilon$ for calculations using EXC4.

Integral	Basis value	INIT1 value	INIT2 value
$\int^{E_F} n_{0,s_1}(\epsilon)d\epsilon$	0.33509919	0.83509919	0.08509919
$\int^{E_F} n_{0,s_2}(\epsilon)d\epsilon$	0.31361983	0.81361983	0.06361983
$\int^{E_F} n_{1,s_1}(\epsilon)d\epsilon$	0.43782165	0.93782165	0.18782165
$\int^{E_F} n_{1,s_2}(\epsilon)d\epsilon$	0.33802355	0.83802355	0.08802355
$\int^{E_F} n_{2,s_1}(\epsilon)d\epsilon$	1.95145546	0.95145546	2.45145546
$\int^{E_F} n_{2,s_2}(\epsilon)d\epsilon$	4.62398033	3.62398033	5.12398033

units of integrals: electrons

$n_{0,s_1}(\epsilon)$ = density of states of s-electrons, with spin s_1

$n_{0,s_2}(\epsilon)$ = density of states of s-electrons, with spin s_2

$n_{1,s_1}(\epsilon)$ = density of states of p-electrons, with spin s_1

$n_{1,s_2}(\epsilon)$ = density of states of p-electrons, with spin s_2

$n_{2,s_1}(\epsilon)$ = density of states of d-electrons, with spin s_1

$n_{2,s_2}(\epsilon)$ = density of states of d-electrons, with spin s_2

Table 3.4: Value of $\int^{E_F} n_{v,l}(\epsilon)d\epsilon$ in initial conditions for FCC Cu

Initial values of $\int^{E_F} n_{v,l}(\epsilon)d\epsilon$ for calculations using EXC1.

Integral	Basis value	INIT1 value	INIT2 value
$\int^{E_F} n_0(\epsilon)d\epsilon$	0.69312236	1.69312236	0.19312236
$\int^{E_F} n_1(\epsilon)d\epsilon$	0.76727729	1.76727729	0.26727729
$\int^{E_F} n_2(\epsilon)d\epsilon$	9.53960035	7.53960035	10.53960035

Initial values of $\int^{E_F} n_{v,l}(\epsilon)d\epsilon$ for calculations using EXC2.

Integral	Basis value	INIT1 value	INIT2 value
$\int^{E_F} n_0(\epsilon)d\epsilon$	0.69329131	1.69329131	0.19329131
$\int^{E_F} n_1(\epsilon)d\epsilon$	0.76124768	1.76124768	0.26124768
$\int^{E_F} n_2(\epsilon)d\epsilon$	9.54546101	7.54546101	10.54546101

Initial values of $\int^{E_F} n_{v,l}(\epsilon)d\epsilon$ for calculations using EXC3.

Integral	Basis value	INIT1 value	INIT2 value
$\int^{E_F} n_0(\epsilon)d\epsilon$	0.69367092	1.69367092	0.19367092
$\int^{E_F} n_1(\epsilon)d\epsilon$	0.76390990	1.76390990	0.26390990
$\int^{E_F} n_2(\epsilon)d\epsilon$	9.54241918	7.54241918	10.54241918

Initial values of $\int^{E_F} n_{v,l}(\epsilon)d\epsilon$ for calculations using EXC4.

Integral	Basis value	INIT1 value	INIT2 value
$\int^{E_F} n_0(\epsilon)d\epsilon$	0.70457614	1.70457614	0.20457614
$\int^{E_F} n_1(\epsilon)d\epsilon$	0.70469579	1.70469579	0.20469579
$\int^{E_F} n_2(\epsilon)d\epsilon$	9.59072807	7.59072807	10.59072807

units of integrals: electrons

$n_0(\epsilon)$ = density of states of s-electrons

$n_1(\epsilon)$ = density of states of p-electrons

$n_2(\epsilon)$ = density of states of d-electrons

Chapter 4

Accuracy of the TB-LMTO ESC Program - Calculation of Some Zero-Kelvin Properties of the First-Row Transition Metals

Having examined its numerical precision, we now evaluate the accuracy of the TB-LMTO ESC program [28]. To do so, we use the TB-LMTO ESC program to predict the crystal structure, the lattice parameters, the bulk modulus, and the magnitude of the magnetic moments of the first-row transition metals at zero Kelvin. We then evaluate the accuracy with which the TB-LMTO ESC program predicts these first-row transition metal properties. In doing so, we indirectly evaluate the accuracy of the minimum total energy and the lowest-energy electron configuration of the first-row transition metals, as calculated using the TB-LMTO ESC program.[1]

[1]We do not evaluate, in this chapter, the accuracy of other solid properties that can be calculated using the TB-LMTO ESC program. The program can calculate, in addition to its minimum total energy and its lowest-energy electron distribution, the dispersion relation $\epsilon\left(\vec{k}\right)$, the density of states function $n_v\left(\epsilon\right)$, and the Fermi surface of a solid. The minimum total energy and the lowest-energy electron distribution are most important to us, given the studies that we shall conduct in the coming chapters.

We are motivated to study the accuracy of the TB-LMTO ESC program [28] because we shall use it to study the magnetism of the FCC-structured first-row transition metals (see chapter 5). The accuracy of the TB-LMTO ESC program will, in large part, determine the accuracy of the results of this latter study. In chapter 7, we shall also use the program to study the thermal expansion of metallic Cu using a theoretical method for calculating the Helmholtz' free energy of a solid presented in chapter 6. To do so, we will use the TB-LMTO ESC program to calculate the minimum total energy versus lattice parameter curve $E_{tot}(a)$ of FCC Cu, as knowledge of this curve, and of its derivatives, is required to calculate the lattice parameter versus temperature curve $a(T)$ of metallic Cu. We wish to ascertain that the $E_{tot}(a)$ curve of FCC Cu can be accurately calculated using the TB-LMTO ESC program, as the accuracy of this curve will determine to a large extent the accuracy of the calculated $a(T)$ curve of metallic Cu.

We begin, in section 4.1, by defining the accuracy of the TB-LMTO ESC program. We also explain that it is not possible, for practical reasons, to evaluate the accuracy with which the TB-LMTO ESC program calculates the minimum total energy or the lowest-energy electron distribution of a material. We then explain that the accuracy of these calculated material properties can be evaluated indirectly by examining the accuracy with which the TB-LMTO ESC program calculates other material properties. In section 4.2, we use the TB-LMTO ESC program to predict the crystal structure, the magnetic structure, the lattice parameters, the bulk modulus, and the magnitude of the magnetic moments of the first-row transition metals (Sc to Zn) at zero Kelvin. We evaluate the accuracy of these calculated first-row transition metal properties. Finally, in section 4.3, we summarise the conclusions of section 4.2 and compare them to the results of other studies of the accuracy of ESC programs.

To our knowledge, this study of the accuracy of the TB-LMTO ESC program in predicting the crystal structure, the magnetic structure, the lattice parameters, the bulk moduli and the magnitude of the magnetic moments of the first-row transition metals at zero Kelvin, has not previously been reported.

4.1 Accuracy of the TB-LMTO ESC Program : Definition

As we already indicated in chapter 3, the physical accuracy of the TB-LMTO ESC program [28] can be defined as the degree of correspondence between the properties of a material as calculated by the ESC program and the real-world, measured properties of the material.[2] To evaluate the accuracy of the TB-LMTO ESC program, the value of a solid property, as calculated by the program, must be compared to the measured value of this solid property.

There are a number of factors affecting the accuracy of the TB-LMTO ESC program [28]. As we indicated in chapters 2 and 3, any calculation conducted using the TB-LMTO ESC program can be carried out using any one of four exchange-correlation functionals (see table 2.1). Each of these exchange-correlation functionals is derived using slightly different physical models and mathematical descriptions of electron exchange. Thus, the accuracy of the TB-LMTO ESC program will be different when it is used in conjunction with different exchange-correlation models. We investigate in this chapter the accuracy of the TB-LMTO ESC program when it is used in conjunction with each of the four exchange-correlation functionals that are available within it.

In addition, it was specified in chapter 2 that the user of the TB-LMTO ESC program must specify whether or not relativistic effects are to be considered when evaluating the kinetic energy of the electrons of a solid (for more information, see [32, p. 219]). The user of the program must also specify whether or not the "combined correction terms" [32, p. 95] are to be used in a given calculation. The choices made by the TB-LMTO ESC program's user in regards to these latter aspects of the program can be expected to affect the program's accuracy. We shall include relativistic effects in all calculations conducted in this chapter, as the kinetic energy of the electrons of the first-row transitions metals is sufficiently large to warrant a relativistic treatment. In addition, that the WS unit cells of the first-row transition metals are not spheres warrants the use of the combined corrections terms to correct for the errors of the ASA. We therefore use the combined correction terms in all

[2]This definition was inspired by the definitions of the French terms "exactitude" and "justesse" given in the "Grand dictionnaire terminologique" of the "Office québécois de la langue française" [73].

our calculations.

Finally, the user of the TB-LMTO ESC program must specify the set of basis functions to be used in modelling the valence electrons of a solid. As indicated in chapter 2, the valence electrons of a solid are modelled, within the TB-LMTO ESC program, using a linear combination of atomic orbitals (see equation 2.29). In all calculations conducted in this chapter, the wave functions of the valence electrons of any first-row transition metal are modelled as linear combinations of s-, p- and d-orbitals only. We shall justify this choice in section 4.2.1.

Before evaluating the accuracy of the TB-LMTO ESC program [28], we must understand exactly what solid properties can be calculated by the program. As indicated in chapter 2, the TB-LMTO ESC program can be used to calculate the minimum total energy of a solid and the lowest-energy electron distribution of a solid. Physical systems, including solid materials, take their lowest-energy state when they have a temperature of zero Kelvin [76]. Thus, the TB-LMTO ESC program is a theoretical tool for calculating the electron distribution and the total energy of solids at zero Kelvin. However, the expression for the total energy of a solid that is implemented within the TB-LMTO ESC program is derived assuming that the atomic nuclei of the solid remain stationary at all times. It is known that the constituent atomic nuclei of all real solids are always in motion, even at zero Kelvin, because of the quantum-mechanical phenomenon of zero point motion [37, p. 416]. Thus, the expression for the total energy of a solid that is implemented within the TB-LMTO ESC program is not a correct description of the total energy of a real solid, even at zero Kelvin. This, however, does not negate the fact that the minimum total energy and lowest-energy electron distribution of a solid, as calculated using the TB-LTMO ESC program, must be considered estimates of the total energy and electron distribution of the solid when it possesses a temperature of zero Kelvin. This is so because the motion of a solid's atomic nuclei is minimal when the solid has a temperature of zero Kelvin [37, p. 416].

In order to evaluate the accuracy of the calculated minimum total energy and lowest-energy electron distribution of a solid, we require a precise measurement of the total en-

ergy and electron distribution of the solid at zero Kelvin. The electron distribution of a solid can be measured precisely using X-ray diffraction techniques [77], but not at zero Kelvin. Nonetheless, using measurements of the solid's electron distribution at a number of temperatures, the electron distribution of the solid at zero Kelvin can be found using extrapolation techniques. Unfortunately, the measurement of the electron distribution of any solid is a complex experiment, and so, that of most first-row transition metals has not been measured. Thus, it is not possible, in practice, to directly verify the accuracy of the lowest-energy electron distribution of the first-row transition metals, as calculated using the TB-FLMTO ESC program. In contrast, the accuracy of the calculated minimum total energy of a solid can be verified using measurements of the solid's cohesive energy. Measurements of the cohesive energy of most solids are commonly published [78]. The cohesive energy of a solid at zero Kelvin is the minimum total energy of the solid relative to the energy of all the solid's atoms when they are separated, stationary, and possessing a neutral electrical charge [79]. Unfortunately, it is not clear that the TB-LMTO ESC program can accurately calculate the minimum total energy of a solid's constituent atoms when they are separated, stationary and neutral, and so we do not attempt, in this study, to calculate the cohesive energy of any solid.

However, it is possible to use the TB-LMTO ESC program to calculate other properties of a solid using its minimum total energy versus lattice parameter curve $E_{tot}(a)$. An $E_{tot}(a)$ curve can be calculated for any solid possessing a given crystal structure, chemical composition and chemical order. For example, an $E_{tot}(a)$ curve can be obtained for a metal consisting only of Fe and possessing the BCC crystal structure, and a second $E_{tot}(a)$ curve can be obtained for FCC Fe. A qualitative evaluation of the accuracy of these calculated curves can be conducted by ensuring that the minimum value of the $E_{tot}(a)$ curve of BCC Fe is smaller than the minimum value of the $E_{tot}(a)$ curve FCC Fe. This must be so, as metallic iron at zero Kelvin has the BCC crystal structure. In addition, the lattice parameter at which the $E_{tot}(a)$ curve of a solid possesses a global minimum is an estimate of the zero-Kelvin lattice parameter of the solid. This calculated zero-Kelvin lattice parameter can be compared to measurements of the lattice parameter of the solid at zero Kelvin,

which can be obtained with great precision by extrapolation, using measurements of the lattice parameter of the solid at many temperatures. Thus, a quantitative evaluation of the accuracy of the location of the global minimum of the calculated $E_{tot}(a)$ curve of a solid can be conducted. Thirdly, the $E_{tot}(a)$ curve of a solid can be used to calculate its zero-Kelvin bulk modulus, a quantity proportional to the second-derivative of the solid's $E_{tot}(a)$ curve. The calculated value of the bulk modulus of a solid can also be compared to measurements. Thus, we can conduct a quantitative evaluation of the accuracy of the curvature of the calculated $E_{tot}(a)$ curve of a solid in the vicinity of its global minimum. Finally, it is also possible to use the calculated lowest-energy electron distribution of a solid to calculate the magnitude of the magnetic moments in the solid at zero Kelvin. This calculated magnetic moment magnitude can be compared to measurements of the magnitude of the magnetic moments of the solid at zero Kelvin, which again can be obtained by extrapolation using measurements of the magnitude of the magnetic moments of the solid at many temperatures. This amounts to an indirect evaluation of the accuracy of the calculated lowest-energy electron distribution of a solid.

4.2 Accuracy of the TB-LMTO ESC Program : Evaluation

We now evaluate the accuracy of the TB-LMTO ESC program [28] in predicting the crystal structure, the magnetic structure, the lattice parameters, the bulk modulus, and the magnitude of the magnetic moments of each of the ten first-row transition metals (Sc to Zn) at zero Kelvin.

In section 4.2.1, we describe the calculations that we perform in order to predict, using the TB-LMTO ESC program [28], the crystal structure, the magnetic structure, the lattice parameters, the bulk modulus, and the magnitude of the magnetic moments of the first-row transition metals at zero Kelvin. The results and accuracy of these calculations are examined in sections 4.2.2 (crystal structure and magnetic structure), 4.2.3 (lattice parameters), 4.2.4 (bulk modulus), and 4.2.5 (magnetic moments).

4.2.1 Zero-Kelvin Properties of the First-Row Transition Metals : Calculation Details

To evaluate the accuracy of the TB-LMTO ESC program in calculating the zero-Kelvin properties of the first-row transition metals, we calculate the minimum total energy versus lattice parameter curve $E_{tot}(a)$ of 30 chemically pure metals, each consisting of one of the ten first-row transition elements (Sc to Zn), and possessing either the BCC, the FCC or the HCP crystal structure. Our purpose is to identify the lattice parameter at which all of these curves possess a global minimum value. Using this information, we can predict the first-row transition metal properties listed above. We restrict ourselves to studying BCC, FCC and HCP metals because all first-row transition metals, with the exception of metallic Mn, possess one of these crystal structures at zero Kelvin.

We calculate three times the $E_{tot}(a)$ curve of each of these 30 metals, once assuming that the metal possesses no magnetic moments (NM magnetic structure), once assuming that it can possess moments arranged in a collinear ferromagnetic structure (FM magnetic structure), and once assuming that it can possess moments arranged in a collinear anti-ferromagnetic structure (AFM magnetic structure). Thus, a total of 90 $E_{tot}(a)$ curves are calculated.

The NM, FM and AFM magnetic structures are defined as follows. Ferromagnetic BCC metals (e.g. FM BCC Fe) are assumed to possess magnetic moments oriented along lines that are perpendicular to the (001) plane. The magnetic moments in the anti-ferromagnetic BCC metals (e.g. AFM BCC Fe) are also assumed to be oriented along lines that are perpendicular to the (001) plane, with atoms possessing magnetic moments oriented in opposite directions arranged in a cesium-chloride structure [37, p. 81]. Ferromagnetic FCC metals (e.g. FM FCC Fe) are assumed to possess magnetic moments oriented along lines that are perpendicular to the (110) plane. The magnetic moments in the AFM FCC metals (e.g. AFM FCC Fe) are also assumed to be oriented along lines perpendicular to the (110) plane, with alternating atomic planes in the (110) direction possessing magnetic moments oriented in opposite directions. The ferromagnetic HCP metals (e.g. FM HCP Fe) are as-

sumed to possess magnetic moments that are oriented along the c-axis of the HCP crystal structure, along lines perpendicular to the (0001) plane. The magnetic moments in the AFM HCP metals (e.g. AFM HCP Fe) are assumed to be oriented along the c-axis of the HCP crystal structure, with alternating atomic planes in the (0001) direction possessing magnetic moments oriented in opposite directions.

The orientation of the magnetic moments of the BCC metals and of the HCP metals, described above, are respectively chosen because real BCC Fe and HCP Co possess magnetic moments oriented in this manner [2]. It should be noted that the magnetic moments in real metallic Ni (the only magnetic FCC-structured first-row transition metal) are oriented along lines that are perpendicular to the (111) plane [2], and not perpendicular to the (110) plane as described above. This is not of concern, as the TB-LMTO ESC program makes no distinction between solids that are identical in every respect other than the orientation of their magnetic moments. This is because the TB-LMTO ESC program calculates the spherical average of the electron distribution around each atom in a solid, as explained in chapter 2. Thus, the TB-LMTO ESC program can not be used to study the magneto-crystalline anisotropy of materials.

As per the results of section 3.2, all 90 minimum total energy versus lattice parameter curves $E_{tot}(a)$ are calculated with convergence tolerances set to a value of 1.0×10^{-5} (Rydberg units for the total energy convergence tolerance, and electrons per cubic Bohr radii for the electron density convergence tolerance), and with the first BZ discretization integers set to $L = M = N = 30$. In all calculations, the motion of the electrons is treated relativistically, and the combined correction terms are utilised (see chapter 2). Also, the single-electron wave functions of the metals' valence electrons are expressed as a linear combination of s-, p- and d-orbitals only. We choose not to include f-orbitals in any of our calculations because these orbitals are not important in the construction of the valence electron distributions of the first-row transition metals. To understand what we mean by this, we must recall that the valence electron distribution of a solid is expressed within the

TB-LMTO ESC program as follows (equation 2.38):

$$\begin{aligned}\rho_v(\vec{r}) &= \frac{1}{4\pi}\sum_l \left|\phi_l(\epsilon_{\mu,l},|\vec{r}|,s_i)\right|^2 \int^{E_F} n_{v,l}(\epsilon)d\epsilon \\ &+ \frac{1}{4\pi}\sum_l 2\phi_l(\epsilon_{\mu,l},|\vec{r}|,s_i)\phi_l'(\epsilon_{\mu,l},|\vec{r}|,s_i)\int^{E_F}(\epsilon-\epsilon_{\mu,l})\,n_{v,l}(\epsilon)d\epsilon \\ &+ \frac{1}{4\pi}\sum_l \left\{\left|\phi_l'(\epsilon_{\mu,l},|\vec{r}|,s_i)\right|^2+\phi_l''(\epsilon_{\mu,l},|\vec{r}|,s_i)\phi_l(\epsilon_{\mu,l},|\vec{r}|,s_i)\right\}\int^{E_F}(\epsilon-\epsilon_{\mu,l})^2\,n_{v,l}(\epsilon)d\epsilon. \end{aligned} \tag{4.1}$$

If f-orbitals are included in the calculation of the valence electron distribution of a solid, then the summation over l in all three terms of equation 4.1 runs over a s-, p-, d- and f-orbital component. When we attempt to calculate the valence electron distributions of the first-row transition metals using s-, p-, d- and f-orbitals, the program terminates with all three integrals $\int^{E_F} n_{v,f}(\epsilon)d\epsilon$, $\int^{E_F}(\epsilon-\epsilon_{\mu,f})\,n_{v,f}(\epsilon)d\epsilon$ and $\int^{E_F}(\epsilon-\epsilon_{\mu,f})^2\,n_{v,f}(\epsilon)d\epsilon$ equal to zero. We thus conclude that f-orbitals are not important in the construction of the valence electron distributions of the first-row transition metals.

Finally, we calculate our 90 $E_{tot}(a)$ curves 4 times, each time using a different one of the exchange-correlation functionals that are available in the TB-LMTO ESC program (see table 2.1). Using a given exchange-correlation functional, each of the 90 $E_{tot}(a)$ curves is calculated over a range of lattice parameter values, typically 0.1 to 0.3 Bohr radii in width, within which the curve possesses a global minimum value. It should be noted that all HCP metals are assumed to possess the ideal c/a ratio of $c/a = \sqrt{8/3}$ [37], with the exception of HCP Sc, HCP Ti, HCP Fe, HCP Co, and HCP Zn. Sc, Ti, Co and Zn possess the HCP crystal structure at zero Kelvin, and we want to test the accuracy of the TB-LMTO ESC program in calculating both the a and c lattice parameters of these metals. Fe, in contrast, is BCC at zero Kelvin, but it is known that the energy of the HCP Fe crystal is only slightly larger than that of the BCC Fe crystal, and as a result, some ESC programs predict that metallic Fe has the HCP crystal structure at zero Kelvin (e.g. [55,57,60,62,64,65,67,72]). Because of this, we want to verify that the TB-LMTO ESC program correctly predicts the ground state crystal structure of metallic Fe. Thus, for HCP Sc, HCP Ti, HCP Fe, HCP Co, and HCP Zn,

we calculate a minimum total energy versus lattice parameter function $E_{tot}(a, c)$, where a and c are the lattice parameters defining the HCP crystal structure [37]. Each function $E_{tot}(a, c)$ is calculated over a two-dimensional lattice parameter space, covering a range of a-parameter values typically 0.25 Bohr radii in width, and a range of values of the c/a ratio typically of width 0.1. The calculated functions $E_{tot}(a, c)$ can be used to calculate both the a and c lattice parameters of the metals HCP Sc, HCP Ti, HCP Fe, HCP Co, and HCP Zn at zero Kelvin. However, the ideal value of the c/a ratio is used when calculating the $E_{tot}(a)$ curves of HCP Zn using exchange-correlation functionals EXC1 and EXC3. This is done because, when used with exchange-correlation functionals EXC1 and EXC3, the TB-LMTO ESC program fails to converge in the vicinity of the global minimum of the $E_{tot}(a, c)$ function of HCP Zn.

We have shown in chapter 3 that the results of a calculation conducted using the TB-LMTO ESC program are dependent on the initial conditions of the calculation. Thus, the $E_{tot}(a)$ curve of a metal, as calculated using a given set of initial conditions, must be viewed as a single realization of the computational measurement of this curve. To properly calculate the $E_{tot}(a)$ curve of a metal, one should calculate the curve numerous times, each time beginning with different initial conditions. This would provide information about the calculation precision error (CPE) in the calculated values of the $E_{tot}(a)$ curve (see chapter 3). However, given the understanding of the numerical precision of the TB-LMTO ESC program that we obtained in chapter 3, only one single computational realization of the $E_{tot}(a)$ curve of a solid is required to predict the crystal structure, magnetic structure, lattice parameters, and magnitude of the magnetic moments of the solid at zero Kelvin.

4.2.2 Accuracy of the Calculated Zero-Kelvin Crystal Structure and Magnetic Structure of the First-Row Transition Metals

We now use the 90 minimum total energy versus lattice parameter curves $E_{tot}(a)$, appropriately calculated using the TB-LMTO ESC program as described in section 4.2.1, to predict the zero-Kelvin crystal structure and magnetic structure of the first-row transition

metals.

Consider, for example, the use of the TB-LMTO ESC program, in conjunction with EXC1 (see table 2.1), to predict the zero-Kelvin crystal structure and magnetic structure of metallic Fe. Figure 4.1 shows the calculated $E_{tot}\,(a)$ curves of NM BCC Fe, FM BCC Fe, and AFM BCC Fe, obtained using exchange-correlation functional EXC1. It is clear that the calculated values of the $E_{tot}\,(a)$ curve of FM BCC Fe are smaller than the calculated values of the $E_{tot}\,(a)$ curve of NM BCC Fe and of AFM BCC Fe. The difference between the smallest calculated value of the $E_{tot}\,(a)$ curve of NM BCC Fe (which is almost identical to the smallest calculated value of the $E_{tot}\,(a)$ curve of AFM BCC Fe) and the smallest calculated value of the $E_{tot}\,(a)$ curve of FM BCC Fe is approximately 0.025 Rydberg per atom. This difference is significant, as we have shown in chapter 3 that the CPE's in the minimum total energy values computed using the TB-LMTO ESC program are of the order of $\pm 2.5 \times 10^{-7}$ Rydberg per atom. It can therefore be concluded that, at zero Kelvin, BCC Fe will possess magnetic moments arranged in the FM magnetic structure. A similar analysis of the calculated $E_{tot}\,(a)$ curves of NM FCC Fe, AFM FCC Fe, FM FCC Fe, NM HCP Fe, AFM HCP Fe and FM HCP Fe, as obtained using exchange-correlation functional EXC1, leads us to conclude that, at zero Kelvin, FCC Fe and HCP Fe possess no magnetic moments (NM magnetic structure).

We now compare the smallest calculated value of the $E_{tot}\,(a)$ curve of FM BCC Fe, of NM FCC Fe, and of NM HCP Fe. We observe that the smallest calculated value of the $E_{tot}\,(a)$ curve of NM HCP Fe is smaller than that of the other two $E_{tot}\,(a)$ curves by approximately 0.0045 Rydberg per atom. This energy difference is also numerically significant, given that the CPE's and the SCE's in the minimum total energy values obtained using the TB-LMTO ESC program are respectively of the order of $\pm 2.5 \times 10^{-7}$ Rydberg per atom and of 5.0×10^{-5} Rydberg per atom. We thus conclude that, when exchange-correlation functional EXC1 is used, the TB-LMTO ESC program predicts that metallic Fe possesses the HCP crystal structure and no magnetic moments (NM magnetic structure) at zero Kelvin.

The analysis described above for metallic Fe can be repeated for all ten first-row tran-

sition metals, and using all four of the exchange-correlation functionals available in the TB-LMTO ESC program. Table 4.1 shows the zero-Kelvin crystal structure and magnetic structure of all ten first-row transition metals, as predicted using the TB-LMTO ESC program. It must be recalled that only the BCC, FCC and HCP crystal structures are considered in this study. Thus, the TB-LMTO ESC program fails to predict the zero-Kelvin crystal structure of metallic Mn because this metal does not possess the BCC, FCC or HCP crystal structure at zero Kelvin [1]. In addition, the TB-LMTO ESC program correctly predicts the zero-Kelvin crystal structure of metallic Cr, but not its zero-Kelvin magnetic structure. This is because metallic Cr possesses magnetic moments oriented in a complex anti-ferromagnetic structure at zero Kelvin [2]. In conducting our calculations, we made no attempt to represent correctly the zero-Kelvin magnetic structure of metallic Cr within the TB-LMTO ESC program. Interestingly, when the local exchange-correlation functionals (EXC1 and EXC3) are used, the TB-LMTO ESC program fails to predict the correct zero-Kelvin crystal structure of metallic Fe. Other studies have revealed that ESC programs using local exchange-correlation functionals fail to correctly predict the zero-Kelvin crystal structure of metallic Fe (e.g. [55,57,60,62,64,65,67,72]).

Table 4.1 illustrates that the TB-LMTO ESC program most accurately predicts the zero-Kelvin crystal structure and magnetic structure of the first-row transition metals when exchange-correlation functional EXC2 or EXC4 is used.

Table 4.1: Predicted zero-Kelvin crystal structure and magnetic structure of the first-row transition metals

Metal	Exch.-correlation func. EXC1	Exch.-correlation func. EXC2	Exch.-correlation func. EXC3	Exch.-correlation func. EXC4
Sc	HCP NM	HCP NM	HCP NM	HCP NM
Ti	HCP NM	HCP NM	HCP NM	HCP NM
V	BCC NM	BCC NM	BCC NM	BCC NM
Cr	(*BCC NM*)	(*BCC NM*)	(*BCC NM*)	(*BCC AFM*)
Mn	(*HCP NM*)	(*HCP NM*)	(*HCP NM*)	(*FCC AFM*)
Fe	(*HCP NM*)	BCC FM	(*HCP NM*)	BCC FM
Co	HCP FM	HCP FM	HCP FM	HCP FM
Ni	FCC FM	FCC FM	FCC FM	FCC FM
Cu	FCC NM	FCC NM	FCC NM	FCC NM
Zn	HCP NM	HCP NM	HCP NM	HCP NM

Crystal structures other than BCC, FCC and HCP are not considered.

In most cases, the correct crystal structure and magnetic configuration are predicted.

Italics and brackets indicate incorrect predictions.

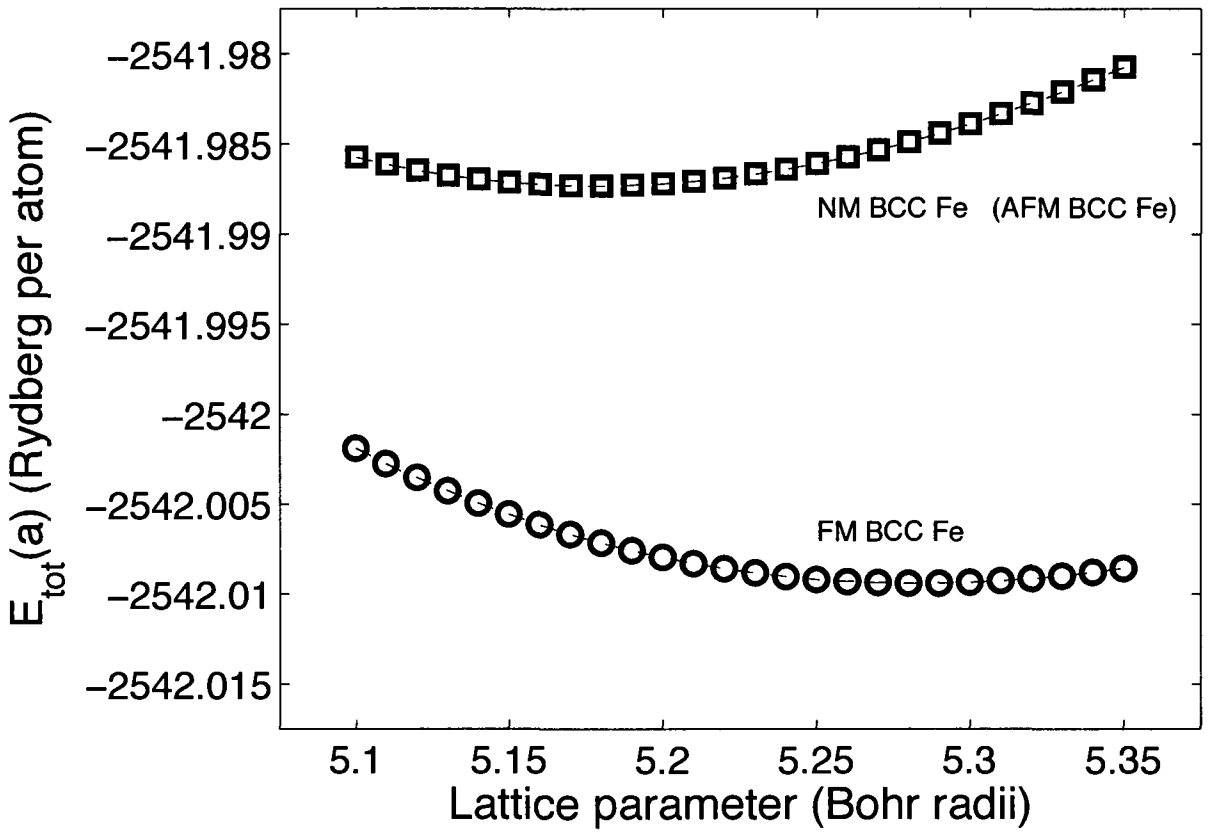

Figure 4.1: Calculated $E_{tot}\,(a)$ curve of FM BCC Fe (circles) and of NM BCC Fe (squares), obtained using the TB-LMTO ESC program and exchange-correlation functional EXC1. The $E_{tot}\,(a)$ curve of NM BCC Fe and of AFM BCC Fe are indistinguishable on this scale. All calculated energy values are precise to $\pm 2.5 \times 10^{-7}$ Rydberg per atom. Error bars denoting the magnitude of the errors in the calculated energy values are smaller than the symbols representing the data.

4.2.3 Accuracy of the Calculated Zero-Kelvin Lattice Parameters of the First-Row Transition Metals

We now use the 90 minimum total energy versus lattice parameter curves $E_{tot}(a)$, appropriately calculated using the TB-LMTO ESC program as described in section 4.2.1, to predict the zero-Kelvin lattice parameters of the first-row transition metals. To do so, we consider only the $E_{tot}(a)$ curves listed in table 4.2. The magnetic and crystal structures there listed are those of real metallic Sc to V, and Fe to Zn at zero Kelvin [1]. We ignore the $E_{tot}(a)$ curves of metallic Mn because this metal does not possess the BCC, FCC or HCP crystal structure at zero Kelvin [1]. Also, using exchange-correlation functional EXC4, we predicted, in section 4.2.2, that metallic Cr takes the AFM BCC structure at zero Kelvin. Thus, we calculate here, using EXC4, the lattice parameters of AFM BCC Cr.

Using the $E_{tot}(a)$ curves calculated as described in section 4.2.1, and knowing that the minimum total energy values calculated using the TB-LMTO ESC program are precise to $\pm 2.5 \times 10^{-7}$ Rydberg per atom, we predict the zero-Kelvin lattice parameters of the first-row transition metals to ± 0.01 Bohr radii. Table 4.3 shows the predicted zero-Kelvin lattice parameters of the first-row transition metals.

To evaluate the accuracy of the TB-LMTO ESC program, we compare the calculated zero-Kelvin lattice parameters of the first-row transition metals to the measurements of the lattice parameters of these metals reported in table 4.4. We obtain the measured lattice parameters reported in table 4.4 using the measured lattice parameters of the first-row transition metals at room temperature [1] and measurements of the thermal expansion of these metals [80]. More specifically, reference [80] reports, as a function of temperature, measurements of the fractional change of the lattice parameters of the first-row transition metals relative to their lattice parameters at room temperature. The temperatures shown in table 4.4 are the lowest temperatures for which a fractional lattice parameter change is reported in reference [80]. The reported precision of the information reported in reference [80] as well as the reported precision of the measured lattice parameters of the first-row transition metals at room temperature [1], lead us to conclude that the measured lattice

parameters reported in table 4.4 are also precise to ± 0.01 Bohr radii.

In figure 4.2, the zero-Kelvin lattice parameters of the first-row transition metals as predicted using the TB-LMTO ESC program (table 4.3) are compared to the measurements reported in table 4.4. It is clear in figure 4.2 that the calculated lattice parameters are usually smaller than the measurements of these lattice parameters. Exceptions to this rule include the calculated a-parameters of the HCP metals (Sc, Ti, and Zn), some of the calculated c-parameters of these metals, and all a-parameters obtained using exchange-correlation functional EXC4. For metallic V, Cr, and Fe to Cu, the calculated zero-Kelvin lattice parameters of the first-row transition metals are within 3% of the measurements of these lattice parameters, regardless of which exchange-correlation functional is used. For Sc, Ti and Zn (the non-magnetic HCP metals), the calculated zero-Kelvin lattice parameters can differ from the measured lattice parameters by as much as 10%.

The difference between the calculated and measured lattice parameters is generally smaller when exchange-correlation functional EXC2 is used. This may be an indication that the TB-LMTO ESC program, when used with exchange-correlation functional EXC2, calculates more accurately the minimum total energy of the first-row transition metals. However, the TB-LMTO ESC, when used in conjunction with exchange-correlation functional EXC2, does not predict very accurately the zero-Kelvin lattice parameters of the HCP metals Sc, Ti and Zn.

It is also interesting that, for all metals except Zn, the calculated zero-Kelvin lattice parameters are, in ascending order, that obtained using EXC1, EXC3, EXC2 and EXC4. EXC2 and EXC4, namely the "non-local" exchange-correlation functionals, are thought to be the better exchange-correlation functionals, as they provide a more complete mathematical description of the physics of electron exchange [39, 47, 81]. Our results are consistent with the view that EXC2 is the most accurate exchange-correlation functional. Also, it is interesting that the zero-Kelvin lattice parameters of the first-row transition metals are consistently overestimated when calculated using EXC4, while they are usually underestimated when calculated using all other exchange-correlation functionals. Understanding

why this is the case may bring to light pathways for further improvement of exchange-correlation functionals.

Table 4.2: Assumed magnetic and crystal structure of the first-row transition metals when calculating their zero-Kelvin lattice parameters

Metal	Exch.-correlation func. EXC1	Exch.-correlation func. EXC2	Exch.-correlation func. EXC3	Exch.-correlation func. EXC4
Sc	HCP NM	HCP NM	HCP NM	HCP NM
Ti	HCP NM	HCP NM	HCP NM	HCP NM
V	BCC NM	BCC NM	BCC NM	BCC NM
Cr	BCC NM	BCC NM	BCC NM	BCC AFM
Mn	-	-	-	-
Fe	BCC FM	BCC FM	BCC FM	BCC FM
Co	HCP FM	HCP FM	HCP FM	HCP FM
Ni	FCC FM	FCC FM	FCC FM	FCC FM
Cu	FCC NM	FCC NM	FCC NM	FCC NM
Zn	HCP NM	HCP NM	HCP NM	HCP NM

Table 4.3: Zero-Kelvin lattice parameters of the first-row transition metals predicted using the TB-LMTO ESC program.

Metal	Exch.-correlation func. EXC1	Exch.-correlation func. EXC2	Exch.-correlation func. EXC3	Exch.-correlation func. EXC4
Sc	a = 6.24 c = 9.05	a = 6.33 c = 9.31	a = 6.26 c = 9.08	a = 6.41 c = 9.42
Ti	a = 5.68 c = 8.07	a = 5.76 c = 8.18	a = 5.69 c = 8.08	a = 5.86 c = 8.32
V	a = 5.61	a = 5.68	a = 5.62	a = 5.79
Cr	a = 5.35	a = 5.41	a = 5.36	a = 5.57
Mn	-	-	-	-
Fe	a = 5.28	a = 5.36	a = 5.30	a = 5.54
Co	a = 4.65 c = 7.49	a = 4.71 c = 7.58	a = 4.66 c = 7.50	a = 4.83 c = 7.78
Ni	a = 6.54	a = 6.61	a = 6.55	a = 6.80
Cu	a = 6.69	a = 6.78	a = 6.71	a = 7.00
Zn	a = 5.03 -	a = 4.83 c = 9.61	a = 5.05 -	a = 5.02 c = 9.99

All lattice parameters are in Bohr radii.

When using EXC1 and EXC3, Zn was assumed to possess the ideal c/a ratio [37].

Table 4.4: Measured lattice parameters of the first-row transition metals

Metal	Measured lattice parameters	Temperature of measurement
Sc	$a = 6.25$ $c = 9.96$	293
Ti	$a = 5.58$ $c = 8.85$	293
V	5.71	5
Cr	5.45	25
Fe	5.41	5
Co	$a = 4.74$ $c = 7.69$	293
Ni	6.64	5
Cu	6.81	1
Zn	$a = 5.03$ $c = 9.19$	5

Lattice parameters are in Bohr radii.
Temperatures are in Kelvin, and represent
the lowest temperature at which
a fractional change in lattice parameter
is reported in reference [80].

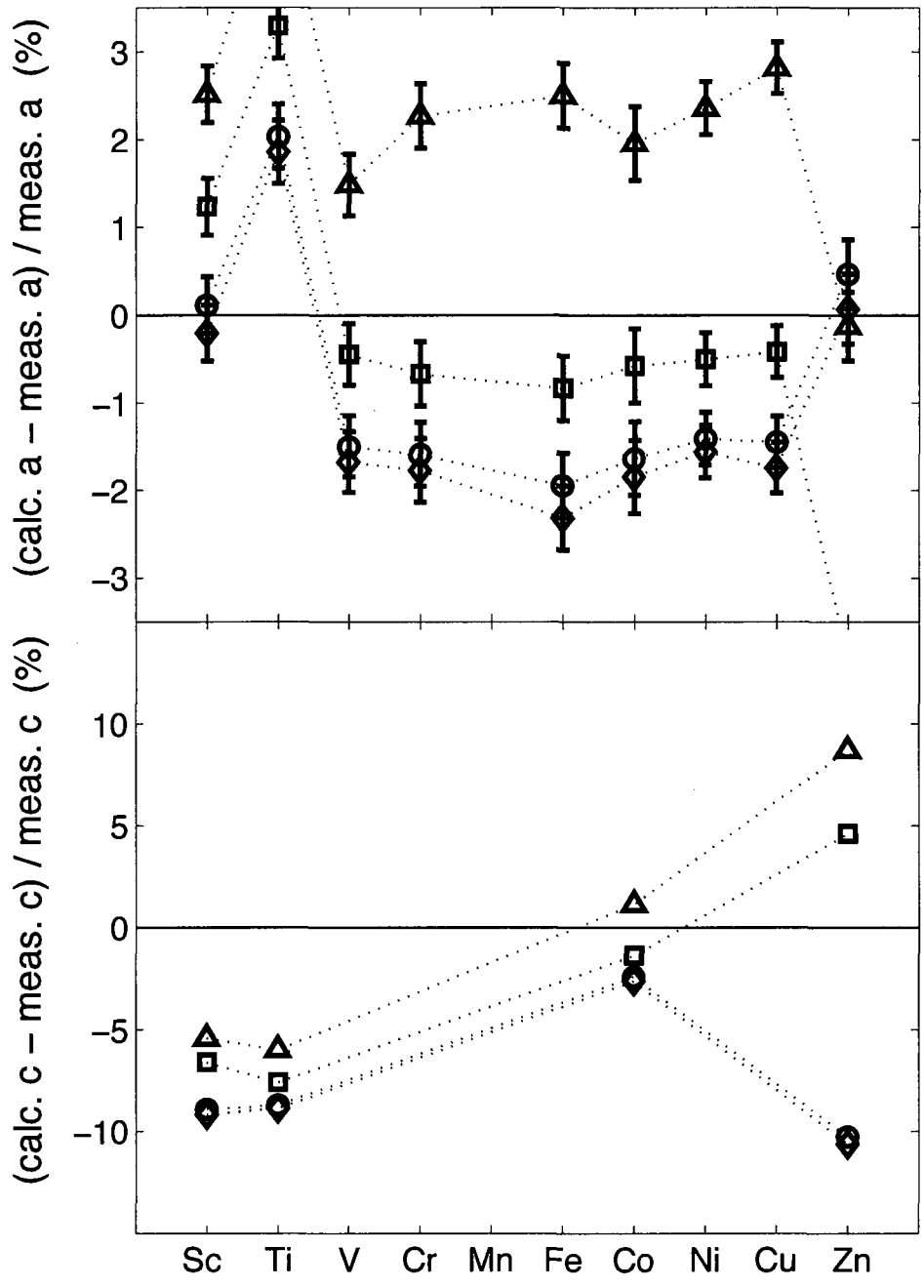

Figure 4.2: Comparison of the measured lattice parameters of the first-row transition metals at low temperatures (table 4.4) and the zero-Kelvin lattice parameters of these metals as predicted by the TB-LMTO ESC program (table 4.3). The upper figure shows the a-parameters, while the lower figure shows the c-parameters. Both figures show ((calculated - measured) / measured) lattice parameters. Lattice parameters were calculated using exchange-correlation functional EXC1 (diamonds), EXC2 (squares), EXC3 (circles) and EXC4 (triangles). Dotted lines guide the eye to data points obtained using the same exchange-correlation functional. Error bars take into account that all calculated and measured lattice parameters are precise to ± 0.01 Bohr radii. Error bars in the bottom plot are smaller than the data symbols. When using EXC1 and EXC3, HCP Zn was assumed to possess the ideal c/a-ratio.

4.2.4 Accuracy of the Calculated Bulk Modulus of the First-Row Transition Metals

We now use the TB-LMTO ESC program to predict the bulk modulus of the first-row transition metals at zero Kelvin. To do so, we simply calculate the bulk modulus of these metals at the lattice parameters identified in table 4.3, namely the zero-Kelvin lattice parameters of the metals as calculated using the TB-LMTO ESC program.

The bulk modulus B of a solid at zero Kelvin is defined as [37, p. 39]:

$$B = v_0 \frac{d^2}{dv^2} E_{tot}(v)\Big|_{v=v_0}, \tag{4.2}$$

where $E_{tot}(v)$ is the minimum total energy of the solid as a function of its atomic volume v, and v_0 is the zero-Kelvin atomic volume of the solid. We calculate the bulk modulus of each first-row transition metals using the chain rule and its calculated $E_{tot}(a)$ curve as follows:

$$B = v_0 \frac{d^2}{da^2} E_{tot}(a)\Big|_{a=a_0} \left(\frac{d}{dv} a(v)\Big|_{v=v_0} \right)^2, \tag{4.3}$$

where $E_{tot}(a)$ is the minimum total energy versus lattice parameter curve of the metal, and a_0 is its zero-Kelvin lattice parameter.

It is a simple matter to evaluate B for the cubic metals (V, Cr, Fe, Ni and Cu) using equation 4.3, as $a(v) = (4v)^{\frac{1}{3}}$ for the FCC metals, and $a(v) = (2v)^{\frac{1}{3}}$ for the BCC metals. The calculation of B for the HCP metals is more difficult. Under isotropic pressure, the partial derivatives of the $E_{tot}(a, c)$ curve of a HCP solid must obey the following relationship:

$$\frac{\delta}{\delta a} E_{tot}(a, c) = 2\frac{c}{a}\frac{\delta}{\delta c} E_{tot}(a, c). \tag{4.4}$$

We observe that near the global minimum of the $E_{tot}(a, c)$ curve of HCP Sc, Ti, Co and Zn, this relationship is well-respected when the c/a ratio of the metals is kept constant at its zero-Kelvin value. We thus evaluate the bulk modulus of these metals using equation 4.3, taking $a(v) = \left(\frac{4}{\sqrt{3}(c/a)}\right)^{\frac{1}{3}} v^{\frac{1}{3}}$ where c/a is treated as a constant and calculated using the a- and c-parameters of table 4.3.

In calculating the bulk modulus of the first-row transition metals, we evaluate the derivatives $\frac{d}{dv}a\left(v\right)\Big|_{a=a_0}$ analytically and obtain the second-derivatives $\frac{d^2}{da^2}E_{tot}\left(a\right)\Big|_{a=a_0}$ using standard numerical differentiation techniques [74]. Our calculated bulk modulus values are precise to three significant figures and are shown in table 4.5. Measured values [78] of the bulk modulus of the first-row transition metals are shown in table 4.6. These measurements were taken at room temperature and are precise to the order of magnitude of the least significant reported figure.

In figure 4.3, we compare the measured bulk modulus of the first-row transition metals (table 4.6) and the bulk modulus of the metals as predicted using the TB-LMTO ESC program (table 4.5). The calculated bulk moduli of all metals except Zn are between 5 - 60% of the measured values. Notably, the bulk moduli obtained using exchange-correlation functional EXC4 are most accurate, though often smaller than the measured bulk moduli of the first-row transition metals. This is so even considering that room temperature values of bulk modulus can be approximately 5% smaller than zero-Kelvin values. Bulk modulus values calculated using the other exchange-correlation functionals are less accurate, with those obtained with EXC1 and EXC3 being the least accurate. Like the zero-Kelvin lattice parameters obtained using EXC1 and EXC3, bulk modulus values obtained using EXC1 and EXC3 are very similar.

The results of figure 4.3 provide us interesting insights into the accuracy of the $E_{tot}\left(a\right)$ curves obtained using the TB-LMTO ESC program. It can be shown using equation 4.2 that the zero-Kelvin bulk modulus of a solid is proportional to the second-derivative of its $E_{tot}\left(a\right)$ curve divided by its zero-Kelvin lattice parameter. Recalling that the zero-Kelvin lattice parameters of the first-row transition metals are only 1% too small when calculated using exchange-correlation functional EXC2 (see section 4.2.3), we conclude the second-derivatives of the $E_{tot}\left(a\right)$ curves obtained using EXC2 are about 20% too large. This is so because the bulk modulus values calculated using EXC2 are about 20% too large (figure 4.3). In contrast, we conclude that the second-derivatives of the $E_{tot}\left(a\right)$ curves obtained using EXC4 may be only 1 - 2% too small. This is so because the bulk modulus values obtained using EXC4 (at least for Fe - Cu) are about 5% too small (figure 4.3) while the

zero-Kelvin lattice parameters predicted using EXC4 are 2 - 3% too large (section 4.2.3). This will be discussed further in chapter 7 when we study the thermal expansion of metallic Cu.

Table 4.5: Zero-Kelvin bulk modulus of the first-row transition metals predicted using the TB-LMTO ESC program.

Metal	Exch.-correlation func. EXC1	Exch.-correlation func. EXC2	Exch.-correlation func. EXC3	Exch.-correlation func. EXC4
Sc	65.9	60.4	64.5	59.3
Ti	125	118	125	111
V	206	194	203	176
Cr	292	271	286	148
Mn	-	-	-	-
Fe	246	207	235	162
Co	267	237	261	193
Ni	251	228	246	177
Cu	191	169	184	125
Zn	114	100	106	64.2

Bulk moduli in GN / m^2.

When using EXC1 and EXC3, Zn was assumed to possess the ideal c/a ratio [37].

Table 4.6: Measured bulk moduli of the first-row transition metals

Metal	Measured bulk modulus
Sc	43.5
Ti	105.1
V	161.9
Cr	190.1
Fe	168.3
Co	191.4
Ni	186
Cu	137
Zn	59.8

All bulk moduli in GN / m^2.
Measurements taken at
room temperature.

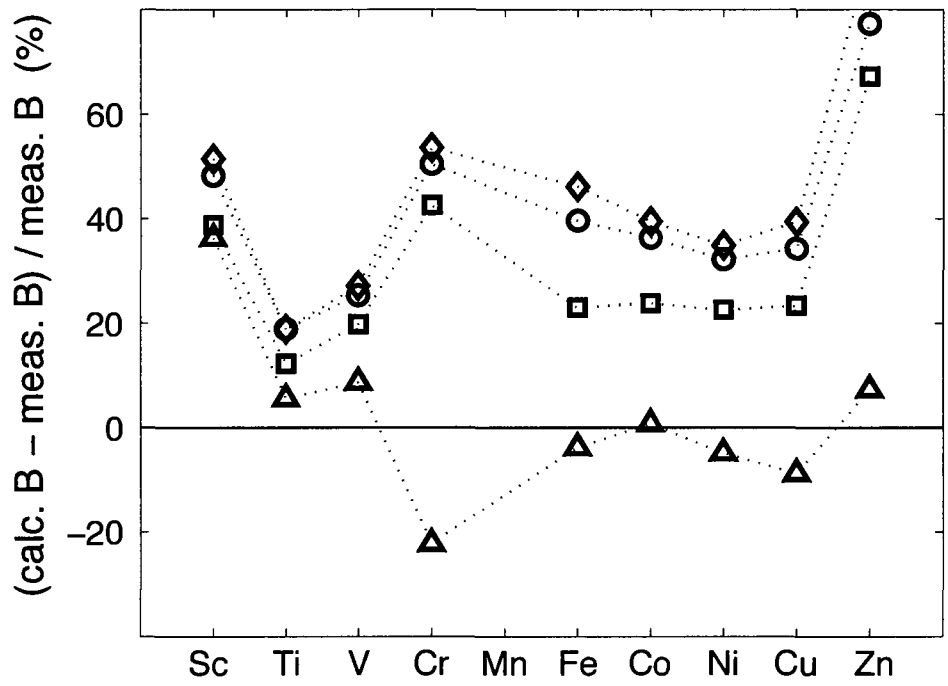

Figure 4.3: Comparison of the measured bulk modulus of the first-row transition metals at room temperatures (table 4.6) and the zero-Kelvin bulk modulus of these metals as predicted by the TB-LMTO ESC program (table 4.5). The figure shows ((calculated - measured) / measured) bulk moduli. Bulk moduli were calculated using exchange-correlation functional EXC1 (diamonds), EXC2 (squares), EXC3 (circles) and EXC4 (triangles). Dotted lines guide the eye to data points obtained using the same exchange-correlation functional. Error bars denoting the numerical precision of the plotted values are omitted as they are smaller than the data symbols.

4.2.5 Accuracy of Calculated Magnitude of the Magnetic Moments of Fe, Co and Ni at Zero-Kelvin

We now use the TB-LMTO ESC program to predict the magnitude of the magnetic moments of the ferromagnetic first-row transition metals (BCC Fe, HCP Co and FCC Ni) at zero Kelvin. To do so, we simply calculate the magnetic moments of FM BCC Fe, FM HCP Co and FM FCC Ni at the lattice parameters identified in table 4.3, namely the zero-Kelvin lattice parameters of the metals as calculated using the TB-LMTO ESC program.

To calculate the magnitude of the magnetic moments of a solid, the TB-LMTO ESC program first calculates the distribution of the valence electrons that have spin quantum number $s = s_1 = +\frac{1}{2}$ and that have spin quantum number $s = s_2 = -\frac{1}{2}$ within the solid. The distributions $\rho_{v,s_1}(\vec{r})$ and $\rho_{v,s_2}(\vec{r})$ are then used to calculate the magnitude of the magnetic moments in the solid as follows:

$$m = \left| \int_{WS} \rho_{v,s_1}(\vec{r})\, d\vec{r} - \int_{WS} \rho_{v,s_2}(\vec{r})\, d\vec{r} \right|, \tag{4.5}$$

where the integrals over $\vec{r}$ are restricted to a single Wigner Seitz unit cell of the solid. It must be recalled that within the TB-LMTO ESC program, this unit cell is modelled as an atomic sphere. Table 4.7 shows the magnitude of the magnetic moments of FM BCC Fe, FM HCP Co and FM FCC Ni at zero Kelvin, as calculated using the TB-LMTO ESC program.

In chapter 3, we showed that the output of the TB-LMTO ESC program is sensitive to the initial conditions of the calculations. We here evaluate the initial-condition sensitivity of the calculated magnitude of the magnetic moments of FM BCC Fe at zero Kelvin. To do so, we calculate the magnitude of these magnetic moments using initial condition sets INIT1 and INIT2 given in section 3.4 of chapter 3. During these calculations, the parameters of the TB-LMTO ESC program are identical to those described in section 4.2.1. The magnitude of the magnetic moments of FM BCC Fe, as obtained using both sets of initial conditions, differ by less than 2.0×10^{-5} Bohr magnetons. We are therefore confident that the calculated magnitude of the magnetic moments of Fe, Co and Ni at zero Kelvin are

precise to ± 0.001 Bohr magnetons.

We then compare the calculated magnetic moment magnitudes to measured values of these magnetic moment magnitudes [2, 82].[3] These experimental values were obtained by extrapolation, using measurements of the magnetization of these metals at multiple temperatures [2, 82]. They are given in table 4.8. Because the values are reported to 0.001 Bohr magnetons [2], we assume that they are precise to ± 0.001 Bohr magnetons.

The calculated and measured magnetic moment magnitudes are compared in figure 4.4. Regardless of which exchange-correlation functional is used, the calculated magnitude of the magnetic moments of the metals at zero Kelvin is within 15% of the measured values of these magnetic moment magnitudes.

At first glance, it appears that no single exchange-correlation functional most accurately predicts the magnitude of the magnetic moments in all the ferromagnetic first-row transition metals at zero Kelvin. However, if we evaluate, for each exchange-correlation functional, the sum of the squared difference of the calculated and measured magnetic moment magnitudes, we conclude that these magnitudes are most accurately predicted using EXC2.

Finally, as observed for the calculated zero-Kelvin lattice parameters, the calculated magnetic moment magnitudes are, in ascending order, those obtained using EXC1, EXC3, EXC2 and EXC4. In general, the magnetic moments in metals become larger when the volume of the metal increases (see chapter 5 and [83]). Therefore, it is not surprising that this is observed for both the calculated zero-Kelvin lattice parameters and magnetic moment magnitudes. Again, understanding why this is the case may bring to light pathways for further improvement of exchange-correlation functionals.

[3] We specifically reproduce here the values reported by Pauthenet [82], as they are reproduced in the Landolt-Börnstein data encyclopedia [2].

Table 4.7: Magnitude of the magnetic moments of BCC Fe, HCP Co and FCC Ni at zero Kelvin, predicted using the TB-LMTO ESC program.

Metal	Exch.-correlation func. EXC1	Exch.-correlation func. EXC2	Exch.-correlation func. EXC3	Exch.-correlation func. EXC4
BCC Fe	2.147	2.287	2.207	2.551
HCP Co	1.550	1.620	1.576	1.667
FCC Ni	0.607	0.644	0.620	0.659

All magnetic moment magnitudes are in Bohr magnetons.

Table 4.8: Measured magnitude of the magnetic moments of BCC Fe, HCP Co and FCC Ni at zero Kelvin

Metal	Measured magnetic moment magnitudes
BCC Fe	2.226
HCP Co	1.728
FCC Ni	0.619

All magnetic moment magnitudes are in Bohr magnetons.
Magnetic moment magnitudes are as reported in [2] and [82].

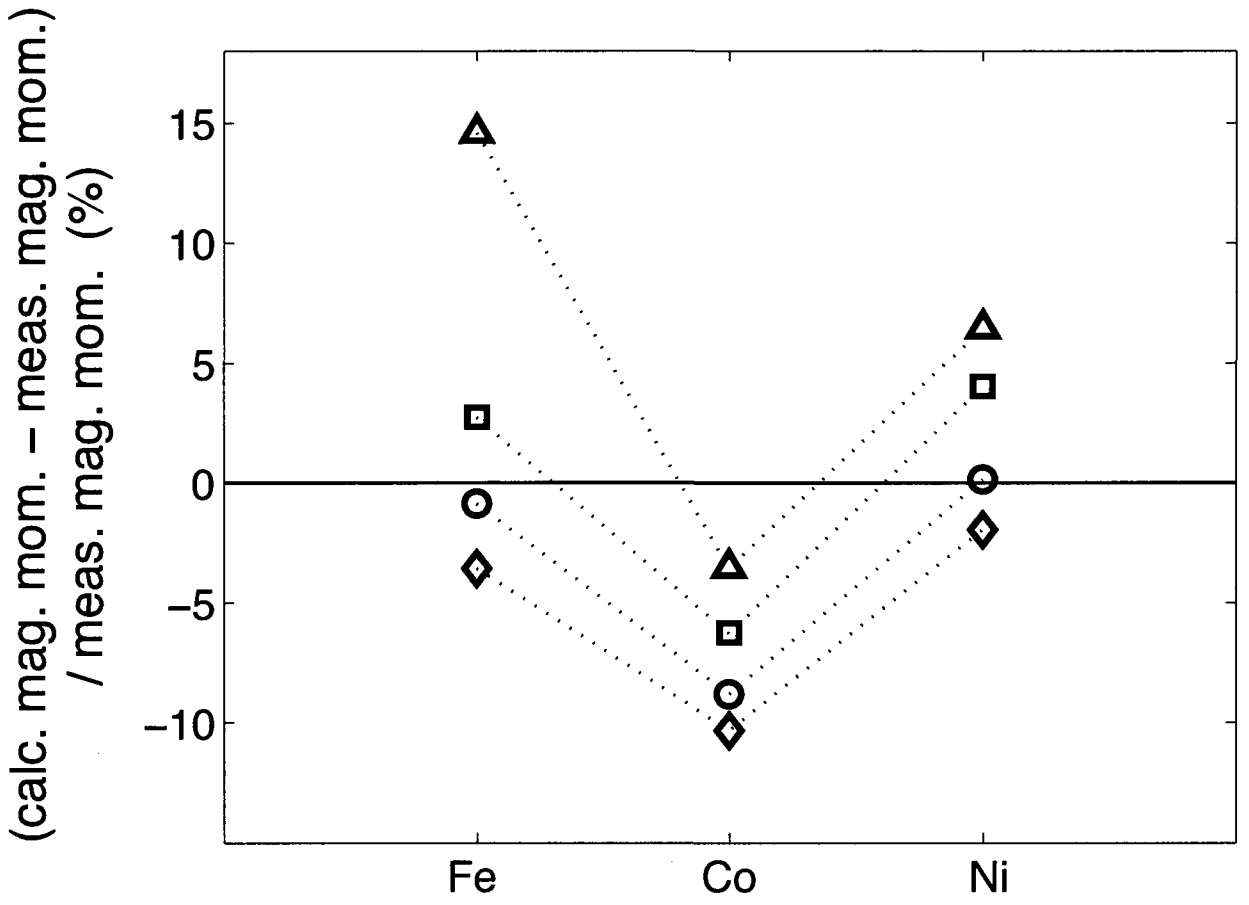

Figure 4.4: Comparison of the measured magnitude of the magnetic moments of the ferromagnetic first-row transition metals, extrapolated to zero Kelvin (table 4.8), and the magnitude of the magnetic moments of these metals as predicted using the TB-LMTO ESC program (table 4.7). The figure shows ((calculated - measured) / measured) magnetic moment magnitudes. Calculations were performed using exchange-correlation functional EXC1 (diamonds), EXC2 (squares), EXC3 (circles) and EXC4 (triangles). Dotted lines guide the eye to data points obtained using the same exchange-correlation functional. Error bars take into account that all calculated and measured magnetic moment magnitudes are precise only to ± 0.001 Bohr magnetons. They are smaller than the symbols representing the data points.

4.3 Accuracy of the TB-LMTO ESC Program : Summary

As indicated in section 4.1, we wished to evaluate the accuracy of the TB-LMTO ESC program [28] in predicting the minimum total energy of solids, and the lowest-energy electron distribution of solids. For practical reasons, it is not possible to evaluate the accuracy with which these solid properties are calculated. Nonetheless, we argued that, by evaluating the accuracy with which the TB-LMTO ESC program calculates other properties of solids at zero Kelvin, it is possible to indirectly obtain information about the accuracy with which the program calculates the minimum total energy and lowest-energy electron distribution of a solid.

In section 4.2.2, we showed that the TB-LMTO ESC program most accurately predicts the zero-Kelvin crystal structure and zero-Kelvin magnetic structure of the first-row transition metals when it is used in conjunction with exchange-correlation functionals EXC2 and EXC4 (see table 2.1). We also saw that, like many other ESC programs [55,57,60,62,64,65, 67,72], the TB-LMTO ESC program fails to predict the correct zero-Kelvin crystal structure of metallic Fe when used in conjunction with local exchange-correlation functionals like EXC1 and EXC3.

In section 4.2.3, we showed that regardless of which exchange-correlation functional is used, the zero-Kelvin lattice parameters of the first-row transition metals V, Cr, and Fe to Cu, as predicted using the TB-LMTO ESC program (table 4.3), are within 3% of available measurements of these lattice parameters (table 4.4). The three remaining first-row transition metals (Sc, Ti and Zn) are HCP structured. The TB-LMTO ESC program predicts that the a-parameters of these metals at zero Kelvin (table 4.3) are within 5% of the measurements of these lattice parameters (table 4.4). In addition, the c-parameters of these metals at zero Kelvin are predicted to be within 10% of measurements of these values. In this regard, the performance of the TB-LMTO ESC program is comparable to the performance of other ESC programs in predicting the zero-Kelvin lattice parameters of solids [54–66, 68–72, 84–86]. We also showed that the TB-LMTO ESC program most accurately predicts the zero-Kelvin lattice parameters of the metals V, Cr and Fe to Cu when

they are calculated using exchange-correlation functional EXC2.

Then, in section 4.2.4, we calculated the bulk modulus of each of the first-row transition metals with the exception of Mn. For all metals except Zn, the calculated bulk moduli are within 5-60% of corresponding measurements. Calculated bulk moduli are most accurate when obtained using exchange-correlation functional EXC4, though typically underestimated. Exchange-correlation functional EXC2 produces the next most accurate bulk modulus values, but they are larger than the measured values. These results allowed us to conclude that the second derivative of the $E_{tot}(a)$ curve obtained using EXC4 at its global minimum is too small while the opposite is true for the $E_{tot}(a)$ curves obtained using EXC1, EXC2 and EXC3.

Finally, in section 4.2.5, we calculated the magnitude of the magnetic moments of BCC Fe, HCP Co and FCC Ni at zero Kelvin using the TB-LMTO ESC program. We showed that these magnetic moment magnitudes, as predicted using the TB-LMTO ESC program, are within 15% of available measured values of these magnitudes. These results are also comparable to those obtained using other common ESC programs [56,58,59,62,64,66,68,72,86]. We also concluded that the magnitude of the magnetic moments in the ferromagnetic first-row transition metals at zero Kelvin is most accurately calculated using EXC2.

In light of the results of sections 4.2.2, 4.2.3 and 4.2.5, it is tempting to conclude that the TB-LMTO ESC program most accurately calculates the minimum total energy of the first-row transition metals when it is used in conjunction with EXC2. However, this may not be the case. It is possible that the $E_{tot}(a)$ curves of the first-row transition metals obtained using EXC2 simply possess a global minimum value at a lattice parameter that is similar to the zero-Kelvin lattice parameters of these metals while the shape of the calculated $E_{tot}(a)$ curves is incorrect. The results of section 4.2.4 suggest that this is indeed the case. That the TB-LMTO ESC program fails to accurately predict the bulk modulus of the first-row transition metals indicates that the curvature of the $E_{tot}(a)$ curves obtained using the program is not accurate. Indeed, the results of section 4.2.4 suggest that the shape of the calculated $E_{tot}(a)$ curves obtained using EXC4 is more accurate than the shape of

the $E_{tot}(a)$ curves obtained using the other exchange-correlation functionals. In addition to the zero-Kelvin lattice parameters that we calculated in this chapter, we could have calculated the dispersion relations $\epsilon\left(\vec{k}\right)$, the density of states functions $n_v(\epsilon)$, and the Fermi surfaces of the first-row transition metals. But even evaluating the accuracy of these calculations does not amount to a direct evaluation of the calculated $E_{tot}(a)$ curves of the first-row transition metals. The only way to directly evaluate the accuracy of these curves is to compare them to cohesive energy measurements, but this requires measurements of cohesive energy as a function of temperature and pressure which are not always available. In chapter 7, we shall illustrate that the indirect evaluation of the accuracy of an $E_{tot}(a)$ curve may be seriously limited.

It also is interesting, though not unexpected, that the TB-LMTO ESC program predicts least accurately the properties of those first-row transition metals that have the HCP crystal structure. As we indicated in section 2.3 of chapter 2, the TB-LMTO ESC program is expected to predict most accurately the properties of metals that have a highly spherical electron distribution. The charge distribution of the cubic metals is certainly more spherical than the charge distribution of the HCP metals, as the crystal symmetry of the atomic nuclei of these metals is more spherical. We believe that this is the reason why the TB-LMTO ESC program predicts more accurately the properties of the cubic first-row transition metals.

Finally, as indicated in sections 4.2.3 and 4.2.5, the results of the study presented in this chapter provide insights into the accuracy of the different exchange-correlation functionals that are available within the TB-LMTO ESC program. First of all, it is interesting that, in the study presented in section 4.2 of this chapter, the results obtained with EXC1 and EXC3 are very similar. This suggests that these two exchange-correlation functionals are similar even though they are derived differently. As indicated in section 2.2.3 of chapter 2, EXC1 is derived analytically from a physical model of a free electron gas, while EXC3 is derived using the results of computer simulations of an electron gas. Given this apparent similarity of EXC1 and EXC3, it is surprising that the results obtained using EXC2 and EXC4 are so different, as EXC2 is simply an extension of EXC1 and EXC4 is itself an ex-

tension of EXC3. To understand the difference between EXC2 and EXC4, it is necessary to recall that to correctly evaluate the electrostatic energy of the electrons in a solid, one must define conditional electron distributions $\rho_{\vec{R}}(\vec{r})$. As indicated in section 2.1.3 of chapter 2, these distributions are typically constructed by removing from the average charge distribution of the solid, $\rho(\vec{r})$, an "exchange hole" centered at $\vec{r} = \vec{R}$. The performance difference of EXC2 and EXC4 may be the result of a very specific assumption about the exchange-correlation hole that is made in developing EXC4. In developing EXC4, its developers have specifically imposed that all distributions $\rho_{\vec{R}}(\vec{r})$ satisfy $\rho_{\vec{R}}(\vec{r}) \leq \rho(\vec{r})$ at all points $\vec{r}$ [49]. This condition may be unphysical, because in real solids, it may be that $\rho_{\vec{R}}(\vec{r}) > \rho(\vec{r})$ at some points $\vec{r}$. The developers of EXC2 have imposed no such condition on the distributions $\rho_{\vec{R}}(\vec{r})$ [48].

Of course, to correctly determine the reason why the zero-Kelvin lattice parameters of the first-row transition metals are most accurately calculated using EXC2 while the bulk moduli of these metals are more accurately calculated using EXC4, it will be necessary to examine the effect of the other assumptions and approximations made in implementing the TB-LMTO ESC program. For instance, the effect of calculating only the spherical average of the electron distributions $\rho_v(\vec{r})$ and $\rho_c(\vec{r})$ should be investigated more carefully. It may very well be that some exchange-correlation functionals simply cancel some of the errors introduced in the output of the TB-LMTO ESC program as a result of some other approximation or assumption that was made in its implementation.

Chapter 5

The LM-HM Transition in the FCC 3d Transition Metals

Recently, it has been shown experimentally that a composition-controlled low-moment to high-moment (LM-HM) transition occurs in the FCC Fe-Ni alloy system [9, 10]. FCC Fe-Ni alloys with less than ≈ 70 atomic % Fe are ferromagnetic materials possessing large magnetic moments with magnitudes that are nearly independent of temperature. Those alloys consisting of approximately 65 atomic % Fe exhibit anomalously low thermal expansion, with the well-known Invar alloy, consisting of 65 atomic % Fe, exhibiting near-zero thermal expansion over a broad range of temperatures [3]. In contrast, FCC Fe-Ni alloys with more than ≈ 70 atomic % Fe have, in their lowest energy state, no magnetic moments or very small magnetic moments. They are termed "anti-Invar alloys" because they exhibit anomalously large thermal expansion as a result of the appearance of magnetic moments within them as they are heated [9]. A theoretical study has also revealed that a composition-controlled LM-HM transition similar to that observed in the FCC Fe-Ni alloy system also occurs in all FCC and HCP Fe-Co, Fe-Ni and Fe-Cu alloy systems [87].

In addition, theoretical investigations have revealed that metallic FCC Fe undergoes a volume-controlled LM-HM transition. Many papers report the calculated minimum total energy versus lattice parameter curve $E_{tot}(a)$ and the magnetic moment versus lattice pa-

rameter curve $\mu(a)$ of FCC Fe, as obtained using different electronic structure calculation programs (e.g. [56, 87–105]). These curves show that, when FCC Fe takes its theoretical zero-Kelvin lattice parameter,[1] it possesses no magnetic moments or very small magnetic moments. However, if its lattice parameter is increased sufficiently, magnetic moments appear in FCC Fe. Similar studies of the $E_{tot}(a)$ and $\mu(a)$ curves of FCC Mn [96, 106], FCC Co [101], and FCC Ni [56] have been published. These studies reveal that a volume-controlled LM-HM transition occurs in these metals as well. In fact, it is expected that all first-row transition metals, regardless of their crystal structure, will undergo a volume-controlled LM-HM transition [83]. This is so because free atoms of the first-row transition elements possess large magnetic moments. However, many metallic solids consisting of these elements are non-magnetic [1, 2]. (It should be noted that, from this point on, the term "LM-HM transition" should be taken to mean "volume-controlled LM-HM transition", unless otherwise indicated.)

We are interested in obtaining a deeper understanding of the volume-controlled LM-HM transition of FCC Fe because it affects a number of the thermal properties of metallic Fe and Fe-bearing alloys. Some have argued that the FCC-structured γ-phase of metallic Fe, which is the stable phase of metallic Fe between 1183 and 1663 Kelvin [1], exists only because a LM-HM transition occurs in FCC Fe [11]. The unconventional thermal properties of the Invar and anti-Invar Fe-Ni alloys, and of other steels and alloys (e.g. [87, 98, 102, 107]), is the result of physical effects arising as a result of the volume-controlled LM-HM transition of FCC Fe. Furthermore, the properties of metallic Fe are currently of interest in the geophysical sciences (e.g. [12–27]). It is believed that the deep core of the Earth consists mostly of metallic Fe [6, p. 421]. In addition, a recent experimental study of typical Earth mantle minerals at high pressures and temperatures has revealed that the Earth's lower mantle may contain small particles of metallic Fe [7]. Understanding the properties of metallic Fe in the Earth's core and deep mantle may require a good understanding of the LM-HM transition in FCC Fe. Finally, volume-controlled LM-HM transitions may also occur in metallic Fe when it takes the HCP or other crystal structures

[1] We use the term "theoretical zero-Kelvin lattice parameter" of a material to refer to the lattice parameter at which the $E_{tot}(a)$ curve of the material has a global minimum value.

(see [87]). Such transitions are also likely to occur in other more complex materials. The study of the magnetism of all mineral constituents of the Earth's core and mantle is a topic of current interest in the geological sciences [108–110].

In an effort to gain a deeper understanding of the volume-controlled LM-HM transition in FCC Fe, and of volume-controlled LM-HM transitions in materials in general, we conduct in this chapter a theoretical study of the first eight first-row transition metals (also known as the "3d metals"), assuming that they possess the FCC crystal structure. Specifically, we discuss, in section 5.1, the theoretical calculation of the total energy versus lattice parameter curves $E_{tot}(a)$ and the magnetic moment versus lattice parameter curves $\mu(a)$ of FCC Sc to FCC Ni. In section 5.2, we show how these calculations allow us to identify a LM-HM transition in all of the eight metals studied. In each metal, the transition is volume-controlled, in that it occurs when the metal has a specific lattice parameter. In section 5.3, we compare some aspects of the LM-HM transition that was identified in all eight metals. We highlight that FCC Fe is special among the metals studied, as its LM-HM transition occurs at a lattice parameter that is only 2.5% larger than its zero-Kelvin lattice parameter. In section 5.4, we focus our attention on the electrons of the first-row transition metals as the LM-HM transition occurs. We illustrate that magnetic moments form in a FCC 3d metal when the resulting increase in the kinetic energy of its electrons is smaller than the accompanying decrease in the total electrostatic energy of the metal. We also examine the evolution of the density of states function $n_v(\epsilon)$ and the spatial distribution $\rho_v(\vec{r})$ of the valence electrons of these metals as their volume is changed, and as the LM-HM transition occurs. We interpret the observed changes in the $n_v(\epsilon)$ and the $\rho_v(\vec{r})$ functions of the FCC 3d metals in terms of the Stoner model of magnetic moment formation in metals [111, 112]. Finally, in section, 5.5, we summarise the observations of the previous sections and highlight avenues of future research.

We have seen no examples in the scientific literature of a broad study of all FCC 3d metals, similar to the one presented here. Some authors have studied theoretically the composition controlled LM-HM transition in first-row transition metal alloys [87], and others have looked at the volume-controlled LM-HM transition in four metals, namely BCC Cr, BCC

Fe, HCP Co and FCC Ni [56], and BCC V, FCC Fe, FCC Co, and BCC Ni [83]. To our knowledge, no comparative study of the volume-controlled LM-HM transition in all FCC 3d metals has been reported previously.

5.1 Calculation of the $\mu\,(a)$ and $E_{tot}\,(a)$ Curves of the FCC 3d Metals

To study the LM-HM transition in FCC Sc to FCC Ni, we calculate the magnetic moment versus lattice parameter curve $\mu\,(a)$ of these eight metals using the TB-LMTO ESC program [28]. We also calculate the minimum total energy versus lattice parameter curve $E_{tot}\,(a)$ of these metals.[2]

The $\mu\,(a)$ and $E_{tot}\,(a)$ curves of each metal are calculated three times, once assuming that the metal possesses no magnetic moments (NM configuration), once assuming that the metal can possess magnetic moments arranged in a collinear anti-ferromagnetic configuration (AFM configuration), and once assuming that the metals can possess magnetic moments arranged in a collinear ferromagnetic configuration (FM configuration). When a metal possesses magnetic moments arranged in the FM configuration, these magnetic moments are oriented along lines that are perpendicular to the (110) plane of the FCC crystal structure. Magnetic moments arranged in the AFM configuration are also oriented along lines perpendicular to the (110) plane, with alternating atomic planes in the (110) direction possessing magnetic moments oriented in opposite directions. These magnetic moment orientations are identical to those described in section 4.2.1 of chapter 4.

All calculations are performed using the TB-LMTO ESC program [28] with convergence tolerances set to a value of 1.0×10^{-5} (Rydberg units for the total energy convergence tolerance, and electrons per cubic Bohr radii for the electron density convergence tolerance),

[2]We use the term "calculating the $E_{tot}\,(a)$ (or $\mu\,(a)$) curve of a material" to refer to the process of calculating the value of a material's $E_{tot}\,(a)$ (or $\mu\,(a)$) curve at a number of lattice parameter values in an effort to gain knowledge of some continuous portion of the material's $E_{tot}\,(a)$ (or $\mu\,(a)$) curve.

and with first BZ discretization integers set to $L = M = N = 16$. In all calculations, the motion of the electrons is treated relativistically, and the combined correction terms are utilised (see chapter 2). Also, the single-electron wave functions of the metals' valence electrons are expressed as a linear combination of s-, p- and d-orbitals only, and exchange-correlation functional EXC1 is used (again, see chapter 2). Finally, the value of all $E_{tot}(a)$ curves is calculated at a number of lattice parameter values, each separated by an interval of 0.01 Bohr radii, within a range that is typically 0.2 to 0.3 Bohr radii in width.

5.2 Identification of the LM-HM Transition in the FCC 3d Metals

To illustrate the identification of a volume-controlled LM-HM transition in a typical FCC 3d metal, we consider, as a first example, the calculated $E_{tot}(a)$ and $\mu(a)$ curves of FCC Co, shown respectively in figures 5.1 and 5.2. It must be recalled that, at a given lattice parameter a, the $E_{tot}(a)$ curve of FCC Co gives the minimum total energy of a Co metal assuming that its constituent atomic nuclei remain stationary on a FCC crystal lattice with lattice parameter a. If, at a given lattice parameter, the minimum total energy of FM FCC Co is smaller than that of AFM FCC Co and of NM FCC Co, then FCC Co has the FM magnetic configuration when it has that lattice parameter. By comparing the $E_{tot}(a)$ curves of NM FCC Co, of AFM FCC Co and of FM FCC Co, we can determine if FCC Co undergoes a low-moment to high-moment transition, and we can identify the lattice parameter a_{tx} at which such a transition occurs.

When comparing the calculated $E_{tot}(a)$ curves of NM FCC Co, AFM FCC Co and FM FCC Co, we must determine if the curves are significantly different or numerically indistinguishable. To do so, we must recall the conclusions of chapter 3, which reports a study of the numerical precision of the TB-LMTO ESC program. In chapter 3, it is shown that the minimum total energy values computed using the TB-LMTO ESC program contain both a calculation precision error (CPE) and a systematic calculation error (SCE). The CPE's in

the calculated minimum total energy values are shown to be of the order of $\pm 2.5 \times 10^{-7}$ Rydberg units per atom when the calculations are conducted with convergence tolerances set to 1.0×10^{-5} (Rydberg for the total energy convergence tolerance, and electrons per cubic Bohr radii for the electron density convergence tolerance). Thus, any two minimum total energy values computed using the TB-LMTO ESC program that differ by less than $\pm 5.0 \times 10^{-7}$ Rydberg units per atom are numerically indistinguishable. It is also shown in chapter 3 that, because of the presence of the SCE's in the calculated minimum total energy values, care must be taken when comparing the calculated minimum total energy of metals possessing different crystal structures. The same is true of metals possessing different magnetic moment configurations. If the difference of two calculated minimum total energy values is smaller than the difference of their SCE's, then the energy values in question are numerically indistinguishable.

The SCE in the calculated minimum total energy of a metal possessing the AFM magnetic configuration can be compared to the SCE in the calculated minimum total energy of the same metal when it takes the NM magnetic configuration by taking the difference $\Delta E_{tot}(a) = \text{AFM } E_{tot}(a) - \text{NM } E_{tot}(a)$ at lattice parameters where the AFM metal has no magnetic moments. If this difference is null, the SCE in the calculated minimum total energy of the AFM metal is the same as that of the NM metal. Table 5.1 shows the SCE in the calculated minimum total energy of the AFM FCC 3d metals, relative to the SCE in the calculated minimum total energy of the metals when they take the NM magnetic configuration. We also compared the SCE's in the calculated minimum total energy of the NM and FM FCC 3d metals. We found that these SCE's have identical magnitudes.

We return now to the calculated $E_{tot}(a)$ and $\mu(a)$ curves of FCC Co, which are respectively shown in figures 5.1 and 5.2. In the lower part of figure 5.1, it is clear that the minimum total energy of AFM FCC Co is slightly larger than that of NM FCC Co at all lattice parameters shown in the figure. However, table 5.1 shows that the SCE in the minimum total energy of AFM FCC Co is of the order of 4×10^{-5} Rydberg units per atom larger than that in the minimum total energy of NM FCC Co. In the lower part of figure 5.1, the error bars denoting these SCE's stretch downward from the center of the data symbols denot-

Table 5.1: SCE's in the $E_{tot}(a)$ curves of the AFM FCC 3d metals relative to the SCE's in the $E_{tot}(a)$ curves of the NM FCC 3d metals

Metal	AFM SCE - NM SCE
FCC Sc	2×10^{-5} Rydberg per atom
FCC Ti	-7×10^{-6} Rydberg per atom
FCC V	5×10^{-6} Rydberg per atom
FCC Cr	1×10^{-5} Rydberg per atom
FCC Mn	2×10^{-5} Rydberg per atom
FCC Fe	-1×10^{-6} Rydberg per atom
FCC Co	4×10^{-5} Rydberg per atom
FCC Ni	-2×10^{-4} Rydberg per atom

ing $\Delta E_{tot}(a) =$ AFM $E_{tot}(a) -$ NM $E_{tot}(a)$, and are approximately as large as these data symbols. As the data symbols denoting $\Delta E_{tot}(a) =$ AFM $E_{tot}(a) -$ NM $E_{tot}(a)$ overlap the line denoting $\Delta E_{tot}(a) = 0$, we conclude that the $E_{tot}(a)$ curves of AFM FCC Co and of NM FCC Co are numerically indistinguishable.

Also, in the lower part of figure 5.1, the minimum total energy of FM FCC Co is numerically indistinguishable from that of NM FCC Co at lattice parameters between 6.20 to 6.22 Bohr radii. In contrast, the minimum total energy of FM FCC Co is significantly larger than that of NM FCC Co at lattice parameters between 6.23 and 6.26 Bohr radii. The upper part of figure 5.2 shows that FM FCC Co has magnetic moments with non-zero magnitude at these latter lattice parameters. In addition, at lattice parameters greater or equal to 6.27 Bohr radii, figure 5.1 shows that the minimum total energy of FM FCC Co is significantly smaller than the energy of NM FCC Co.

These observations lead us to conclude that FCC Co takes the NM magnetic configuration at lattice parameters smaller than or equal to 6.26 Bohr radii, and the FM magnetic configuration at lattice parameters greater than or equal to 6.27 Bohr radii. We also conclude

that FCC Co undergoes a LM-HM transition at a lattice parameter $a_{tx} = 6.265 \pm 0.005$ Bohr radii. The lower part of figure 5.2 shows the magnitude of the magnetic moments in FCC Co as a function of its lattice parameter, as predicted using the TB-LMTO ESC program. This figure shows that, when FCC Co undergoes its LM-HM transition, the magnitude of its magnetic moments increases by $\Delta\mu = 1.36$ Bohr magnetons.

As a second example, we consider now the $E_{tot}(a)$ and $\mu(a)$ curves of FCC Fe, shown respectively in figures 5.3 and 5.5. It is clear that FCC Fe undergoes a LM-HM transition at some lattice parameter a_{tx} as its lattice parameter is increased from 6.50 to 6.65 Bohr radii. To identify a_{tx} with greater precision, we examine more carefully figures 5.3 and 5.5. In doing so, we recall that all minimum total energy values shown in figure 5.3 contain a CPE of the order of $\pm 2.5 \times 10^{-7}$ Rydberg units per atom. In addition, the SCE in the calculated minimum total energy of AFM FCC Fe is approximately 1×10^{-6} Rydberg units per atom smaller than the SCE in the calculated minimum total energy of NM FCC Fe, as shown in figure 5.1.

The lower part of figure 5.3 shows that the $E_{tot}(a)$ curves of NM FCC Fe and FM FCC Fe are numerically indistinguishable at all lattice parameters shown in the figure. Also, the minimum total energy of AFM FCC Fe is numerically indistinguishable from that of NM FCC Fe at lattice parameters between 6.50 and 6.54 Bohr radii. This is more clearly observable in figure 5.4, which shows the same information as the lower part of figure 5.3 but on a finer scale. In figure 5.4 the error bars denoting the SCE's in $\Delta E_{tot}(a) =$ AFM $E_{tot}(a) -$ NM $E_{tot}(a)$ stretch upward from the center of the data symbols denoting this function, and are approximately as large as these data symbols. Because the data symbols denoting $\Delta E_{tot}(a) =$ AFM $E_{tot}(a) -$ NM $E_{tot}(a)$ overlap the line denoting $\Delta E_{tot}(a) = 0$ at lattice parameters between 6.50 and 6.54 Bohr radii, we conclude that the $E_{tot}(a)$ curves of AFM FCC Fe and of NM FCC Fe are numerically indistinguishable at these lattice parameters. In contrast, the minimum total energy of AFM FCC Fe is significantly larger than that of NM FCC Fe between 6.55 and 6.56 Bohr radii. This is so in spite of the fact that AFM FCC Fe has magnetic moments with non-zero magnitude at these lattice parameters, as shown in figure 5.5. Finally, the minimum total energy of AFM FCC Fe is

significantly smaller than that of NM FCC Fe at lattice parameters greater than or equal to 6.57 Bohr radii.

These observations lead us to conclude that FCC Fe undergoes a LM-HM transition from the NM magnetic configuration to the AFM magnetic configuration at a lattice parameter $a_{tx} = 6.565 \pm 0.005$ Bohr radii. The lower part of figure 5.5 shows the magnitude of the magnetic moments in FCC Fe as a function of its lattice parameter, as predicted using the TB-LMTO ESC program. This figure shows that, when FCC Fe undergoes its LM-HM transition, the magnitude of its magnetic moments increases by $\Delta\mu = 0.63$ Bohr magnetons.

Conducting a similar analysis of the calculated $E_{tot}(a)$ and $\mu(a)$ curves of FCC Sc to FCC Ni, we conclude that all eight of these metals undergo a LM-HM transition at some lattice parameter a_{tx}. Table 5.2 shows the nature of the LM-HM transition that occurs in each of the metals, the lattice parameter a_{tx} at which the transition occurs, as well as the change $\Delta\mu$ of the magnitude of the magnetic moments of the metals when the transition occurs. The calculated $E_{tot}(a)$ and $\mu(a)$ curves of FCC Sc to FCC Ni are shown in section 5.6.

Table 5.2: Details of the LM-HM transition in the FCC 3d metals

Metal	Transition type	a_{tx}	$\Delta\mu$
FCC Sc	NM to FM	11.245 Bohr radii	0.98 Bohr magnetons
FCC Ti	NM to AFM	9.265 Bohr radii	0.47 Bohr magnetons
FCC V	NM to AFM	8.135 Bohr radii	0.53 Bohr magnetons
FCC Cr	NM to AFM	7.405 Bohr radii	2.08 Bohr magnetons
FCC Mn	NM to AFM	6.745 Bohr radii	0.77 Bohr magnetons
FCC Fe	NM to AFM	6.565 Bohr radii	0.63 Bohr magnetons
FCC Co	NM to FM	6.265 Bohr radii	1.36 Bohr magnetons
FCC Ni	NM to FM	5.575 Bohr radii	0.35 Bohr magnetons

All values of a_{tx} are precise to ± 0.005 Bohr radii.

All values of $\Delta\mu$ are at worst precise to ± 0.01 Bohr magnetons.

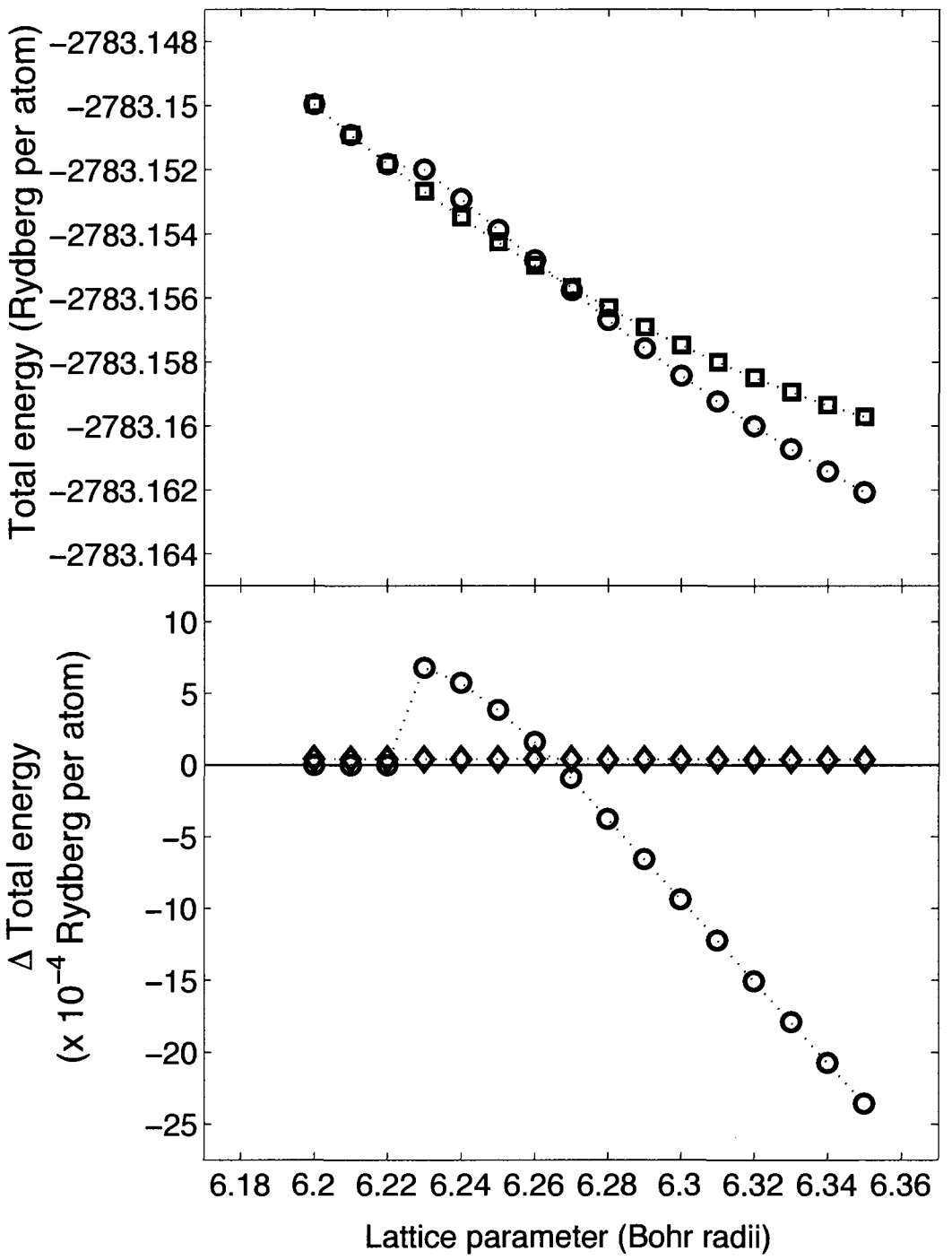

Figure 5.1: Minimum total energy versus lattice parameter curve $E_{tot}(a)$ of FCC Co, calculated using the TB-LMTO ESC program as described in section 5.1. The upper figure shows the $E_{tot}(a)$ curve of NM FCC Co (squares), and of FM FCC Co (circles). The $E_{tot}(a)$ curve of AFM FCC Co has been omitted as it is indistinguishable from that of NM FCC Co on the scale of the figure. The lower figure shows the difference $\Delta E_{tot}(a)$ = AFM $E_{tot}(a)$ - NM $E_{tot}(a)$ (diamonds) and the difference $\Delta E_{tot}(a)$ = FM $E_{tot}(a)$ - NM $E_{tot}(a)$ (circles). The figure reveals that FCC Co undergoes a LM-HM transition at a lattice parameter a_{tx} between 6.26 and 6.27 Bohr radii.

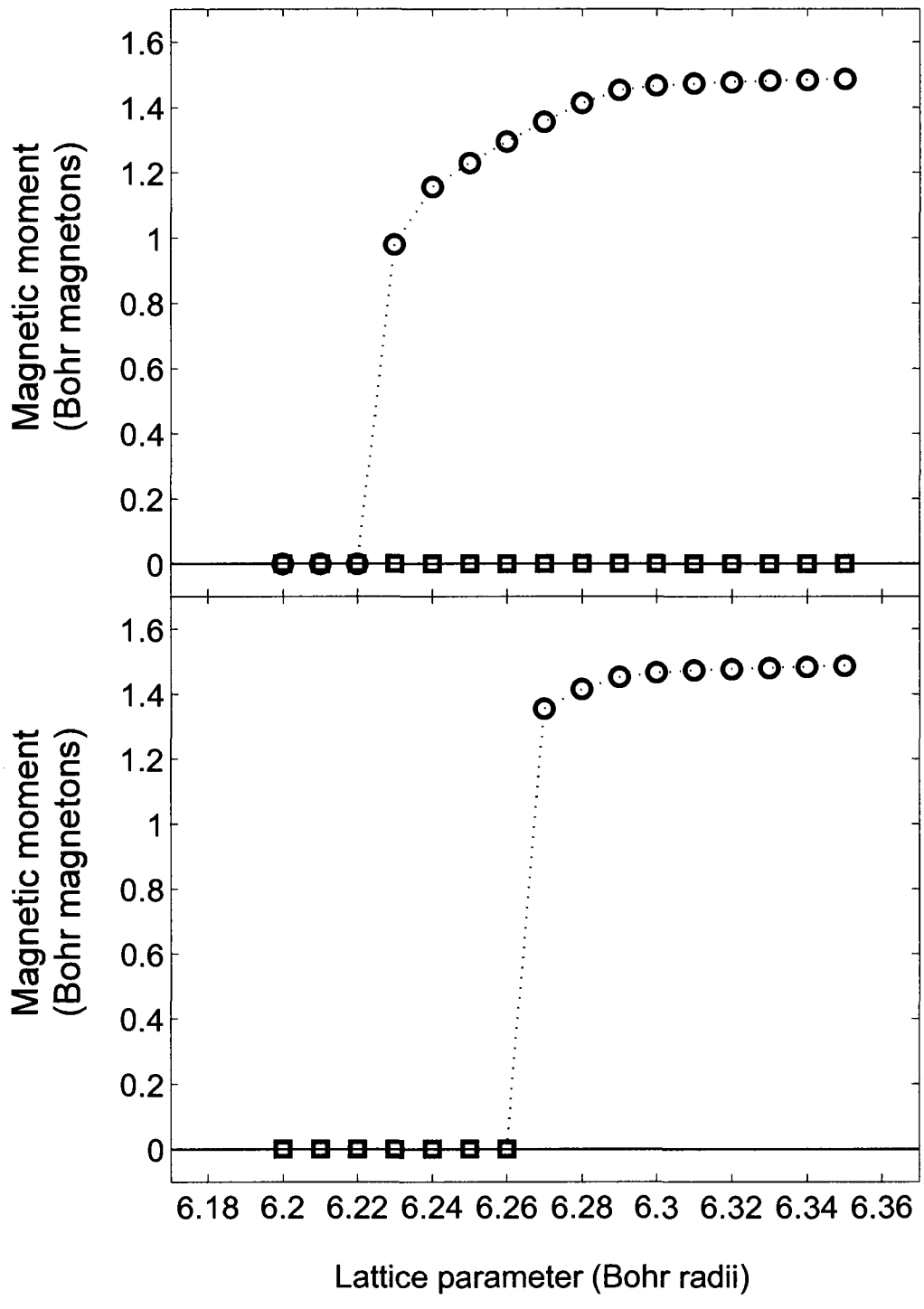

Figure 5.2: Magnetic moment versus lattice parameter curve $\mu(a)$ of FCC Co, calculated using the TB-LMTO ESC program as described in section 5.1. The upper figure shows the $\mu(a)$ curve of NM FCC Co (squares), and of FM FCC Co (circles). The $\mu(a)$ curve of AFM FCC Co has been omitted as it is indistinguishable from that of NM FCC Co on the scale of the figure. The lower figure shows, at a given lattice parameter, the magnetic moment of FCC Co when it takes its lowest-energy magnetic configuration. Squares (circles) indicate that the magnetic moment is that of NM (FM) FCC Co.

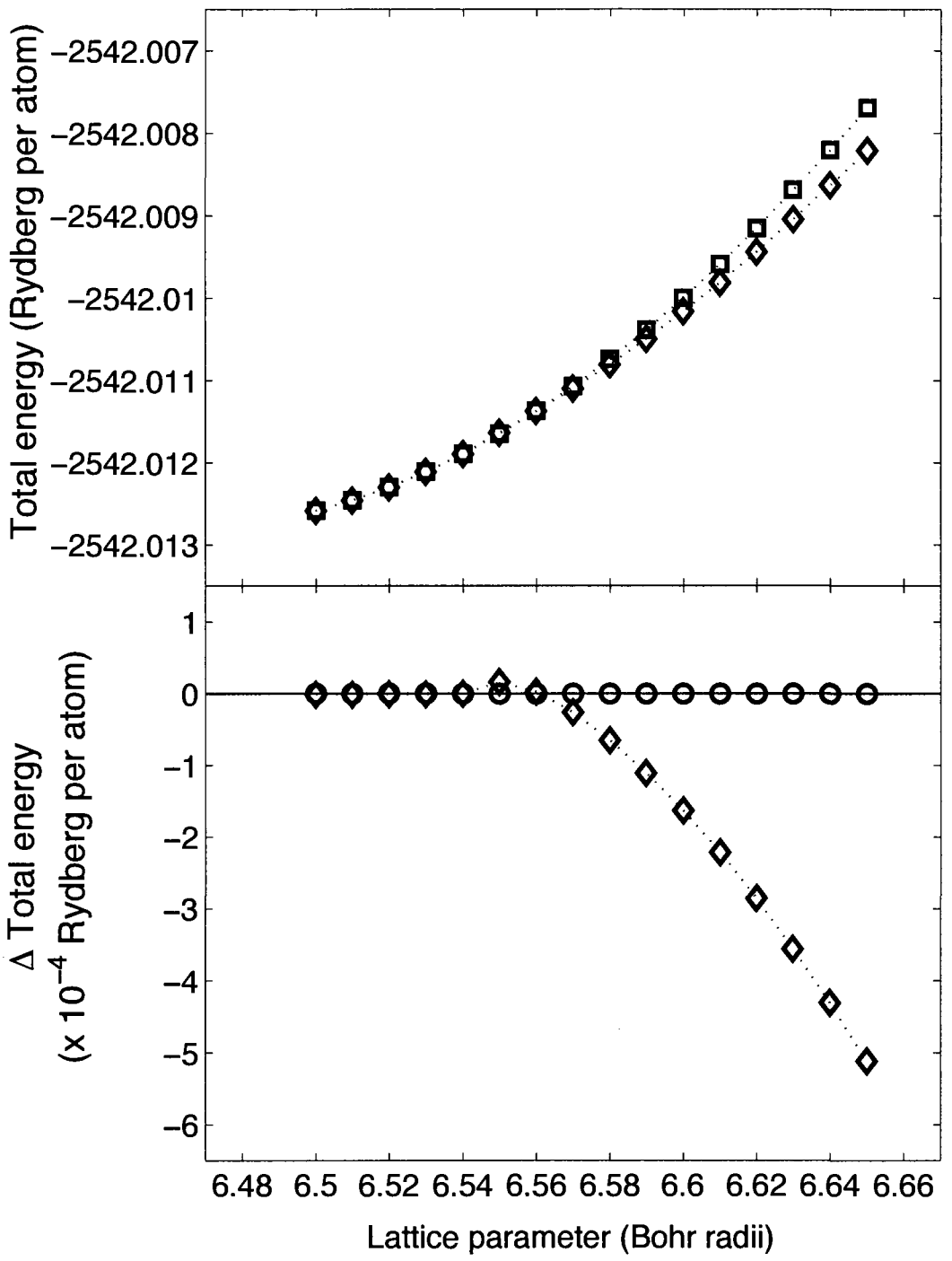

Figure 5.3: Minimum total energy versus lattice parameter curve $E_{tot}(a)$ of FCC Fe, calculated using the TB-LMTO ESC program as described in section 5.1. The upper figure shows the $E_{tot}(a)$ curve of NM FCC Fe (squares), and of AFM FCC Fe (diamonds). The $E_{tot}(a)$ curve of FM FCC Fe has been omitted as it is indistinguishable from that of NM FCC Fe on the scale of the figure. The lower figure shows the difference $\Delta E_{tot}(a)$ = AFM $E_{tot}(a)$ - NM $E_{tot}(a)$ (diamonds) and the difference $\Delta E_{tot}(a)$ = FM $E_{tot}(a)$ - NM $E_{tot}(a)$ (circles). The figure reveals that FCC Fe undergoes a LM-HM transition at a lattice parameter a_{tx} between 6.56 and 6.57 Bohr radii.

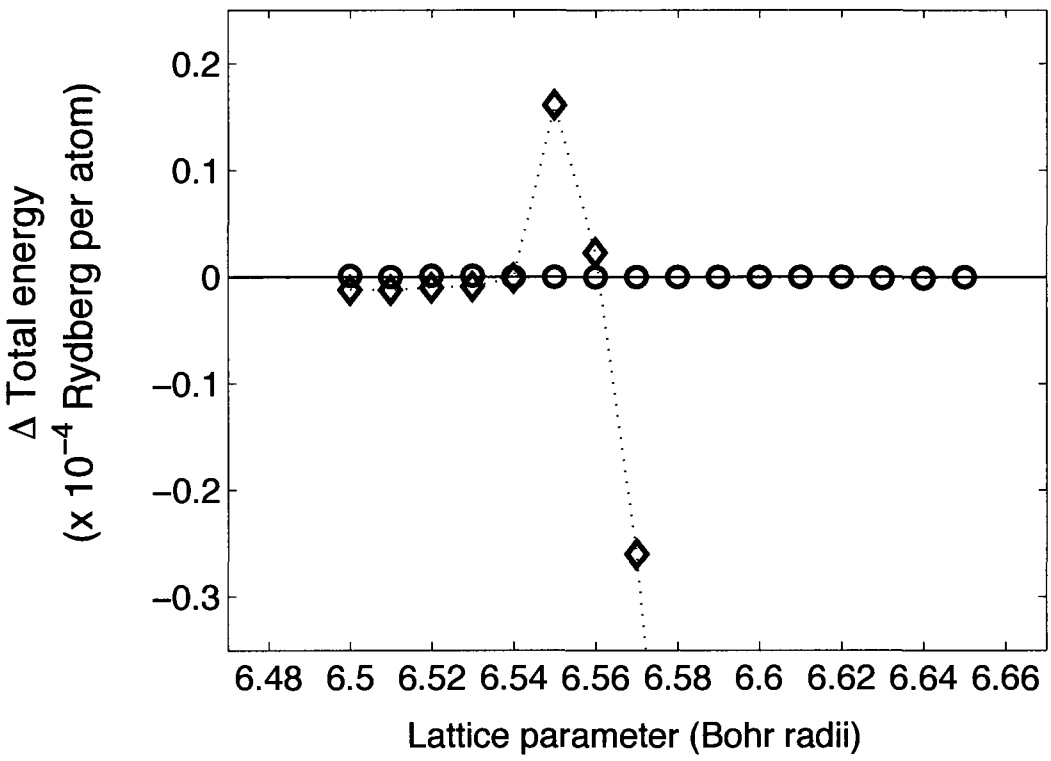

Figure 5.4: Minimum total energy versus lattice parameter curve $E_{tot}(a)$ of FCC Fe, calculated using the TB-LMTO ESC program as described in section 5.1. The figure shows the difference $\Delta E_{tot}(a)$ = AFM $E_{tot}(a)$ - NM $E_{tot}(a)$ (diamonds) and the difference $\Delta E_{tot}(a)$ = FM $E_{tot}(a)$ - NM $E_{tot}(a)$ (circles). The figure reveals that FCC Fe undergoes a LM-HM transition at a lattice parameter a_{tx} between 6.56 and 6.57 Bohr radii.

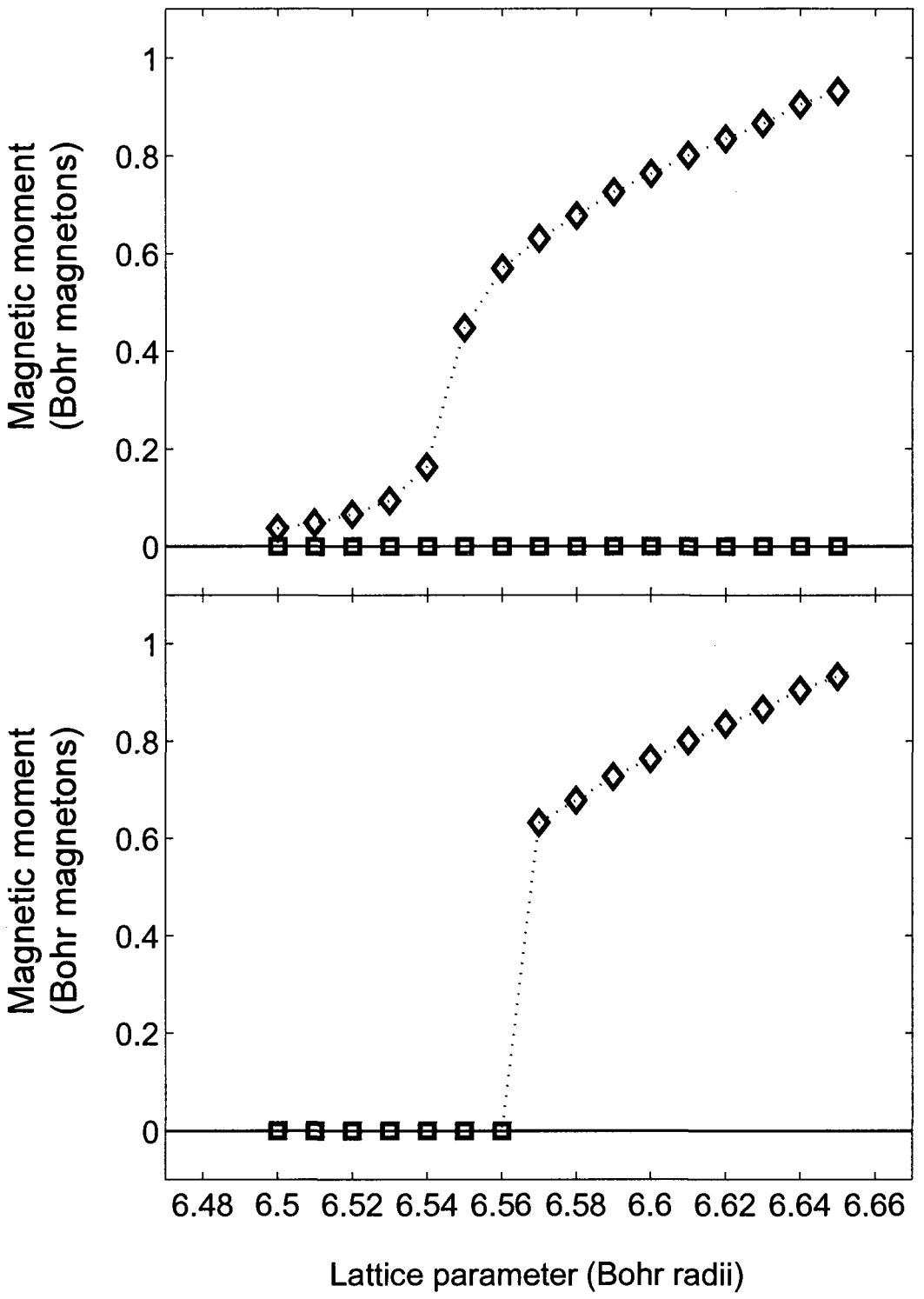

Figure 5.5: Magnetic moment versus lattice parameter curve $\mu_{tot}(a)$ of FCC Fe, calculated using the TB-LMTO ESC program as described in section 5.1. The upper figure shows the $\mu_{tot}(a)$ curve of NM FCC Fe (squares) and of AFM FCC Fe (diamonds). The lower figure shows, at a given lattice parameter, the magnetic moment of FCC Fe when it takes its lowest-energy magnetic configuration. Squares (diamonds) indicate that the magnetic moment is that of NM (AFM) FCC Fe.

5.3 General Aspects of the LM-HM Transition in the FCC 3d Metals

Having found that a volume-controlled LM-HM transition occurs in all FCC 3d metals from FCC Sc to FCC Ni, we compare, in figure 5.6, the change $\Delta\mu$ of the magnitude of the magnetic moments of each FCC 3d metal as they undergo their LM-HM transitions. Figure 5.6 also shows the spin magnetic moment $|\mu_s|$ on a free atom of each first-row transition element assuming that the spins of the outer-shell electrons of these atoms align according to Hund's rules [37, p. 650]. A regular pattern is observed in the value of $|\mu_s|$ as one progresses from Sc to Ni. As one progresses from Sc to Cr, $|\mu_s|$ increases as the outer d-orbitals of the atoms are progressively filled. This is because each subsequent atom in this series possesses one additional electron which occupies alone one of the atom's d-orbitals. The free atom of Cr has the largest $|\mu_s|$ as it possesses five d-orbital electrons and one s-orbital electron [37]. Thus, the outer orbitals of the Cr atom are exactly half-filled. Then, as one progresses from Cr to Ni, $|\mu_s|$ decreases. This is because each subsequent atom in this series possesses one additional electron which is paired up with an electron already occupying one of the atom's outer orbitals. In comparison, the figure shows that there is much variation in $\Delta\mu$ as one progresses through the FCC 3d metal series. Of note is the fact that the largest value of $\Delta\mu$ is that of FCC Cr and that a free atom of Cr has a larger value of $|\mu_s|$ than a free atom of any other 3d element [37]. However, there is no obvious trend in the value of $\Delta\mu$ as one progresses through the FCC 3d metal series.

In contrast, an interesting trend is observed when comparing the lattice parameters a_{tx} at which each FCC 3d metal undergoes a LM-HM transition. Figure 5.7 shows the lattice parameter a_{tx} of FCC Sc to FCC Ni. The figure also shows the zero-Kelvin lattice parameter a_0 of each of these metals, as predicted using the TB-LMTO ESC program. It should be recalled that the global minimum value of the $E_{tot}\,(a)$ curve of a metal occurs at the lattice parameter a_0. It should also be recalled that the zero-Kelvin lattice parameters shown in figure 5.7 are estimates of the lattice parameters that the metals Sc to Ni would possess at zero Kelvin if they possessed the FCC crystal structure at this temperature.

Figure 5.7 illustrates that Fe is positioned at a special location in the series of FCC 3d transition metals. Each metal prior to and including Fe in the series undergoes a LM-HM transition at a lattice parameter a_{tx} that is larger than its zero-Kelvin lattice parameter. In contrast, each metal following Fe in the series undergoes a LM-HM transition at lattice parameter a_{tx} that is smaller than its zero-Kelvin lattice parameter. This means that all metals prior to and including FCC Fe have no magnetic moments at zero Kelvin. However, these metals will acquire magnetic moments if they are expanded sufficiently. In contrast, the metals following FCC Fe in the first-row transition metal series possess magnetic moments arranged in the FM magnetic configuration at zero Kelvin. If they are compressed sufficiently, these latter metals will lose their magnetic moments. The difference between the lattice parameter a_{tx} and the zero-Kelvin lattice parameter a_0 of FCC Fe is smaller than the same difference in all other FCC first-row transition metals.

In figure 5.8, we show the atomic volume $v_{tx} = a_{tx}^3/4$ at which the FCC 3d metals undergo a LM-HM transition. We also show the atomic volume of these metals at zero Kelvin as predicted using the TB-LMTO ESC program, namely $v_0 = a_0^3/4$. We also constructed, but do not show, figures showing $log_2(v_{tx})$, $ln(v_{tx})$, and $log_{10}(v_{tx})$. These latter figures, along with figure 5.8, are very similar to figure 5.7. Unfortunately, they fail to reveal any additional information about the LM-HM transition in the first-row transition metals.

Figure 5.9 shows the lattice parameters a_{tx} of the FCC 3d transition metals as a percentage of the predicted zero-Kelvin lattice parameters a_0 of these metals. A dashed line denoting $(a_{tx} - a_0)/a_0 = 2.5\%$ is included in the figure because those first-row transition metals that in reality possess the FCC structure (namely Ni and Cu) have $(a_{mp} - a_0)/a_0 \approx 2.5\%$, where a_{mp} is the lattice parameter of the metal at its melting point [80]. In figure 5.9, only FCC Fe has $(a_{tx} - a_0)/a_0 \leq 2.5\%$. We therefore expect that, as it is heated from zero Kelvin to its melting point, the normal thermal expansion of FCC Fe will cause its lattice parameter to increase beyond the lattice parameter a_{tx} at which it undergoes a LM-HM transition. We therefore expect that FCC Fe will have no magnetic moments at zero Kelvin, but will acquire magnetic moments as it is heated and its lattice parameter expands beyond a_{tx}. This is the mechanism that is proposed by Lagarec et al. to explain the anti-Invar effect

that is observed in some Fe-rich FCC Fe-Ni alloys [9]. This mechanism is also thought to be important in understanding the phase transition from the BCC α-Fe phase to the FCC γ-Fe phase in real metallic Fe [11]. We believe that understanding this mechanism is likely to be important in understanding the physical properties of the metallic iron thought to be present in the deep mantle and core of the Earth [6,7].

Finally, we show in the upper part of figure 5.10 the work that must be done to change the lattice parameter of each FCC 3d metal from a_0 to a_{tx} at zero Kelvin. This work is simply $W = E_{tot}(a_{tx}) - E_{tot}(a_0)$. Again, this figure shows that FCC Fe is special among the FCC 3d metals, as the work required to change its lattice parameter from a_0 to a_{tx} is smaller than the work required to do the same for all other FCC 3d metals. In the lower part of figure 5.10, we provide an estimate of the pressure that must be applied to each FCC 3d metal to maintain its lattice parameter at a_{tx}. The pressure that must be applied to a metal to maintain its atomic volume v at temperature T is [76, p. 273]:

$$p(v,T) = -\frac{\delta F(v,T)}{\delta v}, \tag{5.1}$$

where $F(v,T)$ is simply the free energy per atom of the metal as a function of its atomic volume v and temperature T [76, p. 268]. When a FCC metal has a temperature of $T = 0$ Kelvin, its free energy function is $F(v,T) \approx E_{tot}(a)$, where $v = \frac{a^3}{4}$. Thus, at zero Kelvin, the pressure that must be applied to a FCC 3d metal to maintain its lattice parameter at a_{tx} is approximately:

$$p_{tx} = -\frac{dE_{tot}(a)}{da} \cdot \left.\frac{da}{dv}\right|_{a=a_{tx}}. \tag{5.2}$$

We estimate these pressures by evaluating numerically the derivative of the $E_{tot}(a)$ curve of each FCC 3d metal at $a = a_{tx}$. In figure 5.10, we see that p_{tx} is negative for all metals prior to and including Fe in the first-row transition metal series. This is sensical, as these metals all have $a_{tx} > a_0$. Thus, to change the lattice parameters of these metals from a_0 to a_{tx}, these metals must be expanded. This requires the application of a negative pressure. However, positive pressures must be applied to FCC Co and FCC Ni to maintain their lattice parameters at a_{tx}. To do so, a pressure of $\approx$ 40 GPa must be applied to FCC Co and a pressure of $\approx$ 390 GPa must be applied to FCC Ni.[3] The pressure at the center of

[3]We identified a paper in which it is reported that FCC Ni remains ferromagnetic beyond $\approx$ 300 GPa,

the Earth is of the order of ≈ 360 GPa and of the order of ≈ 40 GPa at a depth between ≈ 1000 and ≈ 1100 km below the surface of the Earth [114–116]. (It should be noted that the Earth's mantle extends to ≈ 2900 km below the Earth's surface [6, 115].) Thus, we expect that FCC Ni will have large magnetic moments even if it is located at the center of the Earth. In contrast, we expect that FCC Co will have large magnetic moments if it is located at a depth smaller than 1000 km within the Earth, and no magnetic moments if it is located at a depth greater than 1100 km. If it is located at a depth between 1000 and 1100 km, the lattice parameter of FCC Co will be in the vicinity of a_{tx}. We therefore expect that the thermal properties of FCC Co will be affected by its LM-HM transition at these depths.

---

and that the ferromagnetic phase of FCC Co becomes unstable at a pressure somewhat smaller than ≈ 70 GPa [113].

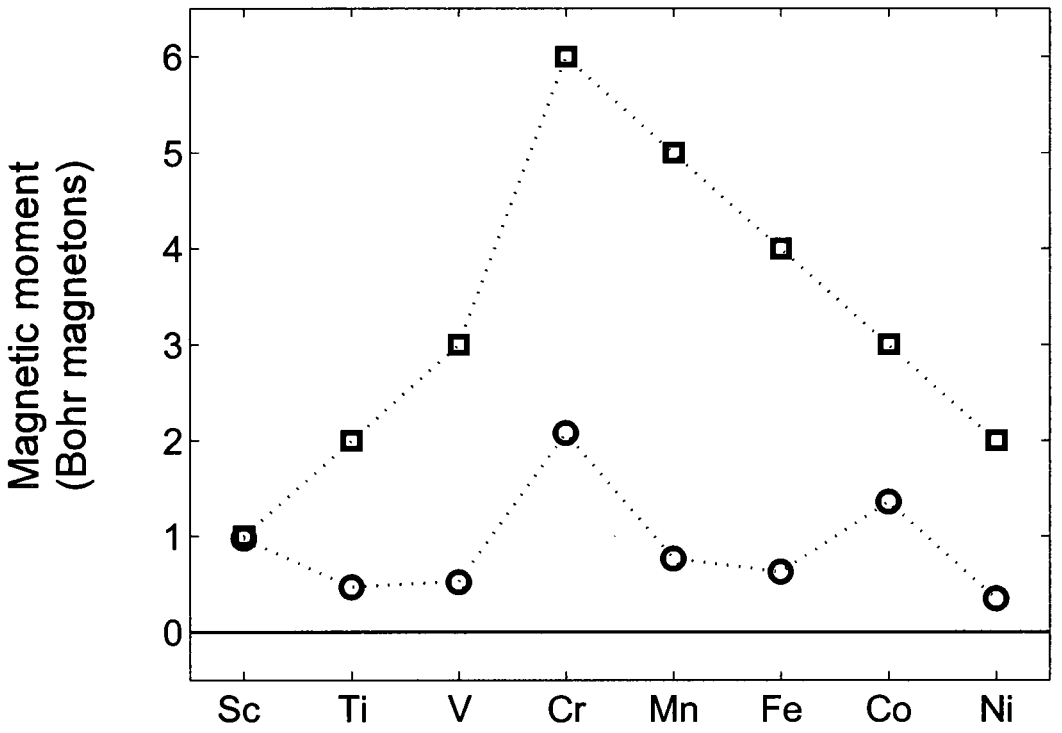

Figure 5.6: Magnetic moment of the first-row transition metals. Circles show the change $\Delta\mu$ of the magnitude of the magnetic moments of the FCC 3d metals as they undergo a LM-HM transition. Squares show the magnitude of the spin magnetic moment μ_s on a free atom of each first-row transition element.

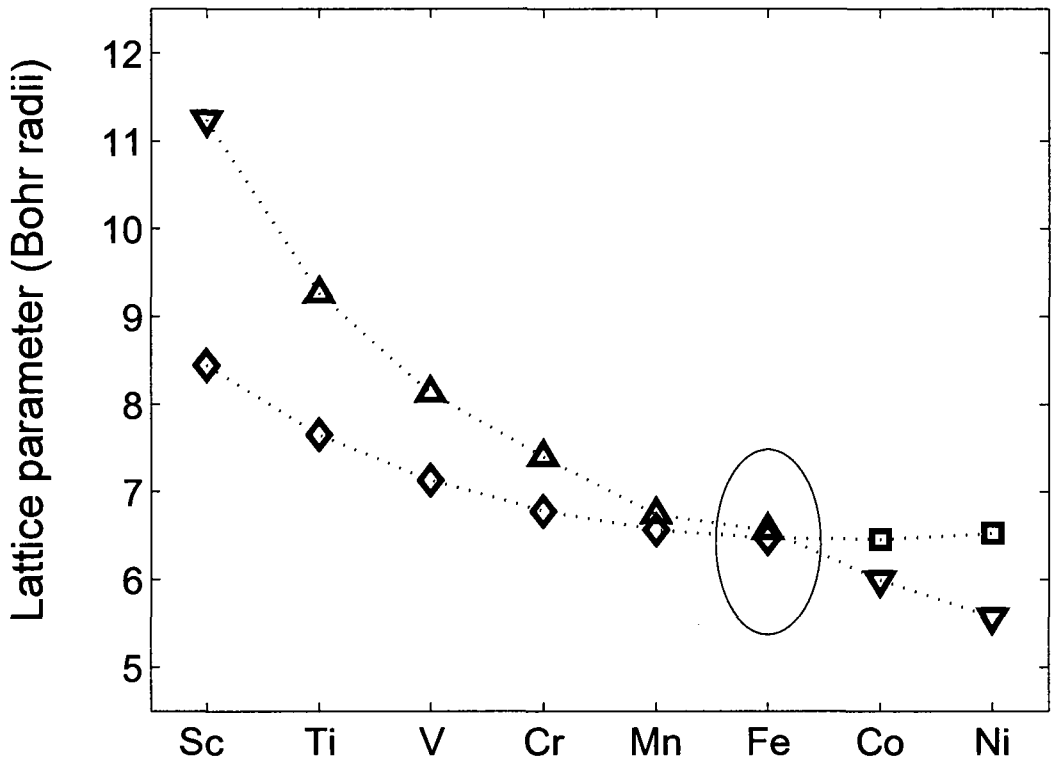

Figure 5.7: Lattice parameters a_{tx} and predicted zero-Kelvin lattice parameters of FCC Sc to FCC Ni. Diamonds and squares show zero-Kelvin lattice parameters predicted using the TB-LMTO ESC program and exchange-correlation functional EXC1. A diamond indicates that a metal has the NM magnetic configuration at zero Kelvin. A square indicates that a metal has the FM magnetic configuration at zero Kelvin. Triangles indicate the lattice parameters a_{tx} at which the metals undergo a LM-HM transition. A downward pointing triangle indicates that a metal undergoes a transition from the NM to the FM magnetic configuration. An upward pointing triangle indicates that a metal undergoes a transition from the NM to the AFM magnetic configuration. The results obtained for FCC Fe are highlighted with an ellipse.

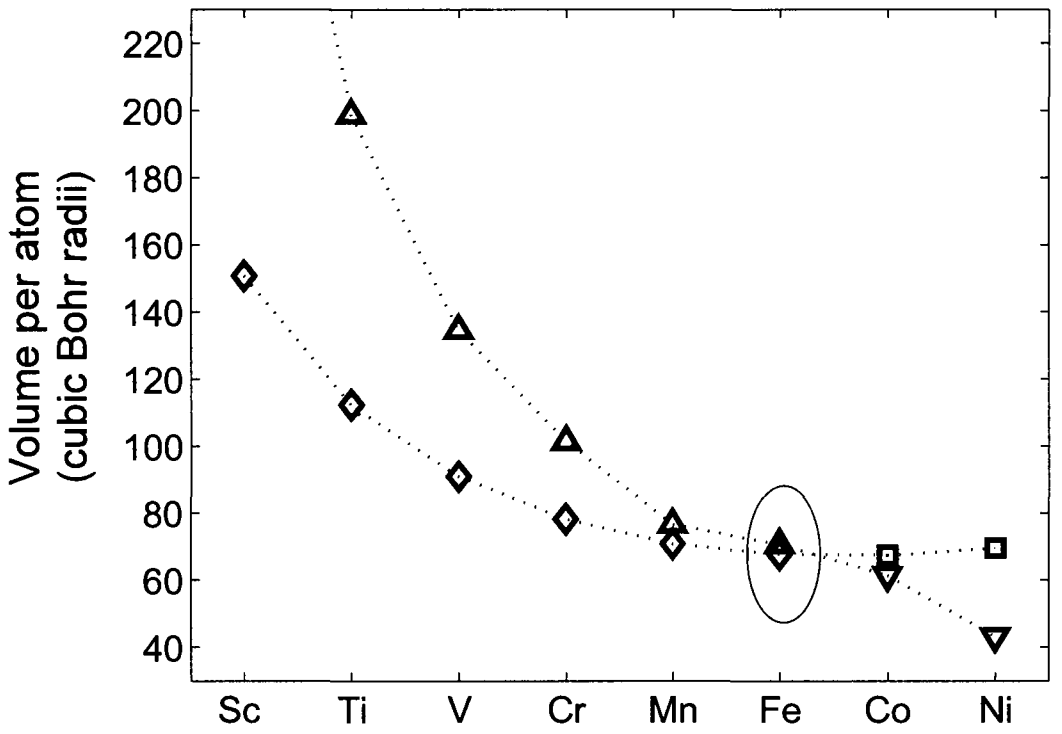

Figure 5.8: Volume per atom of FCC Sc to FCC Ni at the low-moment to high-moment transition and at zero Kelvin. Diamonds and squares show volume per atom at zero Kelvin as predicted using the TB-LMTO ESC program and exchange-correlation functional EXC1. A diamond indicates that a metal has the NM magnetic configuration at zero Kelvin. A square indicates that a metal has the FM magnetic configuration at zero Kelvin. Triangles indicate the volume per atom of a metal as it undergoes a LM-HM transition. A downward pointing triangle indicates that a metal undergoes a transition from the NM to the FM magnetic configuration. An upward pointing triangle indicates that a metal undergoes a transition from the NM to the AFM magnetic configuration. The results obtained for FCC Fe are highlighted with an ellipse.

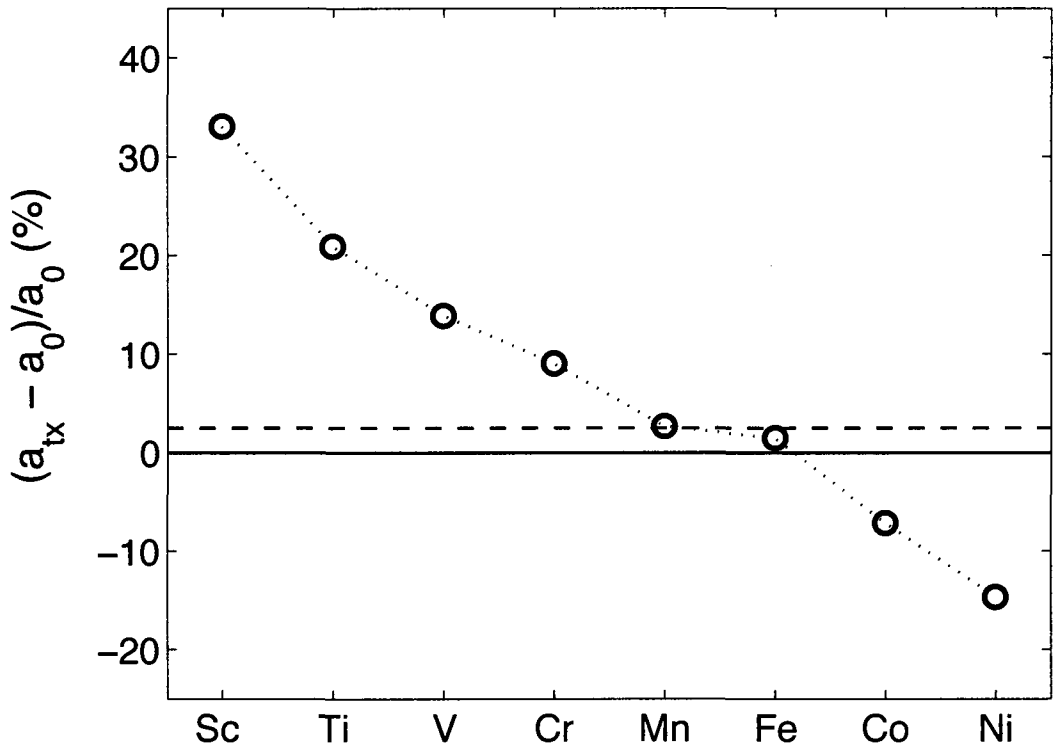

Figure 5.9: Difference of the lattice parameters a_{tx} and the lattice parameters a_0 of FCC Sc to FCC Ni, expressed as a percentage of the lattice parameters a_0. The dashed line indicates $(a_{tx} - a_0)/a_0 = 2.5\%$. This value is highlighted because those 3d metals that have the FCC crystal structure (namely Ni and Cu) have $(a_{tx} - a_0)/a_0 < 2.5\%$ at all temperatures.

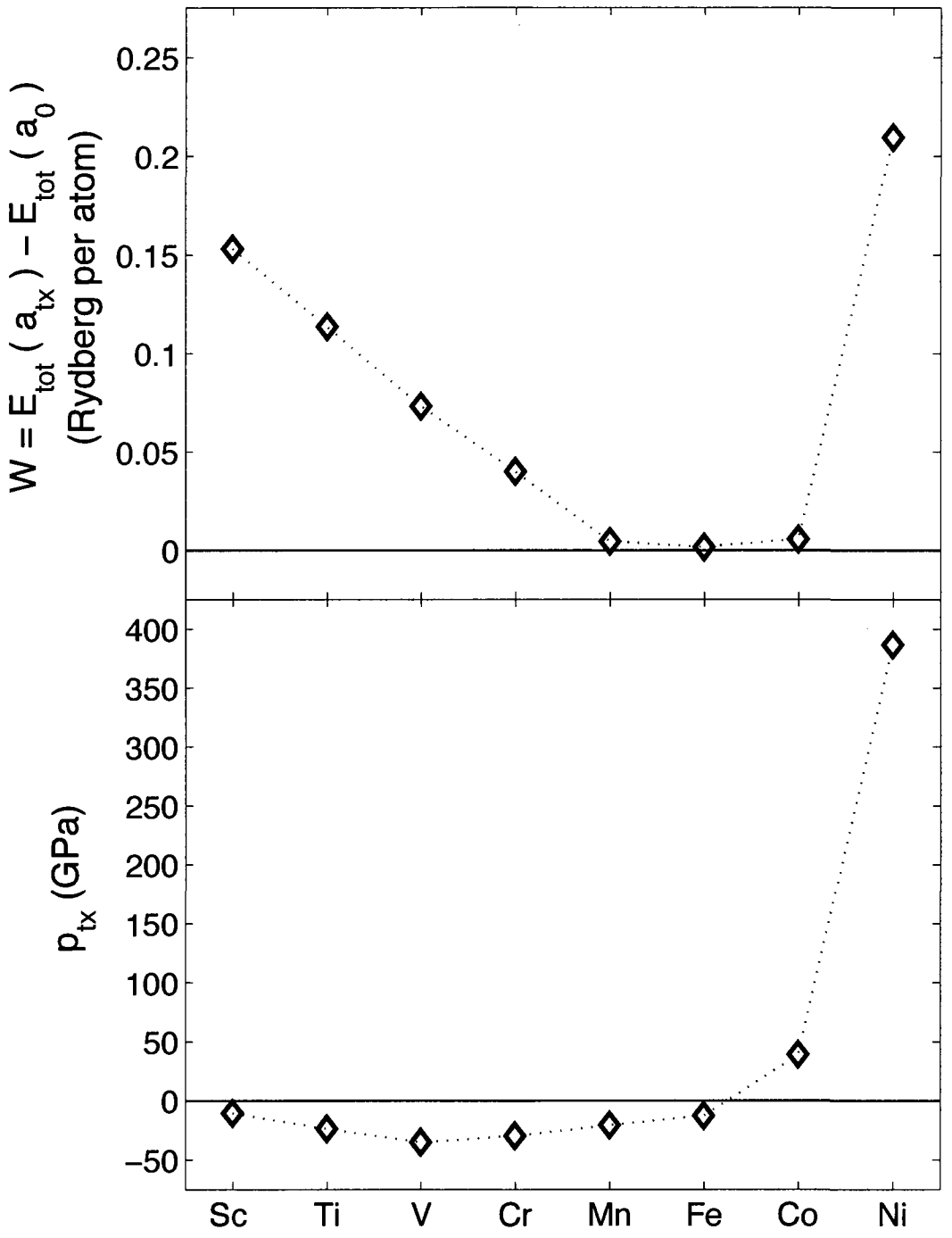

Figure 5.10: The upper figure shows the work required to change the lattice parameter of each FCC 3d metal from a_0 to a_{tx} at zero Kelvin. This work is $W = E_{tot}(a_{tx}) - E_{tot}(a_0)$. The lower figure shows the pressure that must be applied to each FCC 3d metal to maintain its lattice parameter at a_{tx}.

5.4 Electronic Aspects of the LM-HM Transition in the FCC 3d Metals

Having discussed some of the general aspects of the LM-HM transition that occurs in the FCC 3d metals, we now turn our attention to the electrons of these metals. More specifically, we wish to understand how the energy and the spatial distribution of these electrons changes as the LM-HM transition occurs. We believe that this will provide insight into the physical mechanism giving rise to the LM-HM transition in the FCC 3d metals.

To begin, we examine the evolution of the energy of the electrons of the FCC 3d metals as the LM-HM transition occurs. Before we do so, it must be recalled that, within the TB-LMTO ESC program, the minimum total energy of a solid with lattice parameter a is expressed as:

$$E_{tot}(a) = E_{e_{kin}}(a) + U_{e_{tot}}(a) + U_{Mad}(a), \tag{5.3}$$

where $E_{e_{kin}}(a)$ is the total kinetic energy of the solid's electrons when they take their lowest-energy configuration, and $U_{e_{tot}}(a) + U_{Mad}(a)$ is the total electrostatic energy of the solid when its electrons take their lowest-energy configuration (see chapter 2). Because the Madelung term $U_{Mad}(a)$ in the minimum total energy of the FCC 3d metals is always null, we can express the $E_{tot}(a)$ curve of any FCC 3d metal as:

$$E_{tot}(a) = E_{e_{kin}}(a) + U_{e_{tot}}(a). \tag{5.4}$$

We now examine $E_{e_{kin}}(a)$ and $U_{e_{tot}}(a)$ in all FCC 3d metals when these metals have lattice parameters $a = a_{tx} - 0.005$ Bohr radii and $a = a_{tx} + 0.005$ Bohr radii. For each FCC 3d metal, the calculated value of the metal's $E_{tot}(a)$ curve at $a = a_{tx} - 0.005$ Bohr radii is the calculated value of the curve that most immediately precedes the metal's LM-HM transition. Similarly, the calculated value of the metal's $E_{tot}(a)$ curve at $a = a + 0.005$ Bohr radii is the calculated value of the curve that most immediately follows the metal's LM-HM transition.

Figure 5.11 shows the difference $\Delta E_{e_{kin}}$ = HM $E_{e_{kin}}$ − NM $E_{e_{kin}}$ for all FCC 3d metals when these metals possess lattice parameters 0.005 Bohr radii smaller than or larger than

the lattice parameters a_{tx} given in table 5.2. HM $E_{e_{kin}}$ denotes FM $E_{e_{kin}}$ (or AFM $E_{e_{kin}}$) if a given metal undergoes a LM-HM transition from the NM magnetic configuration to the FM configuration (or from the NM magnetic configuration to the AFM configuration), as indicated in table 5.2. Figure 5.11 also shows the difference $\Delta U_{e_{tot}}$ = HM $U_{e_{tot}}$ − NM $U_{e_{tot}}$ for all FCC 3d metals when these metals possess lattice parameters 0.005 Bohr radii smaller than or larger than the lattice parameters a_{tx} given in table 5.2. The figure shows that, at lattice parameters smaller than and larger than the lattice parameter a_{tx}, the kinetic energy $E_{e_{kin}}$ of the electrons in the FCC 3d metals is larger when the metals possess magnetic moments. The opposite is true for $U_{e_{tot}}$. Thus, we conclude that when a FCC 3d metal has magnetic moments, the kinetic energy of its electrons is larger than it would be if the metal had no magnetic moments. In contrast, when a FCC 3d metal has magnetic moments, the total electrostatic energy of the metal is smaller than it would be if the metal had no magnetic moments. In light of this, and realizing that $\Delta E_{e_{kin}}(a) + \Delta U_{e_{tot}}(a)$ = HM $E_{tot}(a)$ − NM $E_{tot}(a)$ (see equation 5.4), we conclude that magnetic moments appear in a FCC 3d metal when their formation brings about an increase in the kinetic energy of the metal's electrons that is smaller than the corresponding decrease in the total electrostatic energy of the metal.

It has previously been reported that, when magnetic moments form in a metallic solid, the kinetic energy of its electrons increases while its total electrostatic energy decreases [117]. Accepted theoretical models of magnetic moment formation in metallic solids [111, 112, 118–121], and of magnetic moment formation on impurity atoms in metallic solids [122], also show that this is the case. The results illustrated in figure 5.11 are thus not surprising. However, published theoretical models of magnetic moment formation in metallic solids examine only the effect of magnetic moment formation on the solid's valence electrons while neglecting the solid's core electrons [111, 112, 118–122]. In contrast, the results of figure 5.11 were obtained using the TB-LMTO ESC program, which considers both the solid's valence electrons and core electrons when calculating the total energy of a solid. To our knowledge, this is the first reported study considering the effect of magnetic moment formation on both the core and valence electrons of a solid.

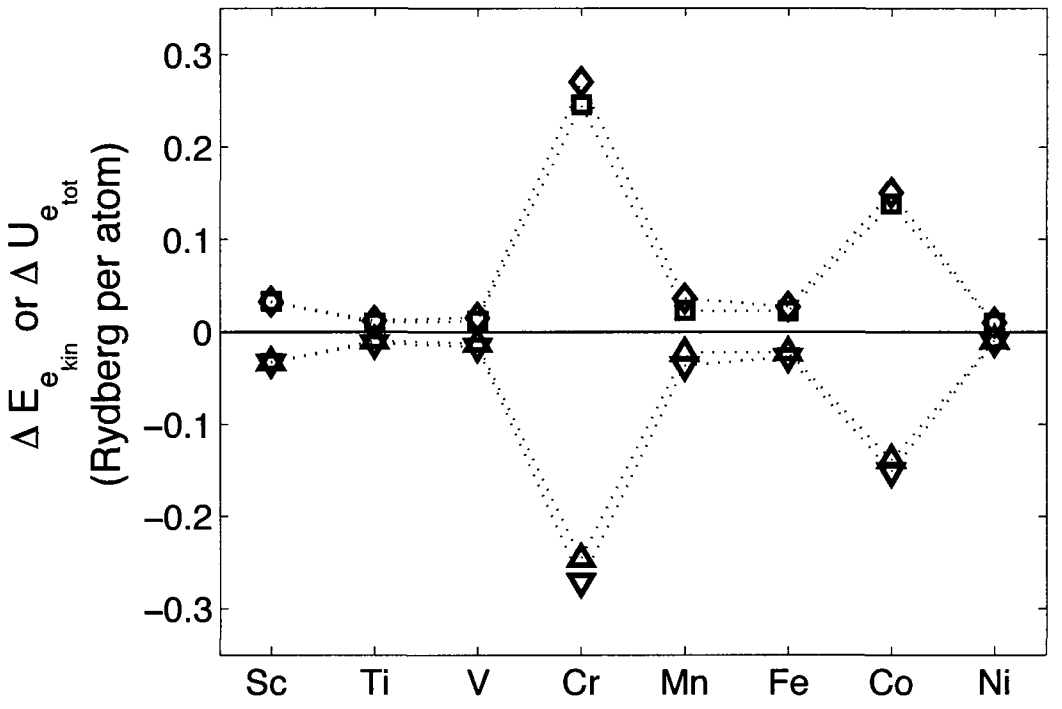

Figure 5.11: Figure shows $\Delta E_{e_{kin}}$ = HM $E_{e_{kin}}$ − NM $E_{e_{kin}}$ and $\Delta U_{e_{tot}}$ = HM $U_{e_{tot}}$ − NM $U_{e_{tot}}$. Squares (diamonds) indicate $\Delta E_{e_{kin}}$ at lattice parameters 0.005 Bohr radii smaller (larger) than the lattice parameters a_{tx} given in table 5.2. Upward pointing triangles (downward pointing triangles) show $\Delta U_{e_{tot}}$ at lattice parameters 0.005 Bohr radii smaller (larger) than the lattice parameters a_{tx} given in table 5.2.

Having examined the energy of all the electrons of the FCC 3d metals as they undergo a LM-HM transition, we now focus our attention on the valence electrons of these metals. We examine these electrons in greater detail as they are the ones that participate in the formation of the magnetic moments in the FCC 3d metals. We specifically examine the density of states function of these electrons ($n_v(\epsilon)$), as well as the spatial distribution of these electrons ($\rho_v(\vec{r})$).

As indicated in chapter 2, the TB-LMTO ESC program calculates the spherical average of the spatial distribution of the valence electrons of a metal, which we label $\rho_v(\vec{r})$. The distribution $\rho_v(\vec{r})$ is defined as follows (see equation 2.38):

$$\begin{aligned}
\rho_v(\vec{r}) &= \frac{1}{4\pi}\sum_l |\phi_l(\epsilon_{\mu,l}, |\vec{r}|, s_i)|^2 \int^{E_F} n_{v,l}(\epsilon)d\epsilon \\
&+ \frac{1}{4\pi}\sum_l 2\phi_l(\epsilon_{\mu,l}, |\vec{r}|, s_i)\phi_l'(\epsilon_{\mu,l}, |\vec{r}|, s_i) \int^{E_F} (\epsilon - \epsilon_{\mu,l})\, n_{v,l}(\epsilon)d\epsilon \\
&+ \frac{1}{4\pi}\sum_l \left\{|\phi_l'(\epsilon_{\mu,l}, |\vec{r}|, s_i)|^2 + \phi_l''(\epsilon_{\mu,l}, |\vec{r}|, s_i)\phi_l(\epsilon_{\mu,l}, |\vec{r}|, s_i)\right\} \int^{E_F} (\epsilon - \epsilon_{\mu,l})^2\, n_{v,l}(\epsilon)d\epsilon,
\end{aligned} \tag{5.5}$$

but in our study of the FCC 3d metals, we take $\rho_v(\vec{r})$ to be as follows:

$$\begin{aligned}
\rho_v(\vec{r}) &= \frac{1}{4\pi}\sum_l |\phi_l(\epsilon_{\mu,l}, |\vec{r}|, s_i)|^2 \int^{E_F} n_{v,l}(\epsilon)d\epsilon \\
&= \rho_{v,s}(\vec{r}) + \rho_{v,p}(\vec{r}) + \rho_{v,d}(\vec{r}).
\end{aligned} \tag{5.6}$$

We term the distributions $\rho_{v,s}(\vec{r})$, $\rho_{v,p}(\vec{r})$ and $\rho_{v,d}(\vec{r})$ the s-orbital, p-orbital and d-orbital components of $\rho_v(\vec{r})$.

In equation 5.6, the last two terms of equation 5.5 are simply dropped. This is justified because the integrals $\int^{E_F}(\epsilon - \epsilon_{\mu,l})\, n_{v,l}(\epsilon)d\epsilon$ and $\int^{E_F}(\epsilon - \epsilon_{\mu,l})^2\, n_{v,l}(\epsilon)d\epsilon$ are typically two orders of magnitude smaller than the integral $\int^{E_F} n_{v,l}(\epsilon)d\epsilon$ while the order of magnitude of the functions $\phi_l(\epsilon_{\mu,l}, |\vec{r}|, s_i)$, $\phi_l'(\epsilon_{\mu,l}, |\vec{r}|, s_i)$ and $\phi_l''(\epsilon_{\mu,l}, |\vec{r}|, s_i)$ is identical at almost all values of $|\vec{r}|$. We thus estimate that the last two terms of equation 5.5 represent approximately

$\pm 2\%$ of the total value of $\rho_v(\vec{r})$ at any $\vec{r}$. As a result, we consider that the distribution $\rho_v(\vec{r})$, as defined in equation 5.6, contains an error of the order of $\pm 2\%$ of its value. This error is much larger than the calculation precision errors that are present in the calculated values of $\rho_v(\vec{r})$.

For reasons indicated in section 4.1, we do not have at our disposal experimental measurements that would permit us to evaluate the accuracy of the distribution of the valence electrons of the FCC 3d metals, as calculated using the TB-LMTO ESC program. However, the accuracy of the TB-LMTO ESC program in calculating electron distributions has been tested by others (see [77]). These tests convince us that the TB-LMTO ESC program can calculate the electron distribution of the valence electrons of the FCC 3d metals with sufficient accuracy to allow for a qualitative study of the evolution of these distributions as a LM-HM transition occurs in these metals.

Furthermore, in calculating the minimum total energy of a metal, the TB-LMTO ESC program calculates, as an intermediate step, the density of states function $n_v(\epsilon)$ of the metal's valence electrons (see section 2.2.2). To understand the significance of the $n_v(\epsilon)$ function of a metal, it must be recalled that within the TB-LMTO ESC program, the kinetic energy of the electrons in a metal is calculated as follows (see equation 2.40):

$$E_{e_{kin}} = \sum_{i,core} \epsilon_i + \sum_{i,valence} \epsilon_i$$

$$- \left\{ - \int d\vec{r} \sum_I \frac{Q_I q}{\left|\vec{R}_I - \vec{r}\right|} \rho(\vec{r}) + \int\int d\vec{r} d\vec{r}' \frac{q^2}{|\vec{r} - \vec{r}'|} \rho(\vec{r}) \rho(\vec{r}') - \sum_s \int d\vec{r} V_{XC}(\vec{r}, s) \rho_s(\vec{r}) \right\}, \tag{5.7}$$

where ϵ_i is the energy of the i^{th} electron in the metal treated as an independent particle in a potential that is the result of its electrostatic interaction with all other electrons and atomic nuclei in the metal. The density of states function provides information about the single-electron energy values ϵ_i of the valence electrons of a metal. Specifically, the product $n_v(\epsilon)\, d\epsilon$ is the number of valence electrons in the metal that have energy within an infinitesimal interval $d\epsilon$ of ϵ. We expect that as magnetic moments form within any FCC

3d metal, or as the lattice parameter of the metal is changed, the single-electron energy values of the metal's valence electrons will also change. This will cause the density of states function of the metal to change.

Before proceeding with a study of the $n_v(\epsilon)$ functions of the FCC 3d metals, we must evaluate the accuracy and precision of these functions, as they are calculated using the TB-LMTO ESC program. To do so, we calculate the $n_v(\epsilon)$ function of a FCC Cu solid with lattice parameter $a = 6.69$ Bohr radii (namely the zero-Kelvin lattice parameter of metallic Cu as predicted using the TB-LMTO ESC program and exchange-correlation functional EXC1). Metallic Cu is one of only two first-row transition metals that takes the FCC crystal structure at room temperature and ambient pressure. Also, measurements of the density of states function of metallic Cu are available [123,124]. This makes possible the evaluation of the accuracy of the $n_v(\epsilon)$ function of FCC Cu, as calculated using the TB-LMTO ESC program.

Our results reveal that the calculated density of states function of FCC Cu is precise to ± 0.001 electrons per Rydberg unit at all values of ϵ. In addition, we compare, in figure 5.12, our calculated $n_v(\epsilon)$ function of FCC Cu to experimental measurements of this function. Specifically, we compare our calculations to measurements performed by W. E. Spicer [123] and by Krolikowski and Spicer [124]. These measurements are reproduced in figure 5.12 as they are reported in the Landolt-Börnstein data encyclopedia [125]. In this latter publication, calculations of the density of states function of FCC Cu are compared to both of these measurements. However, most calculations are more similar to the measurement of Spicer [123] than to that of Krolikowski and Spicer [124].

Like the calculations reported in the Landolt-Börnstein encyclopedia, our calculated $n_v(\epsilon)$ function is more similar to the measurement of W. E. Spicer [123] than to that of Krolikowski and Spicer [124]. Our calculation is similar to the measurement of Spicer in that as ϵ is decreased from the Fermi energy E_F, both $n_v(\epsilon)$ functions possess an initial sharply rising feature as well as a series of three seemingly corresponding peaks and troughs. (In the figure, the Fermi level is $\epsilon = 0$.) The features of our calculated $n_v(\epsilon)$ function occur

at an energy approximately 0.05 Rydberg units larger than the energy at which seemingly corresponding features occur in the measurement of Spicer. The accuracy of our calculation is comparable to that of other calculated $n_v(\epsilon)$ functions of metallic Cu that are reported in the Landolt-Börnstein encyclopedia [125]. We thus conclude that the TB-LMTO ESC program can calculate the $n_v(\epsilon)$ functions of the first-row transition metals with sufficient accuracy to allow for a qualitative study of the evolution of these functions as the first-row transition metals undergo a LM-HM transition.

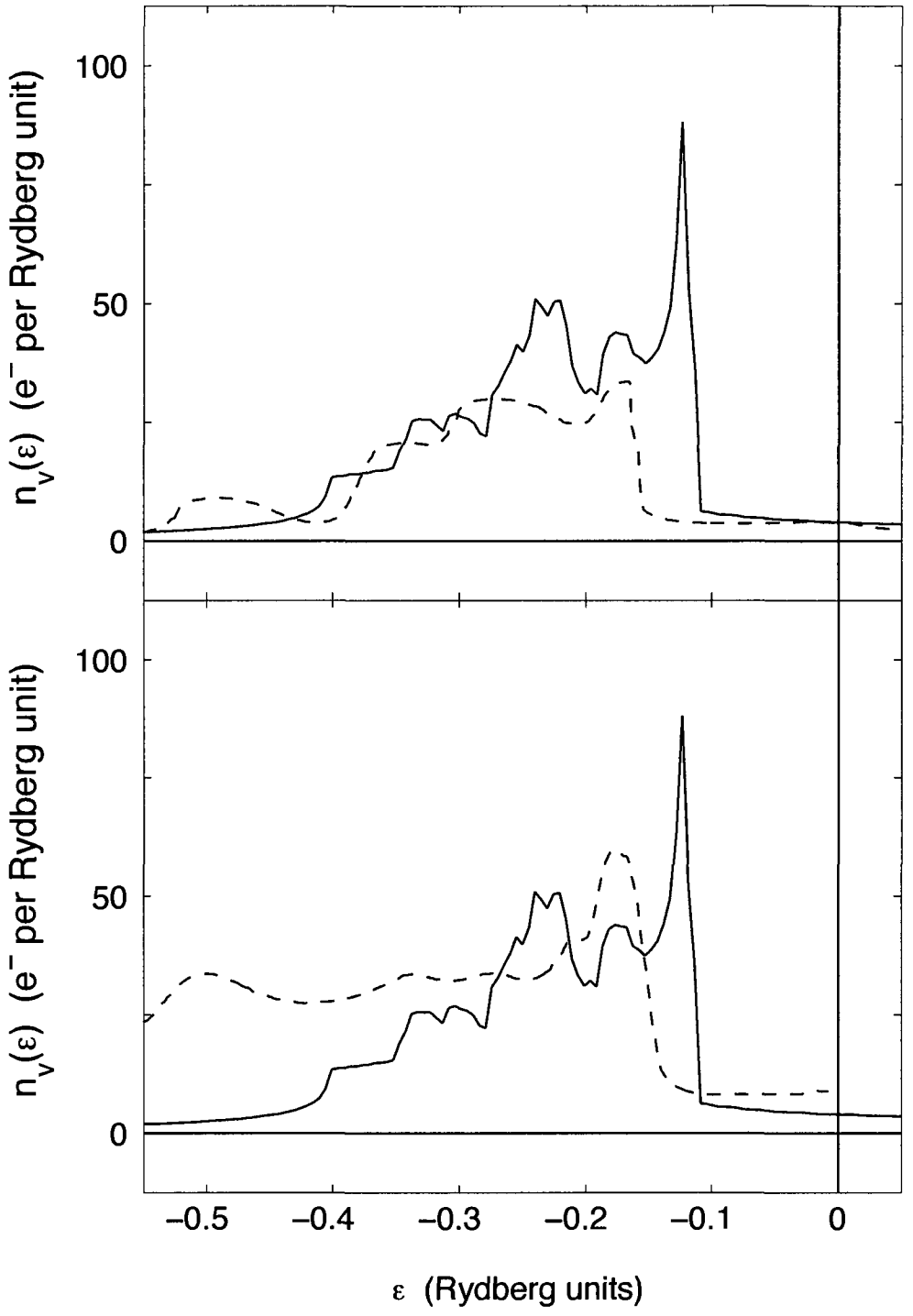

Figure 5.12: Calculated and measured density of states function $n_v(\epsilon)$ of FCC Cu. In both figures, the solid line denotes the density of states function of FCC Cu as calculated using the TB-LMTO ESC program. In the upper figure (lower figure), a dashed line denotes the measurement of Spicer [123] (of Krolikowski and Spicer [124]). Error bars denoting the precision of the calculated and measured values are omitted as they are smaller than the thickness of the plot lines.

We now examine the effect of the formation of magnetic moments on the valence electrons of the FCC 3d metals. In figures 5.13 and 5.14, we compare the $n_v(\epsilon)$ and $\rho_v(\vec{r})$ functions of the NM FCC 3d metals and the HM FCC 3d metals. The HM magnetic moment configuration is the FM (or AFM) configuration if a given metal undergoes a LM-HM transition from the NM to the FM configuration (or from the NM to the AFM configuration), as indicated in table 5.2. Also, in all calculations, the metals adopt the lattice parameters a_{tx} reported in table 5.2. In both figures, solid lines (dashed lines) denote the $n_v(\epsilon)$ functions or the $\rho_v(\vec{r})$ functions of the NM FCC 3d metals (HM FCC 3d metals). Finally, it should be noted that figure 5.13 is shown in two parts.

Figure 5.13 illustrates that the $n_v(\epsilon)$ functions of the HM FCC 3d metals differ from those of the NM FCC 3d metals. For most metals, significant differences between these $n_v(\epsilon)$ functions occur at energies in the range $(E_F - 0.1) < \epsilon < E_F$ Rydberg units. This suggests that the electrons with ϵ in the vicinity of the Fermi energy play an important role in the magnetic moment formation process in the FCC 3d metals. Significant differences in the $n_v(\epsilon)$ functions also occur at energies greater than the Fermi energy. We consider these differences to be less important, as they concern single-electron energy states that are not occupied when the metal has a temperature of zero Kelvin.

In figure 5.14, we show the valence electron distributions $\rho_v(\vec{r})$ of the NM FCC 3d metals and the HM FCC 3d metals. More specifically, we show the radial components of $\rho_v(\vec{r})$, which we label $\rho_v(|\vec{r}|)$, versus $|\vec{r}|$. The figure illustrates that in all FCC 3d metals, $\rho_v(|\vec{r}|)$ is essentially unchanged upon the formation of magnetic moments. We therefore conclude that any changes in $\rho_v(\vec{r})$ that accompany the formation of magnetic moments are strictly changes to the angular components of these distributions.

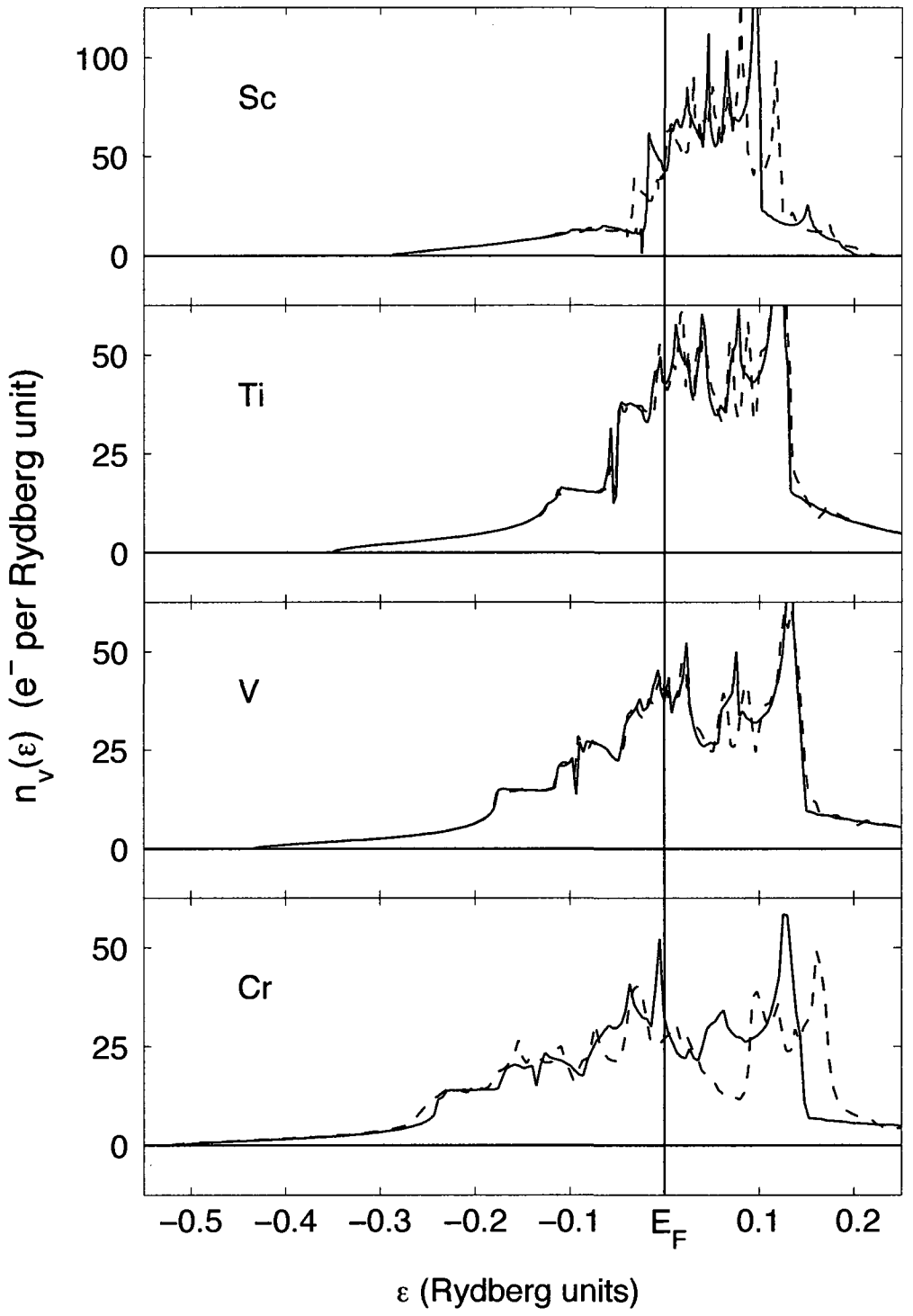

Figure 5.13: Calculated density of states functions $n_v(\epsilon)$ of the FCC 3d metals Sc to Cr with lattice parameter a_{tx}. Solid lines (dashed lines) denote the $n_v(\epsilon)$ functions of the NM FCC 3d metals (HM FCC 3d metals). When they possess magnetic moments, Sc takes the FM magnetic moment configuration while Ti, V and Cr take the AFM magnetic moment configuration. Error bars denoting the numerical precision of the calculated values are omitted as they are smaller than the thickness of the plot lines.

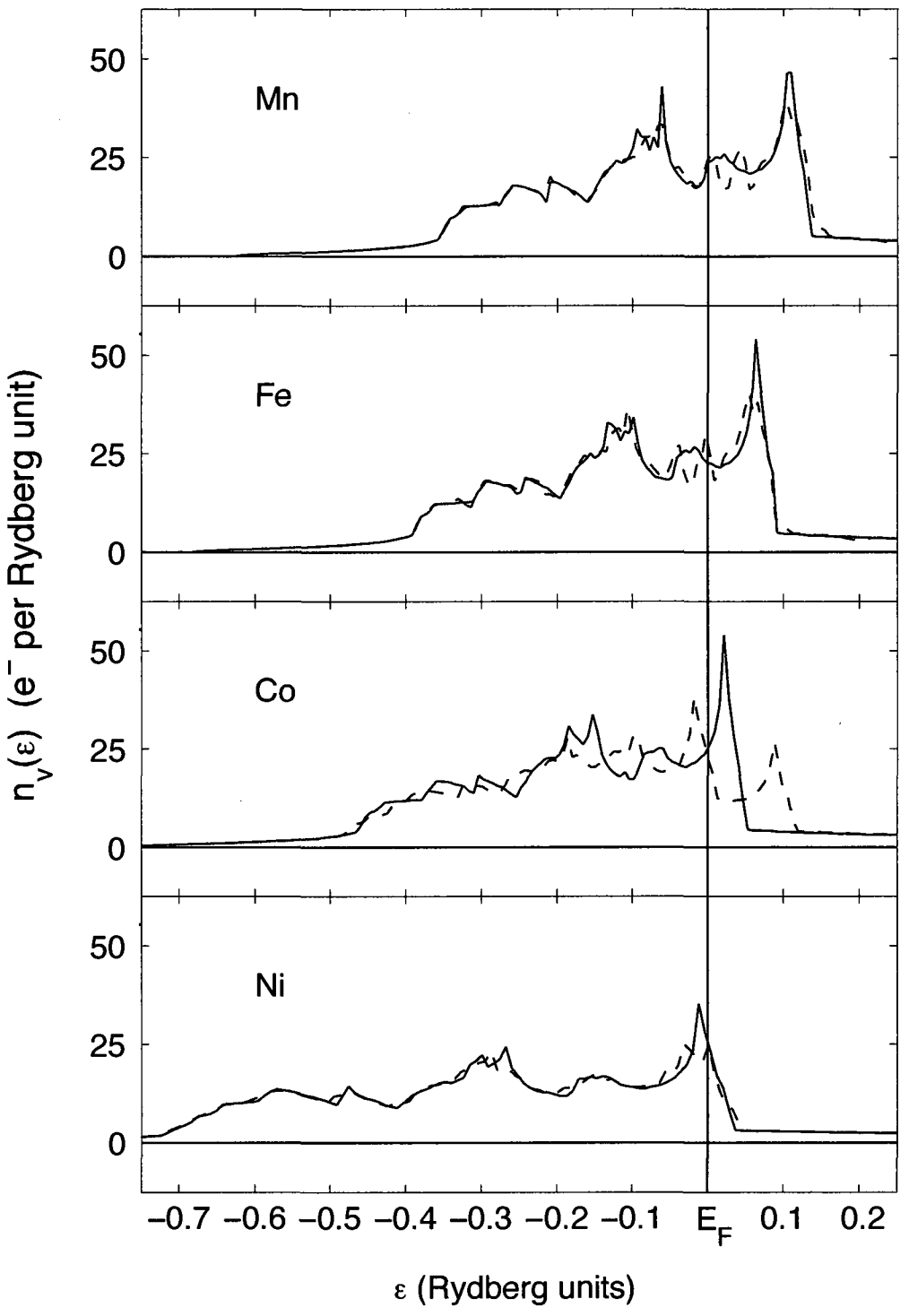

Figure 5.13: Calculated density of states functions $n_v(\epsilon)$ of the FCC 3d metals Mn to Ni with lattice parameter a_{tx}. Solid lines (dashed lines) denote the $n_v(\epsilon)$ functions of the NM FCC 3d metals (HM FCC 3d metals). When they possess magnetic moments, Co and Ni take the FM magnetic moment configuration while Mn and Fe take the AFM magnetic moment configuration. Error bars denoting the numerical precision of the calculated values are omitted as they are smaller than the thickness of the plot lines.

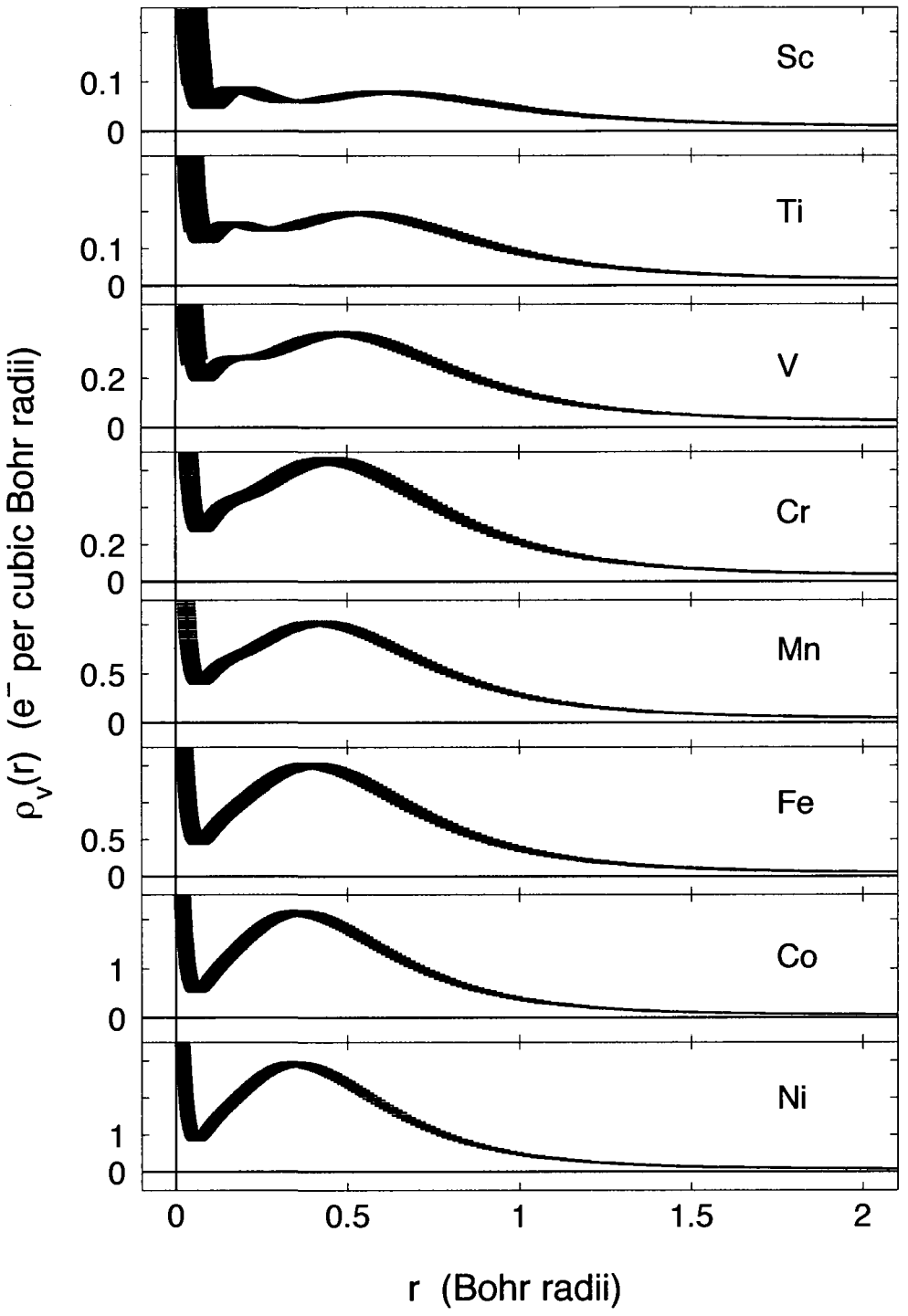

Figure 5.14: Calculated electron distributions of the NM and HM FCC 3d metals, $\rho_v(|\vec{r}|)$ versus $|\vec{r}|$. In all calculations the FCC 3d metals have lattice parameter a_{tx}. The electron distributions of the NM FCC 3d metals and of the HM FCC 3d metals are indistinguishable in the figure. When they possess magnetic moments, Sc, Co and Ni take the FM magnetic moment configuration while Ti, V, Cr, Mn and Fe take the AFM magnetic moment configuration. The thickness of each plot line is chosen to represent the numerical uncertainty of the calculated values.

In an effort to understand the conditions that must be met in order for magnetic moments to form in the FCC 3d metals, we now compare, in figures 5.15, 5.16 and 5.17, the calculated $n_v(\epsilon)$ and $\rho_v(\vec{r})$ functions of the NM FCC 3d metals when they adopt their zero-Kelvin lattice parameters a_0, and when they adopt the lattice parameters a_{tx} reported in table 5.2. In all three figures, a solid line (dashed line) denotes the $n_v(\epsilon)$ function or the $\rho_v(\vec{r})$ function of a metal when its lattice parameter is a_{tx} (is a_0).

In figure 5.15, the calculated $n_v(\epsilon)$ functions of the FCC 3d metals are shown. Clearly, the calculated $n_v(\epsilon)$ functions of Mn and Fe are similar at a_0 and at a_{tx}. This is not surprising as both Mn and Fe have $(a_{tx} - a_0)/a_0 < 5\%$. We thus expected that the $n_v(\epsilon)$ functions of these metals would be similar at a_0 and at a_{tx} because these lattice parameters are themselves similar. For all other metals, the $n_v(\epsilon)$ function at a_0 is significantly different of that at a_{tx}. In most metals, the most significant differences occur at energy values within 0.1 Rydberg units of the Fermi energy E_F. Specifically, $n_v(E_F)|_{a=a_0} < n_v(E_F)|_{a=a_{tx}}$ for Sc to Cr while the opposite is true for Co and Ni. Recalling that $a_{tx} > a_0$ for Sc to Cr, that $a_{tx} \approx a_0$ for Mn and Fe, and that $a_{tx} < a_0$ for Co and Ni (see figure 5.7), figure 5.15 indicates that as the lattice parameter of a FCC 3d metal is increased, the width of the energy bands of its valence electrons is decreased. This is accompanied by an increase in the density of states of its valence electrons at E_F.

In figure 5.16, we show the calculated valence electron distributions $\rho_v(\vec{r})$ of the NM FCC 3d metals. Then, in figure 5.17, we show the calculated d-orbital components of these electron distributions, $\rho_{v,d}(\vec{r})$. More precisely, the figures show plots of the radial components of these distributions, which we label $\rho_v(|\vec{r}|)$ and $\rho_{v,d}(|\vec{r}|)$, versus $|\vec{r}|$. In analyzing the results of figures 5.16 and 5.17, it must again be recalled that for Sc to Fe, $a_{tx} > a_0$, while $a_{tx} < a_0$ for Co and Ni. Keeping this in mind, the results of figure 5.16 (in particular those for Sc, Ti, V and Cr) show that when the lattice parameters of the FCC 3d metals are increased, their valence electrons move further away from their atomic nuclei (which are located at $|\vec{r}| = 0$). This is sensical because when a metal has a larger lattice parameter, there is more space available between its atomic nuclei for its valence electrons to occupy. Interestingly, the results of figure 5.17 indicate that the distributions $\rho_{v,d}(|\vec{r}|)$

do not change significantly when the lattice parameters of the metals are changed. Thus, the changes in the electron distributions of the FCC 3d metals that are evident in figure 5.16 are almost exclusively changes in the s-orbital and the p-orbital components of these distributions.

That the distributions $\rho_{v,d}(|\vec{r}|)$ do not change very much when the lattice parameters of the FCC 3d metals are changed is surprising to us. It is known that the magnetic moments of the FCC 3d metals are mostly the result of the spin-polarization of their d-electrons. This means that the d-orbital distributions $\rho_{v,d}(\vec{r})$ are the distributions of those electrons that participate most meaningfully in the formation of magnetic moments in the FCC 3d metals. We expected that at lattice parameters smaller than a_{tx}, the distributions of these electrons would be non-conducive to the formation of magnetic moments, but that they would become conducive to the formation of magnetic moments as the lattice parameters of the FCC 3d metals were increased. We thus expected that the distributions $\rho_{v,d}(\vec{r})$ would change significantly as the lattice parameters of the FCC 3d metals were increased.

The results of figures 5.13 to 5.17 can be meaningfully interpreted in terms of the Stoner model of magnetic moment formation in metals [111,112]. According to the Stoner model, magnetic moments form in a metal when $I \times n_v(E_F)/2 > 1$, where the "Stoner parameter" I is the reduction in electrostatic energy that accompanies the alignment of the spins of two of the metal's electrons, initially with counter-aligned spins. Typically, the electrostatic energy of a pair of electrons is lower when their spins are aligned because the exchange term of the electrostatic energy expression is more negative when this is the case (see section 2.1.2). The Stoner criterion is a very simple theory that cannot capture all the complexities of magnetic moment formation in real metals. Nonetheless, the essence of the Stoner criterion is that two conditions must simultaneously be met in order for magnetic moments to form in a metal. Specifically, $n_v(E_F)$ must be sufficiently large, and there must be a sufficiently large reduction in electrostatic energy when the spins of the electrons of the metal become aligned.

In light of this understanding, figures 5.13 and 5.15 suggest that at small lattice parame-

ters, the value of $n_v(E_F)$ is too small for magnetic moments to form within the FCC 3d metals. Then, as the lattice parameters of the metals are increased to a_{tx}, $n_v(E_F)$ becomes sufficiently large to permit the formation of magnetic moments. The increase in $n_v(E_F)$ is itself the result of the narrowing of the energy bands of the valence electrons of the FCC 3d metals, as illustrated in figure 5.13. This narrowing can be understood in terms of the tight-binding theory of energy band formation (for a good description of this theory, see [37,126]). It is generally understood that this theory is appropriate for modelling the formation of the energy bands of the d-electrons in the FCC 3d metals [37, p. 176]. Essentially, as the lattice parameters of the FCC 3d metals are increased, the d-electrons located on different atomic nuclei within the metals move further and further apart. As a result, the overlap of their orbitals becomes less and less significant, and this causes the energy bands of the FCC 3d metals to become narrower [126, p. 141].

That the d-electron distributions of the FCC 3d metals do not change significantly as the lattice parameters of the metals are changed, as illustrated in figure 5.17, suggests that magnetic moments do not form at lattice parameters smaller than a_{tx} exclusively because the value of $n_v(E_F)$ is too small. However, figures 5.16 and 5.17 together suggest that the s- and p-orbital electrons may be impeding the formation of magnetic moments in the FCC 3d metals at lattice parameters smaller than a_{tx}. Together, these figures indicate that a larger number of s- and p-electrons are located between the atomic nuclei and the d-electrons at small lattice parameters. The s- and p-electrons may be screening the electrostatic interaction of d-electrons located on different sides of the atomic nuclei, thus reducing the Stoner parameter I. As the lattice parameters of the FCC 3d metals are increased, their s- and p-electrons move away from their atomic nuclei, thus allowing their d-electrons to interact more strongly.

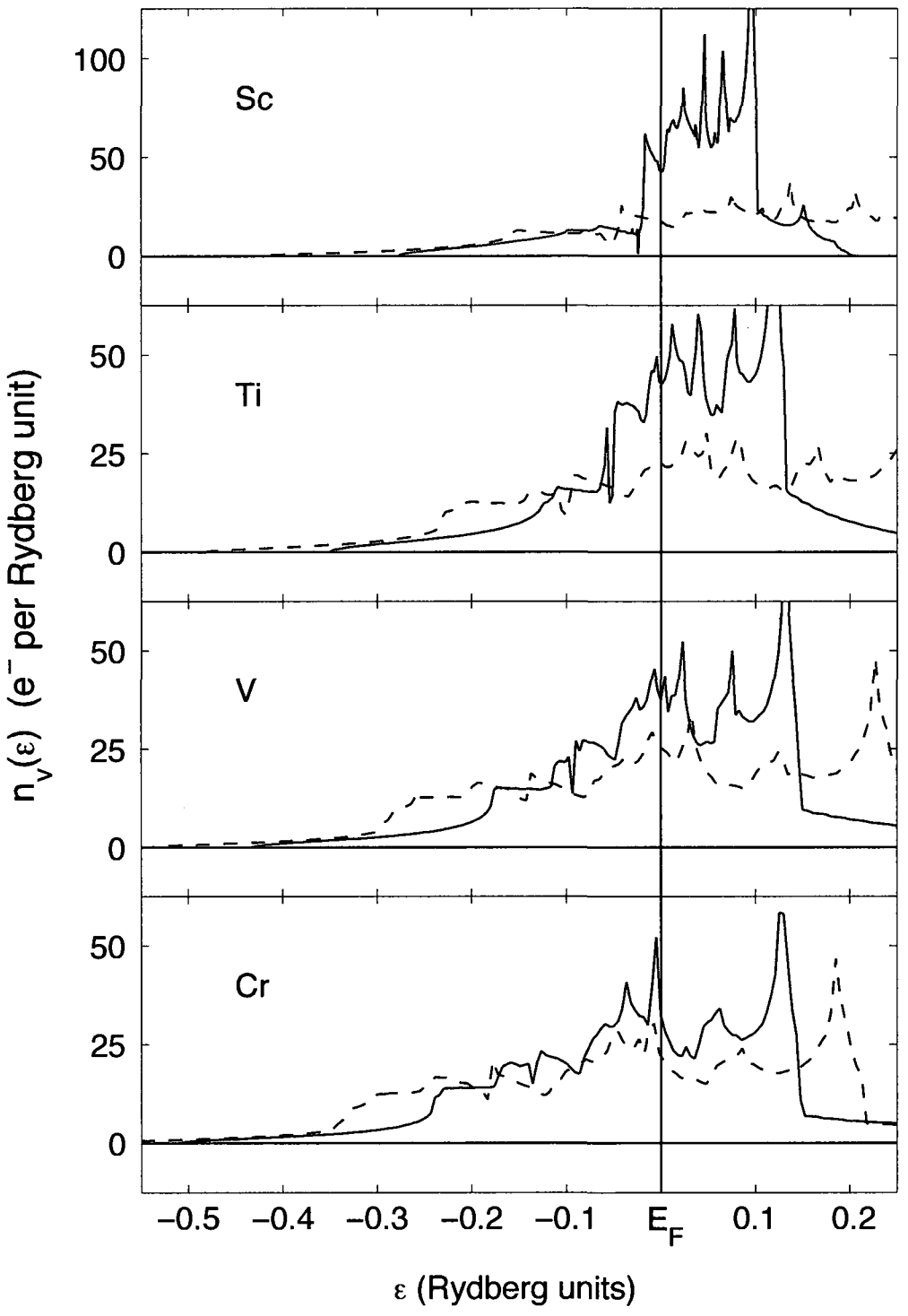

Figure 5.15: Calculated density of states functions $n_v(\epsilon)$ of the NM FCC 3d metals Sc to Cr. Solid lines (dashed lines) denote the $n_v(\epsilon)$ functions of metals with lattice parameter a_{tx} (with lattice parameter a_0). Error bars denoting the numerical precision of the calculated values are omitted as they are smaller than the thickness of the plot lines.

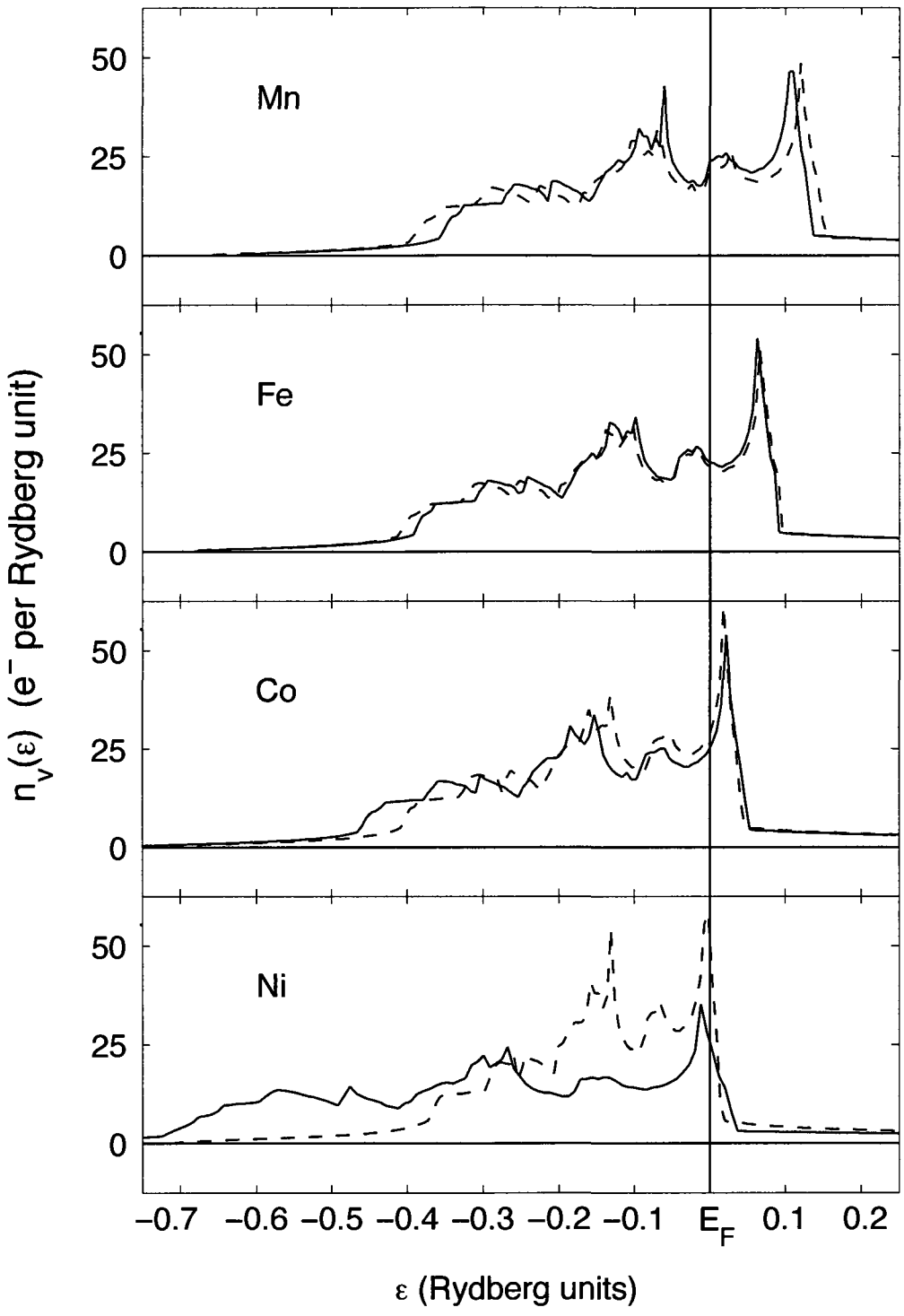

Figure 5.15: Calculated density of states functions $n_v(\epsilon)$ of the NM FCC 3d metals Mn to Ni. Solid lines (dashed lines) denote the $n_v(\epsilon)$ functions of metals with lattice parameter a_{tx} (with lattice parameter a_0). Error bars denoting the numerical precision of the calculated values are omitted as they are smaller than the thickness of the plot lines.

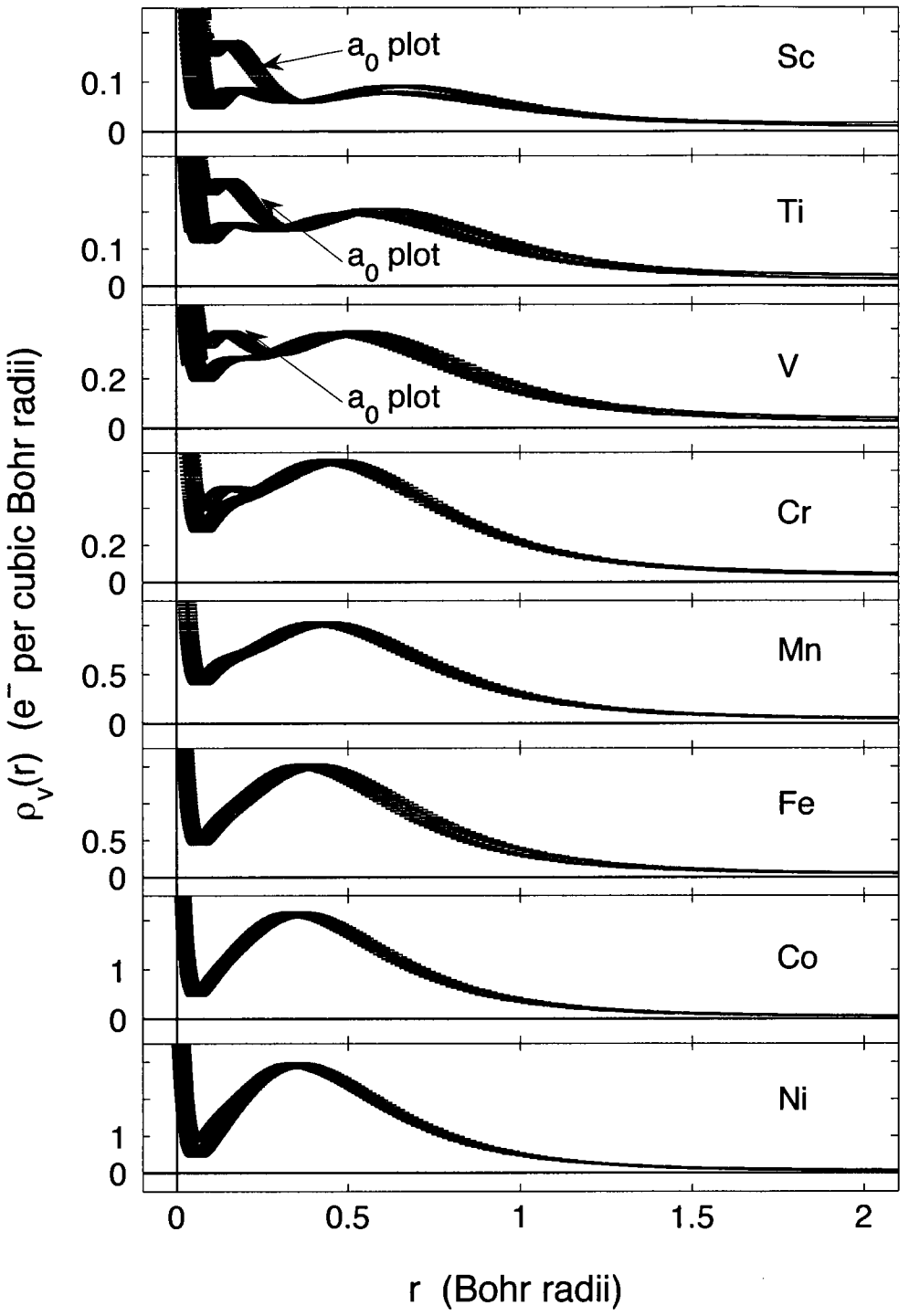

Figure 5.16: Calculated electron distributions of the NM FCC 3d metals, $\rho_v(|\vec{r}|)$ versus $|\vec{r}|$. Generally, the electron distributions of metals with lattice parameter a_{tx} and with lattice parameter a_0 are indistinguishable in the figure. When they are distinguishable, the a_0 electron distribution is identified with a text label. The thickness of each plot line is chosen to represent the numerical uncertainty of the calculated values.

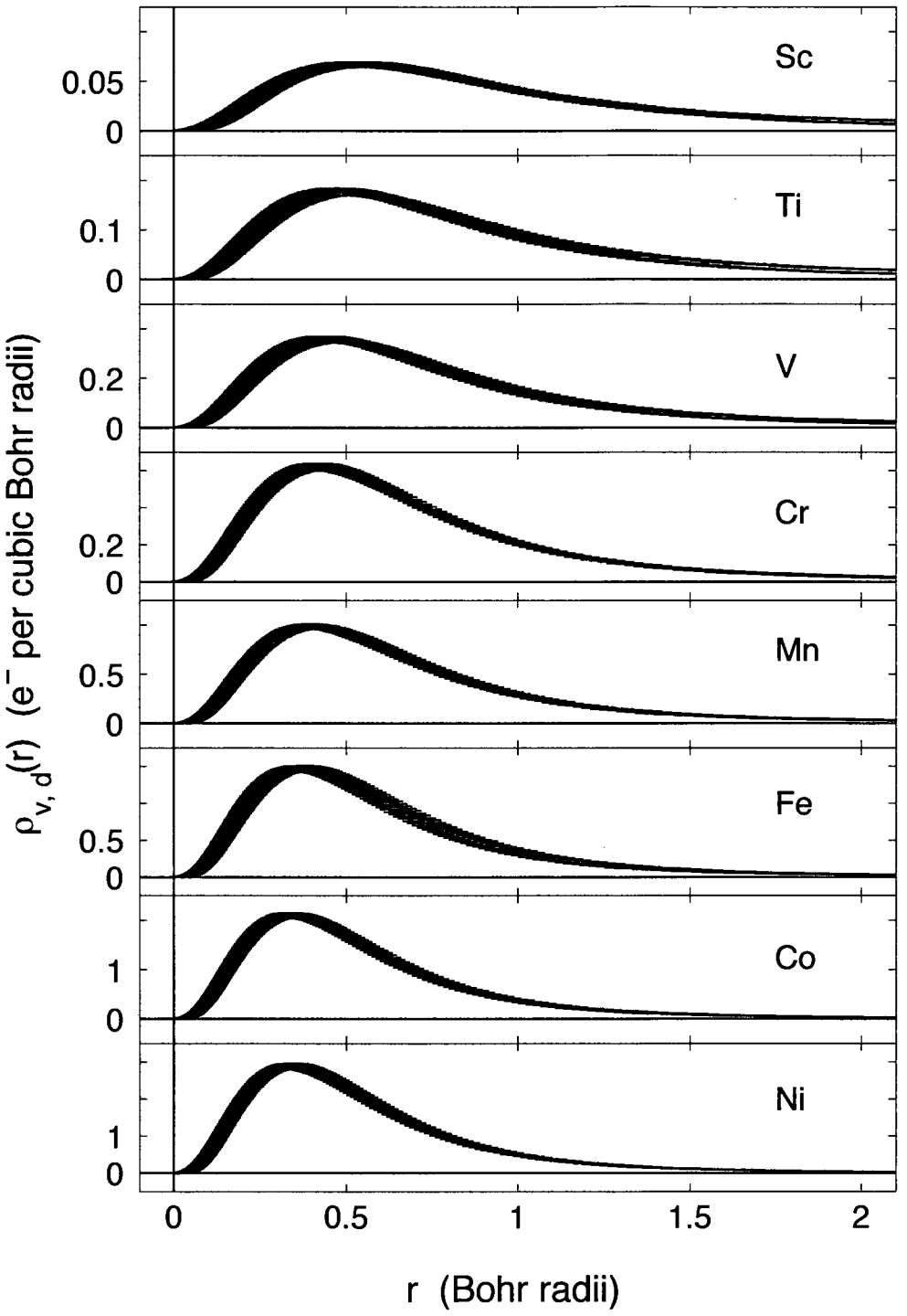

Figure 5.17: Calculated d-orbital components of the electron distributions of the NM FCC 3d metals, $\rho_{v,d}(|\vec{r}|)$ versus $|\vec{r}|$. The d-electron distributions of metals with lattice parameter a_{tx} and with lattice parameter a_0 are indistinguishable in the figure. The thickness of each plot line is chosen to represent the numerical uncertainty of the calculated values.

5.5 Summary and Future Work

We have shown that all FCC 3d metals from FCC Sc to FCC Ni undergo a volume-controlled LM-HM transition at some lattice parameter a_{tx}. In the metals FCC Sc to FCC Mn, a_{tx} is much larger than the zero-Kelvin lattice parameter a_0 of the metal. As a result, the LM-HM transition does not affect the thermal properties of these metals. However, in FCC Fe, a_{tx} is less than 2.5% larger than a_0. Because of this, the LM-HM transition in FCC Fe affects the thermal properties of the metal, even at zero pressure [11]. The properties of FCC-structured alloys containing Fe are also affected by this LM-HM transition (e.g. [9, 10]). Finally, a_{tx} is smaller than a_0 in FCC Co and FCC Ni. The thermal properties of these metals at zero pressure is not affected by their LM-HM transitions. However, if these metals are subjected to sufficiently large pressures, their thermal properties may be affected by their LM-HM transition. We predict that this will occur for FCC Co if the metal is located at a depth between $\approx$ 1000 km and $\approx$ 1100 km below the surface of the Earth, in the Earth's mantle. In contrast, we predict that FCC Ni should have large magnetic moments even if it is located at the center of the Earth. This latter result may have important implications in planetary science, as the common mineral constituents of iron meteorites, believed to have originated deep within the interiors of asteroids or planets, contain important quantities of nickel (see for example [127]).

We have also shown that the formation of magnetic moments in the FCC 3d metals brings about an increase in the kinetic energy of the metals' electrons and a decrease in the electrostatic energy of the metals. We illustrated that magnetic moments appear in a FCC 3d metal when their formation brings about an increase in the kinetic energy of the metal's electrons that is smaller than the corresponding decrease in the total electrostatic energy of the metal. This is consistent with published models of magnetic moment formation in metals [111, 112, 118–122]. Finally, we attempted to understand the conditions that must be met in order for magnetic moment formation to occur in the FCC 3d metals by studying the density of states functions $n_v(\epsilon)$ and the spatial distributions $\rho_v(\vec{r})$ of the valence electrons of the FCC 3d metals. We observed that when the lattice parameters of the FCC

3d metals are increased, the value of $n_v(E_F)$ increases. We also observed that the s- and p-orbital electrons of the FCC 3d metals move away from their atomic nuclei as their lattice parameters are increased. We believe that this may allow the electrostatic interaction of the metals' d-electrons to become more important, which should increase the reduction in electrostatic energy that accompanies the alignment of the spins of these electrons. At the lattice parameter a_{tx}, both the latter reduction in electrostatic energy and the value of $n_v(E_F)$ become sufficiently large to allow the formation of magnetic moments to occur.

It should be noted that the results highlighted in sections 5.2, 5.3 and 5.4 must be treated with some caution. As stated in section 5.1, the lattice parameters a_{tx} are obtained using the TB-LMTO ESC program in conjunction with exchange-correlation functional EXC1 (see table 2.1 of chapter 2). We expect that if the study of the FCC 3d metals conducted here were to be repeated using a different exchange-correlation functional, different values of the lattice parameters a_{tx} and a_0 would be obtained for all metals. In addition, recent theoretical studies of the magnetism of FCC Fe have revealed that this metal may possess magnetic moments arranged in non-collinear orientations at zero Kelvin (e.g. [128, 129]). We have made no attempt to study such non-collinear magnetic moment configurations in any of the FCC 3d metals. We expect that we would obtain different values of a_{tx} and a_0 for some of the FCC 3d metals if such non-collinear magnetic configurations were considered. Finally, the TB-LMTO ESC program calculates only the spherical average of the electron distribution of solids. We expect that an ESC program that is capable of calculating the angular components of the spatial distribution of a solid's electrons would provide information about the magnetic moment formation process that the TB-LMTO ESC program cannot. Nonetheless, we believe that the results of sections 5.2, 5.3 and 5.4 illustrate the key features of a real phenomenon that occurs in the FCC 3d metals.

In future investigations of the volume-controlled LM-HM transition of the FCC 3d metals, the effect of both the valence electrons and the core electrons of these metals in the magnetic moment formation process should be clearly elucidated. In addition, studies of the LM-HM transition of the 3d metals assuming that they possess different crystal structures, and studies of the LM-HM transition of other materials, should be undertaken.

5.6 Calculated $E_{tot}(a)$ and $\mu(a)$ Curves of FCC Sc to Ni

We present here the calculated $E_{tot}(a)$ and $\mu(a)$ curves of FCC Sc to FCC Ni, with the exception of FCC Fe and FCC Co. The $E_{tot}(a)$ and $\mu(a)$ curves of FCC Fe are shown respectively in figures 5.3 and 5.4, while those of FCC Co are shown in figures 5.1 and 5.2. The error bars in the figures showing the calculated $E_{tot}(a)$ curves denote the SCE's in the calculated values of these curves. These SCE's are shown in table 5.1.

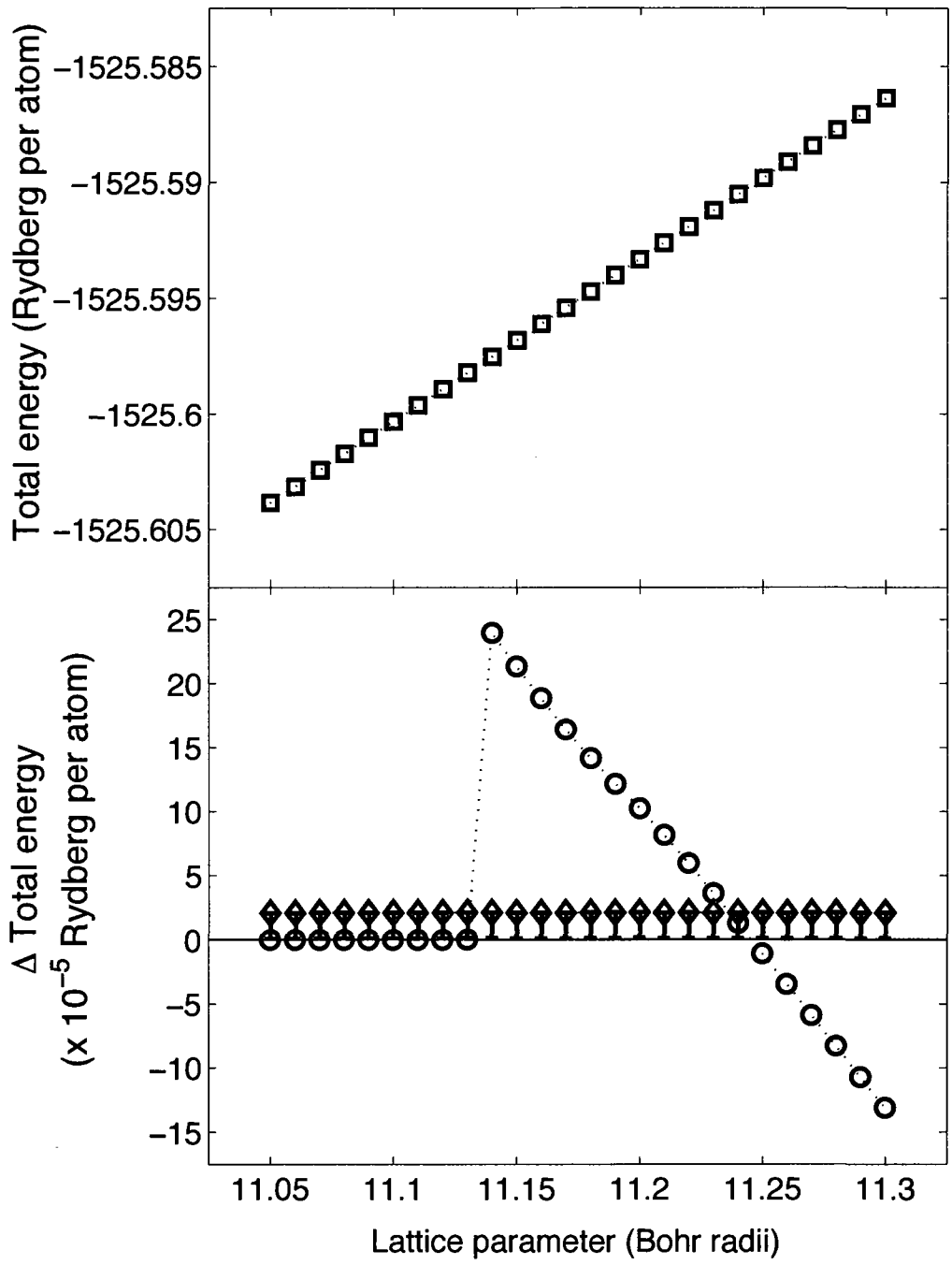

Figure 5.18: Minimum total energy versus lattice parameter curve $E_{tot}(a)$ of FCC Sc, calculated using the TB-LMTO ESC program as described in section 5.1. The upper figure shows the $E_{tot}(a)$ curve of NM FCC Sc only. The $E_{tot}(a)$ curves of AFM FCC Sc and of FM FCC Sc have been omitted as they are indistinguishable from that of NM FCC Sc on the scale of the figure. The lower figure shows the difference $\Delta E_{tot}(a)$ = AFM $E_{tot}(a)$ - NM $E_{tot}(a)$ (diamonds) and the difference $\Delta E_{tot}(a)$ = FM $E_{tot}(a)$ - NM $E_{tot}(a)$ (circles). Error bars indicate the SCE's in the difference $\Delta E_{tot}(a)$ = AFM $E_{tot}(a)$ - NM $E_{tot}(a)$. The figure reveals that FCC Sc undergoes a LM-HM transition at a lattice parameter a_{tx} between 11.24 and 11.25 Bohr radii.

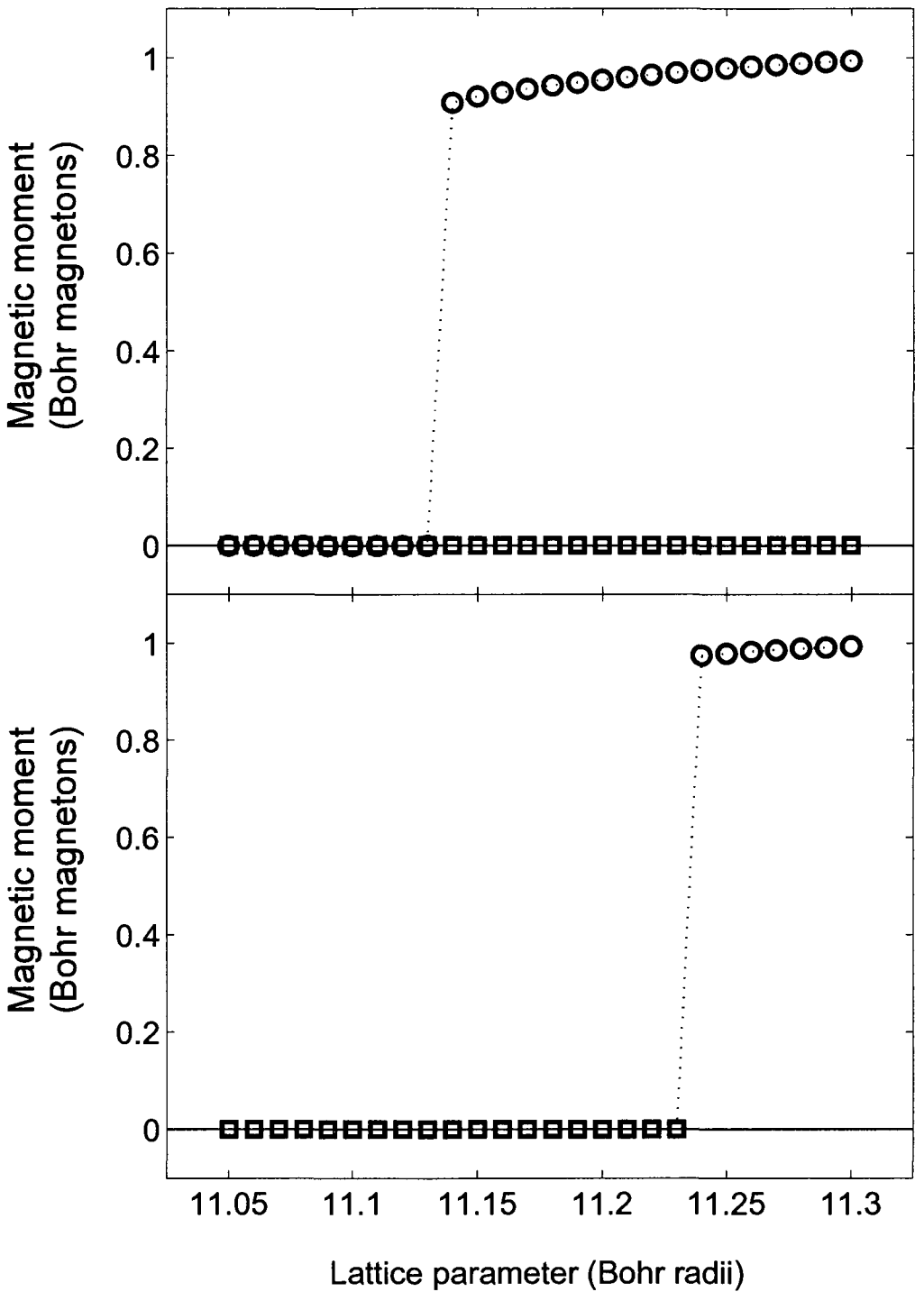

Figure 5.19: Magnetic moment versus lattice parameter curve $\mu(a)$ of FCC Sc, calculated using the TB-LMTO ESC program as described in section 5.1. The upper figure shows the $\mu(a)$ curve of NM FCC Sc (squares), and of FM FCC Sc (circles). The $\mu(a)$ curve of AFM FCC Sc has been omitted as it is indistinguishable from that of NM FCC Sc on the scale of the figure. The lower figure shows, at a given lattice parameter, the magnetic moment of FCC Sc when it takes its lowest-energy magnetic configuration. Squares (circles) indicate that the magnetic moment is that of NM (FM) FCC Sc.

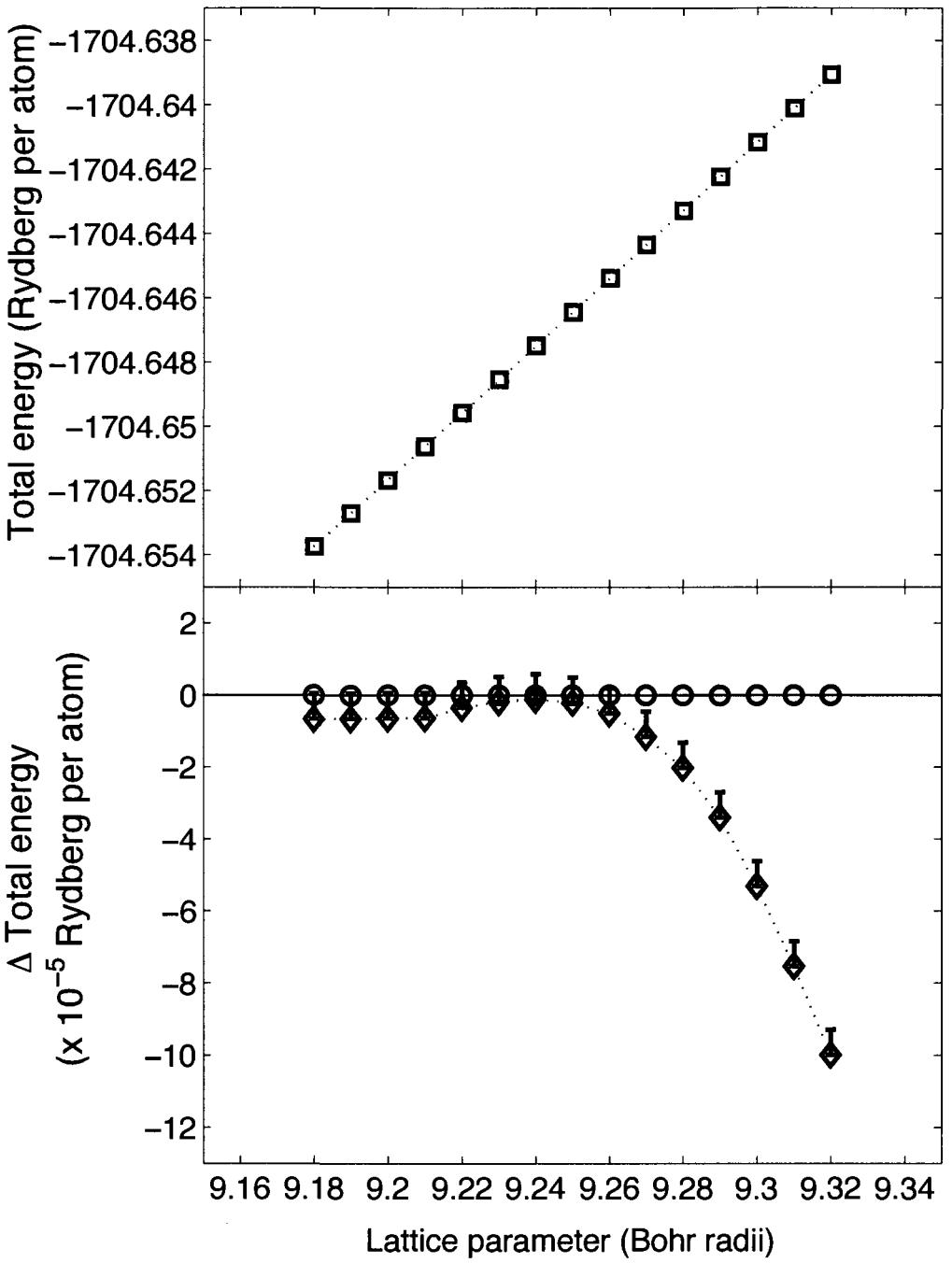

Figure 5.20: Minimum total energy versus lattice parameter curve $E_{tot}(a)$ of FCC Ti, calculated using the TB-LMTO ESC program as described in section 5.1. The upper figure shows the $E_{tot}(a)$ curve of NM FCC Ti only. The $E_{tot}(a)$ curves of FM FCC Ti and of AFM FCC Ti have been omitted as they are indistinguishable from that of NM FCC Ti on the scale of the figure. The lower figure shows the difference $\Delta E_{tot}(a)$ = AFM $E_{tot}(a)$ - NM $E_{tot}(a)$ (diamonds) and the difference $\Delta E_{tot}(a)$ = FM $E_{tot}(a)$ - NM $E_{tot}(a)$ (circles). Error bars indicate the SCE's in the difference $\Delta E_{tot}(a)$ = AFM $E_{tot}(a)$ - NM $E_{tot}(a)$. The figure reveals that FCC Ti undergoes a LM-HM transition at a lattice parameter a_{tx} between 9.26 and 9.27 Bohr radii.

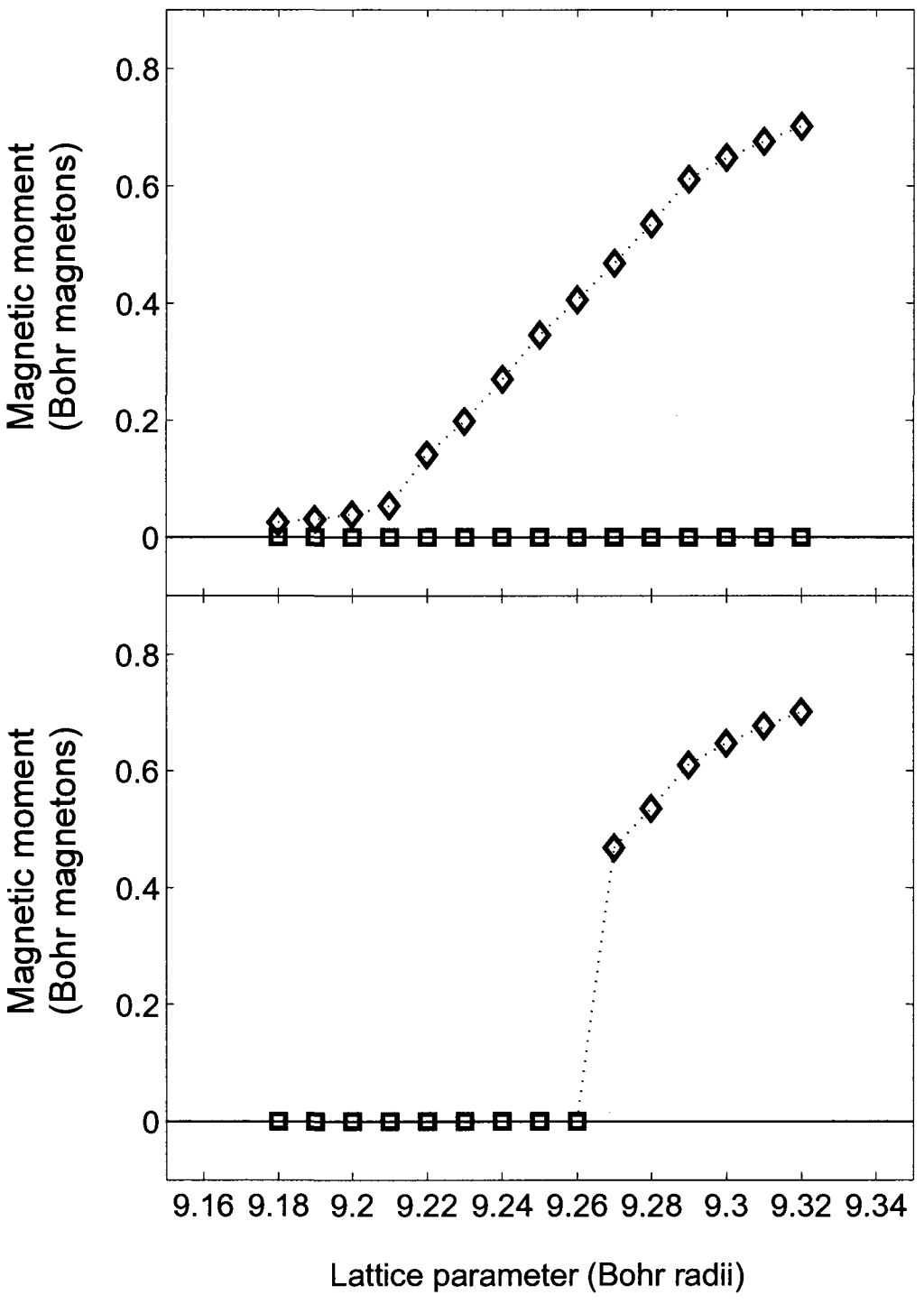

Figure 5.21: Magnetic moment versus lattice parameter curve $\mu(a)$ of FCC Ti, calculated using the TB-LMTO ESC program as described in section 5.1. The upper figure shows the $\mu(a)$ curve of NM FCC Ti (squares), and of AFM FCC Ti (diamonds). The $\mu(a)$ curve of FM FCC Ti has been omitted as it is indistinguishable from that of NM FCC Ti on the scale of the figure. The lower figure shows, at a given lattice parameter, the magnetic moment of FCC Ti when it takes its lowest-energy magnetic configuration. Squares (diamonds) indicate that the magnetic moment is that of NM (AFM) FCC Ti.

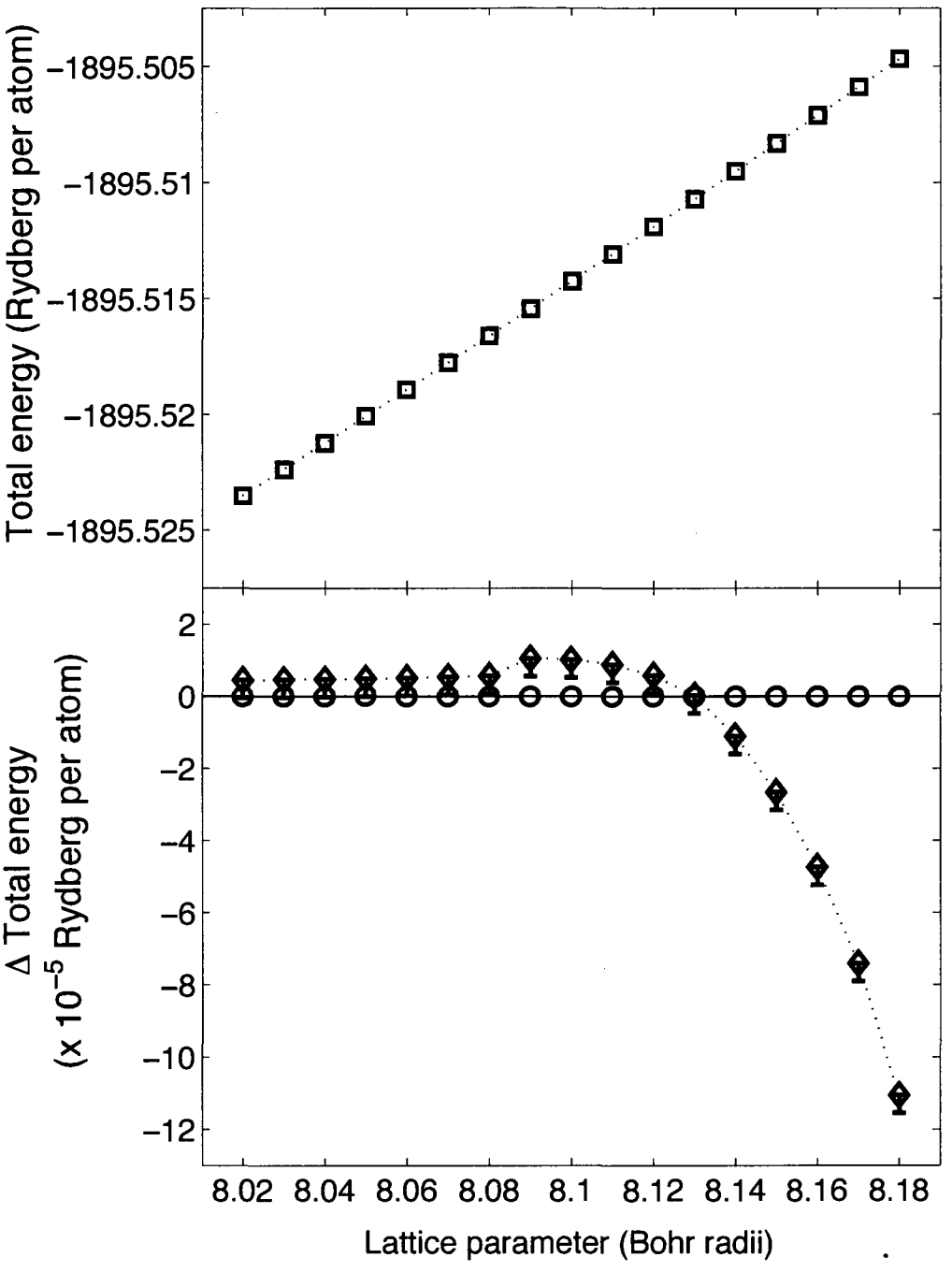

Figure 5.22: Minimum total energy versus lattice parameter curve $E_{tot}(a)$ of FCC V, calculated using the TB-LMTO ESC program as described in section 5.1. The upper figure shows the $E_{tot}(a)$ curve of NM FCC V only. The $E_{tot}(a)$ curve of FM FCC V and of AFM FCC V have been omitted as they are indistinguishable from that of NM FCC V on the scale of the figure. The lower figure shows the difference $\Delta E_{tot}(a)$ = AFM $E_{tot}(a)$ - NM $E_{tot}(a)$ (diamonds) and the difference $\Delta E_{tot}(a)$ = FM $E_{tot}(a)$ - NM $E_{tot}(a)$ (circles). Error bars indicate the SCE's in the difference $\Delta E_{tot}(a)$ = AFM $E_{tot}(a)$ - NM $E_{tot}(a)$. The figure reveals that FCC V undergoes a LM-HM transition at a lattice parameter a_{tx} between 8.13 and 8.14 Bohr radii.

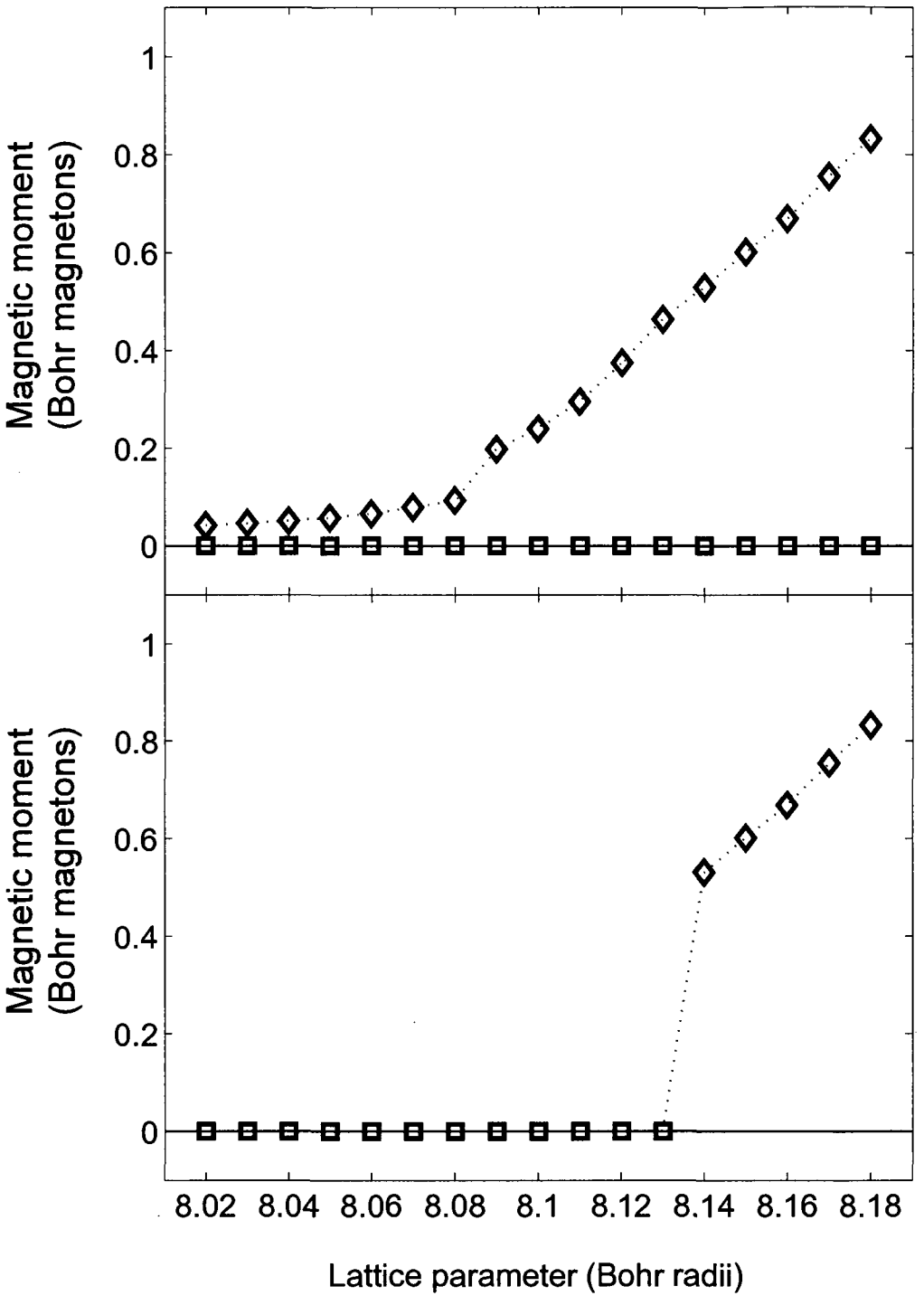

Figure 5.23: Magnetic moment versus lattice parameter curve $\mu(a)$ of FCC V, calculated using the TB-LMTO ESC program as described in section 5.1. The upper figure shows the $\mu(a)$ curve of NM FCC V (squares), and of AFM FCC V (diamonds). The $\mu(a)$ curve of FM FCC V has been omitted as it is indistinguishable from that of NM FCC V on the scale of the figure. The lower figure shows, at a given lattice parameter, the magnetic moment of FCC V when it takes its lowest-energy magnetic configuration. Squares (diamonds) indicate that the magnetic moment is that of NM (AFM) FCC V.

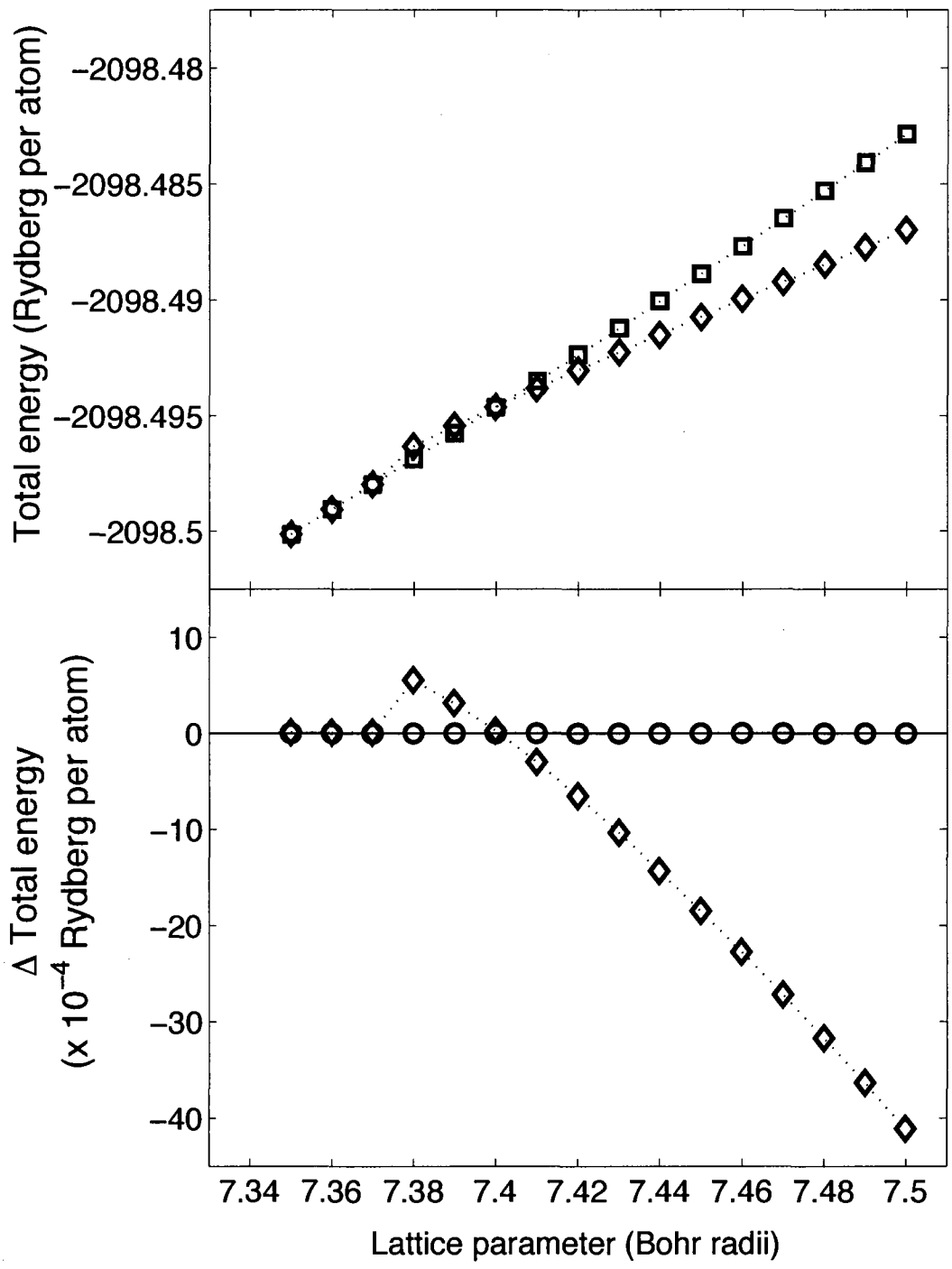

Figure 5.24: Minimum total energy versus lattice parameter curve $E_{tot}(a)$ of FCC Cr, calculated using the TB-LMTO ESC program as described in section 5.1. The upper figure shows the $E_{tot}(a)$ curve of NM FCC Cr (squares), and of AFM FCC Cr (diamonds). The $E_{tot}(a)$ curve of FM FCC Cr has been omitted as it is indistinguishable from that of NM FCC Cr on the scale of the figure. The lower figure shows the difference $\Delta E_{tot}(a)$ = AFM $E_{tot}(a)$ - NM $E_{tot}(a)$ (diamonds) and the difference $\Delta E_{tot}(a)$ = FM $E_{tot}(a)$ - NM $E_{tot}(a)$ (circles). The figure reveals that FCC Cr undergoes a LM-HM transition at a lattice parameter a_{tx} between 7.40 and 7.41 Bohr radii.

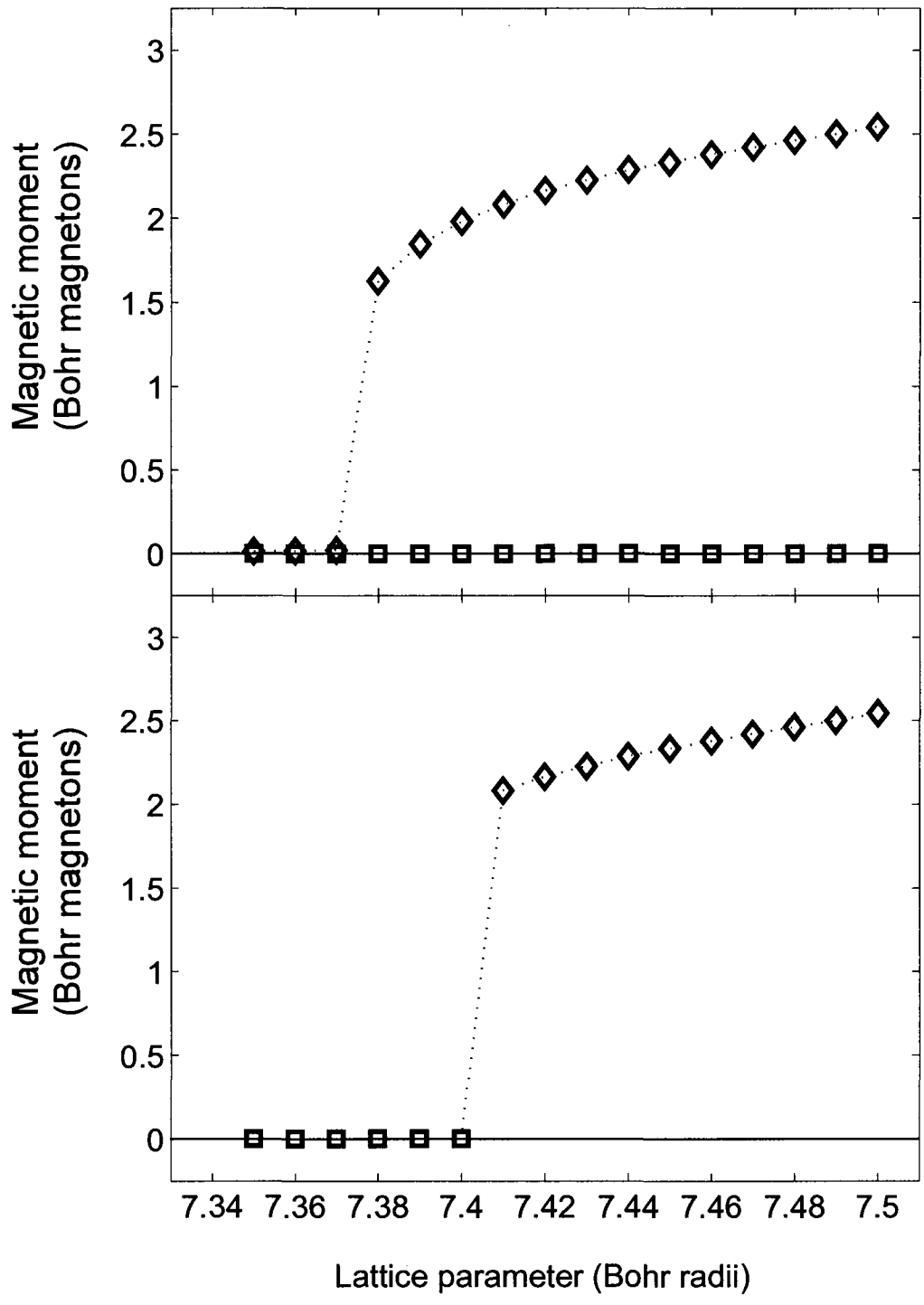

Figure 5.25: Magnetic moment versus lattice parameter curve $\mu(a)$ of FCC Cr, calculated using the TB-LMTO ESC program as described in section 5.1. The upper figure shows the $\mu(a)$ curve of NM FCC Cr (squares), and of AFM FCC Cr (diamonds). The $\mu(a)$ curve of FM FCC Cr has been omitted as it is indistinguishable from that of NM FCC Cr on the scale of the figure. The lower figure shows, at a given lattice parameter, the magnetic moment of FCC Cr when it takes its lowest-energy magnetic configuration. Squares (diamonds) indicate that the magnetic moment is that of NM (AFM) FCC Cr.

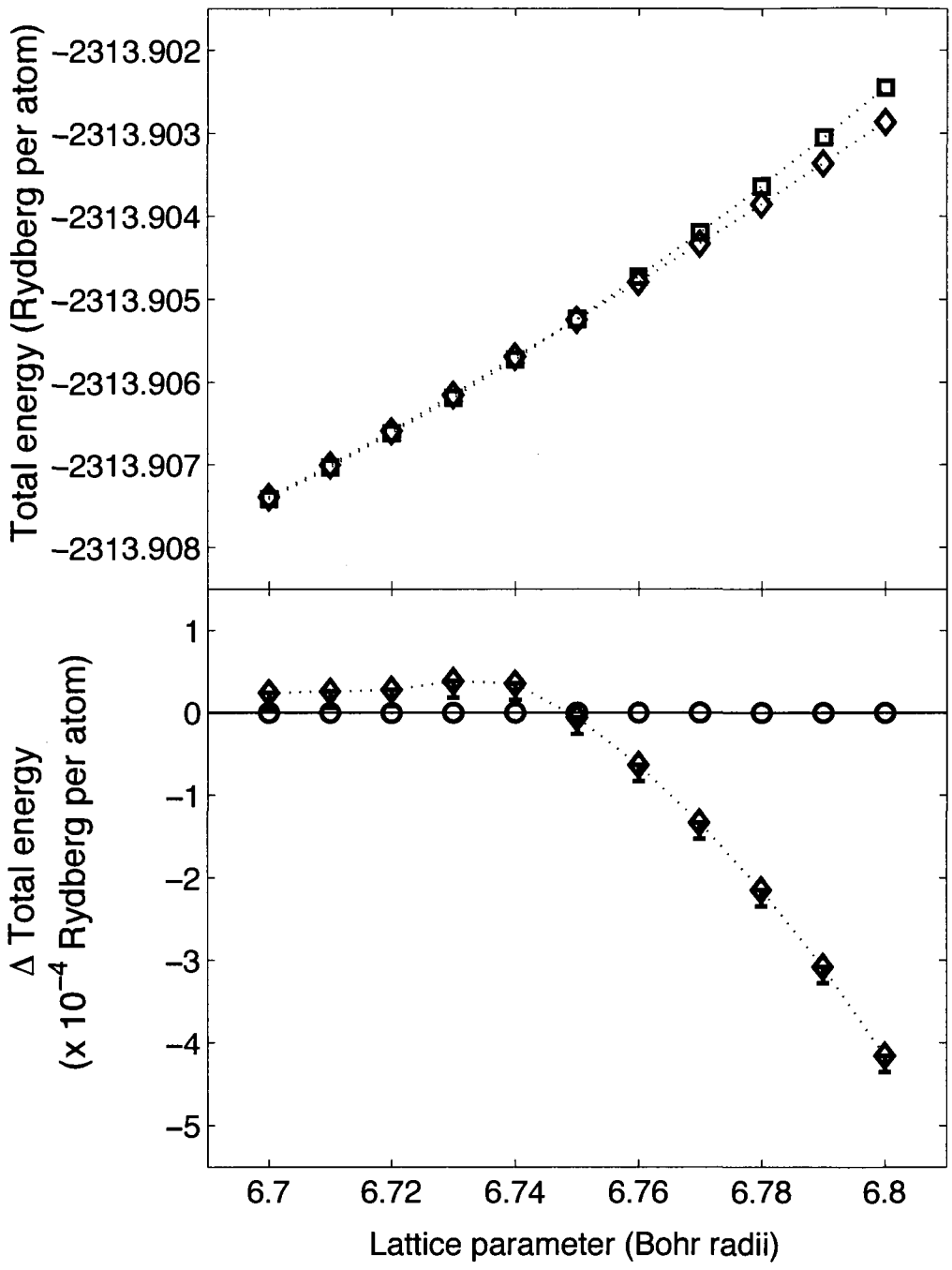

Figure 5.26: Minimum total energy versus lattice parameter curve $E_{tot}(a)$ of FCC Mn, calculated using the TB-LMTO ESC program as described in section 5.1. The upper figure shows the $E_{tot}(a)$ curve of NM FCC Mn (squares), and of AFM FCC Mn (diamonds). The $E_{tot}(a)$ curve of FM FCC Mn has been omitted as it is indistinguishable from that of NM FCC Mn on the scale of the figure. The lower figure shows the difference $\Delta E_{tot}(a) =$ AFM $E_{tot}(a)$ - NM $E_{tot}(a)$ (diamonds) and the difference $\Delta E_{tot}(a) =$ FM $E_{tot}(a)$ - NM $E_{tot}(a)$ (circles). Error bars indicate the SCE's in the difference $\Delta E_{tot}(a) =$ AFM $E_{tot}(a)$ - NM $E_{tot}(a)$. The figure reveals that FCC Mn undergoes a LM-HM transition at a lattice parameter a_{tx} between 6.74 and 6.75 Bohr radii.

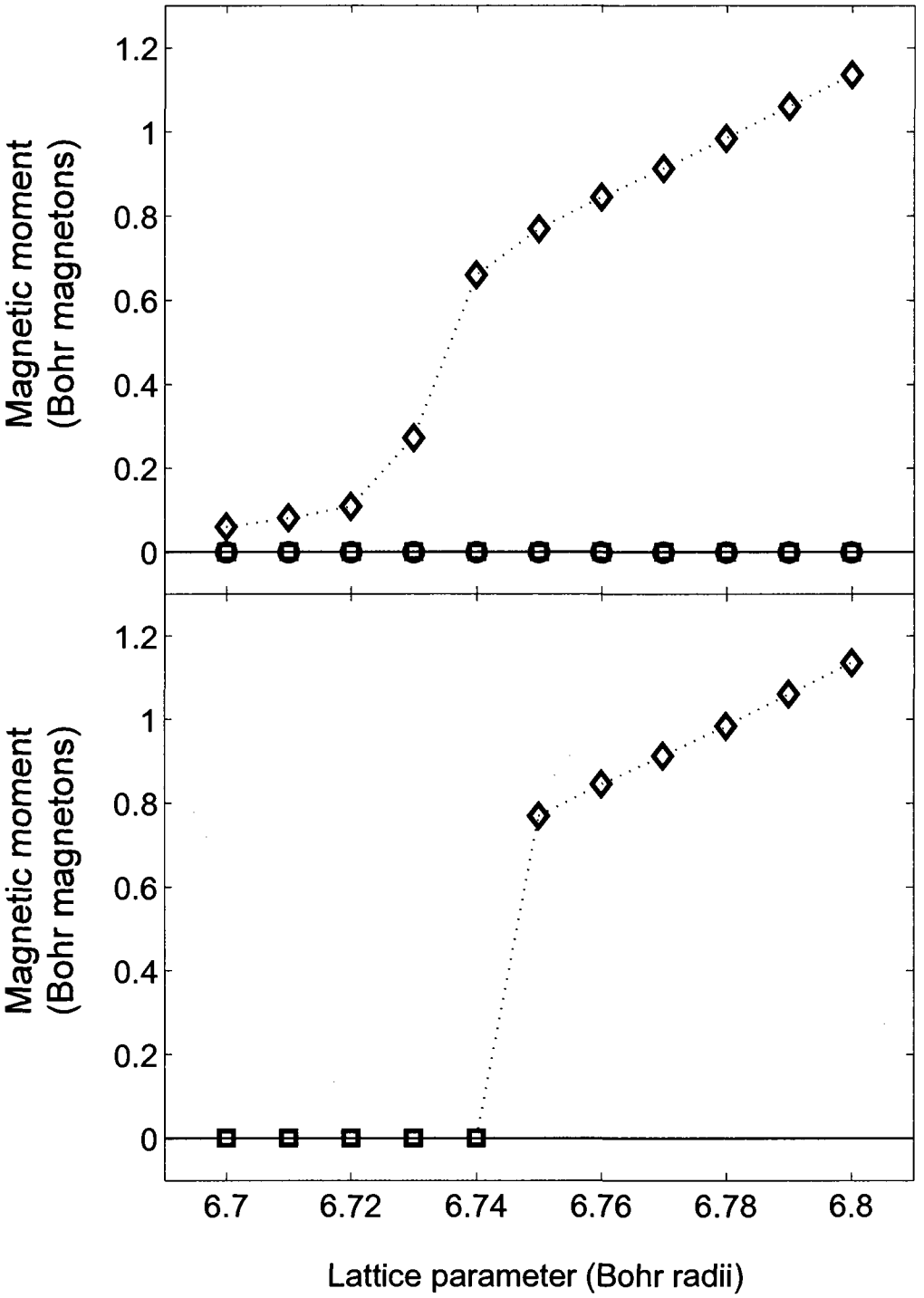

Figure 5.27: Magnetic moment versus lattice parameter curve $\mu(a)$ of FCC Mn, calculated using the TB-LMTO ESC program as described in section 5.1. The upper figure shows the $\mu(a)$ curve of NM FCC Mn (squares), and of AFM FCC Mn (diamonds). The $\mu(a)$ curve of FM FCC Mn has been omitted as it is indistinguishable from that of NM FCC Mn on the scale of the figure. The lower figure shows, at a given lattice parameter, the magnetic moment of FCC Mn when it takes its lowest-energy magnetic configuration. Squares (diamonds) indicate that the magnetic moment is that of NM (AFM) FCC Mn.

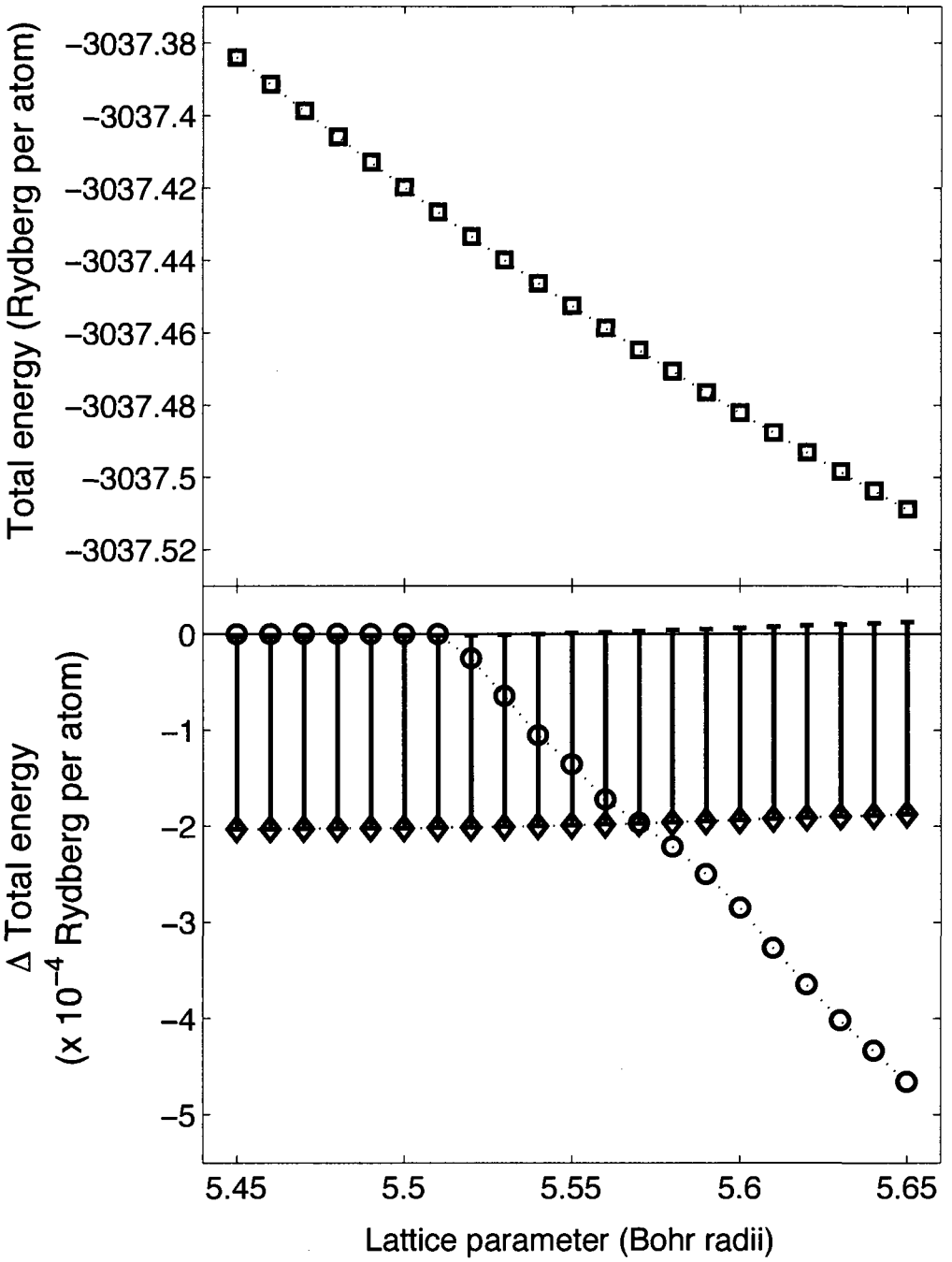

Figure 5.28: Minimum total energy versus lattice parameter curve $E_{tot}(a)$ of FCC Ni, calculated using the TB-LMTO ESC program as described in section 5.1. The upper figure shows the $E_{tot}(a)$ curve of NM FCC Ni only. The $E_{tot}(a)$ curve of FM FCC Ni and of AFM FCC Ni have been omitted as they are indistinguishable from that of NM FCC Ni on the scale of the figure. The lower figure shows the difference $\Delta E_{tot}(a)$ = AFM $E_{tot}(a)$ - NM $E_{tot}(a)$ (diamonds) and the difference $\Delta E_{tot}(a)$ = FM $E_{tot}(a)$ - NM $E_{tot}(a)$ (circles). Error bars indicate the SCE's in the difference $\Delta E_{tot}(a)$ = AFM $E_{tot}(a)$ - NM $E_{tot}(a)$. The figure reveals that FCC Ni undergoes a LM-HM transition at a lattice parameter a_{tx} between 6.57 and 6.58 Bohr radii.

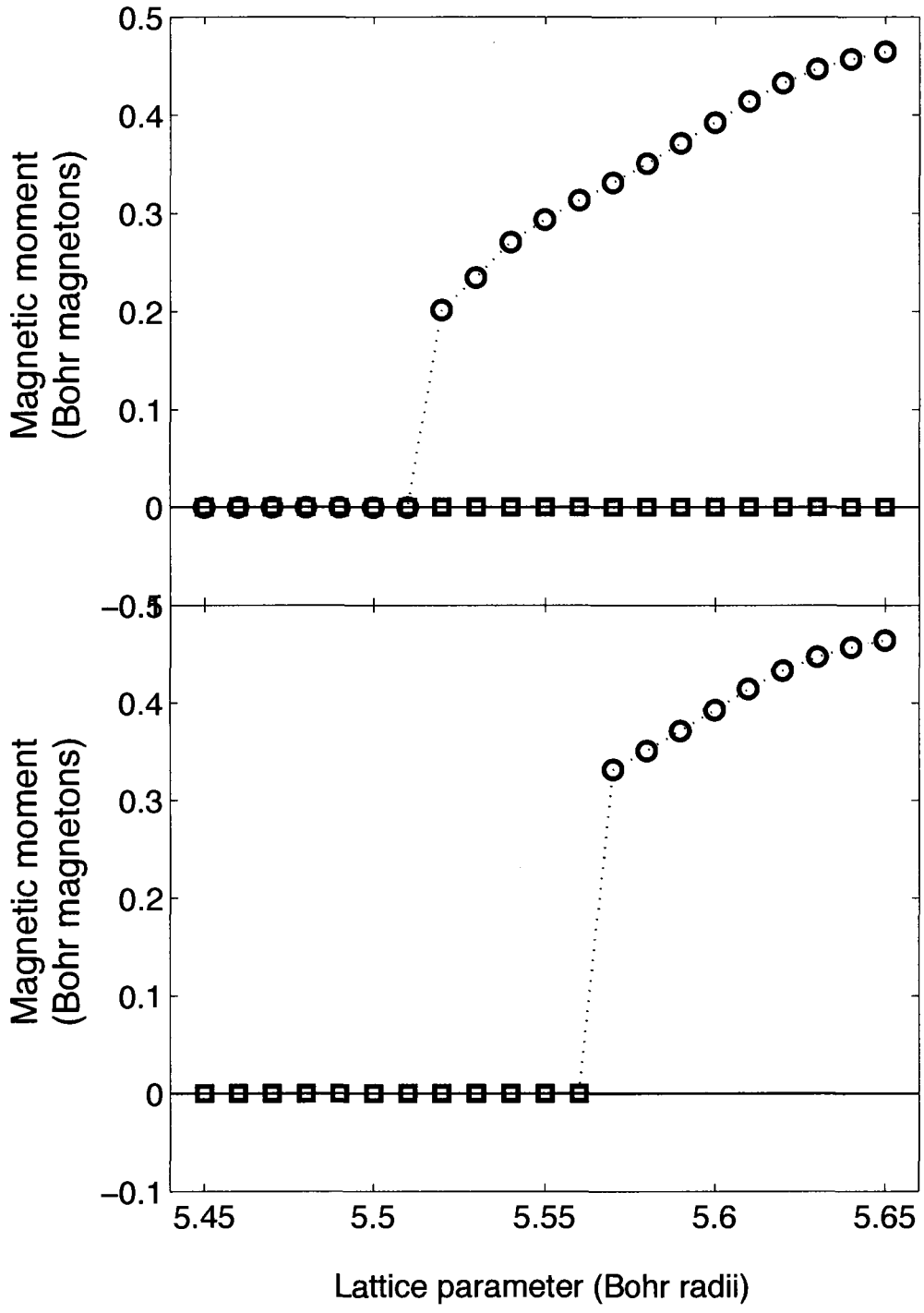

Figure 5.29: Magnetic moment versus lattice parameter curve $\mu(a)$ of FCC Ni, calculated using the TB-LMTO ESC program as described in section 5.1. The upper figure shows the $\mu(a)$ curve of NM FCC Ni (squares), and of FM FCC Ni (circles). The $\mu(a)$ curve of AFM FCC Ni has been omitted as it is indistinguishable from that of NM FCC Ni on the scale of the figure. The lower figure shows, at a given lattice parameter, the magnetic moment of FCC Ni when it takes its lowest-energy magnetic configuration. Squares (circles) indicate that the magnetic moment is that of NM (FM) FCC Ni.

Chapter 6

A Theoretical Method for Calculating the Helmholtz' Free Energy of Crystalline Solids

Having studied a number of the zero-Kelvin properties of the first-row transition metals, we begin, in this chapter, the development of a method for calculating the thermal properties of these metals. More specifically, we present here a method for calculating the Helmholtz' free energy as a function of atomic volume and temperature of an infinitely large (bulk), non-magnetic, crystalline solid consisting of one single atomic species. Knowledge of the Helmholtz' free energy function of a solid allows for the calculation of its non-zero temperature properties, like its equilibrium volume as a function of its temperature [76].

We intend that the method presented here be a first step in the development of a method for calculating the Helmholtz' free energy of complex magnetic materials, like metallic Fe and its alloys. Metallic Fe and some of its alloys, like the Invar and anti-Invar alloys, possess unconventional thermal properties and unconventional magnetic properties [9, 10, 102, 130–136]. We also intend that this method be useful for calculating the Helmholtz' free energy of materials under conditions of high pressure and temperature.

The method assumes only that an inter-atomic interaction potential $E_{a-a}(x)$ can be derived from the minimum total energy versus lattice parameter curve $E_{tot}(a)$ of a solid, and that this potential $E_{a-a}(x)$ can accurately reproduce the energy increase that occurs when the atomic nuclei of the solid move away from their mean equilibrium positions as they undergo small amplitude thermal oscillations. The method is entirely theoretical, as it makes use of the results of Chen, Chen and Wei [137] in deriving the potential $E_{a-a}(x)$ from the minimum total energy versus lattice parameter curve $E_{tot}(a)$ of a solid. (We shall discuss this in greater detail in sections 6.2 and 6.3.)

We thus begin, in section 6.1, with a brief discussion of the theoretical calculation of the Helmholtz' free energy of solids and the use of the Helmholtz' free energy of a solid to calculate its thermal properties. Then, in section 6.2, we provide a detailed description of a method for calculating the Helmholtz' free energy of a solid. In section 6.3, we discuss the major assumptions of the method, as well as the novelty of the method. Finally, in section 6.4, we discuss the validation of the method, which is the focus of the remainder of this thesis. Section 6.5 is a mathematical appendix to section 6.2.

6.1 Calculating the Thermal Properties of a Solid - General Considerations

Consider an infinitely large crystalline solid[1] consisting of one single chemical species in thermal equilibrium with its environment. Exchanges of energy, but not of material, are possible between the solid and its environment. Thus, the solid is in the "canonical situation" [76, p. 255]. In addition, because the solid under consideration is infinitely large, it consists of an infinity of atoms and electrons. It can therefore be said that this solid is a physical system in the "thermodynamic limit" [76, p. 280]. The solid in question, even though the number of its constituent atoms and its volume are infinite, has a finite

[1] We use the term "crystalline solid" to refer to a solid that has atoms with average positions defined by vectors $\left\langle \vec{R}_I \right\rangle$ which also define points on a crystal lattice.

atomic volume $v = \frac{V}{N}$, where N is the number of atoms in the solid and V is the volume of the solid. (If a solid's crystal structure can be specified using a single lattice parameter (ie. cubic solids), then v is uniquely defined in terms of this single lattice parameter. In contrast, more than one lattice parameter is needed to specify the crystal structure of some solids (ie. hexagonal solids). The atomic volume v of these solids is a function of all its lattice parameters.)

We wish to calculate the average value of some observable property A of the solid over a long period of time during which the solid is in thermal equilibrium with its environment at temperature T, and during which the solid has a constant atomic volume v. To do so, we must calculate [76, p. 29]:

$$\langle A(v,T)\rangle = \lim_{t_0\to\infty} \frac{1}{t_0} \int_{t_0} A(v,T,t)\, dt, \tag{6.1}$$

where $\langle A(v,T)\rangle$ represents the time-averaged value of a property A of a solid that has temperature T and atomic volume v. In equation 6.1, the integral is evaluated over a time interval of breadth t_0, and $A(v,T,t)$ is the value of the property A at time t when the solid has temperature T and atomic volume v. The property A changes with time as a result of the energy exchanged between the solid and its environment.

Because the time-variation of $A(v,T,t)$ can be described as a stationary statistical process, we can replace the time average of equation 6.1 with an average over the ensemble of quantum states that the solid can possess [76, p. 30], commonly termed the ensemble of "accessible microstates" of the solid [76, p. 12].[2] This is known as the "ergodic approximation" [76, p. 32]. Thus, the average value of the property A when the solid has temperature T and atomic volume v can be expressed as [76, p. 31]:

$$\langle A(v,T)\rangle = \sum_i A_i P_i(v,T), \tag{6.2}$$

where the sum is over all accessible microstates of the solid when it has volume v, A_i is the value of property A when the solid is in microstate i, and $P_i(v,T)$ is the probability that the solid is in microstate i when it has temperature T and atomic volume v.

[2]Diu et. al use the term "état microscopique" to designate a "microstate" [76, p.12].

In order to evaluate the average value of the property A using equation 6.2, the probabilities $P_i(v,T)$ must be known. These probabilities can be expressed as [76, p. 259]:

$$P_i(v,T) = \frac{1}{Z(v,T)} e^{-\frac{E_i}{k_B T}}, \tag{6.3}$$

where E_i is the energy of the solid when it is in microstate i, k_B is Boltzman's constant [76, p. 9], T is the temperature of the solid, and $Z(v,T)$ is termed the "partition function" of the solid [76, p. 260]. The partition function is simply the normalization factor of the probabilities $P_i(v,T)$. It is defined as [76, p. 260]:

$$Z(v,T) = \sum_i e^{-\frac{E_i}{k_B T}}, \tag{6.4}$$

where the summation runs over all accessible microstates of the solid when it has atomic volume v. The partition function of a solid is a function of its atomic volume v because the accessible microstates of a solid are different when it has different atomic volumes.

Knowing the partition function of the solid, the solid's Helmholtz' free energy function $F(v,T)$ can be defined as [76, p. 268]:

$$F(v,T) = -k_B T ln\left(Z(v,T)\right). \tag{6.5}$$

In equation 6.5, ln represents a natural logarithm and all other symbols are as in equation 6.3. Knowledge of the Helmholtz' free energy function of a solid makes possible the calculation of the atomic volume of the solid when it is in thermal equilibrium at temperature T and when its volume is unconstrained. The pressure that must be applied to a solid to maintain its atomic volume at a value v_0 is [76, p. 273]:

$$p(v_0,T) = -\frac{1}{N}\frac{\delta}{\delta v} F(v,T)\Big|_{v=v_0}, \tag{6.6}$$

where $\frac{\delta}{\delta v} F(v,T)\big|_{v=v_0}$ denotes the partial derivative of the function $F(v,T)$ with respect to the atomic volume v, evaluated at $v = v_0$.[3] When a solid's volume is unconstrained,

[3]Equation 6.6 is a general equation for an isotropic pressure applied to a solid possessing any crystal structure as long as the differential δv represents an infinitesimal change in the volume of the solid under an applied isotropic pressure. This is so if $\delta v = 3a^2\delta a$ when the solid has the simple cubic structure, if $\delta v = \frac{3}{4}a^2\delta a$ when the solid has the FCC structure, and if $\delta v = 2ab\delta a + a^2\delta b$ when the solid has a rectangular structure.

the pressure that is applied to the solid is $p(v,T) = 0$. Therefore, to calculate the atomic volume v of a free solid in thermal equilibrium with its environment at temperature T, we must calculate the atomic volume v at which its Helmholtz' free energy function $F(v,T)$ is minimised.

6.2 Calculating the Helmholtz' Free Energy of a Crystalline Solid

We now describe a method for calculating the Helmholtz' free energy function $F(v,T)$ of an infinitely large (bulk), non-magnetic, crystalline solid consisting of an infinite number of atoms of a single chemical species. This requires that we first identify the accessible microstates of the solid and calculate their energy. Then, we must calculate the partition function of the solid and evaluate its Helmholtz' free energy $F(v,T)$ as per equations 6.4 and 6.5.

6.2.1 The Microstates of a Solid and Their Energy

Each microstate of a solid is a quantum state of the solid [76, p. 12]. Thus, all microstates of the solid are eigenstates of the solid's Hamiltonian, which can be expressed as:

$$H_{tot} = \sum_I \frac{\vec{P}_I^{\,2}}{2M_I} + \sum_i \frac{\vec{p}_i^{\,2}}{2m} + U\left((\ldots), \vec{R}_I, (\ldots), \vec{r}_i, (\ldots)\right). \tag{6.7}$$

In equation 6.7, the summation over I runs over all atomic nuclei in the solid, while the summation over i runs over all electrons in the solid. In addition, the first term of the equation is the operator giving the total kinetic energy of the solid's atomic nuclei, the second term is the operator giving the total kinetic energy of the solid's electrons, and the potential $U\left((\ldots), \vec{R}_I, (\ldots), \vec{r}_i, (\ldots)\right)$ is the result of the electrostatic interaction between each pair of electrons in the solid, between each pair of atomic nuclei in the solid, and between each electron and each atomic nucleus in the solid. This potential is a function of

only the positions of the solid's atomic nuclei, specified by vectors $\vec{R}_I$, and the positions of the solid's electrons, specified by vectors $\vec{r}_i$. The Hamiltonian H_{tot} is discussed in greater detail in section 2.1.1 of chapter 2.

The process of finding the eigenstates of the Hamiltonian of a crystalline solid can be simplified by considering the physical processes occurring within such a solid. In a crystalline solid, the majority of the atomic nuclei remain in the vicinity of their mean positions, specified by vectors $\left\langle \vec{R}_I \right\rangle$ [37,78]. The vectors $\left\langle \vec{R}_I \right\rangle$ define points on a Bravais lattice [37,78]. In addition, when the solid is in thermal equilibrium at temperature T, energy can be transferred between the solid's environment and the solid's atomic nuclei and electrons. Because they are fermions, the state of the solid's electrons is only minutely affected by the energy that is transferred between the solid and its environment [37,78]. Most of the energy that is transferred to and from the solid is transferred to and from the solid's atomic nuclei in the form of kinetic energy [138, p. 646]. As a result, the solid's atomic nuclei oscillate about their mean positions.

We therefore find the eigenstates of H_{tot} by expressing it as follows:

$$H_{tot} = H_{vib} + H'_{tot}, \tag{6.8}$$

where:

$$H'_{tot} = \sum_i \frac{\vec{p}_i^{\,2}}{2m} + U\left((\ldots), \left\langle \vec{R}_I \right\rangle, (\ldots), \vec{r}_i, (\ldots)\right), \tag{6.9}$$

and:

$$H_{vib} = \sum_I \frac{\vec{P}_I^{\,2}}{2M_I} + U_{vib}\left((\ldots), \left\langle \vec{R}_I \right\rangle + \Delta\vec{R}_I, (\ldots)\right). \tag{6.10}$$

The Hamiltonian H'_{tot} gives the total energy of the solid when its atomic nuclei remain stationary at their mean positions, defined by vectors $\left\langle \vec{R}_I \right\rangle$. We use H'_{tot} to calculate the eigenstates $|\Psi(v)\rangle$ of the solid's electrons. The potential $U\left((\ldots), \left\langle \vec{R}_I \right\rangle, (\ldots), \vec{r}_i, (\ldots)\right)$ appearing in H'_{tot} is the result of the electrostatic interaction between each pair of electrons in the solid, between each pair of atomic nuclei in the solid, and between each electron and each atomic nucleus in the solid when these atomic nuclei remain stationary at their

mean positions $\left\langle \vec{R}_I \right\rangle$. H_{vib} gives the energy of the solid's atomic nuclei as they oscillate about their mean positions $\left\langle \vec{R}_I \right\rangle$ in a "vibration potential" $U_{vib}\left((\ldots), \left\langle \vec{R}_I \right\rangle + \Delta\vec{R}_I, (\ldots)\right)$. We shall discuss the vibration potential in greater detail later. We use H_{vib} to calculate the eigenstates $|\Theta(v)\rangle$ of the solid's atomic nuclei. Each eigenstate $|\Phi(v)\rangle$ of H_{tot} can thus be expressed as:

$$|\Phi(v)\rangle = |\Psi(v)\rangle \otimes |\Theta(v)\rangle, \tag{6.11}$$

where $\otimes$ denotes a tensor product. The eigenstates and eigenvalues of the Hamiltonian H_{tot} can be expressed as functions of the solid's atomic volume v because the vectors $\left\langle \vec{R}_I \right\rangle$ appearing in the Hamiltonians H'_{tot} and H_{vib} are defined for a solid possessing a specific atomic volume.

The process of finding the eigenstates $|\Psi(v)\rangle$ of H'_{tot} is discussed in detail in chapter 2 of this thesis. In this latter chapter, we indicate that an electronic structure calculation (ESC) program can be used to calculate the lowest energy eigenstate and smallest eigenvalue of the Hamiltonian H'_{tot}. We propose that all accessible eigenstates of H_{tot} can be expressed as:

$$|\Phi(v)\rangle = |\Psi_{min}(v)\rangle \otimes |\Theta(v)\rangle, \tag{6.12}$$

where $|\Psi_{min}(v)\rangle$ is the lowest-energy eigenstate of the Hamiltonian H'_{tot}. In doing so, we implicitly assume that, when a solid is in thermal equilibrium with its environment, all the energy that is transfered between the solid and its environment is transferred to and from the solid's atomic nuclei only. As this occurs, the solid's electrons remain configured, on average, as though the solid's atomic nuclei remain stationary at their mean positions $\left\langle \vec{R}_I \right\rangle$, in the lowest energy configuration that is available to them under these circumstances. We shall discuss this assumption in greater detail in section 6.3.

To find the eigenstates $|\Theta(v)\rangle$ of the solid's atomic nuclei, we must have a clear definition of the vibration potential $U_{vib}\left((\ldots), \left\langle \vec{R}_I \right\rangle + \Delta\vec{R}_I, (\ldots)\right)$. We define the vibration potential as:

$$U_{vib}\left((\ldots), \left\langle \vec{R}_I \right\rangle + \Delta\vec{R}_I, (\ldots)\right) = E_{tot}\left((\ldots), \left\langle \vec{R}_I \right\rangle + \Delta\vec{R}_I, (\ldots)\right) - E_{tot}\left((\ldots), \left\langle \vec{R}_I \right\rangle, (\ldots)\right), \tag{6.13}$$

where $E_{tot}\left(\left(\ldots\right),\left\langle \vec{R}_I \right\rangle + \Delta\vec{R}_I,\left(\ldots\right)\right)$ is the minimum total energy of a solid when its atomic nuclei are stationary at positions $\vec{R}_I = \left\langle \vec{R}_I \right\rangle + \Delta\vec{R}_I$, and $E_{tot}\left(\left(\ldots\right),\left\langle \vec{R}_I \right\rangle,\left(\ldots\right)\right)$ is the minimum total energy of the solid when its atomic nuclei remain stationary at their mean positions $\left\langle \vec{R}_I \right\rangle$. $U_{vib}\left(\left(\ldots\right),\left\langle \vec{R}_I \right\rangle + \Delta\vec{R}_I,\left(\ldots\right)\right)$ is therefore the increase in energy that occurs when all of the atomic nuclei in the solid are located a small displacement $\Delta\vec{R}_I$ away from their mean positions $\left\langle \vec{R}_I \right\rangle$. This energy increase is the combined result of:

1. any changes in the electrostatic interaction of the atomic nuclei of the solid that occur when its atomic nuclei are displaced from their mean positions $\left\langle \vec{R}_I \right\rangle$,
2. any changes in the electrostatic interaction of the electrons of the solid that occur when its atomic nuclei are displaced from their mean positions $\left\langle \vec{R}_I \right\rangle$,
3. any changes in the electrostatic interaction between the atomic nuclei and the electrons of the solid that occur when its atomic nuclei are displaced from their mean positions $\left\langle \vec{R}_I \right\rangle$, and
4. any changes in the kinetic energy of the electrons of the solid that occur when its atomic nuclei are displaced from their mean positions $\left\langle \vec{R}_I \right\rangle$.

We indicated in the introduction of this chapter that the method presented here assumes that an inter-atomic interaction potential $E_{a-a}\left(x\right)$ can be derived from the minimum total energy versus lattice parameter curve $E_{tot}\left(a\right)$ of a solid and that this potential $E_{a-a}\left(x\right)$ can accurately reproduce the energy increase that occurs when the atomic nuclei of the solid move away from their mean equilibrium positions as they undergo small amplitude thermal oscillations. By this, we mean that $U_{vib}\left(\left(\ldots\right),\left\langle \vec{R}_I \right\rangle + \Delta\vec{R}_I,\left(\ldots\right)\right)$ can be accurately expressed in terms of an inter-atomic interaction potential $E_{a-a}\left(x\right)$ that can be derived from the $E_{tot}\left(a\right)$ curve of a solid using the results of Chen, Chen and Wei [137]. To do so, we first consider a solid which has atomic volume v and which has I^{th} and J^{th} atomic nuclei respectively located at their mean positions $\left\langle \vec{R}_I \right\rangle$ and $\left\langle \vec{R}_J \right\rangle$. We express the minimum total energy of the solid when its atomic nuclei remain stationary at their mean

positions, $E_{tot}\left((\ldots),\left\langle\vec{R}_I\right\rangle,(\ldots)\right)$, in terms of $E_{a-a}(x)$ as follows:[4]

$$E_{tot}\left((\ldots),\left\langle\vec{R}_I\right\rangle,(\ldots)\right)=\frac{1}{2}\sum_I\sum_{J\neq I}E_{a-a}\left(\left|\left\langle\vec{R}_I\right\rangle-\left\langle\vec{R}_J\right\rangle\right|\right). \tag{6.14}$$

The implicit assumptions that are made in expressing $E_{tot}\left((\ldots),\left\langle\vec{R}_I\right\rangle,(\ldots)\right)$ in terms of $E_{a-a}(x)$ shall be discussed in section 6.3. For now, it must simply be recalled that $E_{tot}\left((\ldots),\left\langle\vec{R}_I\right\rangle,(\ldots)\right)$ is the smallest eigenvalue of the Hamiltonian H'_{tot} given in equation 6.9, and that it can be calculated using an ESC program. Consider now the same solid but with I^{th} and J^{th} atomic nuclei still stationary but located at positions defined by the vectors $\vec{R}_I=\left\langle\vec{R}_I\right\rangle+\Delta\vec{R}_I$ and $\vec{R}_J=\left\langle\vec{R}_J\right\rangle+\Delta\vec{R}_J$. We express the energy of the solid under these conditions as:

$$E_{tot}\left((\ldots),\left\langle\vec{R}_I\right\rangle+\Delta\vec{R}_I,(\ldots)\right)=\frac{1}{2}\sum_I\sum_{J\neq I}E_{a-a}\left(\left|\left\langle\vec{R}_I\right\rangle+\Delta\vec{R}_I-\left\langle\vec{R}_J\right\rangle-\Delta\vec{R}_J\right|\right). \tag{6.15}$$

The potential $U_{vib}\left((\ldots),\left\langle\vec{R}_I\right\rangle+\Delta\vec{R}_I,(\ldots)\right)$, as defined in equation 6.13, is simply the difference of equations 6.15 and 6.14, namely:

$$\begin{aligned}U_{vib}\left((\ldots),\left\langle\vec{R}_I\right\rangle+\Delta\vec{R}_I,(\ldots)\right) &= \frac{1}{2}\sum_I\sum_{J\neq I}E_{a-a}\left(\left|\left\langle\vec{R}_I\right\rangle+\Delta\vec{R}_I-\left\langle\vec{R}_J\right\rangle-\Delta\vec{R}_J\right|\right)\\ &- \frac{1}{2}\sum_I\sum_{J\neq I}E_{a-a}\left(\left|\left\langle\vec{R}_I\right\rangle-\left\langle\vec{R}_J\right\rangle\right|\right).\end{aligned} \tag{6.16}$$

The inter-atomic interaction potential $E_{a-a}(x)$ can be obtained from the minimum total energy versus lattice parameter curve $E_{tot}(a)$ of the solid [137], which itself can be calculated using an ESC program. Specifically, the minimum total energy versus lattice parameter curve of a crystalline solid can be expressed as [137]:

$$E_{tot}(x)=\frac{N}{2}\sum_{n=1}^{\infty}r[n]\,E_{a-a}(b[n]\,x). \tag{6.17}$$

[4]In the paper of Chen, Chen and Wei [137], it is the cohesive energy $E_{coh}(a)$ of a solid, and not its total energy $E_{tot}(a)$, that is expressed in terms of a pair-wise inter-atomic interaction potential $E_{a-a}(x)$. Because $E_{coh}(a)=E_{tot}(a)-N\,E_{atom}$, where N is the number of atoms in the solid and E_{atom} is the energy of one of the solid's atoms when it is in its free state, it can be shown that a potential $E_{a-a}(x)$ constructed using $E_{coh}(a)$ has the same functional form as a potential $E_{a-a}(x)$ constructed using $E_{tot}(a)$, only shifted vertically by a constant proportional to E_{atom}.

To understand equation 6.17, it must be understood that it is simply an alternative form of equation 6.14. In equation 6.17, x is the smallest distance separating any pair of atomic nuclei in the solid. In crystalline solids, there is a straightforward relationship between x and the solid's lattice parameter a. Thus, $b[1]x = x$ is the distance between a specific atomic nucleus, termed a "reference atom", and its nearest neighbouring atomic nuclei. Similarly, $b[n]x$ is the distance separating the reference atom from its n^{th} nearest neighbours. Finally, $r[n]$ is the number of atomic nuclei located a distance $b[n]x$ away from the reference atom. Having understood that the minimum total energy of the solid can be expressed in this way, the inter-atomic interaction potential $E_{a-a}(x)$ can be expressed as [137]:

$$E_{a-a}(x) = \frac{2}{N}\sum_{n=1}^{\infty} I[n]\left(E_{tot}\left(b[n]x\right)\right), \tag{6.18}$$

where the coefficients $I[n]$ can be expressed as a function of the quantities $r[n]$ and $b[n]$ appearing in equation 6.17 [137].

The process of finding the eigenstates $|\Theta(v)\rangle$ of H_{vib} can be simplified by constructing the Taylor expansion of $U_{vib}\left((\ldots), \left\langle \vec{R}_I \right\rangle + \Delta\vec{R}_I, (\ldots)\right)$, treating it as a function of the components ΔR_{Ix}, ΔR_{Iy}, and ΔR_{Iz} of all vectors $\Delta\vec{R}_I$. The zeroth-order, first-order and second-order terms of this Taylor expansion are given in section 6.5 of this chapter. All terms of the Taylor expansion of $U_{vib}\left((\ldots), \left\langle \vec{R}_I \right\rangle + \Delta\vec{R}_I, (\ldots)\right)$ are defined in terms of only the mean positions of the solid's atomic nuclei, specified by the vectors $\left\langle \vec{R}_I \right\rangle$, and the potential $E_{a-a}(x)$ and its derivatives. Because the minimum total energy versus lattice parameter curve of a solid can be calculated from first principles using an ESC program, the inter-atomic interaction potential $E_{a-a}(x)$ can be obtained entirely theoretically via equation 6.18. Thus, all terms of the Taylor expansion of the potential $U_{vib}\left((\ldots), \left\langle \vec{R}_I \right\rangle + \Delta\vec{R}_I, (\ldots)\right)$ can be obtained theoretically.

Having defined the vibration potential $U_{vib}\left((\ldots), \left\langle \vec{R}_I \right\rangle + \Delta\vec{R}_I, (\ldots)\right)$, we now present two methods for finding the eigenstates $|\Theta(v)\rangle$ of the Hamiltonian H_{vib} and for calculating the Helmholtz' free energy function $F(v,T)$ of a solid.

6.2.2 F (v, T) Curve of a Solid - Mean-Field Potential Method

The simplest method for finding the eigenstates $|\Theta(v)\rangle$ of H_{vib} requires that we take the spherical average of the vibration potential $U_{vib}\left((\ldots),\left\langle\vec{R}_I\right\rangle+\Delta\vec{R}_I,(\ldots)\right)$. As shown in section 6.2.1, $U_{vib}\left((\ldots),\left\langle\vec{R}_I\right\rangle+\Delta\vec{R}_I,(\ldots)\right)$ is a complex function of the displacements $\Delta\vec{R}_I$ of the solid's atomic nuclei from their mean positions. A simpler expression for $U_{vib}\left((\ldots),\left\langle\vec{R}_I\right\rangle+\Delta\vec{R}_I,(\ldots)\right)$ can be obtained by taking the spherical average of all displacements $\Delta\vec{R}_I$. To do so, we must evaluate:

$$\left\langle U_{vib}\left((\ldots),\left\langle\vec{R}_I\right\rangle+\Delta\vec{R}_I,(\ldots)\right)\right\rangle\Big|_{(\ldots),\theta_I,\phi_I,(\ldots)}=$$

$$(\ldots)\int_{\theta_I=0}^{2\pi}\int_{\phi_I=0}^{\pi}\frac{\{sin(\phi_I)\,d\theta_I d\phi_I\}}{4\pi}(\ldots)\,U_{vib}\left((\ldots),\left\langle\vec{R}_I\right\rangle+\Delta\vec{R}_I,(\ldots)\right), \tag{6.19}$$

where the angles θ_I and ϕ_I are the angles defining the direction of the vector $\Delta\vec{R}_I$ in spherical coordinates. We label $\left\langle U_{vib}\left((\ldots),\left\langle\vec{R}_I\right\rangle+\Delta\vec{R}_I,(\ldots)\right)\right\rangle\Big|_{(\ldots),\theta_I,\phi_I,(\ldots)}$ the potential $U_{vib}\left((\ldots),\left\langle\vec{R}_I\right\rangle+\Delta\vec{R}_I,(\ldots)\right)$ when all displacements $\Delta\vec{R}_I$ are spherically averaged.

When the spherical average defined in equation 6.19 is performed on the first-order and second-order terms of the Taylor expansion of the potential $U_{vib}\left((\ldots),\left\langle\vec{R}_I\right\rangle+\Delta\vec{R}_I,(\ldots)\right)$, one obtains:

$$\left\langle U_{vib}\left((\ldots),\left\langle\vec{R}_I\right\rangle+\Delta\vec{R}_I,(\ldots)\right)\right\rangle\Big|_{(\ldots),\theta_I,\phi_I,(\ldots)}=$$

$$\sum_I\left\{\sum_{J\neq I}\left\{E^{(2)}_{a-a}\left(\left|\left\langle\vec{R}_I\right\rangle-\left\langle\vec{R}_J\right\rangle\right|\right)+\frac{2E^{(1)}_{a-a}\left(\left|\left\langle\vec{R}_I\right\rangle-\left\langle\vec{R}_J\right\rangle\right|\right)}{\left|\left\langle\vec{R}_I\right\rangle-\left\langle\vec{R}_J\right\rangle\right|}\right\}\right.$$

$$\left.\times\left\{\frac{\{\Delta R_{Ix}\}^2+\{\Delta R_{Iy}\}^2+\{\Delta R_{Iz}\}^2}{6}\right\}\right\}. \tag{6.20}$$

In equation 6.20, $E^{(n)}_{a-a}\left(\left|\left\langle\vec{R}_I\right\rangle-\left\langle\vec{R}_J\right\rangle\right|\right)$ must be understood as the n^{th} derivative of the inter-atomic interaction potential $E_{a-a}(x)$ with respect to its complete argument x, and evaluated at $x=\left|\left\langle\vec{R}_I\right\rangle-\left\langle\vec{R}_J\right\rangle\right|$. For each atomic nucleus in the solid, the potential $\left\langle U_{vib}\left((\ldots),\left\langle\vec{R}_I\right\rangle+\Delta\vec{R}_I,(\ldots)\right)\right\rangle\Big|_{(\ldots),\theta_I,\phi_I,(\ldots)}$ describes a three-dimensional harmonic potential that is defined in terms of only the mean positions of the solid's atomic nuclei. For this reason, we term this potential a "mean-field potential" [76, p. 379].

If the potential $U_{vib}\left(\left(\ldots\right),\left\langle\vec{R}_I\right\rangle+\Delta\vec{R}_I,\left(\ldots\right)\right)$ in the Hamiltonian H_{vib} is replaced with the potential $\left\langle U_{vib}\left(\left(\ldots\right),\left\langle\vec{R}_I\right\rangle+\Delta\vec{R}_I,\left(\ldots\right)\right)\right\rangle\Big|_{(\ldots),\theta_I,\phi_I,(\ldots)}$ defined in equation 6.20, then H_{vib} becomes the Hamiltonian of a series of N uncoupled harmonic oscillators [139, p. 814], the oscillators in question being the solid's atomic nuclei. The frequency of oscillation of the solid's I^{th} atomic nucleus is [139, p. 814]:

$$\omega\left(v\right)=\sqrt{\frac{1}{3M_I}\sum_{J\neq I}\left\{E^{(2)}_{a-a}\left(\left|\left\langle\vec{R}_I\right\rangle-\left\langle\vec{R}_J\right\rangle\right|\right)+\frac{2E^{(1)}_{a-a}\left(\left|\left\langle\vec{R}_I\right\rangle-\left\langle\vec{R}_J\right\rangle\right|\right)}{\left|\left\langle\vec{R}_I\right\rangle-\left\langle\vec{R}_J\right\rangle\right|}\right\}},\tag{6.21}$$

where M_I is the mass of the atomic nucleus. It must be noted that the frequency $\omega\left(v\right)$ is dependent upon the atomic volume of the solid via the average positions of the solid's atomic nuclei, $\left\langle\vec{R}_I\right\rangle$.

When the solid is modelled in this manner, the vibrational Helmholtz' free energy of all of its atomic nuclei is [76, p. 381]:

$$F_{vib}\left(v,T\right)=N\times\left\{\frac{3}{2}\hbar\omega\left(v\right)+3k_BTln\left\{1-e^{\frac{-\hbar\omega(v)}{k_BT}}\right\}\right\},\tag{6.22}$$

where k_B is Boltzmann's constant, T is the solid's temperature, $\hbar$ is Planck's constant divided by 2π, and $\omega\left(v\right)$ is as given in equation 6.21.

Once the vibrational Helmholtz' free energy of the solid is known, the total Helmholtz' free energy of the solid is simply:

$$F\left(v,T\right)=E_{tot}\left(v\right)+F_{vib}\left(v,T\right),\tag{6.23}$$

where $E_{tot}\left(v\right)$ is the smallest eigenvalue of the Hamiltonian H'_{tot}, as defined for a solid with atomic volume v.

6.2.3 F (v, T) Curve of a Solid - Phonon Spectrum Method

A second method for calculating the eigenstates $\left|\Theta\left(v\right)\right\rangle$ of the Hamiltonian H_{vib} can be developed by considering without spherical averaging the zeroth-, first- and second-order terms of the Taylor expansion of $U_{vib}\left(\left(\ldots\right),\left\langle\vec{R}_I\right\rangle+\Delta\vec{R}_I,\left(\ldots\right)\right)$. This results in a more

complete description of the physics of solids than that of the method presented in section 6.2.2 because some of the Taylor expansion terms of $U_{vib}\left(\left(\ldots\right),\left\langle\vec{R}_I\right\rangle+\Delta\vec{R}_I,\left(\ldots\right)\right)$ (see section 6.5) are proportional to components of displacement vectors $\Delta\vec{R}_I$ and $\Delta\vec{R}_J$ describing the positions of two of the solid's atomic nuclei. These terms couple the motion of the solid's atomic nuclei, and are lost when $U_{vib}\left(\left(\ldots\right),\left\langle\vec{R}_I\right\rangle+\Delta\vec{R}_I,\left(\ldots\right)\right)$ is spherically averaged. Because they are coupled, the atomic nuclei of a solid do not oscillate independently about their mean positions. Rather, they oscillate collectively, in normal modes of oscillation [76, 139]. A collective oscillation of all atomic nuclei in a solid is termed a phonon [139, p.586]. All eigenstates $|\Theta\left(v\right)\rangle$ of the Hamiltonian H_{vib}, when $U_{vib}\left(\left(\ldots\right),\left\langle\vec{R}_I\right\rangle+\Delta\vec{R}_I,\left(\ldots\right)\right)$ is considered to second-order in the components of the vectors $\Delta\vec{R}_I$ without spherical averaging, are states where all atomic nuclei in the solid are oscillating about their mean positions in a single phonon mode.

When the atomic nuclei in a solid are oscillating in a single phonon mode, the I^{th} atomic nucleus oscillates about its mean position $\left\langle\vec{R}_I\right\rangle$. Its displacement relative to its mean position as a function of time is [76,139]:

$$\Delta\vec{R}_I\left(t\right)=\vec{u}\times cos\left(\vec{k}\cdot\left\langle\vec{R}_I\right\rangle-\Omega\left(\vec{k},v\right)t\right), \tag{6.24}$$

where $\vec{u}$ is a vector in the direction of the oscillation, $\vec{k}$ is an inverse-space vector in the solid's first Brillouin zone (see the text of Ashcroft and Mermin for a description of a solid's first Brillouin zone [37, p. 89]), $\Omega\left(\vec{k},v\right)$ is the frequency of oscillation of the nucleus, and t is time. In a three-dimensional solid consisting of only one chemical species, there are three phonon modes for every vector $\vec{k}$ in the solid's first Brillouin zone [76, p. 389].

The frequency of oscillation of the phonon modes of a solid can be found by calculating the force on its I^{th} atomic nucleus as it oscillates in the potential $U_{vib}\left(\left(\ldots\right),\left\langle\vec{R}_I\right\rangle+\Delta\vec{R}_I,\left(\ldots\right)\right)$ [139, p. 586]. This force is equal to:

$$\begin{aligned}M_I\frac{d^2}{dt^2}\Delta\vec{R}_I\left(t\right) &= -M_I\Omega^2\left(\vec{k},v\right)\Delta\vec{R}_I\left(t\right)\\ &= -\vec{\nabla}_I U_{vib}\left(\left(\ldots\right),\left\langle\vec{R}_I\right\rangle+\Delta\vec{R}_I,\left(\ldots\right)\right),\end{aligned} \tag{6.25}$$

where $\vec{\nabla}_I$ is the gradient operator $\hat{x}\frac{d}{d\Delta R_{Ix}} + \hat{y}\frac{d}{d\Delta R_{Iy}} + \hat{z}\frac{d}{d\Delta R_{Iz}}$. Equation 6.25 is a vectorial equation. It defines a set of three coupled linear equations that can be solved for the components of the vector $\vec{u}$ defining the direction of oscillation of the atomic nucleus. The characteristic polynomial of this set of coupled linear equations is a third-order polynomial that can be solved for the frequencies $\Omega\left(\vec{k}, v\right)$ of the three phonon modes associated to each vector $\vec{k}$ in the solid's first Brillouin zone. It must be noted that the frequencies $\Omega\left(\vec{k}, v\right)$ are dependent upon the solid's atomic volume because the potential $U_{vib}\left((\ldots), \left\langle \vec{R}_I \right\rangle + \Delta\vec{R}_I, (\ldots)\right)$ is dependent upon the atomic volume of the solid via the vectors $\left\langle \vec{R}_I \right\rangle$.

Once the phonon frequencies $\Omega\left(\vec{k}, v\right)$ are known, the vibrational Helmholtz' free energy of the solid's atomic nuclei can be calculated as follows [76, p. 389]:

$$\begin{aligned} F_{vib}(v,T) &= N \times \left\{ \frac{1}{2} \sum_{\lambda=1}^{3} \frac{v}{(2\pi)^3} \int_{BZ} \hbar\Omega_\lambda\left(\vec{k}, v\right) d\vec{k} \right. \\ &+ \left. k_B T \sum_{\lambda=1}^{3} \frac{v}{(2\pi)^3} \int_{BZ} ln\left\{ 1 - e^{-\frac{\hbar\Omega_\lambda(\vec{k},v)}{k_B T}} \right\} d\vec{k} \right\}. \end{aligned} \tag{6.26}$$

In equation 6.26, the integrals over $d\vec{k}$ are restricted to the first Brillouin zone of the solid, and the summations over λ run over all three frequencies $\Omega\left(\vec{k}, v\right)$ associated to each vector $\vec{k}$ in the solid's first Brillouin zone.

Again, once the vibrational Helmholtz' free energy of the solid is known, the total Helmholtz' free energy of the solid is simply:

$$F(v,T) = E_{tot}(v) + F_{vib}(v,T), \tag{6.27}$$

where $E_{tot}(v)$ is the smallest eigenvalue of the Hamiltonian H'_{tot}, as defined for a solid with atomic volume v.

6.3 Major Assumptions of and Novelty of the Method

In deriving the method for calculating the Helmholtz' free energy of solids presented in section 6.2, we have made four important assumptions.

Firstly, our method assumes that the atomic nuclei of a solid remain in the vicinity of well-defined mean positions at all temperatures below the solid's melting point. For many crystalline solids, this is a valid assumption. Nonetheless, in making this assumption, we fail to describe within our method a number of phenomena known to occur in real solids, like vacancy formation and atomic diffusion processes [5, 37, 78, 140]. However, these phenomena are of minute importance to the calculation of the Helmholtz' free energy of large solids, as the thermal properties of such solids are mostly the result of the thermal oscillation of their atomic nuclei [5, 37, 78].

Secondly, we have explicitly expressed the accessible microstates of a solid as per equation 6.12, where the eigenstate $|\Psi_{min}(v)\rangle$ is the lowest energy eigenstate of the Hamiltonian H'_{tot} given in equation 6.9. In doing so, we implicitly assume that the energy that is transfered between the solid and its environment is transferred exclusively to the solid's atomic nuclei. In reality, energy can be transfered directly between a solid's electrons and its environment. However, it is generally accepted that the core electrons of a solid do not change their state as a result of such energy transfers because they always remain in the vicinity of a single atomic nucleus, in well-defined atomic orbitals, at all temperatures below the solid's melting point. In contrast, a solid's valence electrons can change their state as a result of energy transferred between them and the solid's environment. This phenomenon is most significant in metallic solids. However, a metal's valence electrons can be modelled as a plasma with Fermi temperature much higher than the melting point of the metal [37, 78]. Thus, the state of a metal's valence electrons is also essentially the same at all temperatures below its melting point. Therefore, it is defensible to assume, even for a metallic solid, that no energy is directly transferred between the solid's valence electrons and its environment.

The thermal excitation of electrons is ignored in many previous attempts to calculate the thermal properties of a metal (e.g. [141–143]). However, the thermal excitation of a metal's valence electrons is considered in some previously published papers (e.g. [144–147]). In

these papers, the Helmholtz' free energy of a metal's valence electrons is calculated as:

$$F_{el}(v,T) = \int_{-\infty}^{\infty} n_v(\epsilon,v) f(\epsilon) \epsilon d\epsilon - \int_{-\infty}^{E_F} n_v(\epsilon,v) \epsilon d\epsilon$$

$$- k_B T \int_{-\infty}^{\infty} n_v(\epsilon,v) \{f(\epsilon) ln(f(\epsilon)) + (1-f(\epsilon)) ln(1-f(\epsilon))\} d\epsilon, \quad (6.28)$$

where $n_v(v,T)$ is the density of states of the metal's valence electrons when the metal has atomic volume v (see section 2.2.2 of chapter 2), E_F is the metal's Fermi energy [37, p. 142], $f(\epsilon)$ is the Fermi distribution [76, p. 774], and k_B is Boltzman's constant. In chapter 7, we shall calculate $F_{el}(v,T)$ and compare it to the remainder of the Helmholtz' free energy of a metal, as obtained using the methods presented in sections 6.2.2 and 6.2.3. Of course, the electrons of any solid are perturbed by the thermal oscillation of its atomic nuclei. In the method presented in this chapter, this is captured in the inter-atomic interaction potential $E_{a-a}(x)$ (more on this below).

Thirdly, in the method for calculating the Helmholtz' free energy of a crystalline solid presented in this chapter, the vibration potential $U_{vib}\left(\left(\ldots\right), \left\langle \vec{R}_I \right\rangle + \Delta\vec{R}_I, \left(\ldots\right)\right)$ is only considered to second-order in the components of the vectors $\Delta\vec{R}_I$. In doing so, we recognize that $U_{vib}\left(\left(\ldots\right), \left\langle \vec{R}_I \right\rangle + \Delta\vec{R}_I, \left(\ldots\right)\right)$ is dependent on the average positions $\left\langle \vec{R}_I \right\rangle$ of the atomic nuclei of the solid, and thus, the terms of its Taylor expansion are dependent on the lattice parameter of the solid. This is termed a "quasi-harmonic approximation". A number of authors have argued that the effect of the quasi-harmonic approximation on the accuracy of the calculation of the thermal properties of solids can be significant (see for example [148,149]). Thus, the effect of neglecting the higher order terms of the Taylor expansion of $U_{vib}\left(\left(\ldots\right), \left\langle \vec{R}_I \right\rangle + \Delta\vec{R}_I, \left(\ldots\right)\right)$ on the accuracy of the calculated Helmholtz' free energy of a solid should be verified. We shall discuss this matter further in chapter 7.

Fourthly, the method presented in this chapter makes use of an inter-atomic interaction potential $E_{a-a}(x)$ to model the chemical cohesion of solids. Changing the lattice parameter of a solid amounts to changing the mean positions of its atomic nuclei. Changing the mean position of all atomic nuclei in a solid produces:

1. changes in the electrostatic interaction of the atomic nuclei of the solid,

2. changes in the electrostatic interaction of the electrons of the solid,

3. changes in the electrostatic interaction between the atomic nuclei and the electrons of the solid, and

4. changes in the kinetic energy of the electrons of the solid.

The $E_{tot}(a)$ curve of a solid captures the change in the solid's minimum total energy that occurs as a result of all of the changes enumerated above. And so, by expressing the $E_{tot}(a)$ curve of a solid in terms of an inter-atomic interaction potential $E_{a-a}(x)$ (as per equation 6.14), we are implicitly assuming that $E_{a-a}(x)$ is an accurate model of the changes in the electrostatic interaction of the atomic nuclei of the solid, of the changes in the electrostatic interaction of the electrons of the solid, of the changes in the electrostatic interaction between the atomic nuclei and the electrons of the solid, and of the changes in the kinetic energy of the electrons of the solid that occur when its lattice parameter is changed.

We derive the inter-atomic interaction potential $E_{a-a}(x)$ from knowledge of the $E_{tot}(a)$ curve of a solid using the results of Chen, Chen and Wei [137]. The $E_{tot}(a)$ curve of a solid can be calculated theoretically using an ESC program, and the results of Chen, Chen and Wei [137] provide a rigorous mathematical formula for constructing an inter-atomic interaction potential $E_{a-a}(x)$ once the $E_{tot}(a)$ curve is known. The potential $E_{a-a}(x)$ thus obtained is unique, and accurately reproduces the value of the $E_{tot}(a)$ curve at any lattice parameter. For this reason, we believe that the results of Chen, Chen and Wei [137] provide a means for producing a potential $E_{a-a}(x)$ that is an accurate model of the changes in the electrostatic interaction of the atomic nuclei of a solid, of the changes in the electrostatic interaction of the electrons of a solid, of the changes in the electrostatic interaction between the atomic nuclei and the electrons of a solid, and of the changes in the kinetic energy of the electrons of a solid that occur when its lattice parameter is changed. (These are precisely the changes enumerated in the previous paragraph.)

Having so constructed the inter-atomic interaction potential $E_{a-a}(x)$, we then assume that the vibration potential $U_{vib}\left(\left(\ldots\right), \left\langle \vec{R}_I \right\rangle + \Delta\vec{R}_I, \left(\ldots\right)\right)$ can be accurately expressed in terms of the potential $E_{a-a}(x)$ (equation 6.16). In doing so, we implicitly assume that when the atoms of a solid are displaced from their mean positions as they undergo small amplitude thermal oscillations, the resulting increase in the total energy of the solid (excluding the kinetic energy of the atomic nuclei) can be modelled using the same inter-atomic interaction potential $E_{a-a}(x)$ that models the increase in the total energy of the solid when its lattice parameter is changed. Some may be skeptical of the validity of this assumption because atomic nuclei change their spatial symmetry as they undergo thermal oscillations. Previously published research suggests that inter-atomic interaction potentials fail to accurately predict the properties of solids that involve changes of the spatial symmetry of their atomic nuclei, like a solid's elastic constants [150]. In spite of this, we believe that the assumption is valid because thermal oscillations do not induce a macroscopically observable change in the spatial symmetry of the atomic nuclei of a solid (as does the application of a symmetry breaking stress to the solid). Rather, thermal oscillations only cause the atomic nuclei of solids to be displaced slightly from their mean positions, which themselves typically maintain the same spatial symmetry over a broad range of temperatures. We believe that the assumption is valid as long as the inter-atomic interaction potential $E_{a-a}(x)$ is used only to model the thermal oscillations of the atoms of a solid possessing a specific crystal structure, namely the crystal structure that the solid was assumed to possess when calculating the $E_{tot}(a)$ curve used to derive the potential $E_{a-a}(x)$. We shall discuss this matter further in chapter 7.

The results of Chen, Chen and Wei [137] are very powerful. For instance, they shed new light on the use of inter-atomic interaction potentials in the calculation of solid properties. It is now generally accepted that the chemical cohesion of the atomic nuclei of real solids, especially metallic solids, cannot rigorously be modelled as the result of independent, pair-wise inter-atomic interactions (see for example [150, 151]). As a result, some researchers have suggested that a pair-wise inter-atomic interaction potential is entirely incapable of accurately modelling the properties of any solid. However, it appears that an

inter-atomic model of chemical bonding fails most importantly in the prediction of solid properties involving a change of the spatial symmetry of its atomic nuclei, like a solid's elastic constants [150]. The results of Chen, Chen and Wei [137] indicate that an inter-atomic interaction potential can only be defined for a solid possessing a specific chemical composition and a specific crystal structure. Thus, to calculate the properties of two solids, both consisting of the same elements but each possessing a different crystal structure, two different inter-atomic interaction potentials must be defined. The results of Chen, Chen and Wei [137] can be used to define both of these potentials. In addition, the calculation of solid properties involving a change of the spatial symmetry of its atomic nuclei requires the calculation of a number of appropriate inter-atomic interaction potentials, all of which can again be constructed using the results of Chen, Chen and Wei [137].

In addition, the results of Chen, Chen and Wei provide an entirely theoretical method for constructing an inter-atomic interaction potential $E_{a-a}(x)$ [137]. This is so because the $E_{tot}(a)$ curve that is required to construct the potential $E_{a-a}(x)$ using the results of Chen, Chen and Wei can be calculated using an ESC program based entirely on first principles. Thus, to calculate the thermal properties of a solid using the method presented in this chapter, all that is required is knowledge of the average positions of the atomic nuclei in a solid, specified by vectors $\left\langle \vec{R}_I \right\rangle$. In contrast, a number of popular methods for constructing inter-atomic potentials, like the embedded atom method (EAM) [151], are empirical or semi-empirical methods. They provide a theoretical basis for deriving appropriate functional forms for inter-atomic interaction potentials which are then adjusted to reproduce the measured properties of materials of interest [151]. The potentials thus obtained appear to be generally applicable to the modelling of a number of material properties, as they have successfully been used to model defect formation, surface adsorption and other phenomena occurring in solids (see for example [151–153]). Using the results of Chen, Chen and Wei, we obtain an inter-atomic potential that is less generally applicable (in the sense that it is only useful for constructing the vibration potential $U_{vib}\left((\ldots), \left\langle \vec{R}_I \right\rangle + \Delta\vec{R}_I, (\ldots)\right)$ of atomic nuclei in a specific solid), but that can be calculated entirely theoretically.

Finally, the results of Chen, Chen and Wei provide an exact procedure for constructing a

potential $E_{a-a}(x)$ that reproduces the $E_{tot}(a)$ curve of a solid without artificially imposing any restrictions on the range of action of $E_{a-a}(x)$. Prior to the publication of the results of Chen, Chen and Wei, the method of Carlsson, Gelatt and Ehrenreich [154,155], or slightly modified versions of this method (e.g. [156–160]), was often used to construct inter-atomic interaction potentials. This so-called "Carlsson-Gelatt method" [154] provides an exact expression for a potential $E_{a-a}(x)$ in terms of the $E_{tot}(a)$ curve of a solid as long as $E_{a-a}(x)$ acts only between a given atomic nucleus in the solid and its first nearest neighbours. If the range of $E_{a-a}(x)$ is longer, the Carlsson-Gelatt method provides only an approximate procedure for constructing it. The results of Chen, Chen and Wei do not suffer from this limitation.

Since the publication of the results of Chen, Chen and Wei, they have been used to calculate inter-atomic interaction potentials for the purpose of studying a number of complex materials. For instance, they have been used in the study of complex alloys (e.g. [161–194]), and of small material clusters (e.g. [193, 195–197]). They have also been used in a study of the adsorption of atoms on material surfaces [198]. We have not found any publications discussing the use of the results of Chen, Chen and Wei in a method for calculating the Helmholtz' free energy of bulk materials consisting of a single chemical species, like the method presented in this chapter. We thus believe that the theoretical method that we present here is novel.

6.4 Validation of the Method

We next wish to evaluate the performance of the method presented in this chapter in calculating the $F(v,T)$ curve of a real solid. The remainder of this thesis discusses the calculation of the $F(v,T)$ curve of metallic Cu. More specifically, in the next chapter, we calculate the $F(v,T)$ curve of metallic Cu and use it to calculate the lattice parameter versus temperature curve $a(T)$ curve of metallic Cu. We also compare the calculated $a(T)$ curve of metallic Cu to the measured $a(T)$ curve of this metal [80]. This amounts to an

indirect evaluation of the accuracy of the $F(v,T)$ curve of metallic Cu, as calculated using the theoretical method presented in this chapter. We also use this information to evaluate the validity of the assumptions that were made in deriving the method presented in this chapter.

6.5 Appendix: Taylor Expansion of the Potential $\mathbf{U_{vib}}\left((\ldots),\left\langle\tilde{\mathbf{R}}_\mathbf{I}\right\rangle+\boldsymbol{\Delta}\tilde{\mathbf{R}}_\mathbf{I},(\ldots)\right)$

It is possible to express the function $U_{vib}\left((\ldots),\left\langle\vec{R}_I\right\rangle+\Delta\vec{R}_I,(\ldots)\right)$, as defined in equation 6.16, as a $3N$-dimensional Taylor expansion [199]. The independent variables of this Taylor expansion are the components of the vectors $\Delta\vec{R}_I$, namely ΔR_{Ix}, ΔR_{Iy}, and ΔR_{Iz}.

The zeroth-order term of this Taylor expansion is simply:

$$\begin{aligned} U_{vib}\left((\ldots),\left\langle\vec{R}_I\right\rangle,(\ldots)\right) &= \frac{1}{2}\sum_I\sum_{J\neq I}E_{a-a}\left(\left|\left\langle\vec{R}_I\right\rangle-\left\langle\vec{R}_J\right\rangle\right|\right)-E_{tot}(v) \\ &= 0 \end{aligned} \tag{6.29}$$

The first-order terms of the Taylor expansion are of the form:

$$\sum_{J\neq I}E^{(1)}_{a-a}\left(\left|\left\langle\vec{R}_I\right\rangle-\left\langle\vec{R}_J\right\rangle\right|\right)\times\left\{\frac{\langle R_{Iq}\rangle-\langle R_{Jq}\rangle}{\left|\left\langle\vec{R}_I\right\rangle-\left\langle\vec{R}_J\right\rangle\right|}\right\}\times\Delta R_{Iq}, \tag{6.30}$$

where the summation over J runs over every atom in the solid, and $\langle R_{Iq}\rangle$ is the q-component of the vector $\left\langle\vec{R}_I\right\rangle$. It must be recalled that the vector $\left\langle\vec{R}_I\right\rangle$ is the average position of the solid's I^{th} atomic nucleus. Also, $E^{(n)}_{a-a}\left(\left|\left\langle\vec{R}_I\right\rangle-\left\langle\vec{R}_J\right\rangle\right|\right)$ must be understood as the n^{th}-derivative of the inter-atomic interaction potential $E_{a-a}(x)$ with respect to its full argument x, evaluated at $x=\left|\left\langle\vec{R}_I\right\rangle-\left\langle\vec{R}_J\right\rangle\right|$. There are three Taylor expansion terms of the form given in equation 6.30 for every atomic nucleus in the solid, one proportional to ΔR_{Ix}, to ΔR_{Iy} and to ΔR_{Iz}. Equation 6.30 shows a term associated with the I^{th} atomic nucleus.

The second-order terms of the Taylor expansion are more numerous. Firstly, there are $3N$ terms of the form:

$$\frac{1}{2}\sum_{J\neq I} \left\{ E^{(2)}_{a-a}\left(\left|\left\langle \vec{R}_I \right\rangle - \left\langle \vec{R}_J \right\rangle\right|\right) \times \left\{ \frac{\langle R_{Iq}\rangle - \langle R_{Jq}\rangle}{\left|\langle \vec{R}_I\rangle - \langle \vec{R}_J\rangle\right|} \right\}^2 \right. \tag{6.31}$$
$$\left. + \; E^{(1)}_{a-a}\left(\left|\left\langle \vec{R}_I \right\rangle - \left\langle \vec{R}_J \right\rangle\right|\right) \times \left\{ \frac{\left|\langle \vec{R}_I\rangle - \langle \vec{R}_J\rangle\right|^2 - \left\{\langle R_{Iq}\rangle - \langle R_{Jq}\rangle\right\}^2}{\left|\langle \vec{R}_I\rangle - \langle \vec{R}_J\rangle\right|^3} \right\} \right\} \times \left\{\Delta R_{Iq}\right\}^2,$$

one proportional to $\left\{\Delta R_{Ix}\right\}^2$, to $\left\{\Delta R_{Iy}\right\}^2$ and to $\left\{\Delta R_{Iz}\right\}^2$ for each atom in the solid.

Secondly, there are $3N$ terms of the form:

$$\sum_{J\neq I} \left\{ E^{(2)}_{a-a}\left(\left|\left\langle \vec{R}_I \right\rangle - \left\langle \vec{R}_J \right\rangle\right|\right) \times \left\{ \frac{\left\{\langle R_{Iq}\rangle - \langle R_{Jq}\rangle\right\}\left\{\langle R_{Ip}\rangle - \langle R_{Jp}\rangle\right\}}{\left|\langle \vec{R}_I\rangle - \langle \vec{R}_J\rangle\right|^2} \right\} \right. \tag{6.32}$$
$$\left. - \; E^{(1)}_{a-a}\left(\left|\left\langle \vec{R}_I \right\rangle - \left\langle \vec{R}_J \right\rangle\right|\right) \times \left\{ \frac{\left\{\langle R_{Iq}\rangle - \langle R_{Jq}\rangle\right\}\left\{\langle R_{Ip}\rangle - \langle R_{Jp}\rangle\right\}}{\left|\langle \vec{R}_I\rangle - \langle \vec{R}_J\rangle\right|^3} \right\} \right\} \times \left\{\Delta R_{Iq}\right\}\left\{\Delta R_{Ip}\right\},$$

one proportional to $\left\{\Delta R_{Ix}\right\}\left\{\Delta R_{Iy}\right\}$, to $\left\{\Delta R_{Ix}\right\}\left\{\Delta R_{Iz}\right\}$ and to $\left\{\Delta R_{Iy}\right\}\left\{\Delta R_{Iz}\right\}$ for each atom in the solid.

Thirdly, there are $\frac{3}{2}(N)(N-1)$ terms of the form:

$$-\left\{ E^{(2)}_{a-a}\left(\left|\left\langle \vec{R}_I \right\rangle - \left\langle \vec{R}_J \right\rangle\right|\right) \times \left\{ \frac{\left\{\langle R_{Iq}\rangle - \langle R_{Jq}\rangle\right\}^2}{\left|\langle \vec{R}_I\rangle - \langle \vec{R}_J\rangle\right|^2} \right\} \right. \tag{6.33}$$
$$\left. + \; E^{(1)}_{a-a}\left(\left|\left\langle \vec{R}_I \right\rangle - \left\langle \vec{R}_J \right\rangle\right|\right) \times \left\{ \frac{\left|\langle \vec{R}_I\rangle - \langle \vec{R}_J\rangle\right|^2 - \left\{\langle R_{Iq}\rangle - \langle R_{Jq}\rangle\right\}^2}{\left|\langle \vec{R}_I\rangle - \langle \vec{R}_J\rangle\right|^3} \right\} \right\} \times \left\{\Delta R_{Iq}\right\}\left\{\Delta R_{Jq}\right\},$$

one proportional to $\left\{\Delta R_{Ix}\right\}\left\{\Delta R_{Jx}\right\}$, to $\left\{\Delta R_{Iy}\right\}\left\{\Delta R_{Jy}\right\}$ and to $\left\{\Delta R_{Iz}\right\}\left\{\Delta R_{Jz}\right\}$ for each pair of atoms in the solid.

Finally, there are $3(N)(N-1)$ terms of the form:

$$-\left\{ E^{(2)}_{a-a}\left(\left|\left\langle \vec{R}_I \right\rangle - \left\langle \vec{R}_J \right\rangle\right|\right) \times \left\{ \frac{\left\{\langle R_{Iq}\rangle - \langle R_{Jq}\rangle\right\}\left\{\langle R_{Ip}\rangle - \langle R_{Jp}\rangle\right\}}{\left|\langle \vec{R}_I\rangle - \langle \vec{R}_J\rangle\right|^2} \right\} \right. \tag{6.34}$$
$$\left. - \; E^{(1)}_{a-a}\left(\left|\left\langle \vec{R}_I \right\rangle - \left\langle \vec{R}_J \right\rangle\right|\right) \times \left\{ \frac{\left\{\langle R_{Iq}\rangle - \langle R_{Jq}\rangle\right\}\left\{\langle R_{Ip}\rangle - \langle R_{Jp}\rangle\right\}}{\left|\langle \vec{R}_I\rangle - \langle \vec{R}_J\rangle\right|^3} \right\} \right\} \times \left\{\Delta R_{Iq}\right\}\left\{\Delta R_{Jp}\right\},$$

one proportional to $\left\{\Delta R_{Ix}\right\}\left\{\Delta R_{Jy}\right\}$, to $\left\{\Delta R_{Ix}\right\}\left\{\Delta R_{Jz}\right\}$, to $\left\{\Delta R_{Iy}\right\}\left\{\Delta R_{Jx}\right\}$, to $\left\{\Delta R_{Iy}\right\}\left\{\Delta R_{Jz}\right\}$, to $\left\{\Delta R_{Iz}\right\}\left\{\Delta R_{Jx}\right\}$ and to $\left\{\Delta R_{Iz}\right\}\left\{\Delta R_{Jy}\right\}$ for each pair of atoms in the solid.

The sum of the expressions given in equations 6.29 to 6.34 is the Taylor expansion of the potential $U_{vib}\left((\ldots), \left\langle \vec{R}_I \right\rangle + \Delta\vec{R}_I, (\ldots)\right)$, given in equation 6.16, to second-order in the

variables ΔR_{Ix}, ΔR_{Iy} and ΔR_{Iz}. All terms of this Taylor expansion are defined in terms of only the vectors $\left\langle \vec{R}_I \right\rangle$, and the inter-atomic interaction potential $E_{a-a}(x)$ and its derivatives.

Chapter 7

Calculation of the Thermal Expansion of Metallic Copper

In this chapter, we study theoretically the thermal expansion of metallic Cu. More specifically, we calculate the lattice parameter versus temperature curve $a(T)$ of metallic Cu, and evaluate its accuracy by comparing it to published measurements of this curve. The $a(T)$ curve of metallic Cu gives the lattice parameter of a bulk metallic Cu solid in thermal equilibrium with its environment at temperature T. It can be constructed from the Helmholtz' free energy function $F(a,T)$ of metallic Cu by finding the value of the lattice parameter a at which the partial derivative $\frac{\delta}{\delta a}F(a,T)=0$, as a function of the temperature T.

We wish to calculate the $a(T)$ curve of metallic Cu for two reasons. Firstly, the accurate calculation of the $a(T)$ curve of solids is itself a topic of current interest in materials science (e.g. [141–147, 200]). Secondly, because we calculate the $a(T)$ curve of metallic Cu using its $F(a,T)$ curve, the evaluation of the accuracy of the former curve is in fact an indirect evaluation of the accuracy of the latter. We wish to evaluate the accuracy of the $F(a,T)$ curve of solids, as calculated using the theoretical method presented in chapter 6.

To calculate the $F(a,T)$ curve of metallic Cu using the method of chapter 6, we must

calculate the minimum total energy versus lattice parameter curve $E_{tot}(a)$ of FCC Cu. We discuss the calculation of three such $E_{tot}(a)$ curves in section 7.1. We also discuss, in this latter section, the construction of the inter-atomic interaction potential $E_{a-a}(x)$ using the $E_{tot}(a)$ curves and the results of Chen, Chen and Wei [137]. In section 7.2, we describe the calculation of the $F(a,T)$ curve of metallic Cu using the mean-field potential method and the phonon spectrum method, presented respectively in sections 6.2.2 and 6.2.3 of chapter 6. In section 7.3, we use these $F(a,T)$ curves to calculate $a(T)$ curves of metallic Cu. We also evaluate the accuracy of these curves. Finally, in section 7.4, we summarise the results of sections 7.2 and 7.3, and discuss the information that these results provide about the theoretical method for calculating the Helmholtz' free energy of solids presented in chapter 6.

7.1 The $E_{tot}(a)$ Curve and the Potential $E_{a-a}(x)$ of FCC Cu

The first step in calculating the $a(T)$ curve of metallic Cu using the theoretical method presented in chapter 6 is the calculation of the minimum total energy versus lattice parameter curve $E_{tot}(a)$ of FCC Cu. We calculate two such curves using the TB-LMTO ESC program [28] and two of the exchange-correlation functionals that are available within the program. We specifically calculate the $E_{tot}(a)$ curve of FCC Cu because the atoms of real metallic Cu are arranged in the FCC crystal structure at all temperatures smaller than the metal's melting point [1].

We calculate the first $E_{tot}(a)$ curve of FCC Cu, which we label the "EXC2 $E_{tot}(a)$ curve", using exchange-correlation functional EXC2 (see table 2.1 of chapter 2). It is shown in chapter 4 that the TB-LMTO ESC program [28] most accurately predicts the crystal structure, the lattice parameters and the magnitude of the magnetic moments of the first-row transition metals at zero Kelvin when it is used in conjunction with this exchange-correlation functional. We calculate the EXC2 $E_{tot}(a)$ curve of FCC Cu assuming that this solid always possesses no magnetic moments (NM configuration) regardless of its lattice

parameter. (Real metallic Cu possesses no spontaneous magnetization (ie. remains diamagnetic) at all temperatures below its melting point [1,2]. However, it is expected that metallic Cu will become magnetic if its lattice parameter is increased sufficiently, for reasons discussed in chapter 5 and noted by Moruzzi [83].) The EXC2 $E_{tot}\,(a)$ curve is shown in figure 7.1. In the range $5.0 \leq a \leq 10.0$ Bohr radii, we calculate the value of the EXC2 $E_{tot}\,(a)$ curve at 51 lattice parameter values, all uniformly separated by an interval of 0.1 Bohr radii. In the range $10.0 < a \leq 50.0$ Bohr radii, we calculate the value of the curve at 80 lattice parameter values, all uniformly separated by an interval of 0.5 Bohr radii.

We calculate the second $E_{tot}\,(a)$ curve of FCC Cu, which we label the "EXC4 $E_{tot}\,(a)$ curve", using the TB-LMTO ESC program [28] and exchange-correlation functional EXC4 (again see table 2.1 of chapter 2). In chapter 4, it is shown that EXC4 is different from the three other exchange-correlation functionals that are available in the TB-LMTO ESC program in that the program overestimates most of the zero-Kelvin lattice parameters of the first-row transition metals when used in conjunction with EXC4. In contrast, these lattice parameters are underestimated by the program when it is used in conjunction with any of the three other available exchange-correlation functionals. In addition, the bulk modulus of the first-row transition metals is more accurately calculated using EXC4. We calculate the EXC4 $E_{tot}\,(a)$ curve of FCC Cu assuming that the metal always possesses no magnetic moments (NM configuration), regardless of the value of its lattice parameter. This $E_{tot}\,(a)$ curve is also shown in figure 7.1. In the range $5.0 \leq a \leq 12.0$ Bohr radii, we calculate the value of the EXC4 $E_{tot}\,(a)$ curve at 71 lattice parameter values, all uniformly separated by an interval of 0.1 Bohr radii. In the range $12.0 < a \leq 50.0$ Bohr radii, we calculate the value of the curve at 76 lattice parameter values, all uniformly separated by an interval of 0.5 Bohr radii.

All values of both $E_{tot}\,(a)$ curves are calculated with first BZ discretization integers set to $L = M = N = 16$. The value of the convergence tolerances are set to different values in different lattice parameter ranges, as shown in table 7.1. This is because, as the lattice parameter of FCC Cu is increased, the TB-LMTO ESC program converges with greater and greater difficulty. Thus, it is necessary to relax the program's convergence tolerances

as the lattice parameter of FCC Cu is increased. In all calculations, the electron density convergence tolerance and the total energy convergence tolerance are assigned identical values (ie. 1.0×10^{-3} Rydberg units for the total energy convergence tolerance and 1.0×10^{-3} electrons per cubic Bohr radii for the electron density convergence tolerance). Finally, the single-electron wave functions of the metals' valence electrons are expressed as a linear combination of s-, p- and d-orbitals only.

Table 7.1: Convergence tolerances for calculating the $E_{tot}(a)$ curve of FCC Cu

Value of convergence tolerances	Lattice par. range when calculating using EXC2	Lattice par. range when calculating using EXC4
1.0×10^{-5}	$5.0 \leq a \leq 21.0$ Bohr radii	$5.0 \leq a \leq 20.0$ Bohr radii
1.0×10^{-4}	$21.5 \leq a \leq 32.0$ Bohr radii	$20.5 \leq a \leq 28.0$ Bohr radii and $29.0 \leq a \leq 50.0$ Bohr radii
1.0×10^{-3}	$32.5 \leq a \leq 50.0$ Bohr radii	$a = 28.5$ Bohr radii

The total energy convergence tolerance has Rydberg units, while the electron density convergence tolerance has units of electrons per cubic Bohr radii.

The EXC2 and EXC4 $E_{tot}(a)$ curves are both shown in figure 7.1. The EXC4 $E_{tot}(a)$ curve is shown translated upward by approximately 3.395 Rydberg units in the figure. This makes the smallest calculated value of this curve approximately equal to that of the EXC2 $E_{tot}(a)$ curve, thus facilitating the comparison of the two curves. The figure shows only the portion of each curve that lies between 2.5 and 27.5 Bohr radii even though we calculate both curves between 5.0 and 50.0 Bohr radii. This represents no significant loss of information, as both curves are essentially constant at all lattice parameters greater than

$a \approx 25.0$ Bohr radii. Figure 7.1 makes clear that the shape of the two $E_{tot}(a)$ curves is different. To more clearly emphasize some of the differences between the EXC2 and the EXC4 $E_{tot}(a)$ curves, we show, in figure 7.2, the calculated values of these curves in the vicinity of their global minima. The EXC4 $E_{tot}(a)$ curve is shown translated upward by approximately 3.395 Rydberg units in this latter figure as well. It is clearly apparent in figure 7.2 that the global minimum value of the EXC2 and the EXC4 curves occur at different lattice parameters. Also, though this is not immediately evident when observing figure 7.1 or figure 7.2, the curve obtained with EXC2 has a local maximum while that obtained with EXC4 does not. (The local maximum of the EXC2 $E_{tot}(a)$ curve is visible in figure B.6 of appendix B.) Table 7.2 highlights other notable features of the two $E_{tot}(a)$ curves and indicates the lattice parameters at which these features occur.

Table 7.2: Notable features of the calculated $E_{tot}(a)$ curves of FCC Cu

Feature	Location of feature in EXC2 curve	Location of feature in EXC4 curve
global minimum	$a = 6.8 \pm 0.1$ Bohr radii	$a = 7.0 \pm 0.1$ Bohr radii
1^{st} inflection point	$a = 8.1 \pm 0.1$ Bohr radii	$a = 8.4 \pm 0.1$ Bohr radii
local maximum	$a = 18.0 \pm 0.5$ Bohr radii	-
2^{nd} inflection point	$a = 19.5 \pm 0.5$ Bohr radii	-

In addition to the EXC2 and the EXC4 $E_{tot}(a)$ curves, we show in figure 7.2 a curve that we label the "EXC4′ $E_{tot}(a)$ curve". This curve is constructed by translating leftward by 0.2 Bohr radii the EXC4 $E_{tot}(a)$ curve. By shifting leftward the EXC4 $E_{tot}(a)$ curve in this manner, the smallest calculated value of this curve is aligned with the smallest calculated value of the EXC2 $E_{tot}(a)$ curve. Like the EXC4 $E_{tot}(a)$ curve, the EXC4′ $E_{tot}(a)$ curve is shown translated upward by approximately 3.395 Rydberg units in figure 7.2. Examining the EXC2 and the EXC4′ $E_{tot}(a)$ curves, it is clear that the curvature of these curves in the vicinity of their global minima is different. We shall later use the EXC2 and the EXC4′ $E_{tot}(a)$ curves to demonstrate that the curvature of the $E_{tot}(a)$ curve of FCC Cu significantly affects the shape of the calculated $a(T)$ curve of metallic Cu.

Finally, in order to calculate the $a\,(T)$ curve of metallic Cu using the method of chapter 6, it must be possible to obtain the value of the $E_{tot}\,(a)$ curve of FCC Cu, and of the first- and second-derivatives of this curve, at almost any value of lattice parameter a. To make this possible, we parametrize the EXC2 and the EXC4 $E_{tot}\,(a)$ curves of FCC Cu using appropriate model functions. This is described in appendix B of this thesis. In this appendix, we also estimate the numerical precision of the calculated $E_{tot}\,(a)$ curves, as well as that of their first- and second-derivatives. In sections 7.2 and 7.3, we use this information to evaluate the numerical precision of the $F\,(a,T)$ curves and $a\,(T)$ curves that we calculate.

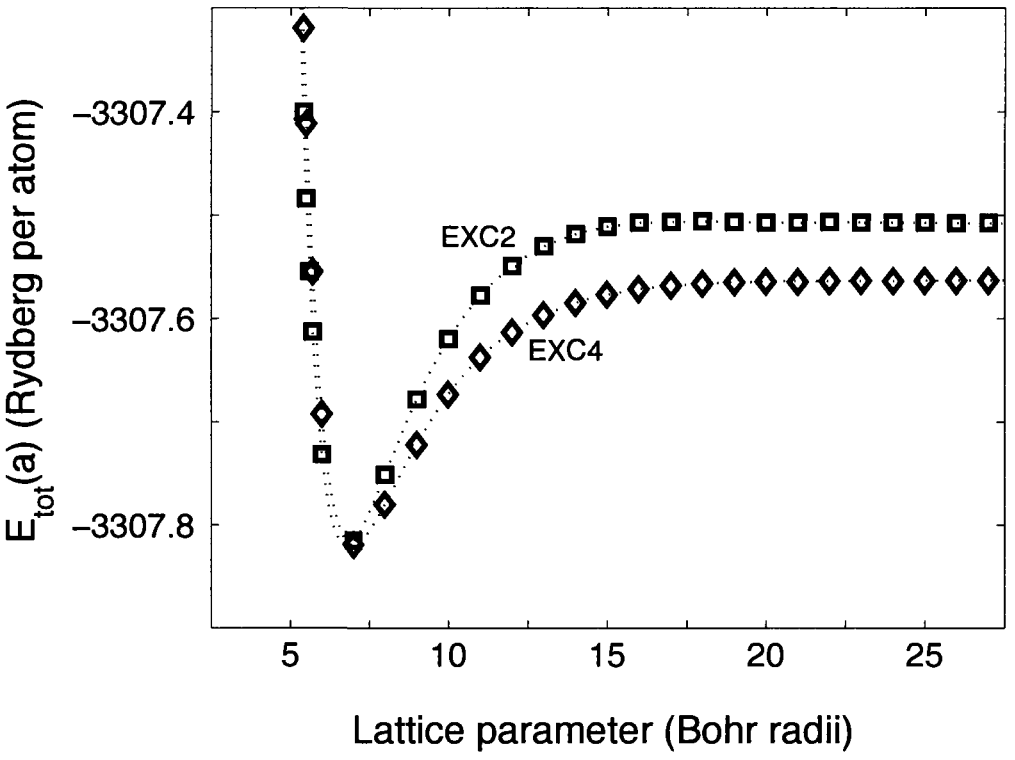

Figure 7.1: Calculated $E_{tot}\,(a)$ curve of FCC Cu obtained using the TB-LMTO ESC program. Squares (diamonds) denote the EXC2 (EXC4) $E_{tot}\,(a)$ curve. Data symbols indicate actual calculated values of the two curves. To maintain the clarity of the figure, some calculated values are not denoted. Also, to facilitate the comparison of the two curves, the EXC4 $E_{tot}\,(a)$ curve is shown translated upward by 3.39462 Rydberg units. Error bars denoting the numerical uncertainty of the calculated values are omitted as they are smaller than the data symbols.

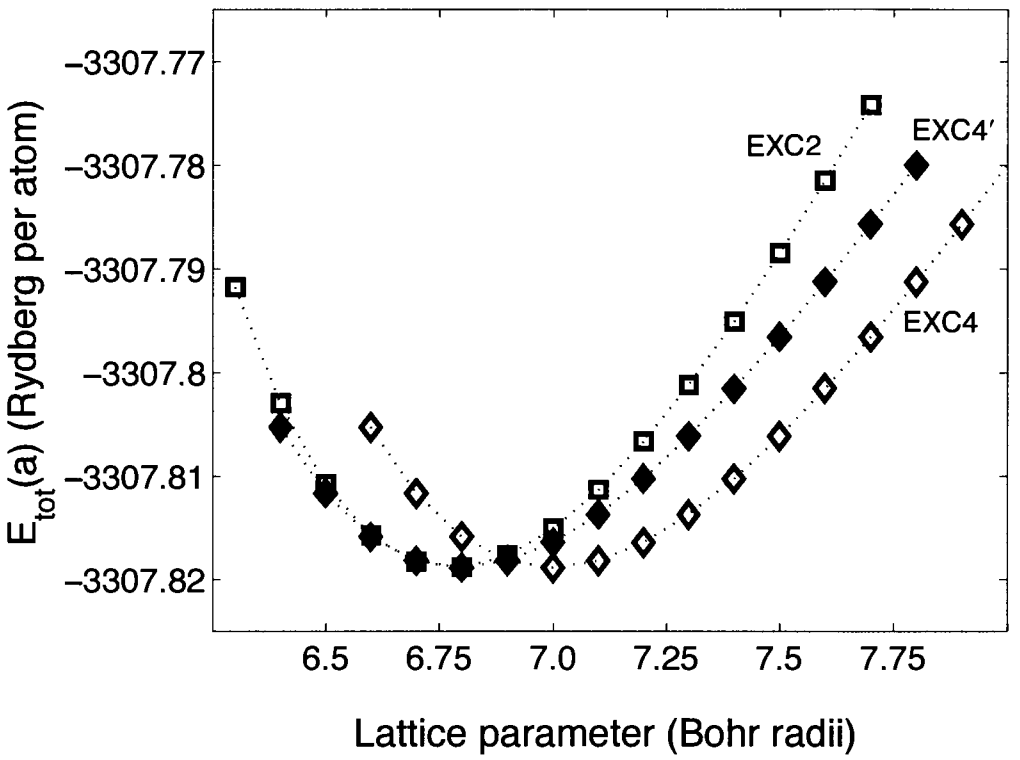

Figure 7.2: Calculated $E_{tot}\,(a)$ curve of FCC Cu in the vicinity of its global minimum value. Squares (open diamonds) denote the EXC2 (EXC4) $E_{tot}\,(a)$ curve. Filled diamonds denote the EXC4′ $E_{tot}\,(a)$ curve, which is constructed by translating leftward by 0.2 Bohr radii the EXC4 $E_{tot}\,(a)$ curve. To facilitate the comparison of the curves, the EXC4 and EXC4′ $E_{tot}\,(a)$ curves are shown translated upward by 3.39462 Rydberg units. Data symbols indicate actual calculated values of the curves. Error bars denoting the numerical uncertainty of the calculated values are omitted as they are smaller than the data symbols.

Having calculated the EXC2, EXC4 and EXC4' $E_{tot}(a)$ curves of FCC Cu, we now define three inter-atomic interaction potentials $E_{a-a}(x)$, which we respectively label the EXC2, EXC4 and EXC4' $E_{a-a}(x)$ potential. The inter-atomic interaction potentials that we define act between each pair of atomic nuclei in the metallic Cu solid, and are dependent only upon the separation x of the pair of atomic nuclei. We assume that the minimum total energy versus lattice parameter curve of the FCC Cu solid can be expressed in terms of a potential $E_{a-a}(x)$ as follows (see equation 6.17) [137]:

$$E_{tot}(a) = \frac{1}{2}\sum_{n=1}^{\infty} r[n]\, E_{a-a}\left(\frac{b[n]\, a}{\sqrt{2}}\right) \tag{7.1}$$

Under this assumption, the inter-atomic interaction potential $E_{a-a}(x)$ of FCC Cu can be expressed in terms of the $E_{tot}(a)$ curve of FCC Cu as follows (see equation 6.18) [137]:

$$E_{a-a}(x) = 2\sum_{n=1}^{\infty} I[n]\left(E_{tot}\left(\sqrt{2}b[n]\, x\right)\right). \tag{7.2}$$

Because equations 7.1 and 7.2 specifically apply to a solid possessing the FCC crystal structure, the constants $r[n]$, $b[n]$ and $I[n]$ appearing in the equations are as given in table 7.3. These constants are originally reported, albeit with some errors, in the paper by Chen, Chen and Wei [137]. They are reported without errors in table 7.3. It is also because equations 7.1 and 7.2 apply specifically to a solid possessing the FCC crystal structure that the argument of the $E_{a-a}(x)$ potential appearing on the right hand side of equation 7.1 is proportional to $\frac{a}{\sqrt{2}}$, and that the argument of the $E_{tot}(a)$ curve appearing on the right hand side of equation 7.2 is proportional to $\sqrt{2}x$. If in a FCC solid, the shortest distance between any pair of atoms is x, then the lattice parameter of the solid is $a = \sqrt{2}x$.

Prior to calculating the Helmholtz' free energy curve $F(a,T)$ and the lattice parameter versus temperature curve $a(T)$ of FCC Cu, we illustrate, in figure 7.3, some of the inter-atomic interaction potentials $E_{a-a}(x)$ that we construct using the method of Chen, Chen and Wei. Specifically, figure 7.3 shows four potentials, two obtained using the EXC2 $E_{tot}(a)$ curve, and two obtained using the EXC4 $E_{tot}(a)$ curve. Two of these potentials have range of action restricted to the distance separating any atom in a FCC Cu solid from its first nearest neighbours. We label these potentials the 1NN EXC2 $E_{a-a}(x)$ potential and

Table 7.3: Constants $r\,[n]$, $b\,[n]$ and $I\,[n]$ for the FCC crystal structure

n	1	2	3	4	5	6	7	8
$r\,[n]$	12	6	24	12	24	8	48	6
$b\,[n]$	1	$\sqrt{2}$	$\sqrt{3}$	2	$\sqrt{5}$	$\sqrt{6}$	$\sqrt{7}$	$\sqrt{8}$
$I\,[n]$	$\frac{1}{12}$	$\frac{-1}{24}$	$\frac{-1}{6}$	$\frac{-1}{16}$	$\frac{-1}{6}$	$\frac{1}{9}$	$\frac{-1}{3}$	$\frac{1}{32}$
n	9	10	11	12	13	14	15	
$r\,[n]$	36	24	24	24	72	0	48	
$b\,[n]$	3	$\sqrt{10}$	$\sqrt{11}$	$\sqrt{12}$	$\sqrt{13}$	$\sqrt{14}$	$\sqrt{15}$	
$I\,[n]$	$\frac{1}{12}$	0	$\frac{-1}{6}$	$\frac{7}{72}$	$\frac{-1}{2}$	$\frac{1}{3}$	$\frac{1}{3}$	

All constants are unitless.

the 1NN EXC4 $E_{a-a}\,(x)$ potential. The other two potentials have range of action restricted to the distance separating separating any atom in a FCC Cu solid from its seventh nearest neighbours. We label these potentials the 7NN EXC2 $E_{a-a}\,(x)$ potential and the 7NN EXC4 $E_{a-a}\,(x)$ potential. Figure 7.3 shows only a short segment of the aforementioned potentials. We did not calculate the entirety of these potentials because we only require knowledge of them over a restricted range of inter-atomic separations x in order to calculate the lattice parameter versus temperature curve of metallic Cu using the method of chapter 6.

We also include, in figure 7.3, the inter-atomic interaction potential for FCC Cu published by Carlsson, Gelatt and Ehrenreich [154]. Carlsson, Gelatt and Ehrenreich constructed an inter-atomic interaction potential for FCC Cu and used it to calculate some of the elastic properties of metallic Cu, with moderate success. However, as we indicated in chapter 6, a potential $E_{a-a}\,(x)$ that acts between a given atomic nucleus and its first nearest neighbours can be constructed exactly using the "Carlsson-Gelatt method" [154]. The Carlsson-Gelatt method provides only an approximate procedure for constructing inter-atomic interaction potentials that have a longer range.

In order to meaningfully compare our $E_{a-a}(x)$ potential to that of Carlsson, Gelatt and Ehrenreich, we subtracted the value $\lim_{a\to\infty} E_{tot}(a)$ from the calculated $E_{tot}(a)$ curves before computing the values of $E_{a-a}(x)$ shown in figure 7.3. We do so because Carlsson, Gelatt and Ehrenreich constructed their $E_{a-a}(x)$ potential using a cohesive energy curve $E_{coh}(a)$. The cohesive energy of a solid can be expressed as $E_{coh}(a) = E_{tot}(a) - \lim_{a\to\infty} E_{tot}(a)$. To construct $E_{coh}(a)$ curves using our calculated $E_{tot}(a)$ curves, we evaluated the limit $\lim_{a\to\infty} E_{tot}(a)$ using the parametrization of the 15NNandmore range of our $E_{tot}(a)$ curves (see appendix B).

It is clear, in figure 7.3, that our inter-atomic interaction potentials are significantly different of that of Carlsson, Gelatt and Ehrenreich. We believe that this is due to two factors. Firstly, Carlsson, Gelatt and Ehrenreich derived their inter-atomic interaction potential from a cohesive energy versus lattice parameter curve of FCC Cu calculated using a local exchange-correlation functional [154]. We derive our potentials using $E_{tot}(a)$ curves of FCC Cu obtained using non-local exchange-correlation functionals. We have shown in chapter 4 that the $E_{tot}(a)$ curves of the first-row transition metals calculated using local exchange-correlation functionals are significantly different of the same curves but calculated using a non-local exchange-correlation functional. Secondly, the method used by Carlsson, Gelatt and Ehrenreich to construct their inter-atomic interaction potential differs from the method that we used to derive ours, namely the method of Chen, Chen and Wei [137].

In addition, figure 7.3 illustrates that the EXC2 $E_{a-a}(x)$ potentials are significantly different of the EXC4 $E_{a-a}(x)$ potentials. This is expected, as the EXC2 and EXC4 $E_{tot}(a)$ curves of FCC Cu have significantly different functional forms. We shall return to this later.

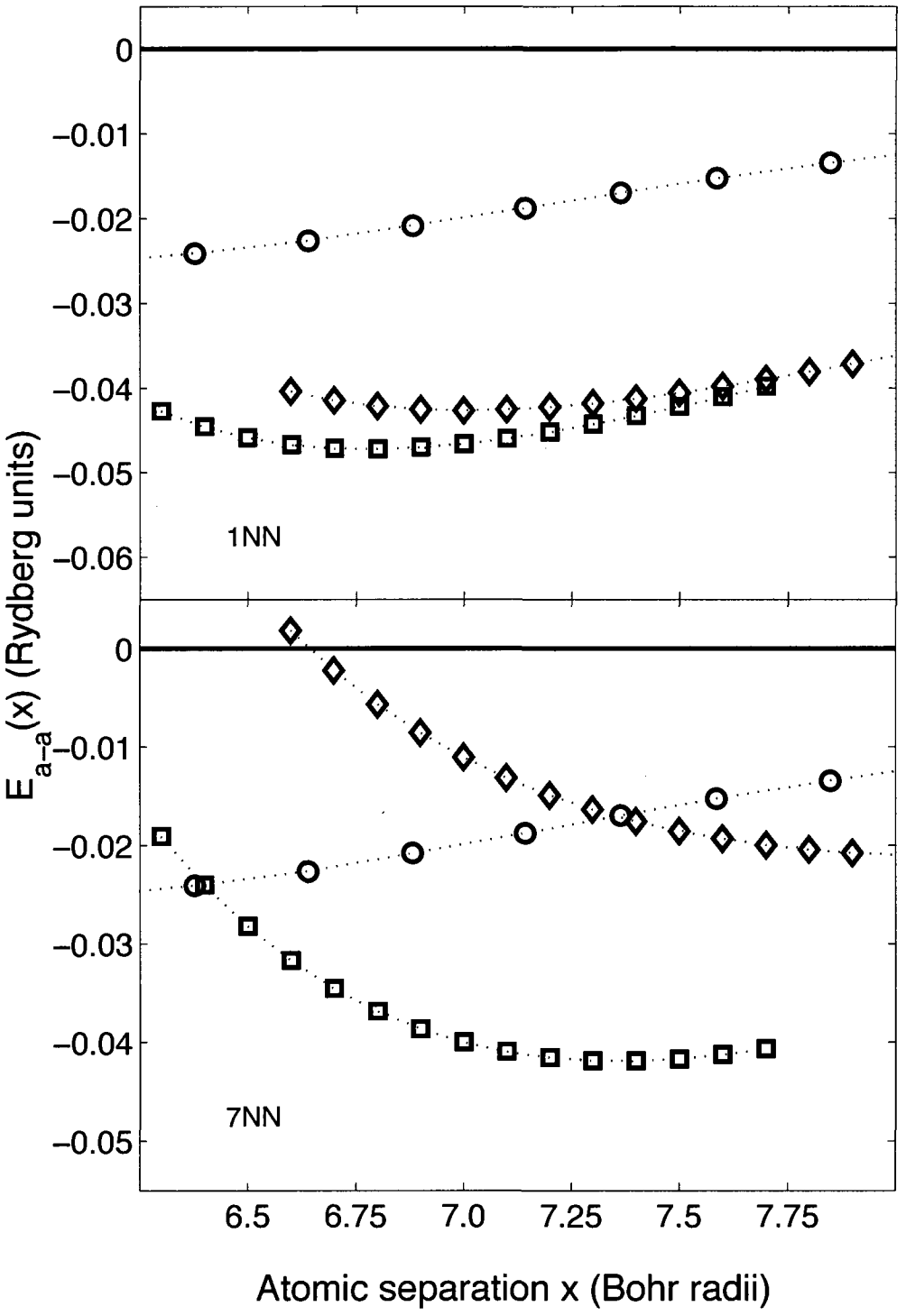

Figure 7.3: Calculated $E_{a-a}(x)$ potentials of FCC Cu obtained using the method of Chen, Chen and Wei. The upper (lower) figure shows 1NN (7NN) potentials. Squares (diamonds) denote the EXC2 (EXC4) $E_{a-a}(x)$ potential. Circles denote the potential of Carlsson, Gelatt and Ehrenreich [154]. Error bars denoting the numerical uncertainty of the calculated values are omitted as they are smaller than the data symbols.

7.2 Calculation of the F (a, T) Curve of Metallic Cu

Having completed the first step in the calculation of the $a\,(T)$ curve of metallic Cu, namely the calculation and parametrization of the $E_{tot}\,(a)$ curve of FCC Cu, we now calculate the $F\,(a,T)$ curve of metallic Cu using the method presented in chapter 6. We here describe how to do so using both the mean-field potential method and the phonon spectrum method, described respectively in sections 6.2.2 and 6.2.3 of chapter 6.

7.2.1 F (a, T) Curve Using the Mean-Field Potential Method

Within the mean-field potential method, the Helmholtz' free energy of a metallic Cu solid, as a function of its lattice parameter a and its temperature T, is:

$$F\,(a,T) = E_{tot}\,(a) + \frac{3}{2}\hbar\omega\,(a) + 3k_BTln\left\{1 - e^{\frac{-\hbar\omega(a)}{k_BT}}\right\}. \tag{7.3}$$

Equation 7.3 is derived from equation 6.23 and gives the Helmholtz' free energy per atom of the metallic Cu solid. In the equation, $E_{tot}\,(a)$ is the minimum total energy versus lattice parameter curve of FCC Cu. Also, $\hbar$ is Planck's constant divided by 2π, k_B is Boltzman's constant, ln denotes a natural logarithm, and $\omega\,(a)$ is the frequency of oscillation of the atomic nuclei of the metallic Cu solid.

Within the mean-field potential method, the atomic nuclei of the metallic Cu solid are modelled as a collection of independent harmonic oscillators oscillating about their mean positions. They oscillate with frequency $\omega\,(a)$ defined as follows:

$$\omega\,(a) = \sqrt{\frac{1}{3M}\sum_{n=1}^{\infty}\left\{r\,[n]\,E^{(2)}_{a-a}\left(b\,[n]\,\frac{a}{\sqrt{2}}\right) + \frac{2r\,[n]\,E^{(1)}_{a-a}\left(b\,[n]\,\frac{a}{\sqrt{2}}\right)}{b\,[n]\,\frac{a}{\sqrt{2}}}\right\}}. \tag{7.4}$$

Equation 7.4 is derived from equation 6.21. In the equation, M is the mass of a Cu atom, and $E^{(1)}_{a-a}\left(b\,[n]\,\frac{a}{\sqrt{2}}\right)$ and $E^{(2)}_{a-a}\left(b\,[n]\,\frac{a}{\sqrt{2}}\right)$ denote respectively the first- and second-derivative of an inter-atomic interaction potential $E_{a-a}\,(x)$, with respect to its full argument x, evaluated at $x = b\,[n]\,\frac{a}{\sqrt{2}}$. In calculating the oscillation frequencies $\omega\,(a)$, we do

not construct the potential $E_{a-a}(x)$ and then evaluate its derivatives. Rather, we calculate the derivatives of the potential $E_{a-a}(x)$ using the derivatives of the $E_{tot}(a)$ curve and the definition of $E_{a-a}(x)$ provided in section 7.1 of this chapter. $E_{a-a}(x)$ is constructed using the $E_{tot}(a)$ curve of FCC Cu as per equation 7.2. Because equations 7.2 and 7.4 specifically apply to a solid possessing the FCC crystal structure, the constants $r[n]$, $b[n]$ and $I[n]$ appearing in these equations are as given in table 7.3.

Equations 7.2, 7.3 and 7.4 are the basis of the calculation of the $F(a,T)$ curve of metallic Cu using the mean-field potential method presented in chapter 6. Using this method, we calculate the value of the $F(a,T)$ curve of metallic Cu at 1296 (a,T)-couples, where T takes one of the temperatures at which we have access to an experimental measurement of the lattice parameter of metallic Cu (these temperatures are shown in table 7.4) [80], and where a takes one of 81 values lying in the interval $6.7 \leq a \leq 7.5$ Bohr radii, all uniformly separated by an interval of 0.01 Bohr radii. We sequentially calculate these 1296 values of the $F(a,T)$ curve of metallic Cu using two "while loops". The first loop runs over the 81 previously described lattice parameter values in the range $6.7 \leq a \leq 7.5$ Bohr radii. This first loop is embedded into a second while loop that runs over all temperatures shown in table 7.4. For each value of lattice parameter a, a frequency $\omega(a)$ is calculated as per equation 7.4. This frequency is then used to calculate the Helmholtz' free energy $F(a,T)$ as per equation 7.3. Values of the Helmholtz' free energy for all (a,T)-couples thus defined are stored for later analysis.

We realize that it would have been more efficient to embed the temperature loop into the lattice parameter loop rather than embedding the lattice parameter loop into the temperature loop as we have done. This is because the oscillation frequencies $\omega(a)$ are independent of temperature. Our implementation of the calculation of the $F(a,T)$ curve of FCC Cu entails multiple calculations of the same frequencies $\omega(a)$. This has not been problematic, as even our calculation could be performed rapidly. Nonetheless, we do intend to implement the more efficient calculation scheme in the future.

When calculating the $F(a,T)$ curve of metallic Cu, we must specify the range of action

of the potential $E_{a-a}(x)$. To do so, we simply restrict the summations in equations 7.4 and 7.2 to some maximum value $n = i$. This effectively restricts the range of action of $E_{a-a}(x)$ to the distance separating a given atomic nucleus in the metallic Cu solid from its i^{th} nearest neighbours. We shall show, in sections 7.2.3 and 7.3, that the range of action of $E_{a-a}(x)$ can significantly affect the accuracy of the calculated $F(a,T)$ curve and of the calculated $a(T)$ curve of metallic Cu. We also require knowledge of the $E_{tot}(a)$ curve of FCC Cu in order to construct the $F(a,T)$ curve of metallic Cu as per equation 7.3, and to calculate the potential $E_{a-a}(x)$ as per equation 7.2. We run each calculation using one of the EXC2, the EXC4 or the EXC4' $E_{tot}(a)$ curve of FCC Cu, as calculated and parametrized in section 7.1.

In addition, we use the numerical precision of the calculated $E_{tot}(a)$ curve of FCC Cu, as well as the numerical precision of its first- and second-derivatives $E_{tot}^{(1)}(a)$ and $E_{tot}^{(2)}(a)$, to estimate the numerical precision of the calculated $F(a,T)$ curve of metallic Cu. The numerical precision of $E_{tot}(a)$, $E_{tot}^{(1)}(a)$ and $E_{tot}^{(2)}(a)$ must be understood as an estimate of the standard deviation of the distribution of the calculation precision errors (CPE's) in the values of these functions (see chapter 3). We estimate the numerical precision of the calculated values of the $F(a,T)$ curve of metallic Cu by propagating the uncertainties of the values of $E_{tot}(a)$, $E_{tot}^{(1)}(a)$ and $E_{tot}^{(2)}(a)$. We do so by treating the uncertainty of a function as a first-order correction of the value of the function. Thus, we take the value of a function $f(x)$, evaluated at $x = x_0 \pm \Delta x_0$, to be:

$$f(x_0 \pm \Delta x_0) = f(x_0) \pm \frac{d}{dx} f(x)\Big|_{x=x_0} \Delta x_0, \tag{7.5}$$

where $\frac{d}{dx} f(x)\big|_{x=x_0}$ is the derivative of $f(x)$ with respect to its full argument x, evaluated at $x = x_0$.

Finally, all physical constants required to calculate the $F(a,T)$ curve of metallic Cu are taken from the web-site of the National Institute of Science and Technology of the United States of America [201], and the mass of a Cu atomic nucleus is taken as reported in the WebElements^{TM} Periodic Table [202].

Table 7.4: Temperatures at which values of the $F(a,T)$ curve of FCC Cu are calculated

Temperature
1 K
5 K
25 K
50 K
100 K
200 K
293 K
400 K
500 K
600 K
700 K
800 K
900 K
1000 K
1200 K
1300 K

7.2.2 F (a, T) Curve Using the Phonon Spectrum Method

Within the phonon spectrum method, the Helmholtz' free energy of a metallic Cu solid, as a function of its lattice parameter a and its temperature T, is:

$$\begin{aligned} F(a,T) &= E_{tot}(a) + \frac{1}{2}\sum_{\lambda=1}^{3}\frac{a^3}{4\cdot(2\pi)^3}\int_{BZ}\hbar\Omega_\lambda\left(\vec{k},a\right)d\vec{k} \\ &+ k_BT\sum_{\lambda=1}^{3}\frac{a^3}{4\cdot(2\pi)^3}\int_{BZ} ln\left\{1-e^{-\frac{\hbar\Omega_\lambda(\vec{k},a)}{k_BT}}\right\}d\vec{k}. \end{aligned} \tag{7.6}$$

Equation 7.6 is derived from equation 6.27 and gives the free energy per atom of the metallic Cu solid. In equation 7.6, $E_{tot}(a)$ is the minimum total energy versus lattice parameter curve of FCC Cu. Also, $\hbar$ is Planck's constant divided by 2π, k_B is Boltzman's constant, ln denotes a natural logarithm, and $\Omega_\lambda\left(\vec{k},a\right)$ is the frequency of oscillation of the atomic nuclei of the metallic Cu solid when they oscillate in a phonon mode with wave vector $\vec{k}$. Finally, the summations over λ run over all three phonon modes associated to wave vector $\vec{k}$, and the integrals run over the first Brillouin zone (BZ) of the metallic Cu solid.[1]

Within the phonon spectrum method, the atomic nuclei of a metallic Cu solid are treated as coupled harmonic oscillators. Thus, they oscillate collectively in well-defined modes of oscillation termed "phonon modes". All phonon modes are associated to a wave vector $\vec{k}$ in the first BZ of the metallic Cu solid. There are in fact three phonon modes associated to each vector $\vec{k}$ in the solid's first BZ. To calculate the frequency of oscillation $\Omega\left(\vec{k},a\right)$ of the atomic nuclei of a metallic Cu solid when they oscillate in a phonon mode associated to a specific vector $\vec{k}$, we must define the characteristic polynomial of the following equation (see equation 6.25):

$$-M\Omega^2\left(\vec{k},a\right)\Delta\vec{R}_I(t) = -\vec{\nabla}_I U_{vib}\left((\ldots),\left\langle\vec{R}_I\right\rangle + \Delta\vec{R}_I(t),(\ldots)\right), \tag{7.7}$$

where M is the mass of a Cu atom, and $\Delta\vec{R}_I(t)$ is the displacement as a function of time of the I^{th} atomic nucleus of the metallic Cu solid, relative to its mean position, as it oscillates in a phonon mode with wave vector $\vec{k}$ (see equation 6.24). Also, $\vec{\nabla}_I$ is the gradient operator $\hat{x}\frac{d}{d\Delta\vec{R}_{Ix}} + \hat{y}\frac{d}{d\Delta\vec{R}_{Iy}} + \hat{z}\frac{d}{d\Delta\vec{R}_{Iz}}$ and $U_{vib}\left((\ldots),\left\langle\vec{R}_I\right\rangle + \Delta\vec{R}_I(t),(\ldots)\right)$ is the vibration potential of the atomic nuclei of a metallic Cu solid with lattice parameter a. We evaluate the gradient of this vibration potential using the Taylor expansion presented in section 6.5 of chapter 6. Because we specifically require the vibration potential of the atomic nuclei of a metallic Cu solid with lattice parameter a, all vectors $\left\langle\vec{R}_I\right\rangle$ in the expression for $U_{vib}\left((\ldots),\left\langle\vec{R}_I\right\rangle + \Delta\vec{R}_I(t),(\ldots)\right)$ describe the average position of one of the atomic nuclei of the metallic Cu solid when it has lattice parameter a. In addition, the Taylor expansion

[1] As previously indicated, the atomic nuclei of metallic Cu are arranged in the FCC crystal structure at all temperatures below its melting point [1]. The geometry of the first BZ of a FCC solid is described in detail in the text of Bradley and Cracknell [203].

of $U_{vib}\left(\left(\ldots\right),\left\langle\vec{R}_I\right\rangle+\Delta\vec{R}_I\left(t\right),\left(\ldots\right)\right)$ is defined in terms of the first- and second-derivative of an inter-atomic interaction potential $E_{a-a}\left(x\right)$, itself defined as per equation 7.2. In calculating the gradient $\vec{\nabla}_I U_{vib}\left(\left(\ldots\right),\left\langle\vec{R}_I\right\rangle+\Delta\vec{R}_I\left(t\right),\left(\ldots\right)\right)$, we do not construct the potential $E_{a-a}\left(x\right)$ and then evaluate its derivatives. Rather, we calculate the derivatives of the potential $E_{a-a}\left(x\right)$ using the derivatives of the $E_{tot}\left(a\right)$ curve and the definition of $E_{a-a}\left(x\right)$ provided in section 7.1. Because $E_{a-a}\left(x\right)$ is an inter-atomic interaction potential acting between the atomic nuclei of a FCC solid, the constants $b\left[n\right]$ and $I\left[n\right]$ appearing in equation 7.2 are as given in table 7.3. The characteristic polynomial of equation 7.7 is a third-order polynomial in $\Omega^2\left(\vec{k},a\right)$. The roots of this polynomial are the squares of the three frequencies $\Omega\left(\vec{k},a\right)$ associated to each of the three phonon modes with wave vector $\vec{k}$.

Equations 7.2, 7.6 and 7.7 are the basis of the calculation of the $F\left(a,T\right)$ curve of metallic Cu using the phonon spectrum method. Using this method, we calculate the value of the $F\left(a,T\right)$ curve of metallic Cu at 1296 (a,T)-couples, where T takes one of the temperatures at which we have access to an experimental measurement of the lattice parameter of metallic Cu (see table 7.4) [80], and where a takes one of 81 values lying in the interval $6.7\leq a\leq 7.5$ Bohr radii, all uniformly separated by an interval of 0.01 Bohr radii. We sequentially calculate these 1296 values of the $F\left(a,T\right)$ curve of metallic Cu using two "while loops". The first loop runs over the 81 previously described lattice parameter values in the range $6.7\leq a\leq 7.5$ Bohr radii. This first loop is embedded into a second while loop that runs over all temperatures shown in table 7.4. For each value of lattice parameter a, we calculate a phonon spectrum for the FCC Cu solid. To do so, we use the characteristic polynomial of equation 7.7 to calculate the three phonon frequencies $\Omega\left(\vec{k},a\right)$ associated to each of approximately 37000 $\vec{k}$-vectors, all located in a volume equal to one 48^{th} of the total volume of the first BZ of metallic Cu. Although knowledge of $\Omega\left(\vec{k},a\right)$ is required throughout the entire first BZ of the metallic Cu solid, it is sufficient to calculate values of $\Omega\left(\vec{k},a\right)$ in only one 48^{th} of this volume because of the geometric symmetry of the first BZ of FCC solids [203]. For each vector $\vec{k}$ just described, we use equation 7.7 to define a third-order polynomial in $\Omega^2\left(\vec{k},a\right)$. We use a bisection method to find the first root of this polynomial. We then use long division to factor the polynomial, and obtain its

two remaining roots using the quadratic formula. Having completed the calculation of the phonon spectrum, we use equation 7.6 to calculate $F(a,T)$. We evaluate the integrals in equation 7.6 using the calculated phonon frequencies $\Omega\left(\vec{k},a\right)$ in a Riemann sum [74]. We ascertained that when they are evaluated using ≈ 37000 $\vec{k}$-vectors, the numerical estimates of the integrals of equation 7.6 contain systematic calculation errors (SCE's) that are sufficiently small to allow for a meaningful comparison of the $F(a,T)$ curve of FCC Cu as obtained using the phonon spectrum method and as obtained using the mean-field potential method. Values of the Helmholtz' free energy at all (a,T)-couples are stored for later analysis.

As in the mean-field potential method, we realize that it would have been more efficient to embed the temperature loop into the lattice parameter loop rather than embedding the lattice parameter loop into the temperature loop as we have done. This is because the phonon frequencies $\Omega\left(\vec{k},a\right)$ are independent of temperature. Our implementation of the calculation of the $F(a,T)$ curve of FCC Cu entails multiple calculations of the same frequencies $\Omega\left(\vec{k},a\right)$. This is time consuming, and we shall therefore implement the more efficient calculation scheme in the future.

When using the phonon spectrum method, we must specify the range of the potential $E_{a-a}(x)$. To do so, we restrict the summation in equation 7.2 to some maximum value $n=i$. This effectively restricts the range of action of $E_{a-a}(x)$ to the distance separating a given atomic nucleus in the metallic Cu solid from its i^{th} nearest neighbours. Importantly, when the range of $E_{a-a}(x)$ is restricted in this manner, the gradient appearing in equation 7.7 must reflect this reality. This is accomplished by including only atomic nuclei within the i^{th} nearest atomic coordination shell of the I^{th} atomic nucleus of the metallic Cu solid when constructing the expression for $U_{vib}\left(\left(\ldots\right),\left\langle\vec{R}_I\right\rangle+\Delta\vec{R}_I(t),\left(\ldots\right)\right)$. We shall show, in sections 7.2.3 and 7.3, that the range of action of $E_{a-a}(x)$ can significantly affect the accuracy of the calculated $F(a,T)$ curve and of the calculated $a(T)$ curve of metallic Cu.When using the phonon spectrum method, we also require knowledge of the $E_{tot}(a)$ curve of FCC Cu in order to construct the $F(a,T)$ curve of metallic Cu as per equation 7.6, and to construct the potential $E_{a-a}(x)$ as per equation 7.2. For this purpose, we use one of the

EXC2, the EXC4 or the EXC4' $E_{tot}(a)$ curves of FCC Cu, as calculated and parametrized in section 7.1.

In addition, we use the estimated numerical precision of the calculated $E_{tot}(a)$ curves of FCC Cu, as well as the estimated numerical precision of their first- and second-derivatives $E_{tot}^{(1)}(a)$ and $E_{tot}^{(2)}(a)$, to estimate the numerical precision of the calculated $F(a,T)$ curve of metallic Cu. We do so by propagating the numerical uncertainties of the values of $E_{tot}(a)$, $E_{tot}^{(1)}(a)$ and $E_{tot}^{(2)}(a)$, treating them as first-order corrections to the value of a function as per equation 7.5.

Finally, all physical constants required to calculate the $F(a,T)$ curve of metallic Cu are taken from the web-site of the National Institute of Science and Technology of the United States of America [201], and the mass of a Cu atomic nucleus is taken as reported in the WebElements^{TM} Periodic Table [202].

7.2.3 A Typical Calculated F (a, T) Curve

We show here some calculated $F(a,T)$ curves of metallic Cu. We show these curves for the purpose of illustrating a typical calculated $F(a,T)$ curve of metallic Cu, and for bringing to the reader's attention some matters of importance to the evaluation of the accuracy of such curves.

Firstly, we show, in figures 7.4 and 7.5, the 1NN EXC2 $F(a,T)$ curve of metallic Cu as obtained using the mean-field potential method and the phonon spectrum method. The curves are shown at $T = 293$ Kelvin and $T = 1300$ Kelvin in figures 7.4 and 7.5 respectively. The $F(a,T)$ curves in question are calculated using the EXC2 $E_{tot}(a)$ curve of FCC Cu. They are also calculated using an inter-atomic interaction potential $E_{a-a}(x)$ with range of action extending only to the distance separating a given atomic nucleus in the metallic Cu solid from its first nearest neighbours. It is for these reasons that we label these curves "1NN EXC2 $F(a,T)$ curves".

It is immediately evident, when observing figures 7.4 and 7.5, that the numerical precision of the $F(a,T)$ curve obtained using the mean-field potential method is greater than that of the curve obtained using the phonon spectrum method. This is due to the fact that we can more precisely evaluate the last two terms of equation 7.3 than the two integrals of equation 7.6. In addition, the numerical precision of both calculated $F(a,T)$ curves is greater at lower temperatures. This is because the numerical precision of the last term of equation 7.3 and of equation 7.6 is higher at lower temperatures.

Also, both calculated $F(a,T)$ curves have $\frac{\delta}{\delta a}F(a,T) = 0$ at a larger value of lattice parameter when T is larger. This is expected, as the equilibrium lattice parameter of metallic Cu is larger at larger temperatures as a result of the metal's thermal expansion. More importantly, the calculated values of the $F(a,T)$ curve obtained using the phonon spectrum method are significantly smaller than those of the $F(a,T)$ curve obtained using the mean-field potential method in both figures 7.4 and 7.5. This is not due to roundoff errors, nor is it due to the presence of SCE's in the numerical estimates of the integrals that must be evaluated when calculating the $F(a,T)$ curve of metallic Cu using the phonon spectrum method. We thus expect that one of these $F(a,T)$ curves is more accurate, in the sense that it is more similar to the $F(a,T)$ curve of real metallic Cu. We do not here evaluate the accuracy of these $F(a,T)$ curves, but we shall revisit this matter in the following sections of this chapter.

In figure 7.6, we show the EXC2 $F(a,T)$ curve of metallic Cu, as obtained using the mean-field potential method and inter-atomic interaction potentials $E_{a-a}(x)$ with different ranges of action. Specifically, we show the 1NN, the 3NN, the 7NN and the 15NN EXC2 $F(a,T)$ curves of metallic Cu, as obtained using the mean-field potential method. The figure clearly shows that the 1NN and 3NN curves are both significantly different of all other curves while the 7NN and 15NN curves are not significantly different of each other. This indicates that the choice of the range of action of the inter-atomic interaction potential $E_{a-a}(x)$ significantly affects the accuracy of the calculated $F(a,T)$ curve of metallic Cu. We shall revisit this matter in the following sections of this chapter as well.

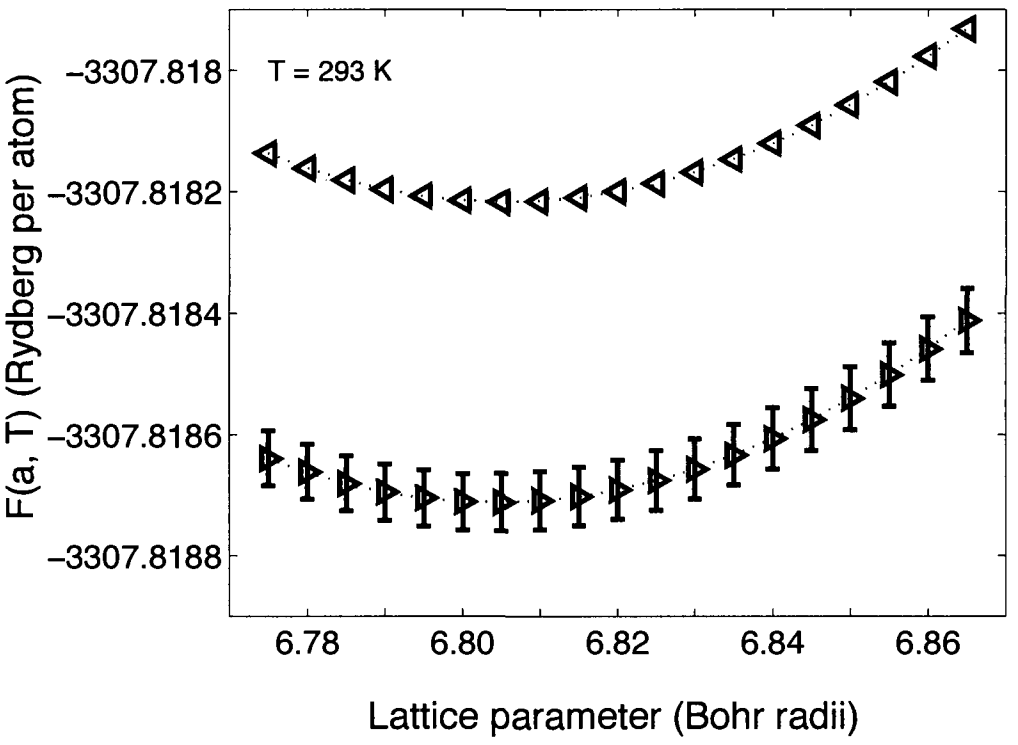

Figure 7.4: 1NN EXC2 $F(a,T)$ curve of metallic Cu at $T = 293$ Kelvin. Leftward-pointing triangles (rightward-pointing triangles) show the curve as obtained using the mean-field potential method (phonon spectrum method). Data symbols denote actual calculated values of the 1NN EXC2 $F(a,T)$ curve. Error bars denote the numerical uncertainty of the calculated values of the curve. No error bars are added to the curve obtained using the mean-field potential method as they are approximately as large as the data symbols.

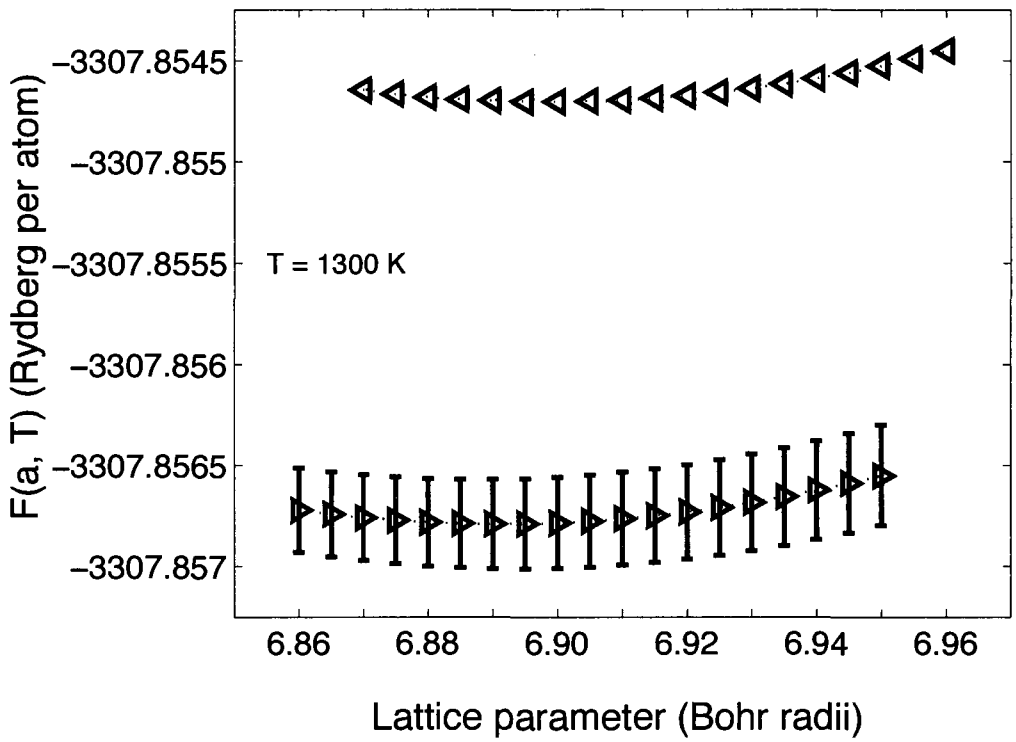

Figure 7.5: 1NN EXC2 $F(a,T)$ curve of metallic Cu at $T = 1300$ Kelvin. Leftward-pointing triangles (rightward-pointing triangles) show the curve as obtained using the mean-field potential method (phonon spectrum method). Data symbols denote actual calculated values of the 1NN EXC2 $F(a,T)$ curve. Error bars denote the numerical uncertainty of the calculated values of the curve. No error bars are added to the curve obtained using the mean-field potential method as they are approximately as large as the data symbols.

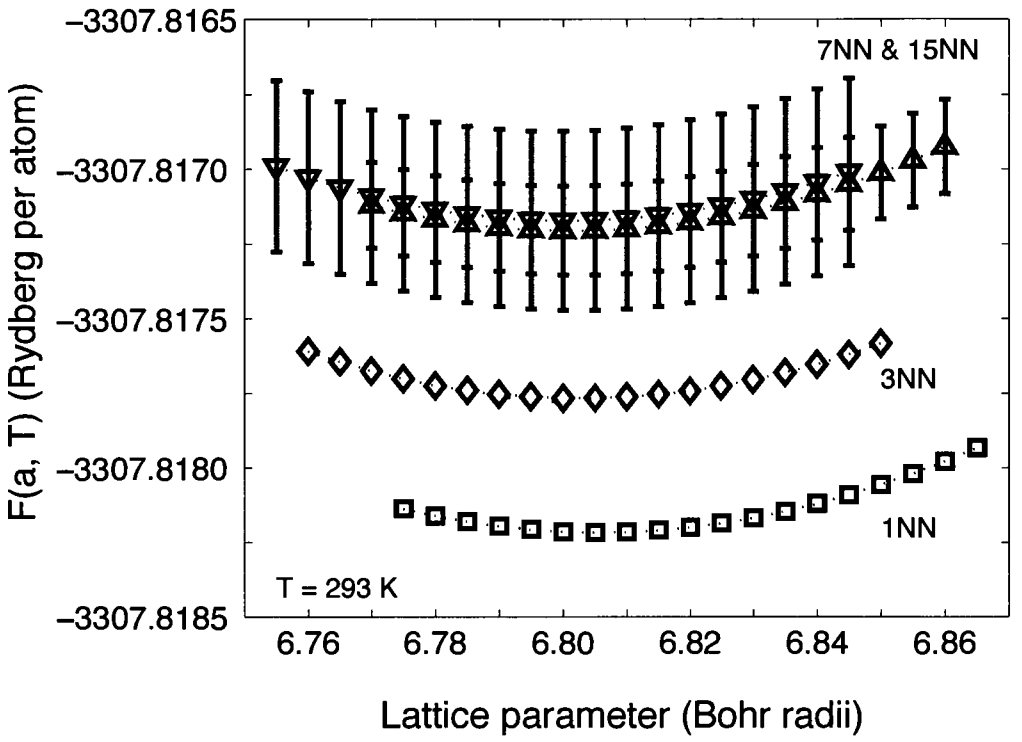

Figure 7.6: EXC2 $F(a,T)$ curve of metallic Cu at $T = 293$ Kelvin, calculated using the mean-field potential method. The figure shows the calculated 1NN (squares), 3NN (diamonds), 7NN (upward-pointing triangles), and 15NN (downward-pointing triangles) EXC2 $F(a,T)$ curves. Data symbols denote actual calculated values of the curves. Error bars denote the numerical uncertainty of the calculated values. They are omitted if they are smaller than the data symbols.

7.3 Calculation of the a (T) Curve of Metallic Cu

We now calculate the lattice parameter versus temperature curve $a\,(T)$ of metallic Cu. As per section 6.1 of chapter 6, the lattice parameter of a bulk metallic Cu solid in thermal equilibrium with its environment at temperature T is that at which $\frac{\delta}{\delta a}F\,(a,T) = 0$. We here calculate the $a\,(T)$ curve of metallic Cu using $F\,(a,T)$ curves calculated as described in section 7.2. We calculate $a\,(T)$ curves using both the mean-field potential method and the phonon spectrum method.

7.3.1 a (T) Curve of Metallic Cu Using the Mean-Field Potential Method

To calculate the $a\,(T)$ curve of metallic Cu using the mean-field potential method, we first calculate the $F\,(a,T)$ curve of metallic Cu as described in section 7.2.1. Of course, this requires that we specify the range of action of the inter-atomic interaction potential $E_{a-a}\,(x)$, and that we use one of the EXC2, the EXC4 or the EXC4' $E_{tot}\,(a)$ curves described in section 7.1. To identify a specific calculated $a\,(T)$ curve, we use a nomenclature similar to that used to designate the calculated $F\,(a,T)$ curves described in section 7.2. For instance, we label the $a\,(T)$ curve obtained from the 1NN EXC2 $F\,(a,T)$ curve the "1NN EXC2 $a\,(T)$ curve". This $a\,(T)$ curve is calculated using the EXC2 $E_{tot}\,(a)$ curve and an inter-atomic interaction potential $E_{a-a}\,(x)$ with range of action restricted to the distance separating a given atomic nucleus in the metallic Cu solid from its first nearest neighbours.

Consider now the calculation of the 1NN EXC2 $a\,(T)$ curve of metallic Cu. We calculate a value of this curve at each temperature reported in table 7.4. To calculate a value of the curve at a specific temperature T, we begin with the 81 values of the 1NN EXC2 $F\,(a,T)$ curve of metallic Cu associated to temperature T and calculated as reported in section 7.2.1. We then identify the smallest of these 81 values of the 1NN EXC2 $F\,(a,T)$ curve, as well as the lattice parameter a_{min} at which it occurs. We then calculate 201 new values of the 1NN EXC2 $F\,(a,T)$ curve, all at temperature T, but each at one of 201 lattice parameters lying in the interval $a_{min} - 0.5 \leq a \leq a_{min} + 0.5$ Bohr radii. These latter lattice

parameters are uniformly separated by an interval of 0.005 Bohr radii. We then fit these 201 new values with a fourth-order polynomial using a standard non-linear least-squares algorithm [204]. We evaluate a one - σ confidence interval for the coefficients of this polynomial using the estimated numerical uncertainty of the calculated values of the 1NN EXC2 $F(a,T)$ curve [204]. Using a bisection method [74], we find the lattice parameter at which the first-derivative of this polynomial is null. This is the value of the 1NN EXC2 $a(T)$ curve of metallic Cu at temperature T. We then evaluate the numerical precision of this lattice parameter using the confidence intervals of the coefficients of the fourth-order polynomial as described in the subsection entitled "Second Approach" in section B.1 of appendix B.

Figure 7.7 shows the calculated $a(T)$ curve of metallic Cu as obtained using the mean-field potential method. The upper part of the figure shows the 1NN, 3NN, 7NN and 15NN EXC2 $a(T)$ curves, while the lower part of the figure shows the same curves as obtained using the EXC4 $E_{tot}(a)$ curve. (The 2NN, 4NN, 5NN, 6NN, and the 8NN to the 14NN $a(T)$ curves are omitted to maintain the clarity of the figure.) For both EXC2 and EXC4, the 1NN and 3NN curves are significantly different of all other curves, while the 7NN and 15NN $a(T)$ curves do not differ significantly of each other. The upper part of figure 7.7 also shows the measured $a(T)$ curve of metallic Cu [80]. This curve does not appear in the lower part of figure 7.7 because it does not lie within the range of lattice parameters highlighted in this figure. It is clear, in figure 7.7, that all calculated EXC2 $a(T)$ curves significantly underestimate the measured $a(T)$ curve of metallic Cu. In contrast, all calculated EXC4 $a(T)$ curves overestimate even more importantly the measured $a(T)$ curve of metallic Cu. This is not surprising to us, as we observed in chapter 4 that the zero-Kelvin lattice parameters of the first-row transition metals are generally underestimated when calculated using exchange-correlation functional EXC2, and more importantly overestimated when calculated using exchange-correlation functional EXC4. In addition, the figure illustrates that the 1NN EXC2 $a(T)$ curve is most similar to the measured $a(T)$ curve of metallic Cu, and that the 1NN EXC4 $a(T)$ curve most significantly overestimates the measured $a(T)$ curve of metallic Cu. Thus, the thermal expansion of metallic Cu (ie.

the expansion of the lattice parameter of metallic Cu relative to its zero-Kelvin lattice parameter, as a function of temperature) is largest when it is calculated using the 1NN $a\,(T)$ curves. Also, when obtained from the 1NN $a\,(T)$ curves, the calculated thermal expansion of metallic Cu is most similar to the measured thermal expansion of metallic Cu.

Interestingly, it appears, in figure 7.7, that as the range of action of the inter-atomic interaction potential $E_{a-a}\,(x)$ is increased, the calculated $a\,(T)$ curve of metallic Cu converges towards a well-defined limit function. We expect the potential $E_{a-a}\,(x)$ to naturally possess a maximum range of action. By this, we mean that if two atomic nuclei are separated by a distance x that is sufficiently large, they do not interact significantly via the potential $E_{a-a}\,(x)$. The convergence observed in figure 7.7 suggests that the range of the potential $E_{a-a}\,(x)$ extends only to the distance separating a given atomic nucleus in the metallic Cu solid from its seventh nearest-neighbour coordination shell. This assertion is further supported by the fact that a similar convergence is observed in figure 7.6. However, it is dangerous to conclude this without further study. The fact that the 1NN $a\,(T)$ curves more accurately predict the thermal expansion of metallic Cu suggests that the vibration potential $U_{vib}\left((\ldots), \left\langle \vec{R}_I \right\rangle + \Delta\vec{R}_I, (\ldots)\right)$ of the atomic nuclei of FCC Cu is more accurately reconstructed using an inter-atomic interaction potential with range of action restricted to the distance separating a given atomic nucleus in the metallic Cu solid from its first nearest neighbours. This seems physically reasonable, as it is likely that the chemical bonds surrounding one atomic nucleus in a metallic Cu solid are most significantly perturbed by changes in the position of the atomic nuclei in the immediate vicinity of this atomic nucleus than by changes in the position of more distant atomic nuclei. This matter requires further study, and will be further discussed in section 7.4.

In figure 7.8, we show the 1NN and 7NN EXC2 and EXC4′ $a\,(T)$ curves calculated using the mean-field potential method. We specifically show the 1NN $a\,(T)$ curves because the thermal expansion of metallic Cu is most accurately calculated using these curves. We also show the 7NN $a\,(T)$ curves as $a\,(T)$ curves obtained using an inter-atomic interaction potential with a larger range of action do not differ significantly from this curve. It is clear in the figure that the 1NN EXC4′ $a\,(T)$ curve is most similar to the measured $a\,(T)$ curve

of metallic Cu.

That the EXC4′ $a\,(T)$ curves are more like the measured $a\,(T)$ curve of metallic Cu than are the EXC2 $a\,(T)$ curves makes clear that the accuracy of the calculated $a\,(T)$ curve of metallic Cu is dependent upon the functional form of the calculated $E_{tot}\,(a)$ curve of FCC Cu. This is so because, as shown in figure 7.2 and discussed in section 7.1, the EXC2 and EXC4′ $E_{tot}\,(a)$ curves of FCC Cu have a global minimum value at almost identical lattice parameters, but differ significantly in their functional form. This point is unacknowledged in a number of publications reporting methods for calculating the $a\,(T)$ curve of a solid using its $E_{tot}\,(a)$ curve (e.g. [142, 144–147]). In some of these publications, the theoretical method that is used to calculate the solid's $a\,(T)$ curve contains adjustable parameters (e.g. [146]). These parameters are adjusted to improve the results of the method, but the effect of the shape of the solid's $E_{tot}\,(a)$ curve on the accuracy of the method is not considered.

Because the EXC4′ $a\,(T)$ curves are more accurate than the EXC2 $a\,(T)$ curves, it may be tempting to conclude that the $F\,(a,T)$ curve of real metallic Cu is more similar to the EXC4′ $F\,(a,T)$ curves than to the EXC2 $F\,(a,T)$ curves. However, this may not be the case. As indicated in section 6.3 of chapter 6, a number of assumptions and approximations are made in deriving the method for calculating the Helmholtz' free energy of solids, which we use to calculate the $F\,(a,T)$ and $a\,(T)$ curves of metallic Cu. Each of these assumptions and approximations can introduce inaccuracies in the calculated $F\,(a,T)$ curve of metallic Cu, and therefore in the calculated $a\,(T)$ curve of metallic Cu. Some of these inaccuracies may be partially cancelled when the $a\,(T)$ curve of metallic Cu is calculated using the EXC4′ $E_{tot}\,(a)$ curve, but not when the EXC2 $E_{tot}\,(a)$ curve is used. We shall revisit this matter in section 7.4.

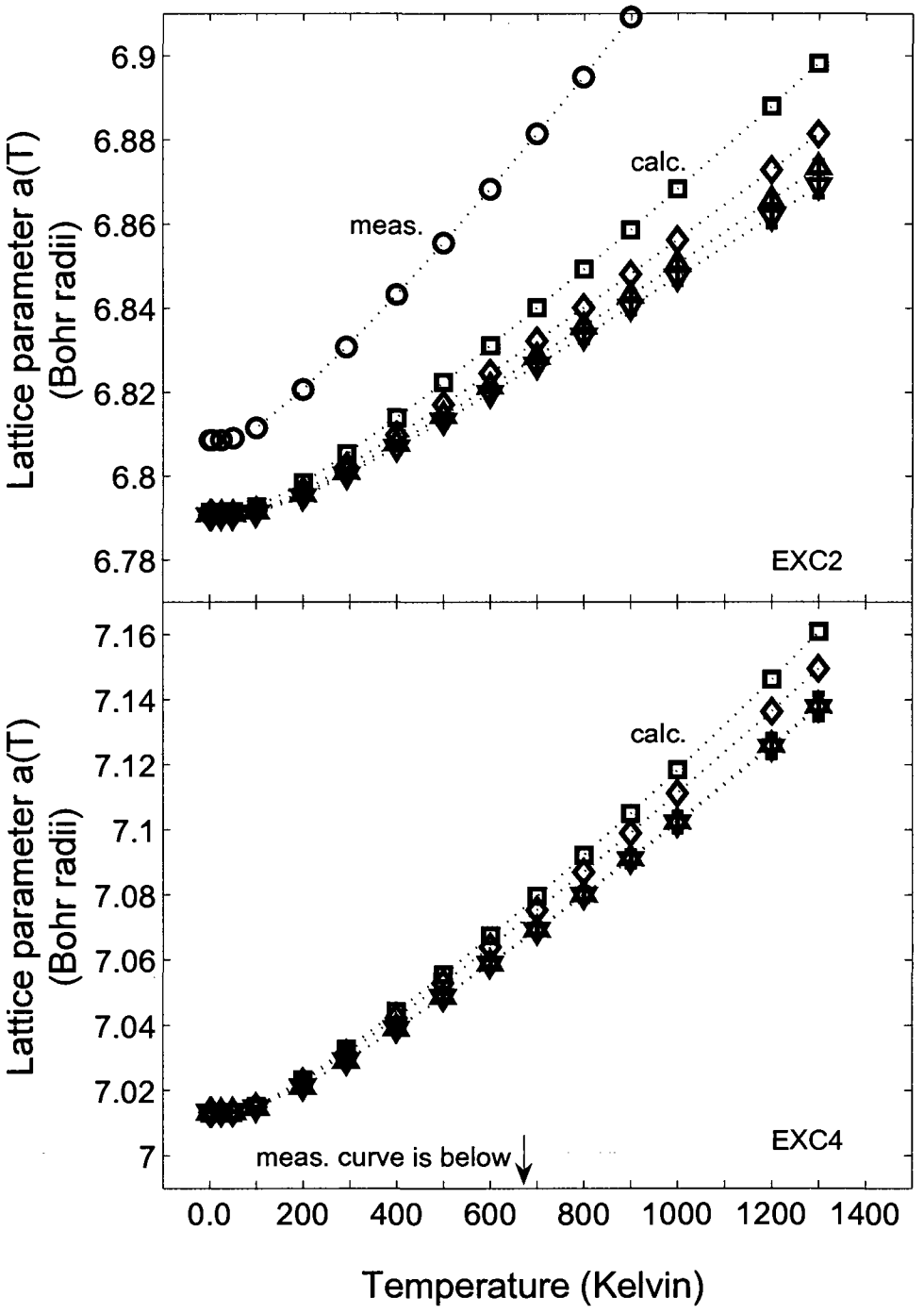

Figure 7.7: Calculated $a\,(T)$ curve of metallic Cu obtained using the mean-field potential method. The figure shows the calculated 1NN (squares), 3NN (diamonds), 7NN (upward-pointing triangles), and 15NN (downward-pointing triangles) $a\,(T)$ curves. The upper (lower) figure shows calculated EXC2 (EXC4) $a\,(T)$ curves. Circles denote the measured $a\,(T)$ curve of metallic Cu. Data symbols denote actual calculated or measured values of a given $a\,(T)$ curve. Error bars indicate the numerical uncertainty of these values. They are omitted if they are smaller than the data symbols.

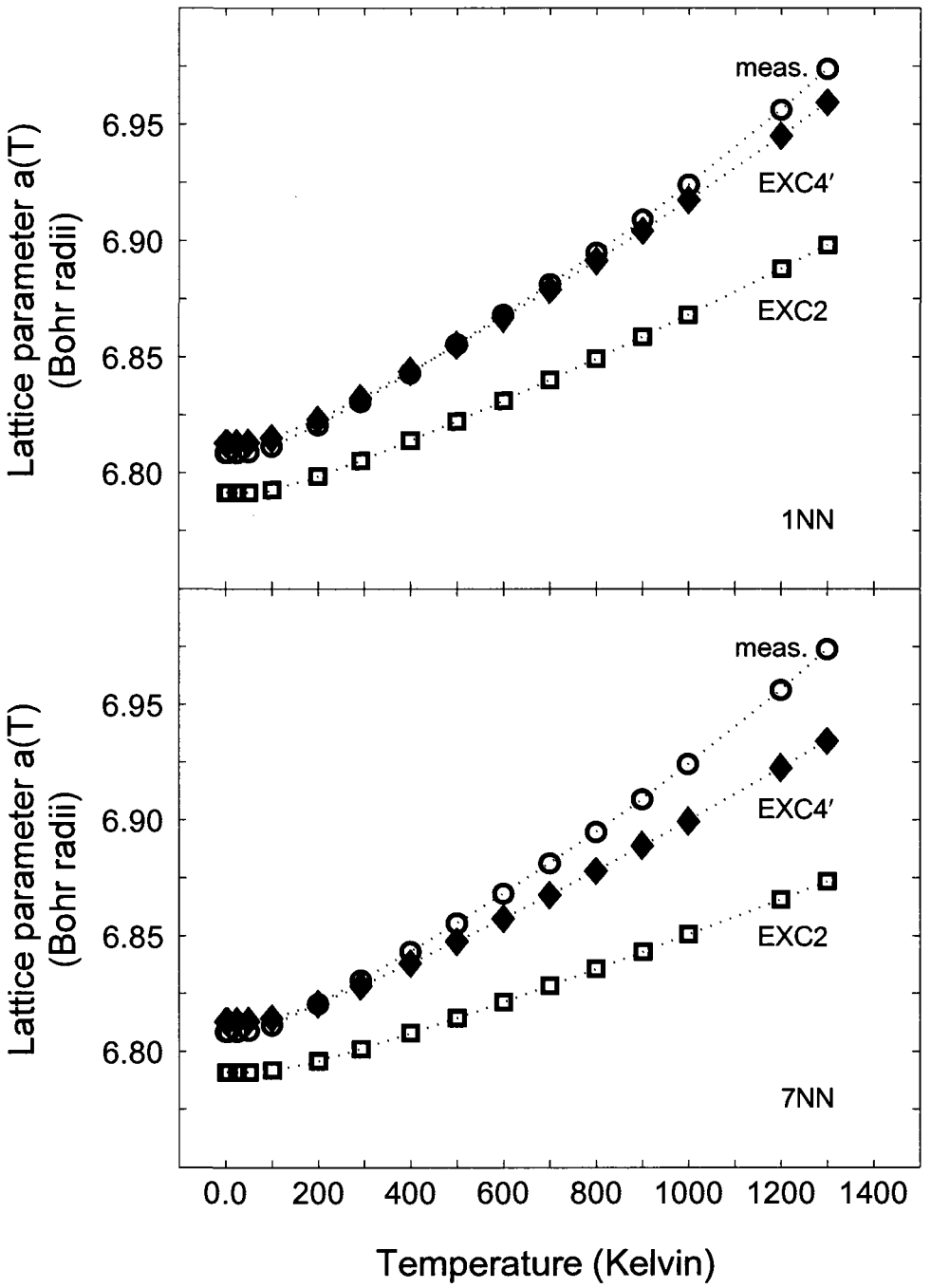

Figure 7.8: Calculated $a\,(T)$ curve of metallic Cu obtained using the mean-field potential method. The figure shows calculated EXC2 (squares) and EXC4′ (filled diamonds) $a\,(T)$ curves. The upper (lower) figure shows calculated 1NN (7NN) $a\,(T)$ curves. Circles denote the measured $a\,(T)$ curve of metallic Cu. Data symbols denote actual calculated or measured values of a given $a\,(T)$ curve. Error bars indicate the numerical uncertainty of these values. They are omitted because they are smaller than the data symbols in the upper figure, and approximately as large as the data symbols in the lower figure.

7.3.2 a (T) Curve of Metallic Cu Using the Phonon Spectrum Method

Having calculated the $a\,(T)$ curve of metallic Cu using the mean-field potential method, we now calculate this curve using the phonon spectrum method. To do so, we first calculate the $F\,(a,T)$ curve of metallic Cu as described in section 7.2.2. Again, this requires that we specify the range of action of the inter-atomic interaction potential $E_{a-a}\,(x)$, and that we use one of the EXC2, the EXC4 or the EXC4' $E_{tot}\,(a)$ curves described in section 7.1. To identify a specific calculated $a\,(T)$ curve, we use a nomenclature similar to that described in section 7.3.1. We also calculate the $a\,(T)$ curve of metallic Cu as described in the first paragraphs of section 7.3.1, only using $F\,(a,T)$ curves calculated using the phonon spectrum method (as per section 7.2.2) instead of the mean-field potential method.

Figure 7.9 shows the calculated 1NN, 3NN and 7NN $a\,(T)$ curve of metallic Cu as obtained using the phonon spectrum method. (The 2NN, 4NN, 5NN and 6NN $a\,(T)$ curves are omitted to maintain the clarity of the figure.) The upper part of the figure shows EXC2 $a\,(T)$ curves, while the bottom part of the figure shows EXC4 $a\,(T)$ curves. These curves are similar to those obtained using the mean-field potential method (figure 7.7). Figure 7.9 illustrates that the 1NN EXC2 $a\,(T)$ curve is significantly different of the 3NN and the 7NN EXC2 curves, at least at temperatures greater than 600 Kelvin. Also, the 3NN and 7NN EXC2 $a\,(T)$ curves do not differ significantly of each other. In contrast, none of the EXC4 $a\,(T)$ curves are significantly different of each other. Furthermore, the EXC2 $a\,(T)$ curves significantly underestimate the measured lattice parameter of metallic Cu at all temperatures below its melting point, while the EXC4 $a\,(T)$ curves even more importantly overestimate the measured lattice parameter of metallic Cu. Figure 7.9 also illustrates that the 1NN EXC2 $a\,(T)$ curve is most similar to the measured $a\,(T)$ curve of metallic Cu, and that the 1NN EXC4 $a\,(T)$ curve most significantly overestimates the measured $a\,(T)$ curve of metallic Cu. Thus, the thermal expansion of metallic Cu is largest when it is calculated using the 1NN $a\,(T)$ curves. Also, when obtained from the 1NN $a\,(T)$ curves, the calculated thermal expansion of metallic Cu is most similar to the measured thermal expansion of metallic Cu.

In figures 7.10 and 7.11, we compare directly $a\,(T)$ curves obtained using the mean-field potential method and using the phonon spectrum method. We compare EXC2 $a\,(T)$ curves and EXC4' $a\,(T)$ curves in figure 7.10 and figure 7.11 respectively. In both figures, the $a\,(T)$ curves obtained with the mean-field potential method and with the phonon spectrum method are not significantly different. This is surprising to us, because the $F\,(a,T)$ curve of metallic Cu obtained using the phonon spectrum method is significantly different of the $F\,(a,T)$ curve of metallic Cu obtained using the mean-field potential method (see figures 7.4 and 7.5). The most important difference between the $a\,(T)$ curves obtained using the mean-field potential method and those obtained using the phonon spectrum method is that the numerical precision of the former curves is greater than that of the latter. This is clearly evident if figure 7.9 is compared to figure 7.7, and is due to the fact that the $F\,(a,T)$ curves obtained using the mean-field potential method are more precise than those obtained using the phonon spectrum method.

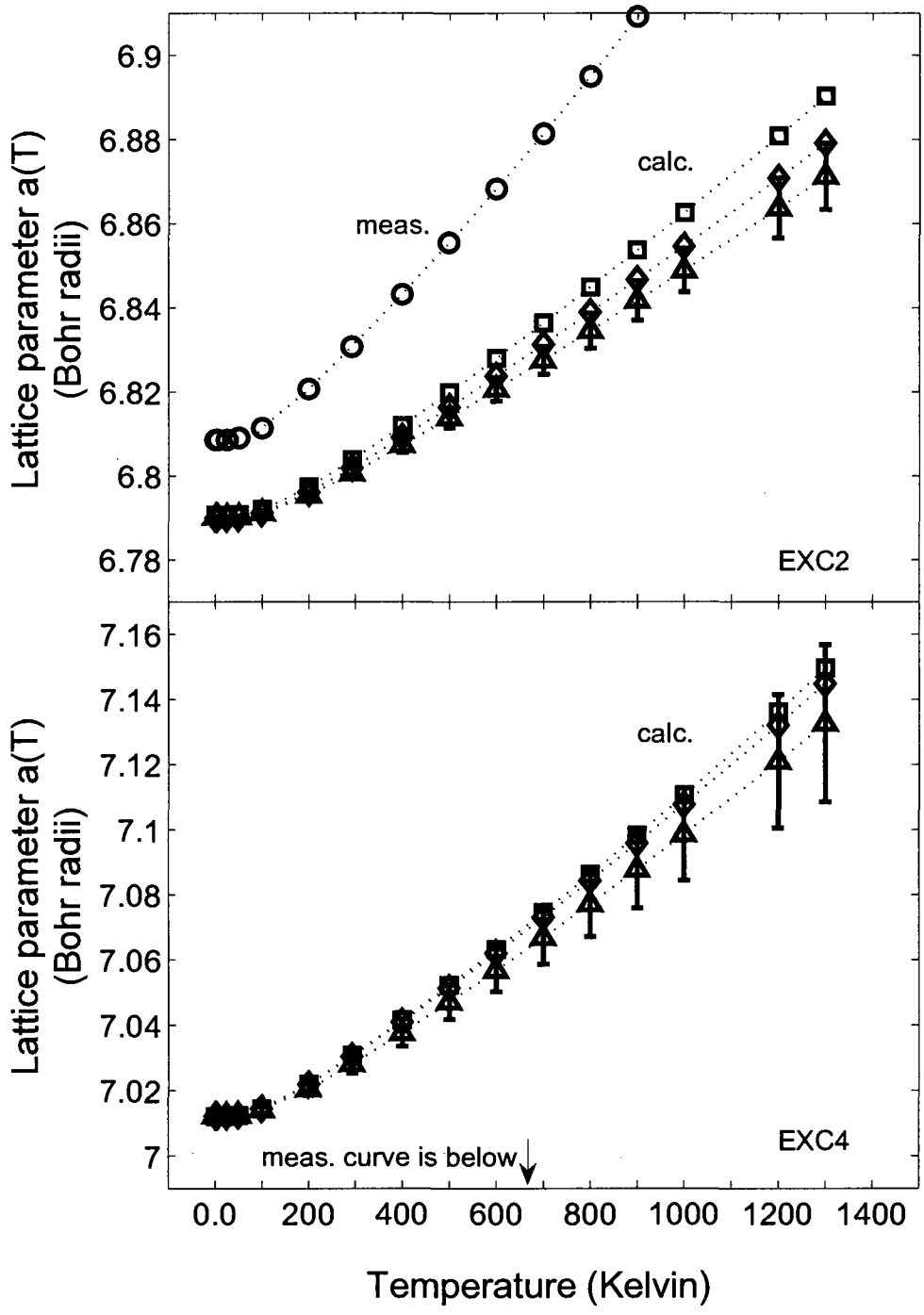

Figure 7.9: Calculated $a\,(T)$ curve of metallic Cu obtained using the phonon spectrum method. The figure shows the 1NN (squares), 3NN (diamonds), and 7NN (upward-pointing triangles) $a\,(T)$ curves. Circles denote the measured $a\,(T)$ curve of metallic Cu. The upper (lower) figure shows EXC2 (EXC4) $a\,(T)$ curves. Data symbols denote actual calculated or measured values of a given $a\,(T)$ curve. Error bars indicate the numerical uncertainty of these values. They are omitted if they are smaller than the data symbols.

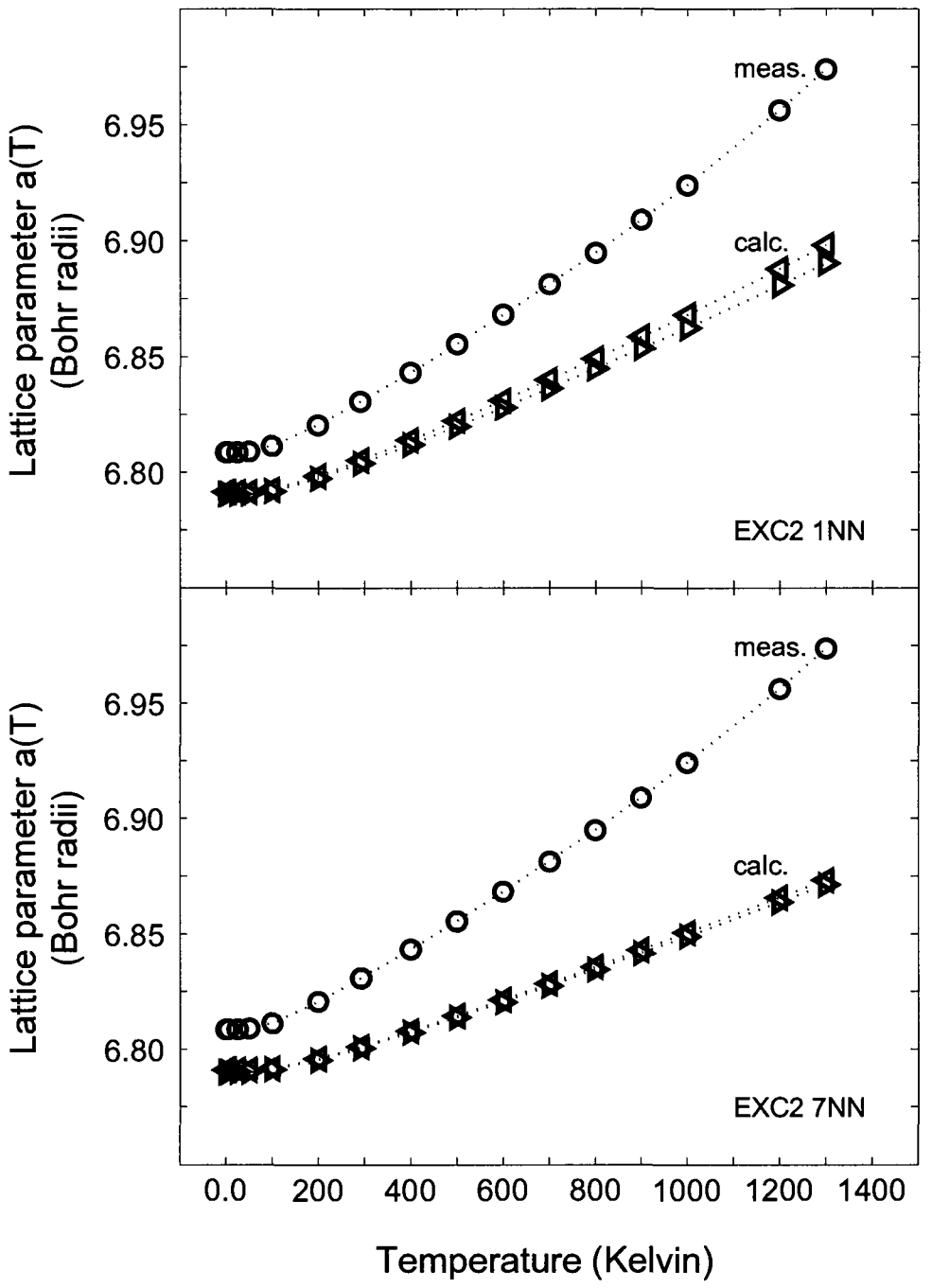

Figure 7.10: Calculated EXC2 $a\,(T)$ curve of metallic Cu. Leftward-pointing triangles (rightward-pointing triangles) denote curves obtained using the mean-field potential method (phonon spectrum method). Circles denote the measured $a\,(T)$ curve of metallic Cu. The upper (lower) figure shows 1NN (7NN) $a\,(T)$ curves. Data symbols denote actual calculated or measured values of a given $a\,(T)$ curve. Error bars indicate the numerical uncertainty of these values. They are omitted if they are smaller than the data symbols.

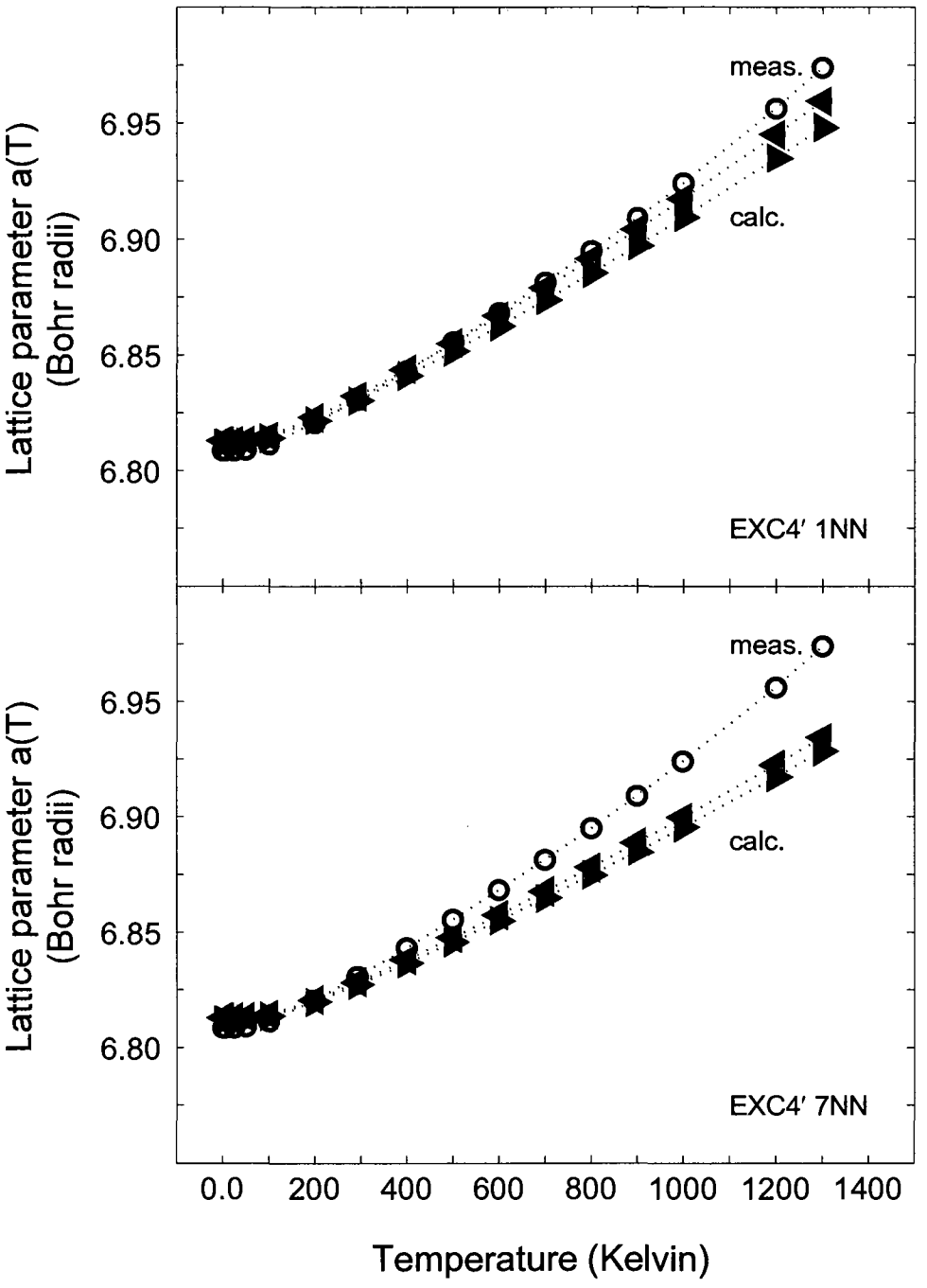

Figure 7.11: Calculated EXC4' $a\,(T)$ curve of metallic Cu. Leftward-pointing triangles (rightward-pointing triangles) denote curves obtained using the mean-field potential method (phonon spectrum method). Circles denote the measured $a\,(T)$ curve of metallic Cu. The upper (lower) figure shows 1NN (7NN) $a\,(T)$ curves. Data symbols denote actual calculated or measured values of a given $a\,(T)$ curve. Error bars indicate the numerical uncertainty of these values. They are omitted if they are smaller than the data symbols.

7.4 Calculated a (T) Curve of Metallic Cu - Summary and Discussion

As indicated in the introduction of this chapter, we calculate here the $a\,(T)$ curve of metallic Cu for two reasons. The first is that the theoretical calculation of the $a\,(T)$ curve of solids is a topic of current interest in the field of materials physics. We therefore wish to test the accuracy of the theoretical method for calculating the Helmholtz' free energy of solids presented in chapter 6 when it is used to calculate the $a\,(T)$ curve of a solid. Secondly, by evaluating the accuracy of the calculated $a\,(T)$ curve of metallic Cu, we indirectly evaluate the accuracy of the calculated $F\,(a,T)$ curve of metallic Cu. We wish to evaluate the accuracy of the $F\,(a,T)$ curve of solids, as calculated using the method of chapter 6. We summarise here the observations that we can make about these matters in light of the results of sections 7.2 and 7.3. But prior to doing so, we discuss the implications of the assumptions and approximations that are made in deriving the method of chapter 6 on the calculations conducted in this chapter.

7.4.1 Implications of the Assumptions Made in Deriving the Method of Chapter 6

The main assumptions made in deriving this method are summarised in section 6.3 of chapter 6. We here address them one by one.

Firstly, it is pointed out, in section 6.3 of chapter 6, that the method presented in this latter chapter specifically allows for the calculation of the $F\,(a,T)$ curve, and therefore the calculation of the $a\,(T)$ curve, of a perfectly crystalline, bulk solid. Therefore, we have calculated in this chapter the $a\,(T)$ curve of a perfectly crystalline bulk metallic Cu solid. It is therefore important that we compare this curve to the measured $a\,(T)$ curve of a perfectly crystalline bulk metallic Cu solid. But, real metallic Cu solids are never perfectly crystalline, as real solids are always finite-sized, and contain atomic vacancies

[140]. Thus, the measured $a\,(T)$ curve of metalllic Cu presented by Touloukian et al. [80] includes the effect of vacancy formation processes in the thermal expansion of metallic Cu. We do not have information about the significance of vacancy formation processes in the thermal expansion of metallic Cu. We simply know that, as the temperature of any solid is increased, additional atomic vacancies form within it, and this causes the thermal expansion of the solid to be greater than it would be if no additional vacancies formed within it [140]. In addition, we know that in metallic aluminium solids, vacancy formation can increase the lattice parameter of the solid by an additional 0.1% of its zero-Kelvin value at temperatures near its melting point [140, p. 112]. Assuming that vacancy formation in metallic Cu has a similar effect on its thermal expansion, we conclude that the measured $a\,(T)$ curve of metallic Cu reported by Touloukian et al. may be 0.007 Bohr radii larger than the $a\,(T)$ curve of a vacancy-free metallic Cu solid at temperatures near its melting point. This quantity is small and has no bearing on the observations that we arrived at in sections 7.2 and 7.3.

Secondly, in deriving the method of chapter 6, we assumed that the thermal excitation of the solid's electrons can be neglected when calculating its $F\,(a,T)$ curve. To test the validity of this assumption, we calculate the Helmholtz' free energy of the valence electrons of a metallic Cu solid as follows (see equation 6.28 of chapter 6):

$$\begin{aligned} F_{el}\,(a,T) &= \int_{-\infty}^{\infty} n_v\,(\epsilon,a)\,f\,(\epsilon)\,\epsilon d\epsilon - \int_{-\infty}^{E_F} n_v\,(\epsilon,a)\,\epsilon d\epsilon \\ &- k_B T \int_{-\infty}^{\infty} n_v\,(\epsilon,a)\,\{f\,(\epsilon)\,ln\,(f\,(\epsilon)) + (1-f\,(\epsilon))\,ln\,(1-f\,(\epsilon))\}\,d\epsilon, \end{aligned} \quad (7.8)$$

where $f\,(\epsilon)$ is the Fermi distribution [76, p. 774], and $n_v\,(\epsilon,a)$ is the density of states of the Cu metal's valence electrons when the metal has lattice parameter a. To calculate $F_{el}\,(a,T)$, we first calculate, using the TB-LMTO ESC program and exchange-correlation functional EXC2, the density of states functions $n_v\,(\epsilon,a)$ of the valence electrons of a number of FCC Cu solids with lattice parameters between $6.69 \leq a \leq 6.82$ Bohr radii. Using these density of states functions, we find that $F_{el}\,(a,T)$ is of the order of -1.0×10^{-6} Rydberg per atom at $T = 293$ Kelvin, and of the order of 1.0×10^{-4} Rydberg per atom at $T = 1300$ Kelvin, regardless of the lattice parameter of the metallic Cu solid. At both $T = 293$ and $T = 1300$

Kelvin, $F_{el}(a,T)$ is of the order of the numerical precision of the calculated values of the $F(a,T)$ curve of metallic Cu, obtained using the mean-field potential method. Thus, the $F(a,T)$ curve of metallic Cu obtained when neglecting $F_{el}(a,T)$ is insignificantly different of the $F(a,T)$ curve of metallic Cu that includes $F_{el}(a,T)$. We also find that, when $F_{el}(a,T)$ is included in the calculation of the $a(T)$ curve of metallic Cu, the difference between this $a(T)$ curve and the $a(T)$ curve obtained without $F_{el}(a,T)$ is no greater than 0.001 Bohr radii at any temperature below the melting point of metallic Cu. Thus, that $F_{el}(a,T)$ is not considered in the calculation of the $F(a,T)$ curves and $a(T)$ curves of sections 7.2 and 7.3 does not invalidate the observations and conclusions that we arrived at in these sections.

Thirdly, we assume in chapter 6 that the Helmholtz' free energy of a solid can be accurately calculated in a quasi-harmonic approximation, using only the first- and second-order terms of the vibration potential $U_{vib}\left(\left(\ldots\right),\left\langle\vec{R}_I\right\rangle+\Delta\vec{R}_I,\left(\ldots\right)\right)$ of its atomic nuclei. Some of the second-order terms of this potential couple the motion of the atomic nuclei of the solid. For instance, in a FCC Cu solid with lattice parameter a, the atomic nucleus located on average at $\left\langle\vec{R}_I\right\rangle=\vec{0}$ is coupled to the atomic nucleus located on average at $\left\langle\vec{R}_J\right\rangle=\frac{a}{2}\hat{x}+\frac{a}{2}\hat{y}$ via nine of the second-order terms of $U_{vib}\left(\left(\ldots\right),\left\langle\vec{R}_I\right\rangle+\Delta\vec{R}_I,\left(\ldots\right)\right)$, one of which is as follows (see equation 6.33 of chapter 6):

$$-\left\{E^{(2)}_{a-a}\left(\frac{a}{\sqrt{2}}\right)\times\left\{\frac{1}{2}\right\}+E^{(1)}_{a-a}\left(\frac{a}{\sqrt{2}}\right)\times\left\{\frac{1}{\sqrt{2}a}\right\}\right\}\times\left\{\Delta R_{Ix}\right\}\left\{\Delta R_{Jx}\right\}. \tag{7.9}$$

If the Cu solid has lattice parameter $a=6.79146$ Bohr radii (ie. the lattice parameter of metallic Cu at 1 Kelvin, as per the 1NN EXC2 $a(T)$ curve of the metal), and if the derivatives $E^{(2)}_{a-a}\left(\frac{a}{\sqrt{2}}\right)$ and $E^{(1)}_{a-a}\left(\frac{a}{\sqrt{2}}\right)$ are those of the 1NN EXC2 $E_{a-a}(x)$ potential evaluated at $x=\frac{a}{\sqrt{2}}$,[2] then the Taylor term of equation 7.9 is approximately equal to $-0.0144\times\left\{\Delta R_{Ix}\right\}\left\{\Delta R_{Jx}\right\}$ Rydberg units. The next Taylor terms of $U_{vib}\left(\left(\ldots\right),\left\langle\vec{R}_I\right\rangle+\Delta\vec{R}_I,\left(\ldots\right)\right)$ that are non-null are the fourth-order terms, and they couple the motion of the atoms at

[2]The "1NN EXC2 $E_{a-a}(x)$ potential" has range of action restricted to the distance separating a given atomic nucleus in the metallic Cu solid from its first nearest neighbours, and is constructed using the EXC2 $E_{tot}(a)$ curve of FCC Cu.

$\left\langle \vec{R}_I \right\rangle$ and $\left\langle \vec{R}_J \right\rangle$ as follows:

$$\left\{ \left\{ \frac{1}{2} \right\} \times E^{(4)}_{a-a}\left(\frac{a}{\sqrt{2}} \right) + \left\{ \frac{3}{\sqrt{2}a} \right\} \times E^{(3)}_{a-a}\left(\frac{a}{\sqrt{2}} \right) - \left\{ \frac{9}{2a^2} \right\} \times E^{(2)}_{a-a}\left(\frac{a}{\sqrt{2}} \right) \right.$$

$$\left. + \left\{ \frac{9}{\sqrt{2}a^3} \right\} \times E^{(1)}_{a-a}\left(\frac{a}{\sqrt{2}} \right) \right\} \times \left\{ \frac{1}{4} \right\} \times \left\{ \Delta R_{Ix} \right\}^2 \left\{ \Delta R_{Jx} \right\}^2 . \tag{7.10}$$

If again the Cu solid has lattice parameter $a = 6.79146$ Bohr radii, and if the derivatives $E^{(4)}_{a-a}\left(\frac{a}{\sqrt{2}} \right)$, $E^{(3)}_{a-a}\left(\frac{a}{\sqrt{2}} \right)$, $E^{(2)}_{a-a}\left(\frac{a}{\sqrt{2}} \right)$ and $E^{(1)}_{a-a}\left(\frac{a}{\sqrt{2}} \right)$ are again those of the 1NN EXC2 $E_{a-a}(x)$ potential evaluated at $x = \frac{a}{\sqrt{2}}$, then the Taylor term of equation 7.10 is approximately equal to $0.0132 \times \left\{ \Delta R_{Ix} \right\}^2 \left\{ \Delta R_{Jx} \right\}^2$ Rydberg units. As a result of the thermal oscillations of the atomic nuclei of the FCC Cu solid, we expect that at maximum, $\Delta R_{Ix} \approx 0.05 \times a$. As a result, the fourth-order term of equation 7.10 will be approximately 10 times smaller than the second-order term of equation 7.9 for typical displacements of the atomic nuclei of the FCC Cu solid. Thus, neglecting the terms of $U_{vib}\left((\ldots), \left\langle \vec{R}_I \right\rangle + \Delta \vec{R}_I, (\ldots) \right)$ of order greater than two may have a significant effect on the accuracy of the calculated Helmholtz' free energy function $F(a, T)$ of FCC Cu. This must be examined in greater detail.

Fourthly, we highlighted, in section 6.3 of chapter 6, the importance of the fact that our theoretical method for calculating the Helmholtz' free energy of a solid makes use of an inter-atomic interaction potential. We explained that we construct this potential theoretically using the results of Chen, Chen and Wei [137], starting from a first-principles calculation of the $E_{tot}(a)$ curve of a solid. We also indicated that we assume that this potential is capable of accurately reproducing the vibration potential $U_{vib}\left((\ldots), \left\langle \vec{R}_I \right\rangle + \Delta \vec{R}_I, (\ldots) \right)$ of the atomic nuclei of a solid, which gives the increase in energy that occurs when a solid's atomic nuclei are displaced from their equilibrium positions as they undergo small amplitude thermal oscillations. We now discuss the results of sections 7.2 and 7.3, and highlight the insights that they provide us about the implications of this assumption.

7.4.2 Accuracy of the Calculated a (T) and F (a, T) Curve of Metallic Cu

As indicated in section 7.3, the accuracy of the $a\,(T)$ curve of metallic Cu, as calculated using the method of chapter 6, is sensitive to the range of action of the inter-atomic interaction potential $E_{a-a}\,(x)$ that appears in the method. We observed, in section 7.3, that the thermal expansion of metallic Cu (ie. the expansion of the lattice parameter of metallic Cu, as a function of temperature, relative to its zero-Kelvin lattice parameter) is most accurately calculated when the range of $E_{a-a}\,(x)$ is restricted to the distance separating a given atomic nucleus in the metallic Cu solid from its first nearest neighbours. We observed, in addition, that $a\,(T)$ curves do not differ significantly when they are calculated using an inter-atomic interaction potential $E_{a-a}\,(x)$ with range of action extending as far as or beyond the distance separating a given atomic nucleus in the metallic Cu solid from its seventh nearest neighbours. We shall discuss this matter in greater detail in section 7.4.3.

Secondly, to calculate the $a\,(T)$ curve of metallic Cu using the method of chapter 6, we require knowledge of the $E_{tot}\,(a)$ curve of FCC Cu. that the $a\,(T)$ curve of metallic Cu is most accurately calculated using the EXC4′ $E_{tot}\,(a)$ curve, even though the global minimum value of both the EXC2 and the EXC4′ $E_{tot}\,(a)$ curves occur at essentially the same lattice parameter. These two $E_{tot}\,(a)$ curves differ significantly in their functional form. Therefore, we conclude that the accuracy of the calculated $a\,(T)$ curve of metallic Cu is sensitive to the shape of the calculated $E_{tot}\,(a)$ curve of FCC Cu. This point is important and entirely unacknowledged in other publications reporting methods for calculating the $a\,(T)$ curve of a solid (e.g. [142, 144–147]). We shall discuss this matter in greater detail in section 7.4.3 as well.

Thirdly, we observed in section 7.3 that the $a\,(T)$ curve of metallic Cu calculated using the mean-field potential method is insignificantly different of the $a\,(T)$ curve of metallic Cu calculated using the phonon spectrum method. This is surprising to us, as the phonon spectrum method is based on a more complete model of the vibration potential $U_{vib}\left((\ldots), \left\langle \vec{R}_I \right\rangle + \Delta\vec{R}_I, (\ldots)\right)$ of the atomic nuclei of a solid than is the mean-field poten-

tial method. Specifically, that the atomic nuclei of a solid are coupled is taken into account within the phonon spectrum method, but not within the mean-field potential method. These results lead us to believe that, in order to calculate the $a\,(T)$ curve of a solid, it is acceptable to neglect the coupling of the solid's constituent atomic nuclei, and to model them as independent oscillators.

In light of the three previous observations, we believe that we have identified a practical and accurate method for calculating the $a\,(T)$ curve of non-magnetic first-row transition metals using the theoretical method presented in chapter 6 and the TB-LMTO ESC program [28]. To do so, the TB-LMTO ESC program should first be used in conjunction with exchange-correlation functional EXC2 to identify the zero-Kelvin lattice parameter of a metal of interest. The zero-Kelvin lattice parameter of a first-row transition metal, as calculated using the TB-LMTO ESC program in conjunction with EXC2, is typically 1% to 5% smaller than the measured zero-Kelvin lattice parameter of the metal (see chapter 4). Secondly, the $E_{tot}\,(a)$ curve of the metal should be calculated using the TB-LMTO ESC program in conjunction with exchange-correlation functional EXC4. This $E_{tot}\,(a)$ curve must then be shifted leftward until its global minimum value occurs at the zero-Kelvin lattice parameter of the metal, as it was identified using the TB-LMTO ESC program and EXC2. Thirdly, the $a\,(T)$ curve of the metal should be calculated using the mean-field potential method in conjunction with the shifted version of the EXC4 $E_{tot}\,(a)$ curve of the metal. During this calculation, the range of action of the inter-atomic interaction potential $E_{a-a}\,(x)$ should be restricted to the distance separating a given atomic nucleus of the metal from its first nearest neighbours. We expect that the $a\,(T)$ curve thus obtained should be no more than 5% smaller than the measured $a\,(T)$ curve of the metal at all temperatures below the metal's melting point. In the future, this approach should be used to calculate the $a\,(T)$ curve of more first-row transition metals in order to further evaluate its accuracy.

Because the 1NN EXC4′ $a\,(T)$ curve is most similar to the measured $a\,(T)$ curve of metallic Cu, it is tempting to conclude that the 1NN EXC4′ $F\,(a,T)$ curve is also most like the $F\,(a,T)$ curve of real metallic Cu. However, the results of sections 7.2 and 7.3 make clear that there are limits to the indirect evaluation of the accuracy of the calculated $F\,(a,T)$

curve of metallic Cu via the evaluation of the accuracy of its calculated $a(T)$ curve. Specifically, we observed in section 7.3 that the $a(T)$ curve of metallic Cu, calculated using the mean-field potential method, is numerically indistinguishable of the $a(T)$ curve of metallic Cu calculated using the phonon spectrum method. In contrast, figures 7.4 and 7.5 clearly indicate that the $F(a,T)$ curve of metallic Cu, calculated using the mean-field potential method, is significantly different of the $F(a,T)$ curve of metallic Cu calculated using the phonon spectrum method. Therefore, by evaluating the accuracy of the calculated $a(T)$ curve of metallic Cu, we cannot ascertain whether the $F(a,T)$ curve of metallic Cu is more accurate when calculated using the phonon spectrum method or when calculated using the mean-field potential method.

The $a(T)$ curve of metallic Cu is not the only measurable property of metallic Cu that can be calculated using the $F(a,T)$ curve of the metal. For instance, the bulk modulus as a function of temperature of metallic Cu can be calculated from its $F(v,T)$ curve as [76]:

$$B(T) = v(T) \left. \frac{\delta^2}{\delta v^2} F(v,T) \right|_{v=v(T)}, \tag{7.11}$$

where $\left. \frac{\delta^2}{\delta v^2} F(v,T) \right|_{v=v(T)}$ is the second-derivative of the $F(v,T)$ curve of metallic Cu evaluated at $v = v(T)$, and $v(T)$ is the equilibrium volume of metallic Cu at temperature T. (It should be recalled that $v(T) = \frac{a(T)^3}{4}$.) Calculating and evaluating the accuracy of the bulk modulus of metallic Cu as a function of temperature would give us information about the accuracy of the curvature of its calculated $F(a,T)$ curve. In addition, the cohesive energy of metallic Cu can be calculated from its $F(a,T)$ curve as [79]:

$$E_{coh}(T) = \lim_{a \to \infty} E_{tot}(a) - F(a(T), T), \tag{7.12}$$

where $a(T)$ is the equilibrium lattice parameter of metallic Cu at temperature T. Calculating and evaluating the cohesive energy of metallic Cu amounts to a more direct evaluation of the accuracy of its $F(a,T)$ curve than we have conducted in this chapter. This research should be pursued in the future.

7.4.3 Conclusions Concerning the Potential $E_{a-a}(x)$

In light of the three observations provided at the beginning of section 7.4.2, it is tempting to come to a number of conclusions about the inter-atomic interaction potential $E_{a-a}(x)$ that we use to calculate the $F(a,T)$ curve of metallic Cu.

First of all, it is tempting to conclude that the vibration potential of the atomic nuclei of a metallic Cu solid, $U_{vib}\left((\ldots),\left\langle\vec{R}_I\right\rangle+\Delta\vec{R}_I,(\ldots)\right)$, is most accurately reproduced by the inter-atomic interaction potential $E_{a-a}(x)$ when its range of action is restricted to the distance separating the atomic nuclei of the FCC Cu solid from their first nearest neighbours. Physically, this seems sensical, as the chemical bonds surrounding one atomic nucleus in a metallic Cu solid are likely to be most significantly perturbed by changes in the position of the atomic nuclei in its immediate vicinity than by changes in the position of more distant atomic nuclei. However, the results of sections 7.2 and 7.3 are consistent with our intuition that the potential $E_{a-a}(x)$ naturally possesses a maximum range of action, beyond which atomic nuclei do not interact significantly. Rigorously, the results of sections 7.2 and 7.3 do not permit us to ascertain the range of the potential $E_{a-a}(x)$ that most accurately reproduces the vibration potential $U_{vib}\left((\ldots),\left\langle\vec{R}_I\right\rangle+\Delta\vec{R}_I,(\ldots)\right)$. The $a(T)$ curve of metallic Cu may be more accurately calculated when $E_{a-a}(x)$ is short-ranged because this short ranged potential better cancels the errors introduced in our calculation of the $a(T)$ curve as a result of inaccuracies in the calculated $E_{tot}(a)$ curve of FCC Cu, or as a result of the neglect of the fourth-order terms of the Taylor expansion of $U_{vib}\left((\ldots),\left\langle\vec{R}_I\right\rangle+\Delta\vec{R}_I,(\ldots)\right)$ (see section 7.4.1). In addition, our calculated $E_{tot}(a)$ curves of FCC Cu are less accurate at larger values of lattice parameter. Because of the way the potential $E_{a-a}(x)$ is constructed, the decreasing accuracy of the $E_{tot}(a)$ curves at larger lattice parameters causes the longer ranged potentials $E_{a-a}(x)$ to be less accurate.

We also expect that the vibration potential $U_{vib}\left((\ldots),\left\langle\vec{R}_I\right\rangle+\Delta\vec{R}_I,(\ldots)\right)$ of the atomic nuclei of metallic Cu will be more accurately reproduced if the $E_{tot}(a)$ curve of FCC Cu is accurately calculated. In light of the results of sections 7.2 and 7.3, we are tempted to conclude that $U_{vib}\left((\ldots),\left\langle\vec{R}_I\right\rangle+\Delta\vec{R}_I,(\ldots)\right)$ is more accurately reproduced using the

EXC4′ $E_{tot}(a)$ curve, and that this $E_{tot}(a)$ curve is more accurate than the EXC2 and the EXC4 $E_{tot}(a)$ curve. However, we are reluctant to make this conclusion given that we showed in chapter 4 that the TB-LMTO ESC program [28] most accurately predicts the zero-Kelvin lattice parameter, crystal structure and magnetic moment magnitudes of the first-row transition metals when it is used in conjunction with exchange-correlation functional EXC2. In addition, the $a(T)$ curve of metallic Cu may here again be more accurately calculated using the EXC4′ $E_{tot}(a)$ curve because this $E_{tot}(a)$ curve better cancels the errors introduced in our calculation of the $a(T)$ curve as a result of the incorrect selection of the range of the inter-atomic interaction potential $E_{a-a}(x)$, or as a result of the neglect of the fourth-order terms of the Taylor expansion of $U_{vib}\left((\ldots), \left\langle \vec{R}_I \right\rangle + \Delta\vec{R}_I, (\ldots)\right)$.

Even though we cannot rigorously confirm it using the results of section 7.2 and 7.3, our intuition is that $U_{vib}\left((\ldots), \left\langle \vec{R}_I \right\rangle + \Delta\vec{R}_I, (\ldots)\right)$ is more accurately reproduced using the EXC4′ $E_{tot}(a)$ curve, and with an inter-atomic interaction potential $E_{a-a}(x)$ with range of action restricted to first nearest neighbour atomic nuclei within the metal. We believe this because, in our opinion, the displacement of an atomic nucleus in a metallic Cu solid from its equilibrium position will not perturb the distribution of the solid's electrons over a very long distance, as the effect of the displacement of the atomic nucleus will be screened by its first nearest neighbours. In addition, we believe that the curvature of the $E_{tot}(a)$ curve of real metallic Cu is more like that of the EXC4′ $E_{tot}(a)$ curve because this curve has a global minimum at essentially the same lattice parameter as the EXC2 $E_{tot}(a)$ curve and has the same curvature as the EXC4 $E_{tot}(a)$ curve. The TB-LMTO ESC program more accurately calculates the zero-Kelvin lattice parameters of the first-row transition metals using EXC2 (see section 4.2.3), but more accurately calculates the bulk moduli of the majority of the first-row transition metals using EXC4 (see section 4.2.4). To further substantiate our belief, we report here the bulk modulus of metallic Cu at zero Kelvin as calculated using the EXC2, EXC4 and EXC4′ $E_{tot}(a)$ curves. These bulk modulus values are shown in table 7.5, along with the lattice parameter at which the bulk modulus values are calculated. The experimental value of the bulk modulus of metallic Cu at room temperature, reported by Kittel [78, p. 57], is also provided in the table. These results reveal that the bulk modulus

of metallic Cu obtained using the EXC4′ $E_{tot}(a)$ curve is most similar to the measured value. Thus, the results of table 7.5 substantiate the view that the curvature of the EXC4′ $E_{tot}(a)$ curve is most like that of the $E_{tot}(a)$ curve of real metallic Cu.

Table 7.5: Calculated and measured bulk modulus of metallic Cu

	Lattice par. (Bohr radii)	Bulk modulus (mRy per cubic Bohr radii)
EXC2	6.78	11.50 ± 0.05
EXC4	7.00	8.52 ± 0.05
EXC4′	6.80	9.39 ± 0.05
meas.*	6.82	9.31 ± 0.07

∗ Measurements taken at 293 Kelvin [78].

Further study is required in order to rigorously gauge the accuracy of the vibration potential $U_{vib}\left((\ldots), \left\langle \vec{R}_I \right\rangle + \Delta\vec{R}_I, (\ldots)\right)$ as constructed using an inter-atomic interaction potential obtained via the results of Chen, Chen and Wei [137]. First of all, it should be possible to study, using an ESC program, the sensitivity of the distribution of the electrons surrounding a given atomic nucleus in a metallic Cu solid to changes in the position of atomic nuclei in its various nearest neighbour coordination shells. The range of $E_{a-a}(x)$ could be chosen according to the results of such a study. Having ascertained the range of $E_{a-a}(x)$ in this manner, super-cell calculations could be conducted in order to obtain $U_{vib}\left((\ldots), \left\langle \vec{R}_I \right\rangle + \Delta\vec{R}_I, (\ldots)\right)$ for a number of physically reasonable displacements of the atomic nuclei of the metallic Cu solid as they undergo small amplitude thermal oscillations. Then, $U_{vib}\left((\ldots), \left\langle \vec{R}_I \right\rangle + \Delta\vec{R}_I, (\ldots)\right)$ could be constructed as per the method of chapter 6 and compared to the results of the super-cell calculations. This would represent a direct test of our assumption that $U_{vib}\left((\ldots), \left\langle \vec{R}_I \right\rangle + \Delta\vec{R}_I, (\ldots)\right)$ can be constructed using an inter-atomic interaction potential obtained via the results of Chen, Chen and Wei [137].

Future research should also seek to understand how the curvature of the $E_{tot}(a)$ curve of

a solid influences the shape of the inter-atomic interaction potential of the solid. How the curvature of the $E_{tot}(a)$ curve influences the lattice parameter dependence of the oscillation frequency $\omega(a)$ of the atoms in the mean-field potential model (see section 7.2.1), or the phonon spectrum $\Omega\left(\vec{k}, a\right)$ of the atoms (see section 7.2.2) should also be examined. Comparing the calculated phonon spectrum of the atoms in a solid to measurements of this spectrum as a function of temperature may be yet another useful way of gauging the accuracy of the method for calculating the Helmholtz' free energy of solids that we presented in chapter 6.

Of course, this research must be conducted with an accurate ESC program in order to produce meaningful results.

Chapter 8

Conclusion

In undertaking the research presented in this thesis, we set out to develop an entirely theoretical method for calculating the Helmholtz' free energy of complex magnetic solids like metallic Fe. We can now report that we have made much headway in this undertaking. Specifically, we developed a method for calculating the Helmholtz' free energy of bulk, non-magnetic metals based on an inter-atomic interaction potential (chapter 6). We also evaluated the accuracy of the method by using it to study the thermal expansion of metallic Cu (chapter 7).

The method of chapter 6 assumes only that an inter-atomic interaction potential $E_{a-a}(x)$ can be derived from the minimum total energy versus lattice parameter curve $E_{tot}(a)$ of a solid, and that this potential $E_{a-a}(x)$ can accurately reproduce the energy increase that occurs when the atomic nuclei of the solid move away from their equilibrium positions as they undergo small amplitude thermal oscillations. The inter-atomic interaction potential is constructed using the results of Chen, Chen and Wei [137], and the $E_{tot}(a)$ curve of the solid is calculated using a first principles ESC program.

When using the method of chapter 6 to study the thermal expansion of metallic Cu, we calculated the $E_{tot}(a)$ curve of FCC Cu using an ESC program [28] based on the tight-binding linear muffin-tin orbitals (TB-LMTO) theory [29–32]. In chapter 2, we described

the mathematical implementation of this TB-LMTO ESC program [28]. We also explained that the program can calculate the minimum total energy and the lowest energy electron distribution of a bulk, crystalline solid possessing a specific lattice parameter, and that this information can be used to calculate the properties of solids at zero Kelvin.

In chapter 3, we evaluated the numerical precision of the TB-LMTO ESC program [28]. We did so acknowledging that the minimum total energy of a solid, and the lowest-energy electron distribution of a solid, is not calculated exactly using the TB-LMTO ESC program. Rather, as a result of some algorithmic processes implemented within the TB-LMTO ESC program, the minimum total energy of a solid, as calculated using the program, contains a statistical calculation precision error (CPE) and a constant systematic calculation error (SCE). We estimated the standard deviation of the CPE's and the magnitude of the SCE's in the minimum total energy of solids, as calculated using the TB-LMTO ESC program. In our view, the discussion presented in chapter 3 is an initial effort in the development of a formal framework for evaluating the numerical precision of ESC programs. This framework acknowledges that the results of calculations performed with ESC programs contain both random and systematic errors that are analogous to the random and systematic errors that are present in any experimental measurement. Such a framework should be further developed in the future.

Having studied the numerical precision of the TB-LMTO ESC program [28], we then used the program to calculate some of the properties of the first-row transition metals (Sc to Zn) at zero Kelvin (chapter 4). We evaluated the accuracy of the calculated properties of these metals by comparing them to their experimental values. Such a study of the zero-Kelvin properties of the first-row transition metals had been conducted before (see appendix A), but not, to our knowledge, using the TB-LMTO ESC program [28]. In conducting this study, we learned that the exchange-correlation functional that is used when conducting calculations using the TB-LMTO ESC program has a significant impact on the program's accuracy. We found that the TB-LMTO ESC program most accurately predicts the zero-Kelvin crystal structure, lattice parameters, and magnetic moment magnitudes of the first-row transition metals when it is used in conjunction with exchange-correlation functional

EXC2. However, the bulk moduli of the first-row transition metals are more accurately calculated using exchange-correlation functional EXC4 (see table 2.1 of chapter 2 for a list of the exchange-correlation functionals that are available within the TB-LMTO ESC program).

Bearing in mind that we ultimately wish to develop a theoretical method for calculating the Helmholtz' free energy of complex magnetic materials like metallic Fe, we then used the TB-LMTO ESC program [28] to study the low-moment to high-moment magnetic transition in the first-row transition metals when they take the FCC crystal structure (chapter 5). We conducted this study because a volume-controlled low-moment to high-moment magnetic transition has recently been identified in some FCC-structured first-row transition metals [9,10], and because a composition controlled low-moment to high-moment transition has been shown to exist in FCC and HCP alloys [9,10,87]. It has also been established that this transition plays an important role in the thermal properties of Fe-bearing alloys like the Invar and anti-Invar alloys [9,10]. It was expected that any metal will undergo a low-moment to high-moment transition if its volume is expanded enough [83]. We showed using first principles calculations that all first-row transition metals, when they take the FCC phase, undergo a volume controlled low-moment to high-moment transition. We showed that FCC Fe occupies a special position in the first-row transition metal series, in that its low-moment to high-moment transition occurs when its volume is only slightly larger than its zero-Kelvin volume. We also predicted that metallic Ni could possess magnetic moments even at pressures of the order of that that exists at the center of the Earth. This may be of interest in the geophysical sciences, where recent efforts have been focussed on understanding the materials existing in the deep interiors of planets. Finally, we argued that magnetic moments are prevented from forming in the FCC 3d metals when they possess small lattice parameters because the energy bands of these metals' valence electrons are too wide at these small lattice parameters.

Finally, after presenting a theoretical method for calculating the Helmholtz' free energy of a bulk, crystalline solid (chapter 6), we applied this method in a study of the thermal expansion of metallic Cu (chapter 7). We specifically calculated the Helmholtz' free en-

ergy function $F(a,T)$ of metallic Cu, and used it to calculate the lattice parameter versus temperature curve $a(T)$ of this metal. We found that the $a(T)$ curve of metallic Cu can be accurately calculated using the theoretical method of chapter 6, but that the accuracy of this curve is dependent upon the exchange-correlation model that is used to calculate the $E_{tot}(a)$ curve of FCC Cu. We also found that the range of action of the inter-atomic interaction potential $E_{a-a}(x)$ appearing in the method of chapter 6 has a significant effect on the accuracy of the calculated $a(T)$ curve of metallic Cu. We thus concluded that the method of chapter 6 constitutes a practical method for calculating the $a(T)$ curves of metals, but that further research is necessary in order to properly evaluate the validity of the assumptions made in deriving the method.

More specifically, the assumption that an inter-atomic interaction potential $E_{a-a}(x)$ can be derived from the minimum total energy versus lattice parameter curve $E_{tot}(a)$ of a solid, and that this potential $E_{a-a}(x)$ can accurately reproduce the energy increase that occurs when the atomic nuclei of the solid move away from their equilibrium positions as they undergo small amplitude thermal oscillations must be further examined. We believe that the best way to do so is to conduct super-cell calculations in order to calculate this energy increase from first principles, and then to compare the results of this calculation to the value of the same energy increase computed using the potential $E_{a-a}(x)$. In addition, the effect of making a quasi-harmonic approximation in deriving the method of chapter 6 must be evaluated. Once this evaluation work is completed, the method of chapter 6 should be extended to make it capable of calculating the Helmholtz' free energy of complex magnetic materials, like metallic Fe. Once extended, the method should be capable of reproducing the microscopic effects responsible for the absence of thermal expansion in Invar alloys, and the appearance of magnetic moments in Fe-Ni alloys with more than 70 atomic % Fe [9,10].

Appendix A

Literature Review: Studies of the First-Row Transition Metals Using ESC Programs

We present here a review of the scientific literature discussing the use of ESC programs to study metallic solids composed of first-row transition elements. Our motivation for conducting this literature review is two-fold. Firstly, we wish to understand, in general, how ESC programs have been used to study the first-row transition metals in the past. We specifically want to understand what information ESC programs can provide about the first-row transition metals and how accurately ESC programs can predict the experimentally observed properties of these metals. Secondly, we want to understand how ESC programs have been used to study the magnetism of the first-row transition metals. We are specifically interested in those papers discussing the use of ESC programs to study the low-moment to high-moment transition in the first-row transition metals.

Our literature review is divided into 2 parts, namely a review of the literature published prior to 1980 (section A.1), and a review of the literature published after 1980 (section A.2). In both sections A.1 and A.2, we identify a number of papers discussing the use of ESC programs to study metals consisting of first-row transition elements and highlight

the main features of these papers. In section A.3, we summarise the information presented in sections A.1 and A.2 and draw three important conclusions. Firstly, we realise that ESC programs can be used to calculate a number of the zero-Kelvin properties of the first-row transition metals. Typically, the calculated zero-Kelvin lattice parameter of a first-row transition metal is within 5% of the experimentally determined value of this lattice parameter. Also, other calculated properties of the first-row transition metals are within 10 - 20% of the experimentally determined value of these properties. Secondly, we realise that ESC programs can be used to calculate the total energy versus lattice parameter curve of a material, but the accuracy of this calculated curve cannot be verified. This is due to the fact that the total energy versus lattice parameter curve of a material cannot be measured. Finally, we conclude that a systematic study of the low-moment to high-moment transition in all of the first-row transition metals has never been previously published.

A.1 Pre-1980 Studies of the First-Row Transition Metals Using ESC Programs

In order to understand how ESC programs have been used to study the first-row transition metals prior to the year 1980, it is useful to refer to a previous literature review published by A. P. Cracknell in 1984 [125]. In this earlier review, approximately 190 papers discussing the use of ESC programs to study the first-row transition metals are cited, all of which were published prior to 1980. Table A.1 shows the number of these papers that discuss the study of each of the first-row transition metals. Interestingly, in the period prior to 1980, ESC programs were most often used to study metallic Cu. Iron was the second-most studied first-row transition metal.

The majority of the 190 papers cited by Cracknell discuss the use of ESC programs to study one single metal consisting of one single first-row transition element, and possessing a specific crystal structure and lattice parameter (e.g., [205–214]). Cracknell states the

Table A.1: Number of papers discussing the use of ESC programs to study the first-row transition metals cited in the review of A. P. Cracknell

Transition metal	Number of papers
Sc	5
Ti	10
V	13
Cr	21
Mn	5
Fe	41
Co	15
Ni	37
Cu	73
Zn	11

All papers are cited in [125].

following in his review:

> In recent years many of the leading researchers working in the field have begun to move away from the pure metallic elements at standard pressures and have started working on the electronic structures of dilute alloys, metallic compounds and of metals under high pressures (...) ([125, p. 8]).

Thus, prior to the publication of Cracknell's review, scientists almost exclusively used ESC programs to study materials composed of only one chemical species. Only a few of the papers cited by Cracknell discuss the use of ESC programs to study many metals, each consisting of the same first-row transition element and each possessing the same crystal structure, but each possessing different lattice parameters [215–223]. Also, only the paper of Perrot [222] and the paper of Snow [223] discuss the use of ESC programs to calculate the total energy versus lattice parameter curve of a metal (FCC Cu in both

cases). A minority of papers discuss the use of ESC programs to study many metals, each composed of the same first-row transition element, but each possessing different crystal structures (e.g., [224–229]). Finally, two papers report the use of ESC programs to study systematically a large group of metals consisting of different transition elements [228,230].

In the 190 papers cited by Cracknell, ESC programs are used to calculate a variety of first-row transition metal properties. For example, ESC programs are used to calculate the band structure [205–207, 209–213, 228, 230–233], the density of electronic states [206, 207, 209–212, 228, 231, 233], and the Fermi surface of these metals [206, 207, 209, 210, 212, 231–233]. In essentially all of these 190 papers, the crystal structure of the first-row transition metal under study is the experimentally observed room-temperature crystal structure of this metal (e.g., [205–207, 209–214]). Additionally, the lattice parameter of the first-row transition metal under study is usually the experimentally observed room-temperature lattice parameter of this metal (e.g., [227, 231, 232, 234–241]). Thus, it appears that the authors of these papers used ESC programs to calculate the room-temperature properties of the first-row transition metals.

Finally, some of the 190 papers cited by Cracknell specifically discuss the use of ESC programs to study the magnetism of the first-row transition metals. Metallic Cr, Mn, Fe, Co and Ni are all magnetic metals [2]. In some papers, these metals are studied using ESC programs that can only provide information about non-magnetic materials (e.g. [242–246]). In other papers, these metals are studied using ESC programs that can provide information about solids possessing magnetic moments arranged in a simple collinear ferromagnetic or anti-ferromagnetic configuration (e.g. [88, 208, 209, 232, 238, 247–251]). (It should be noted that the paper of Andersen et al. [88] is not cited in Cracknell's review.) However, only BCC Fe, HCP Co and FCC Ni possess magnetic moments arranged in a collinear ferromagnetic structure, and so only at zero Kelvin [2]. It is known that, even at zero Kelvin, the magnetic moments of BCC Cr, though collinear, are not arranged in a simple ferromagnetic or anti-ferromagnetic configuration [2]. It is also known that the magnetic moments of FCC Fe are not collinear, even at zero Kelvin (see [128,129,252,253]). Prior to 1980, both BCC Cr and FCC Fe were studied using ESC programs that can calcu-

late the properties of solids possessing collinear magnetic moments in a simple ferromagnetic or anti-ferromagnetic arrangement only (e.g. [232, 247]). Importantly, the magnetic moment versus lattice parameter curves of ferromagnetic BCC Fe, FCC Fe and HCP Fe are reported in the paper of Andersen et al. [88]. None of the other papers published prior to 1980 discuss the low-moment to high-moment transition in any of the first-row transition metals.

A.2 Post-1980 Studies of the First-Row Transition Metals Using ESC Programs

In order to find papers published after 1980 and discussing the use of ESC programs to study the first-row transition metals, the ISI Web of Knowledge^{SM} [254] search engine was used. Table A.2 shows the number of papers identified using the ISI Web of Knowledge^{SM} search engine and discussing the electronic structure of each first-row transition metal. Most papers published after 1980 discuss the electronic structure of metallic iron and iron-bearing metals. This is because iron is an immensely important metal, for it is an important constituent of steel and other useful alloys [5], including the Invar alloys [9, 10, 102, 130–136]. Additionally, metallic iron is believed to be an important constituent of the Earth's inner core [6, p. 421]. Thus, many scientists have studied the properties of metallic iron under very high pressure [12, 13, 19–27].

After 1980, scientists no longer used ESC programs exclusively for studying simple metals composed of one single chemical species. Scientists often used ESC programs to study a variety of complex materials, such as small material clusters [255–263], metallic alloys [9, 102, 130, 134, 264–271], thin films [272–277], and amorphous materials [278, 279]. Scientists regularly calculated, after 1980, the total energy versus lattice parameter curve of the first-row transition metals (e.g. [54,56,58,64,65,68,72,89,91,93,96,104,280–283]). Scientists also regularly used ESC programs to study metals composed of the same first-row transition element, but possessing different crystal structures. For example, many papers

Table A.2: Number of papers discussing the electronic structure of the first-row transition metals published after 1980

Transition metal	Number of papers
Sc	24
Ti	217
V	105
Cr	174
Mn	85
Fe	901
Co	256
Ni	518
Cu	550
Zn	85

published after 1980 report the use of ESC programs to study both BCC Fe and FCC Fe, and sometimes HCP Fe as well [53, 65, 68, 72, 90–93, 104, 282, 284]. Interestingly, this allowed scientists to realise that some ESC programs fail to predict the correct zero-Kelvin crystal structure of metallic Fe (e.g. [55,57,60,62,64,65,67,72]). Additionally, many papers published after 1980 report the use of an ESC program to study a large number of the first-row transition metals (e.g. [60,63,69,71,84,285,286]). Among these latter papers, the paper of Zheng et al. [63] is particularly interesting. In this paper, an ESC program is used to study ten metals, each consisting of only one of the first-row transition elements, and possessing the HCP crystal structure. By studying theoretically these ten metals, Zheng et al. were able to better understand the three first-row transition metals that possess the HCP crystal structure at zero Kelvin (namely Sc, Ti and Zn).

As in the pre-1980 period, scientists used ESC programs to calculate a number of the properties of the first-row transition metals after 1980. After 1980, ESC programs were commonly used to calculate the magnitude of the magnetic moments [53, 56–59, 65, 66,

68,72,83], the elastic constants [53–62,64–66,68–72,84–86,287], and the cohesive energy [53,55,58,62,68–70,72,84] of the first-row transition metals. In contrast to the pre-1980 papers, many post-1980 papers report the use of an ESC program to predict the zero-Kelvin lattice parameter of a first-row transition metal (e.g. [54–72,84–86,287]). To calculate the zero-Kelvin lattice parameter of a given metal, scientists calculate the total energy versus lattice parameter curve of the metal. Then, the lattice parameter at which this calculated curve possesses a global minimum value is identified. This lattice parameter is the zero-Kelvin lattice parameter of the metal, as predicted by the ESC program. Typically, the lattice parameter of a first-row transition metal, as calculated using an ESC program, is within 5% of the experimental value of the zero-Kelvin lattice parameter of this metal. Once the zero-Kelvin lattice parameter of a metal is identified, the ESC program is used to calculate other zero-Kelvin properties of the metal. Typically, these calculated properties are within 10 - 20% of the experimental value of the properties of the metal. Importantly, the accuracy with which the ESC program calculates the total energy versus lattice parameter curve of a metal is never evaluated. This is because it is not possible to measure the total energy versus lattice parameter curve of any material.

Finally, after the year 1980, scientists constructed ESC programs that are capable of providing information about materials possessing complex magnetic properties. After 1980, some of the first-row transition metals were studied using ESC programs capable of providing information about materials possessing magnetic moments arranged in complex, non-collinear configurations (e.g. [99,128,129,252,262,275,288–296]). Some first-row transition metals were also studied using ESC programs that are capable of providing information about materials possessing magnetic moments arranged in a collinear ferromagnetic or anti-ferromagnetic configuration only (e.g. [93,96,100,286]). Importantly, some papers published after 1980 discuss the low-moment to high-moment transition in some of the first-row transition metals [56,58,83,87,89–106,297]. Most of these papers disscuss the low-moment to high-moment transition in BCC Fe and FCC Fe, and sometimes in HCP Fe as well. Some of these latter papers discuss the low-moment to high-moment transition in BCC Cr [58,97], in BCC V [97], in BCC Mn [106], in FCC Mn [96,106], and in FCC Co [101].

One paper reports the calculation of the magnetic moment versus lattice parameter curves of BCC Cr, BCC Fe, HCP Co, and FCC Ni [56], while another reports the magnetic moment versus lattice parameter curves of BCC V, FCC Fe, FCC Co, and BCC Ni [83]. However, no papers reporting a systematic study of the low-moment to high-moment transition in all first-row transition metals were identified.

A.3 Summary of Studies of the First-Row Transition Metals Using ESC Programs

As indicated previously, this literature review was conducted for two major reasons. Firstly, we wished to understand, in general, how ESC programs have been used in the past to obtain information about the first-row transition metals. We specifically wanted to understand what properties of the first-row transition metals can be calculated using ESC programs and how accurately ESC programs can predict the experimentally measured properties of these metals. Secondly, we wished to understand how ESC programs have been used to study the magnetic properties of the first-row transition metals. In particular, we wanted to know how ESC programs have been used to study the low-moment to high-moment transition in the first-row transition metals.

In completing our survey of the scientific literature, we have seen that the papers published after 1980 discuss the use of ESC programs to study materials that are more complex than those studied in the pre-1980 literature. Additionally, a larger number of materials are studied in the more recent papers. This is largely due to the fact that modern computers are more rapid than their forerunners. These more rapid computers have made possible more computationally intensive studies of the first-row transition metals.

We have also seen that scientists now regularly calculate the total energy versus lattice parameter curve of the first-row transition metals. The fact that computers were not rapid enough to allow for the efficient computation of such curves may largely explain why they

were seldom calculated prior to 1980. Scientists now also understand that ESC programs can only provide information about materials possessing a temperature of zero Kelvin. This is due to the fact that, in modern ESC programs, the kinetic energy of the atomic nuclei of solids is explicitly ignored [32, 293]. Thus, ESC programs can only be used to calculate the properties of a solid when its constituent atoms remain absolutely stationary at specific locations in space. At non-zero temperatures, the nuclei of any real material's constituent atoms are constantly in motion. The nuclei of a material's constituent atoms are only stationary when the material has a temperature of zero Kelvin [37, p. 416]. (It should be noted that, according to the quantum-mechanical theory of atomic motion in solids, the nuclei of a material's constituent atoms are never absolutely stationary. Rather, a material's constituent atoms oscillate about their mean positions at all temperatures, but oscillate minimally at zero Kelvin [37, p. 416].) The calculation of the total energy versus lattice parameter curve of a solid is the first step in using an ESC program to predict the zero-Kelvin properties of this solid. At a specific lattice parameter a, the total energy versus lattice parameter curve of a solid gives the minimum value of the energy of the solid when its constituent atoms remain stationary on a specific crystal lattice with lattice parameter a. This curve has a global minimum value, which occurs at a lattice parameter a_{min}. The lattice parameter a_{min} is the zero-Kelvin lattice parameter of the solid, as predicted by the ESC program. The ESC program can also be used to calculate other properties of the solid as a function of lattice parameter. The calculated properties at a_{min} are the zero-Kelvin properties of the solid, as predicted by the ESC program.

The accuracy of ESC programs has been evaluated by comparing the calculated properties of solids with their measured properties. Scientists consider that modern ESC programs can predict the zero-Kelvin properties of solids with reasonable accuracy. However, only certain limited aspects of the information provided by ESC programs can actually be compared with measured data. For instance, the lattice parameter a_{min} at which a solid's total energy versus lattice parameter curve possesses a global minimum can be compared to the true zero-Kelvin lattice parameter of this solid. Even though it is not possible to measure the zero-Kelvin lattice parameter of a solid, it is possible to estimate its value by measuring

the lattice parameter versus temperature curve of the solid and then using extrapolation techniques to estimate the value of the solid's lattice parameter at zero Kelvin. Many other solid properties can be both calculated using an ESC programs and determined experimentally. It is thus possible to gauge the accuracy with which an ESC program can predict these solid properties. However, it is impossible to measure, at any temperature, the total energy of a solid. Thus, the accuracy of the total energy versus lattice parameter curve of a solid, as calculated by an ESC program, cannot be directly verified.

Finally, we have identified only a few papers discussing the low-moment to high-moment transition in the first-row transition metals. Most of these papers discuss the low-moment to high-moment transition in a single metal only, usually metallic Fe. This is because the Invar effect, which is observed in iron-rich FCC Fe-Ni alloys, is intimately connected to the low-moment to high-moment transition in FCC Fe [9, 10]. Importantly, one paper reports a study of the low-moment to high-moment transition in BCC Cr, BCC Fe, HCP Co and FCC Ni [56]. In another interesting paper, an ESC program is used to study a composition-controlled low-moment to high-moment transition in first-row transition metal alloys [87]. However, no papers reporting a systematic study of the low-moment to high-moment transition in all first-row transition metals were identified.

Appendix B

Parametrization of the Calculated $E_{tot}(a)$ Curve of FCC Cu

In chapter 7, we describe the calculation of the lattice parameter versus temperature curve $a(T)$ of metallic Cu using the theoretical method for calculating the Helmholtz' free energy of a material described in chapter 6. In order to calculate the $a(T)$ curve of metallic Cu, knowledge of the minimum total energy versus lattice parameter curve $E_{tot}(a)$ of FCC Cu is required. We describe, in section 7.1 of chapter 7, the calculation of two $E_{tot}(a)$ curves of FCC Cu. We calculate these curves using the TB-LMTO ESC program [28] and two of the exchange-correlation functionals available within the program. Specifically, we calculate one curve using exchange-correlation functional EXC2 and the other using EXC4 (see table 2.1 of chapter 2).

In order to calculate the $a(T)$ curve of metallic Cu, we must be able to obtain the value of the $E_{tot}(a)$ curve of FCC Cu at almost any value of lattice parameter a. For this purpose, we parametrize, in section B.1, the calculated $E_{tot}(a)$ curves of FCC Cu using appropriate model functions. In addition, we indicated in chapter 3 that all values of an $E_{tot}(a)$ curve calculated using the TB-LMTO ESC program contain a calculation precision error (CPE). We also evaluate the magnitude of the CPE's in the calculated $E_{tot}(a)$ curves in section B.1. Finally, the calculation of the $a(T)$ curve of metallic Cu using the theoretical method

of chapter 6 requires knowledge of the first- and second-derivatives of the $E_{tot}(a)$ curve of FCC Cu. In section B.2, we evaluate these derivatives using the parametrization of the $E_{tot}(a)$ curve presented in section B.1. We also evaluate the numerical precision of the first- and second-derivatives of the $E_{tot}(a)$ curve in this latter section.

B.1 Parametrization of and Evaluation of the Numerical Precision of the Calculated $E_{tot}(a)$ Curves

In this section, we parametrize the EXC2 and EXC4 $E_{tot}(a)$ curves, calculated as described in section 7.1 of chapter 7. Then, we evaluate the numerical precision of each of these curves.

B.1.1 Parametrization of the Calculated $E_{tot}(a)$ Curves - General Considerations

In order to facilitate the parametrization of the two $E_{tot}(a)$ curves, we divide them into seven sections extending over specific lattice parameter ranges. We then individually parametrize these sections of the $E_{tot}(a)$ curves.

The parametrization sections are chosen knowing that the $E_{tot}(a)$ curves are used to construct an inter-atomic interaction potential $E_{a-a}(x)$ as per equation 7.2 of chapter 7. The lattice parameter ranges over which the sections extend are shown in table B.1. We label the first section of each curve the "1NN section" because knowledge of only this section of a curve is required if the range of action of $E_{a-a}(x)$ is restricted to the distance separating a given atomic nucleus of the FCC Cu solid from its first nearest-neighbour coordination shell. The 1NN section must cover the entire range of lattice parameter values that can appear in the calculated $a(T)$ curve of metallic Cu. This range must therefore include the lattice parameter at which there is a global minimum in the $E_{tot}(a)$ curve, as this is the

lattice parameter of metallic Cu at zero Kelvin. The range should extend to a lattice parameter that is approximately 10% larger than that at which the $E_{tot}\,(a)$ curve possesses a global minimum, as this lattice parameter is certainly larger than the lattice parameter of metallic Cu at temperatures just below its melting point [80]. A buffer of approximately 0.3 Bohr radii is added on both extremities of the range thus defined in order to ensure that the functional form of the 1NN section of the $E_{tot}\,(a)$ curves is properly captured by the parametrization.

We label the second section of each curve the "2NN section" because knowledge of this section of a curve, in addition to knowledge of its 1NN section, is required if the range of action of the inter-atomic interaction potential $E_{a-a}\,(x)$ is restricted to the distance separating a given atomic nucleus of the FCC Cu solid from its second nearest-neighbour coordination shell. The 2NN section extends over the lattice parameter range defined by multiplying by $\sqrt{2}$ the extremities of the lattice parameter range of the 1NN section.

The third section of each curve is labelled the "3NNto5NN section", as knowledge of this section of a curve, in addition to knowledge of its 1NN and 2NN sections, is required if the range of action of $E_{a-a}\,(x)$ is restricted to the distance separating a given atomic nucleus of the FCC Cu solid from its third, fourth or fifth nearest-neighbour coordination shell. The 3NNto5NN section extends over the lattice parameter range defined by multiplying by $\sqrt{3}$ the lattice parameter defining the left-most extremity of the 1NN section, and by multiplying by $\sqrt{5}$ the lattice parameter defining the right-most extremity of the 1NN section.

All other sections of the $E_{tot}\,(a)$ curves are defined in a manner similar to the 3NNto5NN section, with the exception of the 15NNandmore section. The lattice parameter range of this latter section is defined by multiplying by $\sqrt{15}$ the lattice parameter defining the left-most extremity of the 1NN section. The 15NNandmore section extends from this latter lattice parameter all the way to $a = 50$ Bohr radii, the largest lattice parameter at which the value of the two $E_{tot}\,(a)$ curves is calculated using the TB-LMTO ESC program.

Having divided the two $E_{tot}\,(a)$ curves into sections, we now proceed with the parametriza-

Table B.1: Parametrization sections of the EXC2 and EXC4 $E_{tot}(a)$ curves

Section label	Range of section for EXC2 curve	Range of section for EXC4 curve
1NN	$6.3 \leq a \leq 7.7$ Bohr radii	$6.6 \leq a \leq 8.0$ Bohr radii
2NN	$8.9 \leq a \leq 11.0$ Bohr radii	$9.3 \leq a \leq 11.3$ Bohr radii
3NNto5NN	$10.5 \leq a \leq 17.5$ Bohr radii	$11.0 \leq a \leq 18.0$ Bohr radii
6NNto8NN	$15.0 \leq a \leq 22.0$ Bohr radii	$16.0 \leq a \leq 23.0$ Bohr radii
9NNto11NN	$18.5 \leq a \leq 26.0$ Bohr radii	$19.5 \leq a \leq 27.0$ Bohr radii
12NNto14NN	$21.5 \leq a \leq 29.0$ Bohr radii	$22.5 \leq a \leq 30.0$ Bohr radii
15NNandmore	$24.0 \leq a \leq 50.0$ Bohr radii	$25.5 \leq a \leq 50.0$ Bohr radii

tion of each of these sections. With the exception of the 15NNandmore section, we parametrize all sections of both $E_{tot}(a)$ curves using a polynomial function of the form $E_{tot}(a) = c_n \times a^n + ... + c_2 \times a^2 + c_1 \times a + c_0$, where the constants c_i are parameters to be optimised. We parametrize the 15NNandmore section of both curves using a decaying exponential function of the form $E_{tot}(a) = c_n \times e^{-c_{n-1}a} + ... + c_2 \times e^{-c_1 a} + c_0$. We do so because the 15NNandmore section of each $E_{tot}(a)$ curve is expected to decay toward an asymptotic value as $a \rightarrow \infty$.

Once a given section of an $E_{tot}(a)$ curve has been parametrized, we can estimate the numerical precision of the value of the curve at any lattice parameter within the given section. In the next section of this chapter, we illustrate by example the parametrization and the evaluation of the numerical precision of a section of the $E_{tot}(a)$ curve of FCC Cu.

B.1.2 Parametrization of and Estimation of the Numerical Precision of the 1NN Section of the EXC2 $E_{tot}\,(a)$ Curve

We begin with the parametrization of the 1NN section of the EXC2 $E_{tot}\,(a)$ curve of FCC Cu.

In the 1NN section, the TB-LMTO ESC program was used to calculate the value of the EXC2 $E_{tot}\,(a)$ curve at 15 lattice parameter values lying in the range $6.3 \leq a \leq 7.7$ Bohr radii, all uniformly separated by an interval of 0.1 Bohr radii. Each value of the EXC2 $E_{tot}\,(a)$ curve thus calculated can be expressed as $E^{*}_{tot}\,(a) = E_{tot}\,(a) + \Delta E(a)$. In the previous expression, $E^{*}_{tot}\,(a)$ represents the value of the EXC2 $E_{tot}\,(a)$ curve that was calculated using the TB-LMTO ESC program at some specific lattice parameter a. This value is not the true value of the EXC2 $E_{tot}\,(a)$ curve at this specific lattice parameter a. Rather, it is equal to the true value of the EXC2 $E_{tot}\,(a)$ curve at this lattice parameter a plus some quantity $\Delta E(a)$. This latter quantity is a calculation precision error (CPE). We model the 1NN section of the EXC2 $E_{tot}\,(a)$ curve (containing no CPE's) as a smooth function of the form $E_{tot}\,(a) = c_n \times a^n + ... + c_2 \times a^2 + c_1 \times a + c_0$, where a represents the lattice parameter and the constants c_i are parameters to be determined.

The process of finding the parameters c_i describing the 1NN section of the EXC2 $E_{tot}\,(a)$ curve is analogous to the process of finding a function that accurately describes an experimentally measured data set. In this case, the "experimental data set" is the collection of 15 values of the 1NN section of the EXC2 $E_{tot}\,(a)$ curve that were obtained by conducting 15 computational experiments using the TB-LMTO ESC program. The value of the parameters c_i can be obtained using a least-squares error minimisation routine like the Levenburg-Marquardt otimisation algorithm given in the text "Numerical Recipes in C" [204]. Ordinarily, information about the statistical distribution of the errors in the measured data set is available prior to determining the function that best models this measured data. This information can be used to evaluate confidence intervals on the value of the parameters c_i describing the function that models the measured data set. We simply assume that the process leading to the CPE's in the calculated values of the EXC2 $E_{tot}\,(a)$

curve can indeed be modelled as a zero-mean Gaussian random variable. This assumption allows us to take the parameters c_i computed using the Levenburg-Marquardt algorithm to be the coefficients of a polynomial that describes what is most likely to be the EXC2 $E_{tot}\,(a)$ curve, given that an experiment designed to measure this curve resulted in the 15 values obtained using the TB-LMTO ESC program described above. This assumption will be further discussed later.

In order to parametrize the 1NN section of the EXC2 $E_{tot}\,(a)$ curve, the number of parameters c_i that are needed to represent this curve must be determined. This is equivalent to determining the order of the polynomial that best-describes the 1NN section of the EXC2 $E_{tot}\,(a)$ curve. This is accomplished by first assuming that a 2^{nd}-order polynomial accurately describes this latter curve. The Levenburg-Marquardt algorithm is used to calculate the optimal value of the coefficients of this polynomial. The minimum value of the χ^2 statistic computed using the Levenburg-Marquardt algorithm is noted. Then, it is assumed that the best description of the 1NN section of the EXC2 $E_{tot}\,(a)$ curve is a 3^{rd}-order polynomial. Again, the Levenburg-Marquardt algorithm is used to compute the optimal value of the coefficients of this polynomial. Again, the minimum value of the χ^2 statistic computed using the Levenburg-Marquardt algorithm is noted. This process is repeated, each time assuming that the 1NN section of the EXC2 $E_{tot}\,(a)$ curve is optimally described using a higher order polynomial. Additionally, each time the Levenburg-Marquardt algorithm is run, it is assumed that the process leading to the CPE's in the calculated values of the 1NN section of the EXC2 $E_{tot}\,(a)$ curve can be modelled as a zero-mean Gaussian random variable with unit variance. The plot of the noted χ^2 values versus the order of the polynomial describing the 1NN section of the EXC2 $E_{tot}\,(a)$ curve can then be constructed.

Figure B.1 shows the plot of the base 10 logarithm of the χ^2 values noted as described above versus the order of the polynomial describing the 1NN section of the EXC2 $E_{tot}\,(a)$ curve. In figure B.1, it is clear that, as the polynomial order rises from 2 to 5, the value of $log_{10}\,(\chi^2)$ decreases until it reaches a plateau. Increasing the order of the polynomial from 5 to 6 does not result in as large a reduction in the value of the χ^2 statistic as does increasing the order of the polynomial from 4 to 5. Increasing the order of the polynomial

from 6 to 7 does result in a further reduction of the value of the χ^2 statistic computed using the Levenburg-Marquardt algorithm. However, when the 1NN section of the EXC2 $E_{tot}(a)$ curve is described using a 7^{th}-order polynomial, it is not possible to compute confidence intervals for the coefficients of this polynomial due to the occurrence of numerical overflow during the computation of these confidence intervals (more on confidence intervals later). Thus, it is concluded that the optimal representation of the 1NN section of the EXC2 $E_{tot}(a)$ curve is a 5^{th}-order polynomial. Table B.2 gives the value of the coefficients of this polynomial. We report these coefficients exactly as obtained using the Levenburg-Marquardt algorithm, keeping all calculated figures of the coefficients. We shall discuss the calculation of confidence intervals for these coefficients shortly.

Table B.2: Coefficients of the optimal polynomial description of the 1NN section of the EXC2 $E_{tot}(a)$ curve

Coefficient	Value of coefficient
c_5	-0.00442280974383
c_4	0.169831448569
c_3	-2.62554518236
c_2	20.4344349712
c_1	-80.0079274534
c_0	-3181.91607082

Units of parameter c_i: Rydberg per atom $\times$ (Bohr radii)$^{-i}$

Figure B.2 shows the calculated values of the 1NN section of the EXC2 $E_{tot}(a)$ curve (which we label $E^*_{tot}(a)$), the optimal polynomial representation of the 1NN section of the EXC2 $E_{tot}(a)$ curve (the coefficients of which are given in table B.2) and values of a function $\Delta E(a) = E^*_{tot}(a) - E_{tot}(a)$. We take the values of the function $\Delta E(a)$ to represent the value of the CPE in each of the 15 calculated values $E^*_{tot}(a)$. More specifically, we take each value of the function $\Delta E(a)$ to be an independent manifestation of a single random variable X_{CPE}, which we assume to be Gaussian. This random variable X_{CPE} is meant to describe the process resulting in the CPE's that are present in the calculated values of

the 1NN section of the EXC2 $E_{tot}\,(a)$ curve. The average, standard deviation, root-mean-squared value, and absolute maximum value of the 15 values of the function $\Delta E\,(a)$ can be calculated. These values are shown in table B.3.

Table B.3: Average, standard deviation, root-mean-squared, and absolute maximum value of the function $\Delta E(a)$ shown in figure B.2

Average value of $\Delta E(a)$	-3.3×10^{-13} Rydberg per atom
Standard deviation of $\Delta E(a)$	2.4×10^{-6} Rydberg per atom
Root-mean-squared value of $\Delta E(a)$	2.4×10^{-6} Rydberg per atom
Absolute maximum value of $\Delta E(a)$	4.6×10^{-6} Rydberg per atom

We take the information presented in table B.3 to indicate that the random variable X_{CPE} describing the process leading to the CPE's in the calculated values of the 1NN section of the EXC2 $E_{tot}\,(a)$ curve has a mean of the order of 10^{-13} Rydberg per atom and a standard deviation between $2.4{\times}10^{-6}$ to $4.6{\times}10^{-6}$ Rydberg per atom. Using a Kolmogorov-Smirnov test [204], we evaluate the likelihood that the values of the function $\Delta E(a)$ are manifestations of a Gaussian random variable with standard deviation between 2.4×10^{-6} and 4.6×10^{-6} Rydberg per atom. We find that it is more likely that the values of $\Delta E(a)$ are manifestations of a Gaussian random variable with a standard deviation of 4.5×10^{-6} Rydberg per atom than with standard deviation of 2.5×10^{-6} Rydberg per atom. Thus, we conclude that the CPE's in the calculated values of the 1NN section of the EXC2 $E_{tot}\,(a)$ curve are of the order of 4.5×10^{-6} Rydberg per atom.

Having ascertained the magnitude of the CPE's in the calculated values of the 1NN section of the EXC2 $E_{tot}\,(a)$ curve, we now calculate confidence intervals for the coefficients c_i of the polynomial that describes the 1NN section of the EXC2 $E_{tot}\,(a)$ curve [204]. This is accomplished by re-running the Levenburg-Marquardt program, but this time setting to $\pm 4.5 \times 10^{-6}$ Rydberg units per atom the value of the uncertainty in the calculated values of the 1NN section of the EXC2 $E_{tot}\,(a)$ curve. When used in this manner, the Levenburg-Marquardt algorithm provides one-σ confidence intervals for the parameters c_i [204]. In

table B.4, we show the confidence intervals thus obtained. They will later be used to estimate the numerical precision of the derivatives of the EXC2 $E_{tot}(a)$ curve within the 1NN section of the curve.

Table B.4: One-σ confidence intervals of the coefficients of the optimal polynomial description of the 1NN section of the EXC2 $E_{tot}(a)$ curve

Confidence interval	Value
Δc_5	± 0.00018
Δc_4	± 0.0063
Δc_3	± 0.087
Δc_2	± 0.61
Δc_1	± 2.1
Δc_0	± 3.0

Units of interval Δc_i: Rydberg per atom $\times$ (Bohr radii)$^{-i}$

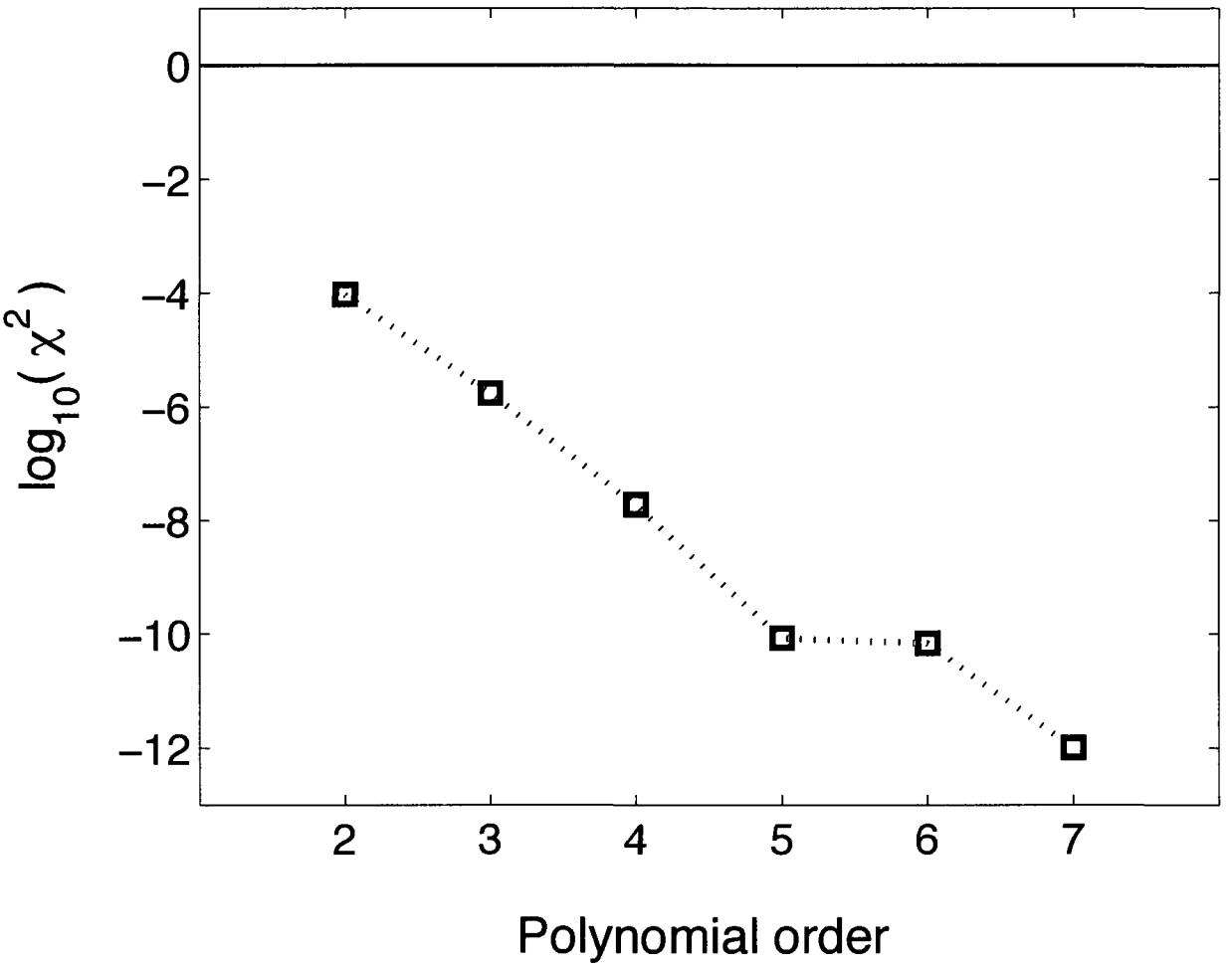

Figure B.1: Base 10 logarithm of the χ^2 statistic versus the order of the polynomial describing the 1NN section of the EXC2 $E_{tot}\,(a)$curve.

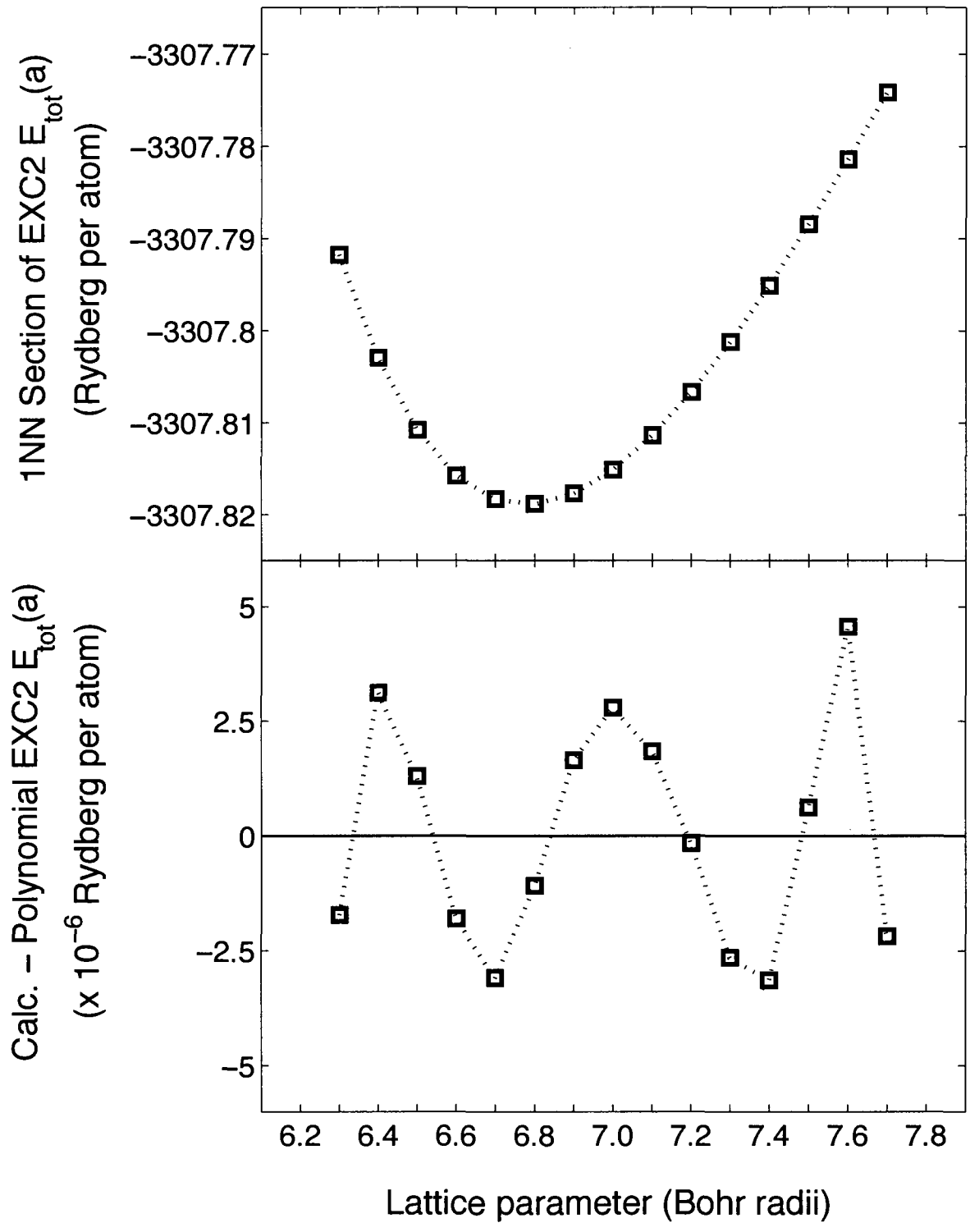

Figure B.2: 1NN section of the EXC2 $E_{tot}(a)$ curve of FCC Cu. Squares in the upper figure represent calculated values $E^{*}_{tot}(a)$ of the 1NN section of the EXC2 $E_{tot}(a)$ curve obtained using the TB-LMTO ESC program. The dotted line in the upper figure represents the optimal polynomial model of this section of the curve. The lower figure shows the function $\Delta E(a) = E^{*}_{tot}(a) - E_{tot}(a)$ in the 1NN section.

B.1.3 Parametrization of and Estimation of the Numerical Precision of All Sections of the EXC2 and EXC4 E_{tot} (a) Curves

The parametrization and the evaluation of the numerical precision of all other sections of the EXC2 and the EXC4 $E_{tot}(a)$ curves is conducted in a similar fashion. In figures B.3 to B.16, we show the calculated values of each section of the two $E_{tot}(a)$ curves, as obtained using the TB-LMTO ESC program. We also show the optimal polynomial or decaying exponential representation of each section of the two curves. In some of these figures, some of the values are illustrated by circular symbols. These values are omitted from the parametrization process, as we believe that they contain excessively large CPE's. Such values appear in the 9NNto11NN section and the 12NNto14NN section of the EXC4 $E_{tot}(a)$ curve.

Table B.5 shows the numerical precision of all sections of the two $E_{tot}(a)$ curves. Each value listed in the table is the standard deviation of a zero-mean Gaussian random variable assumed to describe the process leading to the CPE's in each section of the curve. Tables B.6 and B.8 respectively show the parameters defining the optimal polynomial or decaying exponential description of each section of the EXC2 and EXC4 $E_{tot}(a)$ curves. Tables B.7 and B.9 respectively show one-σ confidence intervals for the parameters of tables B.6 and B.8. These confidence intervals are calculated assuming that the CPE's in each section of the two $E_{tot}(a)$ curves are the result of a zero-mean Gaussian random variable with standard deviation as indicated in table B.5. In the next section of this appendix, these confidence intervals will be used to estimate the numerical precision of the first- and second-derivatives of the two calculated $E_{tot}(a)$ curves.

Before turning our attention to the derivatives of the two calculated $E_{tot}(a)$ curves, we explain the number of figures reported for each of the parameters c_i in tables B.6 and B.8. It is customary when reporting a parameter obtained using the Levenburg-Marquardt routine to treat the confidence interval of the parameter as its numerical error. By this, we mean that ordinarily, we would report the first parameter c_5 reported in table B.6 along with its confidence interval (reported in table B.7) as -0.00442 ± 0.00018. However, we found

that when the fitting parameters of tables B.6 and B.8 are truncated as just explained, the polynomial or decaying exponential functions that they describe are not good models of the calculated $E_{tot}(a)$ curves of FCC Cu. We believe that this is the result of strong correlations between the parameters c_i describing any section of the $E_{tot}(a)$ curve of FCC Cu. Thus, when reporting the parameters c_i, we report all figures provided by the Levenburg-Marquardt routine. In doing so, the functions defined by the parameters c_i are truly the optimal models of each section of the calculated $E_{tot}(a)$ curves of FCC Cu.

Finally, we return briefly to our assumption that the CPE's in the calculated values of the $E_{tot}(a)$ curves are the result of a Gaussian random process. Though the exact distribution of these CPE's is not known, the functions $\Delta E(a)$ of figures B.3 to B.16 provide evidence that the assumption that they are Gaussian is reasonable. First of all, the mean of the available values of each function $\Delta E(a)$ is essentially zero. In addition, approximately half of the available values of each function $\Delta E(a)$ are positive, while the other half are negative. Thirdly, the available values of each function $\Delta E(a)$ span a range that is essentially centered on the value $\Delta E(a) = 0$. None of this is proof that the CPE's in the calculated values of the $E_{tot}(a)$ curves of FCC Cu are the result of a Gaussian random process. However, a set of CPE's produced by a Gaussian random process would possess all three of these properties. We thus believe that modelling the CPE's in the calculated values of the $E_{tot}(a)$ curves of FCC Cu using Gaussian random variables will allow us to propagate these CPE's to obtain good estimates of the numerical precision of the Helmholtz' free energy and of the lattice parameter versus temperature curve of metallic Cu, as calculated using our theoretical method of chapter 6.

Table B.5: Numerical precision of all sections of the EXC2 and EXC4 $E_{tot}(a)$ curves

Curve section	Precision of EXC2 $E_{tot}(a)$ curve	Precision of EXC4 $E_{tot}(a)$ curve
1NN section	$\pm 4.5 \times 10^{-6}$	$\pm 5.0 \times 10^{-6}$
2NN section	$\pm 3.0 \times 10^{-7}$	$\pm 6.0 \times 10^{-6}$
3NNto5NN section	$\pm 3.5 \times 10^{-6}$	$\pm 5.0 \times 10^{-5}$
6NNto8NN section	$\pm 5.5 \times 10^{-5}$	$\pm 1.0 \times 10^{-4}$
9NNto11NN section	$\pm 3.0 \times 10^{-4}$	$\pm 3.0 \times 10^{-5}$
12NNto14NN section	$\pm 3.0 \times 10^{-4}$	$\pm 3.0 \times 10^{-5}$
15NNandmore section	$\pm 3.0 \times 10^{-4}$	$\pm 3.0 \times 10^{-5}$

All uncertainties have Rydberg units per atom.

Table B.6: Parameters describing the EXC2 $E_{tot}\,(a)$ curve

Parameter	Value in 1NN section*	Value in 2NN section*	Value in 3NNto5NN section*	Value in 6NNto8NN section*
c_6	-	-	$9.21655716878 \times 10^{-8}$	-
c_5	-0.00442280974383	$-6.95357491738 \times 10^{-5}$	$-6.03589102783 \times 10^{-6}$	$2.74499203147 \times 10^{-6}$
c_4	0.169831448569	0.00360674707121	0.000129864791984	-0.00025793363804
c_3	-2.62554518236	-0.0742249895124	-0.000215032652317	0.00973513085603
c_2	20.4344349712	0.749720956545	-0.0336417313294	-0.184618095878
c_1	-80.0079274534	-3.62752398301	0.514227959411	1.7599160287
c_0	-3181.91607082	-3301.20539882	-3309.96999416	-3314.25330885
Parameter	Value in 9NNto11NN section*	Value in 12NNto14NN section*	Value in 15NNandmore section**	
c_4	-	-	-	
c_3	$-1.76556892428 \times 10^{-5}$	-	-	
c_2	0.00117971172301	$-9.00777309701 \times 10^{-6}$	3.27137213521	
c_1	-0.0262613444332	0.000241568717902	0.323514026748	
c_0	-3307.31198841	-3307.50758214	-3307.5082555	

* units of parameter c_i: Rydberg per atom $\times$ (Bohr radii)$^{-i}$

** units of parameter c_i: Rydberg per atom, if i is even; (Bohr radii)$^{-1}$, if i is odd

Table B.7: One-σ confidence intervals for the parameters describing all sections of the EXC2 $E_{tot}\,(a)$ curve

Confidence interval	Value in 1NN section*	Value in 2NN section*	Value in 3NNto5NN section*	Value in 6NNto8NN section*
Δc_6	-	-	$\pm 2.1 \times 10^{-8}$	-
Δc_5	± 0.00018	$\pm 2.0 \times 10^{-6}$	$\pm 1.8 \times 10^{-6}$	$\pm 5.7 \times 10^{-7}$
Δc_4	± 0.0062	$\pm 9.7 \times 10^{-5}$	$\pm 6.1 \times 10^{-5}$	$\pm 5.3 \times 10^{-5}$
Δc_3	± 0.087	± 0.0019	± 0.0011	± 0.0019
Δc_2	± 0.61	± 0.019	± 0.012	± 0.036
Δc_1	± 2.1	± 0.093	± 0.064	± 0.32
Δc_0	± 3.0	± 0.18	± 0.14	± 1.2
Confidence interval	Value in 9NNto11NN section*	Value in 12NNto14NN section*	Value in 15NNandmore section**	
Δc_4	-	-	-	
Δc_3	$\pm 8.0 \times 10^{-6}$	-	-	
Δc_2	± 0.00053	$\pm 1.6 \times 10^{-5}$	± 7.2	
Δc_1	± 0.012	± 0.00080	± 0.088	
Δc_0	± 0.086	± 0.010	$\pm 5.6 \times 10^{-5}$	

* units of confidence interval Δc_i: Rydberg per atom $\times$ (Bohr radii)$^{-i}$

** units of confidence interval Δc_i: Rydberg per atom, if i is even; (Bohr radii)$^{-1}$, if i is odd

Table B.8: Parameters describing the EXC4 $E_{tot}\,(a)$ curve

Parameter	Value in 1NN section*	Value in 2NN section*	Value in 3NNto5NN section*	Value in 6NNto8NN section*
c_6	-	-	$-1.32517643681 \times 10^{-6}$	-
c_5	-0.00279998660382	-0.00011141466741	0.000119352773751	-
c_4	0.112194510291	0.00552055574531	-0.00446610332642	-
c_3	-1.80926750227	-0.108921421424	0.0890154094361	$4.16858220288 \times 10^{-5}$
c_2	14.6805112214	1.06318872812	-0.999745900381	-0.00268329951563
c_1	-59.8816736735	-5.05693804525	6.03259428397	0.0577173787305
c_0	-3213.12768402	-3301.95991454	-3326.38660722	-3311.37301938

Parameter	Value in 9NNto11NN section*	Value in 12NNto14NN section*	Value in 15NNandmore section**	
c_4	-	-	-	
c_3	$3.06951755162 \times 10^{-6}$	-	-	
c_2	-0.000240907502717	$-6.15100396858 \times 10^{-6}$	-	
c_1	0.00632216851816	0.000353135018409	-	
c_0	-3311.01323466	-3310.96278321	-3310.95768948	

* units of parameter c_i: Rydberg per atom $\times$ (Bohr radii)$^{-i}$

** units of parameter c_i: Rydberg per atom, if i is even; (Bohr radii)$^{-1}$, if i is odd

Table B.9: One-σ confidence intervals for the parameters describing all sections of the EXC4 $E_{tot}\,(a)$ curve

Confidence interval	Value in 1NN section*	Value in 2NN section*	Value in 3NNto5NN section*	Value in 6NNto8NN section*
Δc_6	-	-	$\pm 3.0 \times 10^{-7}$	-
Δc_5	± 0.00016	$\pm 3.2 \times 10^{-5}$	$\pm 2.6 \times 10^{-5}$	-
Δc_4	± 0.0060	± 0.0016	± 0.00095	-
Δc_3	± 0.087	± 0.034	± 0.018	$\pm 3.3 \times 10^{-6}$
Δc_2	± 0.63	± 0.35	± 0.19	± 0.00020
Δc_1	± 2.3	± 1.8	± 1.1	± 0.0038
Δc_0	± 3.4	± 3.6	± 2.6	± 0.024
Confidence interval	Value in 9NNto11NN section*	Value in 12NNto14NN section*	Value in 15NNandmore section**	
Δc_4	-	-	-	
Δc_3	$\pm 8.1 \times 10^{-7}$	-	-	
Δc_2	$\pm 5.7 \times 10^{-5}$	$\pm 1.7 \times 10^{-6}$	-	
Δc_1	± 0.0013	$\pm 9.2 \times 10^{-5}$	-	
Δc_0	± 0.010	± 0.0012	$\pm 2.8 \times 10^{-5}$	

* units of confidence interval Δc_i: Rydberg per atom $\times$ (Bohr radii)$^{-i}$

** units of confidence interval Δc_i: Rydberg per atom, if i is even; (Bohr radii)$^{-1}$, if i is odd

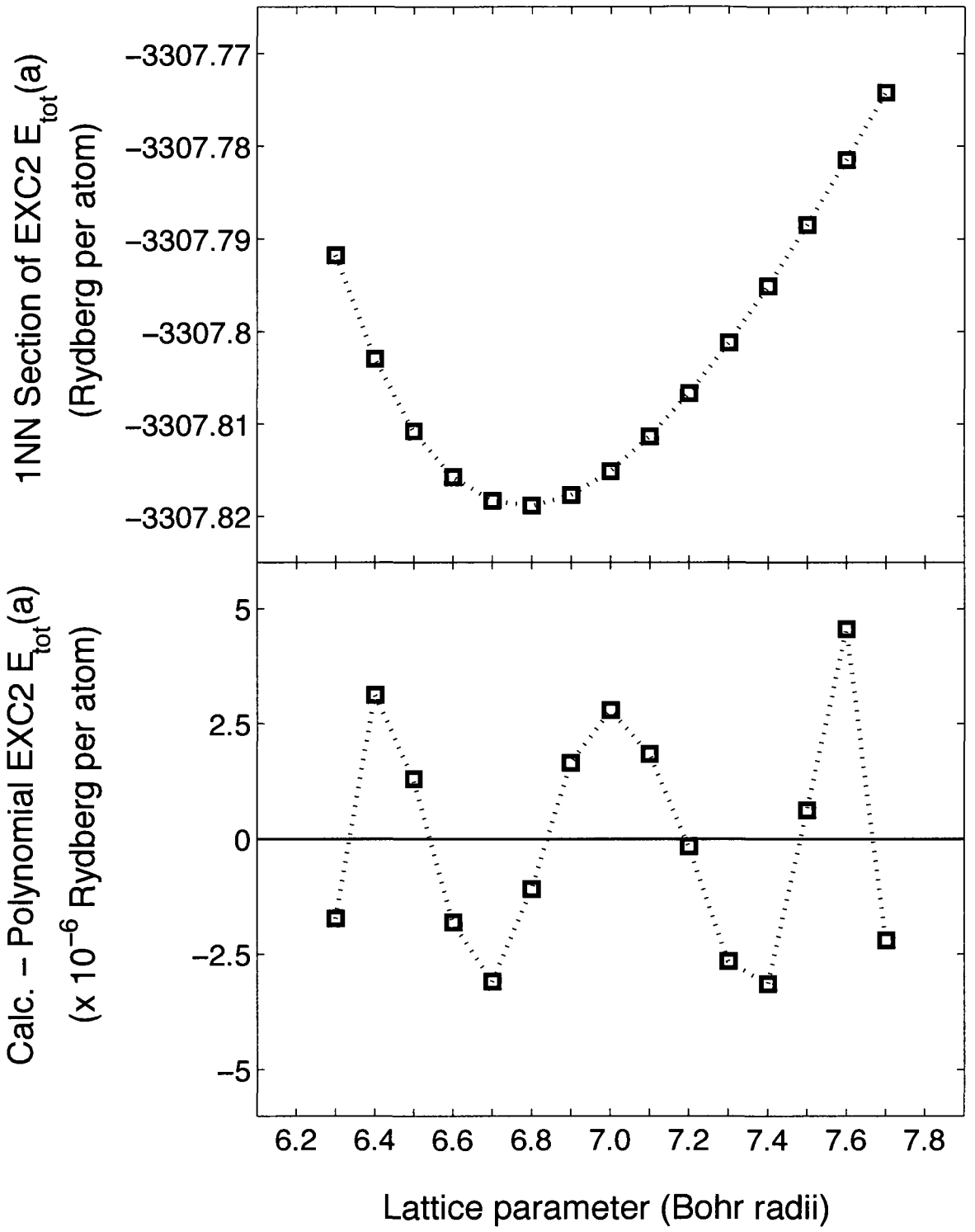

Figure B.3: 1NN section of the EXC2 $E_{tot}(a)$ curve of FCC Cu. Squares in the upper figure represent calculated values $E^{*}_{tot}(a)$ of the 1NN section of the EXC2 $E_{tot}(a)$ curve obtained using the TB-LMTO ESC program. The dotted line in the upper figure represents the optimal polynomial model of this section of the curve. The lower figure shows the function $\Delta E(a) = E^{*}_{tot}(a) - E_{tot}(a)$ in the 1NN section.

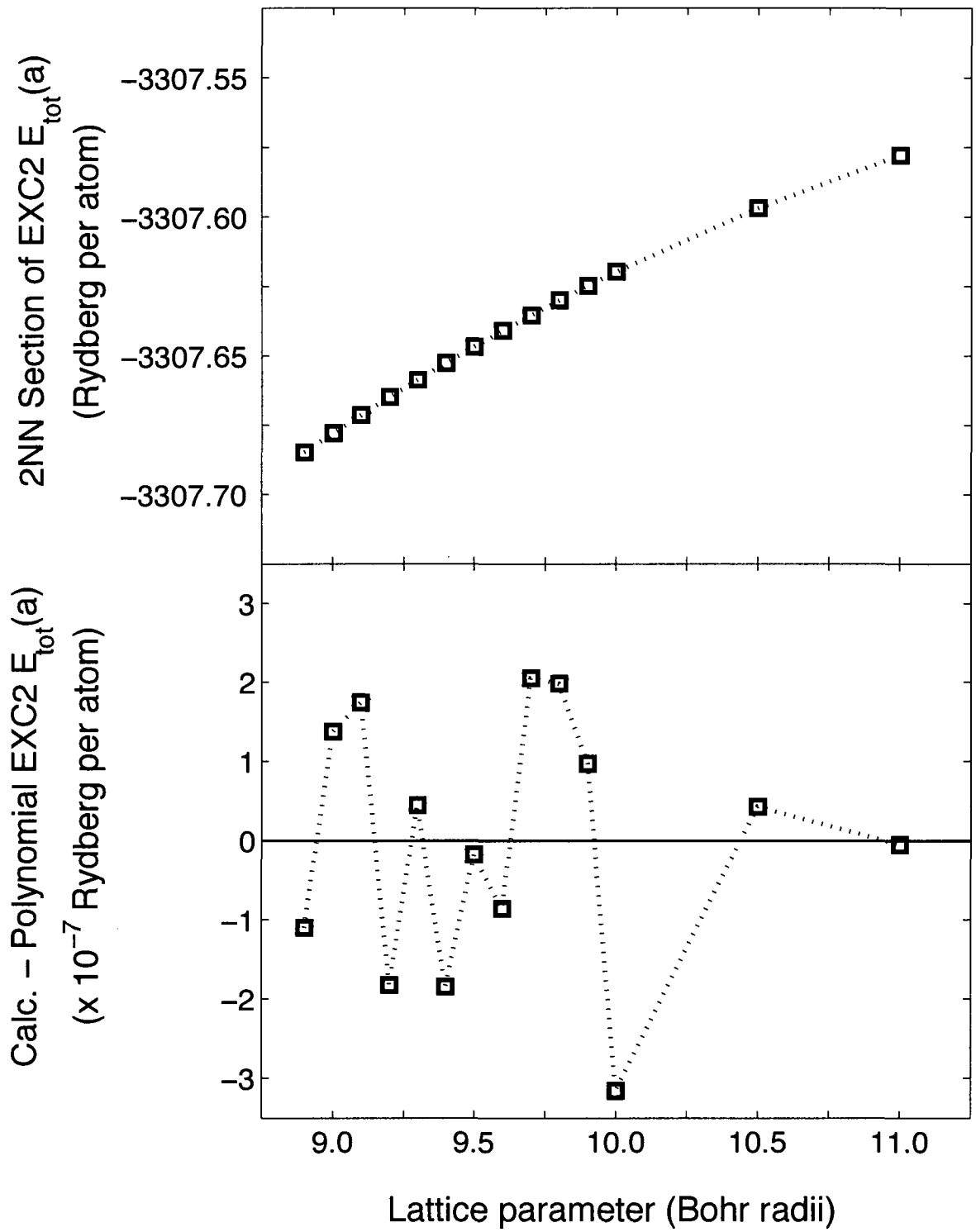

Figure B.4: 2NN section of the EXC2 $E_{tot}(a)$ curve of FCC Cu. Squares in the upper figure represent calculated values $E^{*}_{tot}(a)$ of the 2NN section of the EXC2 $E_{tot}(a)$ curve obtained using the TB-LMTO ESC program. The dotted line in the upper figure represents the optimal polynomial model of this section of the curve. The lower figure shows the function $\Delta E(a) = E^{*}_{tot}(a) - E_{tot}(a)$ in the 2NN section.

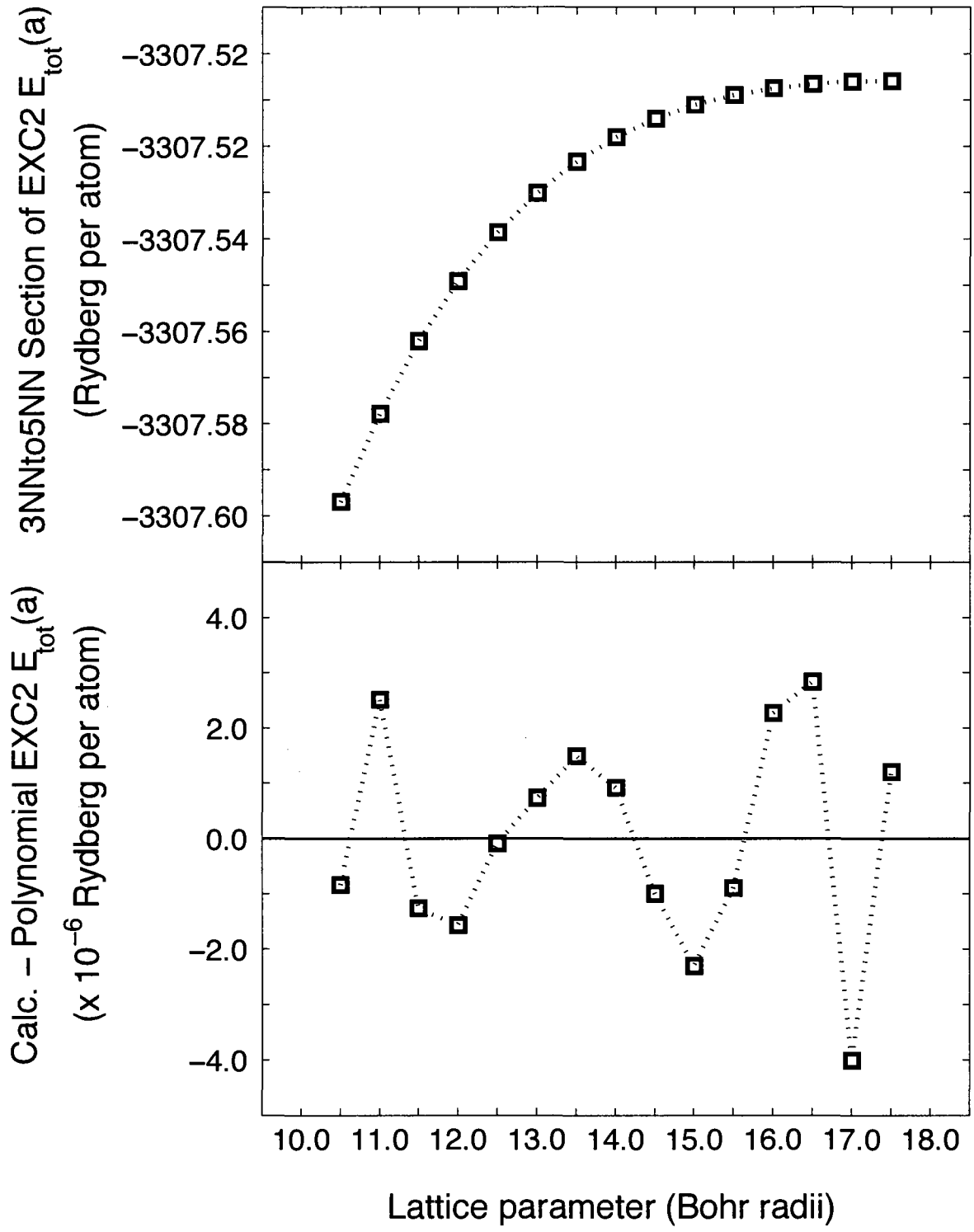

Figure B.5: 3NNto5NN section of the EXC2 $E_{tot}\,(a)$ curve of FCC Cu. Squares in the upper figure represent calculated values $E^{*}_{tot}\,(a)$ of the 3NNto5NN section of the EXC2 $E_{tot}\,(a)$ curve obtained using the TB-LMTO ESC program. The dotted line in the upper figure represents the optimal polynomial model of this section of the curve. The lower figure shows the function $\Delta E(a) = E^{*}_{tot}\,(a) - E_{tot}\,(a)$ in the 3NNto5NN section.

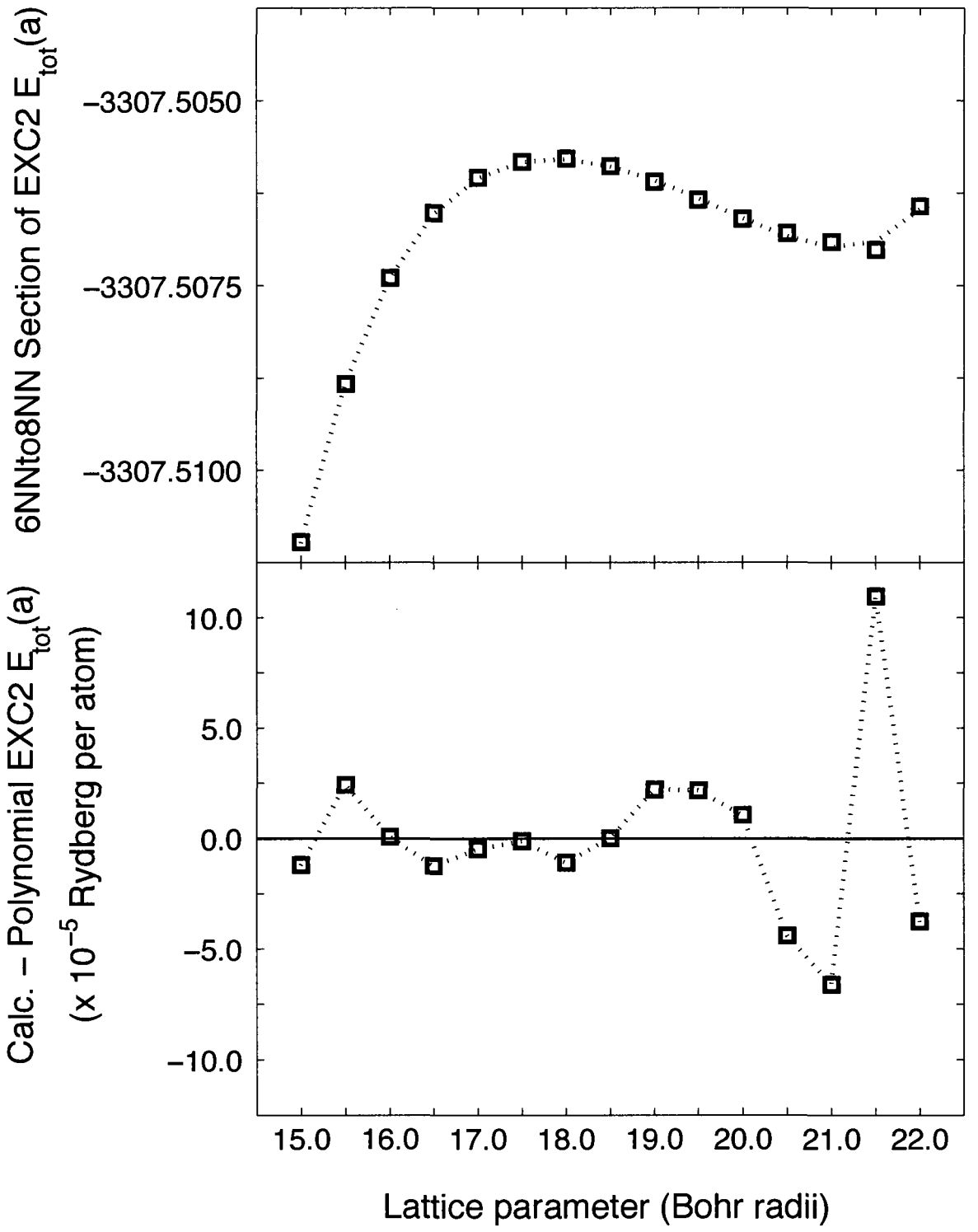

Figure B.6: 6NNto8NN section of the EXC2 $E_{tot}\,(a)$ curve of FCC Cu. Squares in the upper figure represent calculated values $E^{*}_{tot}\,(a)$ of the 6NNto8NN section of the EXC2 $E_{tot}\,(a)$ curve obtained using the TB-LMTO ESC program. The dotted line in the upper figure represents the optimal polynomial model of this section of the curve. The lower figure shows the function $\Delta E(a) = E^{*}_{tot}\,(a) - E_{tot}\,(a)$ in the 6NNto8NN section.

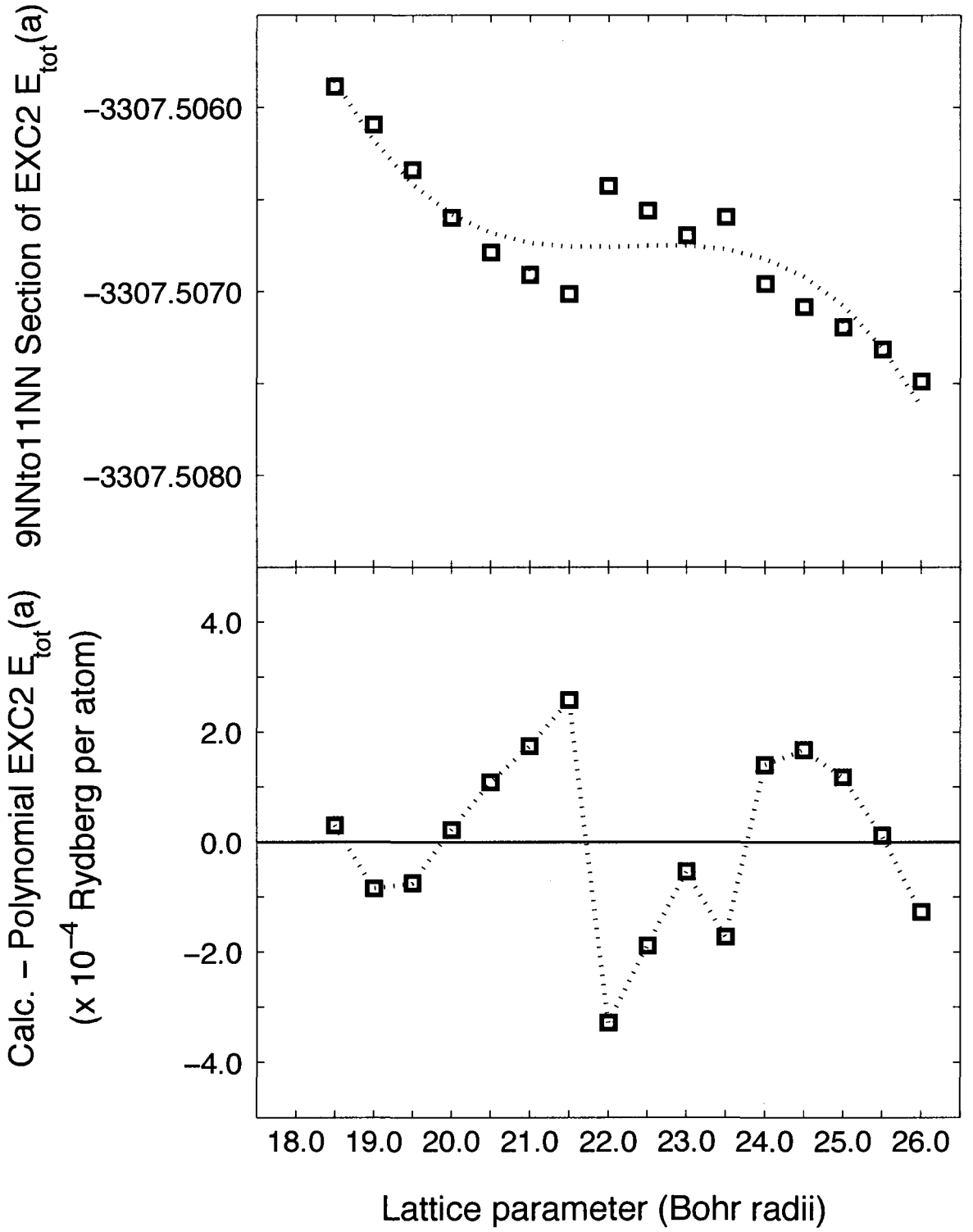

Figure B.7: 9NNto11NN section of the EXC2 $E_{tot}(a)$ curve of FCC Cu. Squares in the upper figure represent calculated values $E^{*}_{tot}(a)$ of the 9NNto11NN section of the EXC2 $E_{tot}(a)$ curve obtained using the TB-LMTO ESC program. The dotted line in the upper figure represents the optimal polynomial model of this section of the curve. The lower figure shows the function $\Delta E(a) = E^{*}_{tot}(a) - E_{tot}(a)$ in the 9NNto11NN range.

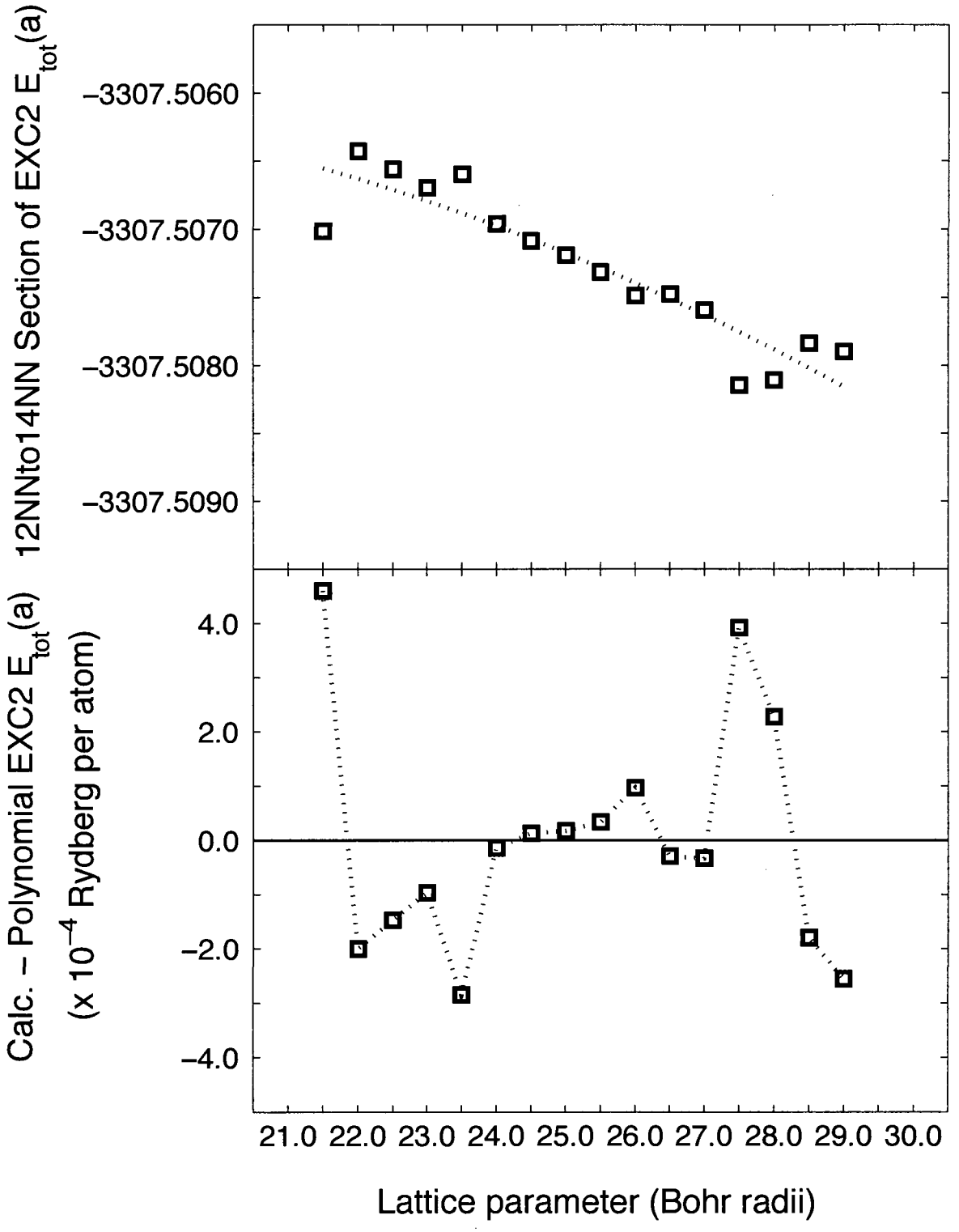

Figure B.8: 12NNto14NN section of the EXC2 $E_{tot}\,(a)$ curve of FCC Cu. Squares in the upper figure represent calculated values $E^{*}_{tot}\,(a)$ of the 12NNto14NN section of the EXC2 $E_{tot}\,(a)$ curve obtained using the TB-LMTO ESC program. The dotted line in the upper figure represents the optimal polynomial model of this section of the curve. The lower figure shows the function $\Delta E(a) = E^{*}_{tot}\,(a) - E_{tot}\,(a)$ in the 12NNto14NN section.

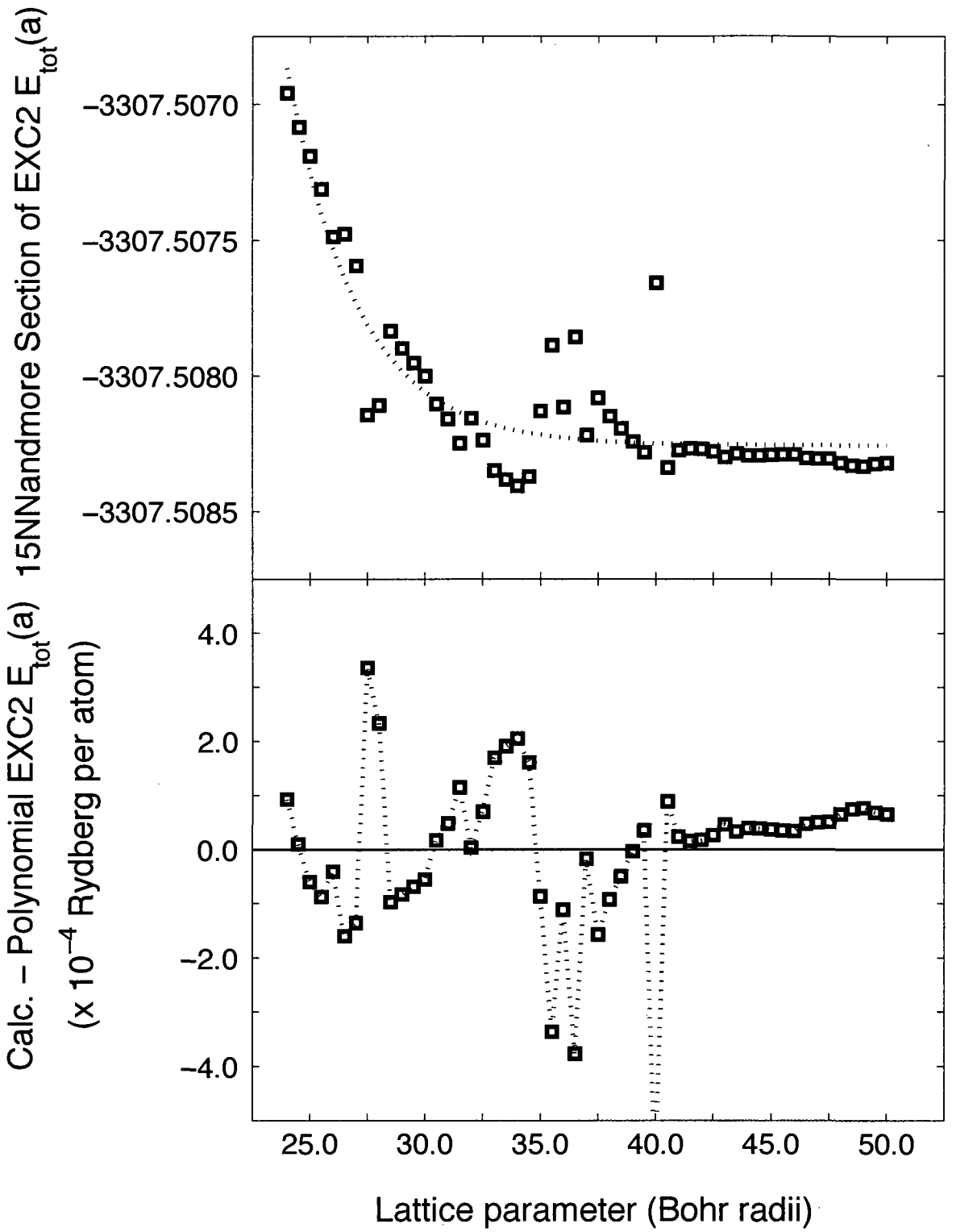

Figure B.9: 15NNandmore section of the EXC2 $E_{tot}\,(a)$ curve of FCC Cu. Squares in the upper figure represent calculated values $E^{*}_{tot}\,(a)$ of the 15NNandmore section of the EXC2 $E_{tot}\,(a)$ curve obtained using the TB-LMTO ESC program. The dotted line in the upper figure represents the optimal decaying exponential model of this section of the curve. The lower figure shows the function $\Delta E(a) = E^{*}_{tot}\,(a) - E_{tot}\,(a)$ in the 15NNandmore section.

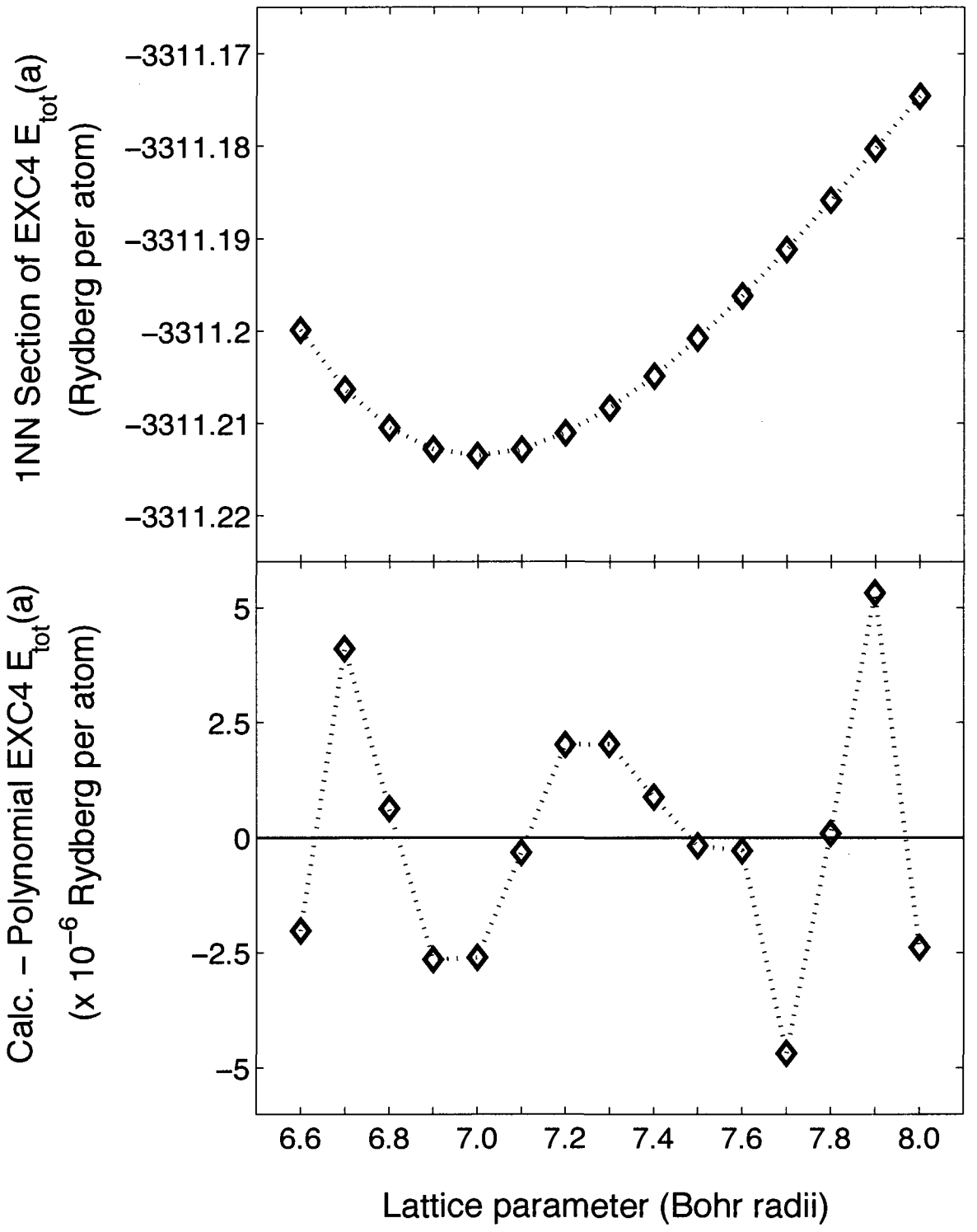

Figure B.10: 1NN section of the EXC4 $E_{tot}(a)$ curve of FCC Cu. Diamonds in the upper figure represent calculated values $E^{*}_{tot}(a)$ of the 1NN section of the EXC4 $E_{tot}(a)$ curve obtained using the TB-LMTO ESC program. The dotted line in the upper figure represents the optimal polynomial model of this section of the curve. The lower figure shows the function $\Delta E(a) = E^{*}_{tot}(a) - E_{tot}(a)$ in the 1NN section.

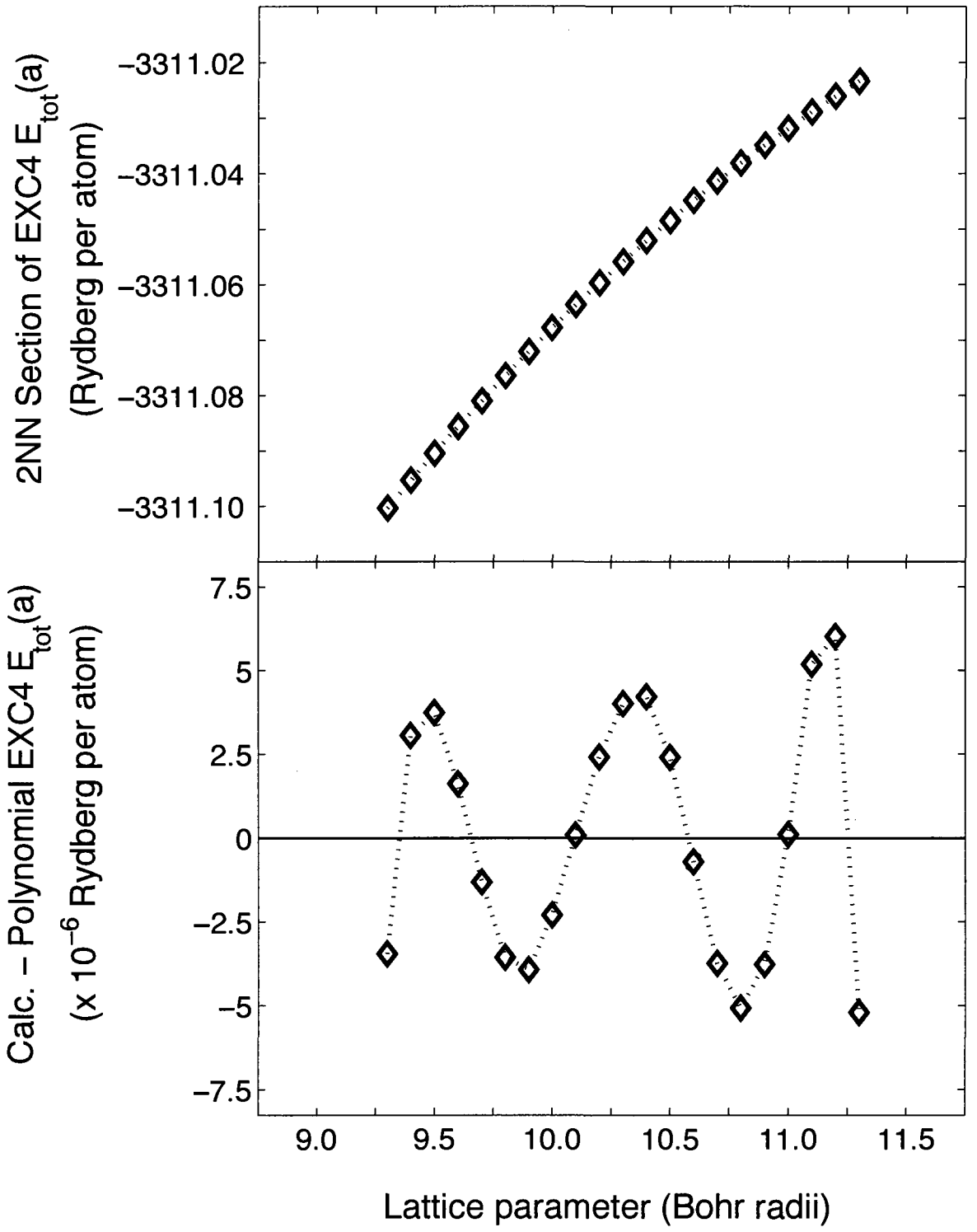

Figure B.11: 2NN section of the EXC4 $E_{tot}\,(a)$ curve of FCC Cu. Diamonds in the upper figure represent calculated values $E^{*}_{tot}\,(a)$ of the 2NN section of the EXC4 $E_{tot}\,(a)$ curve obtained using the TB-LMTO ESC program. The dotted line in the upper figure represents the optimal polynomial model of this section of the curve. The lower figure shows the function $\Delta E(a) = E^{*}_{tot}\,(a) - E_{tot}\,(a)$ in the 2NN section.

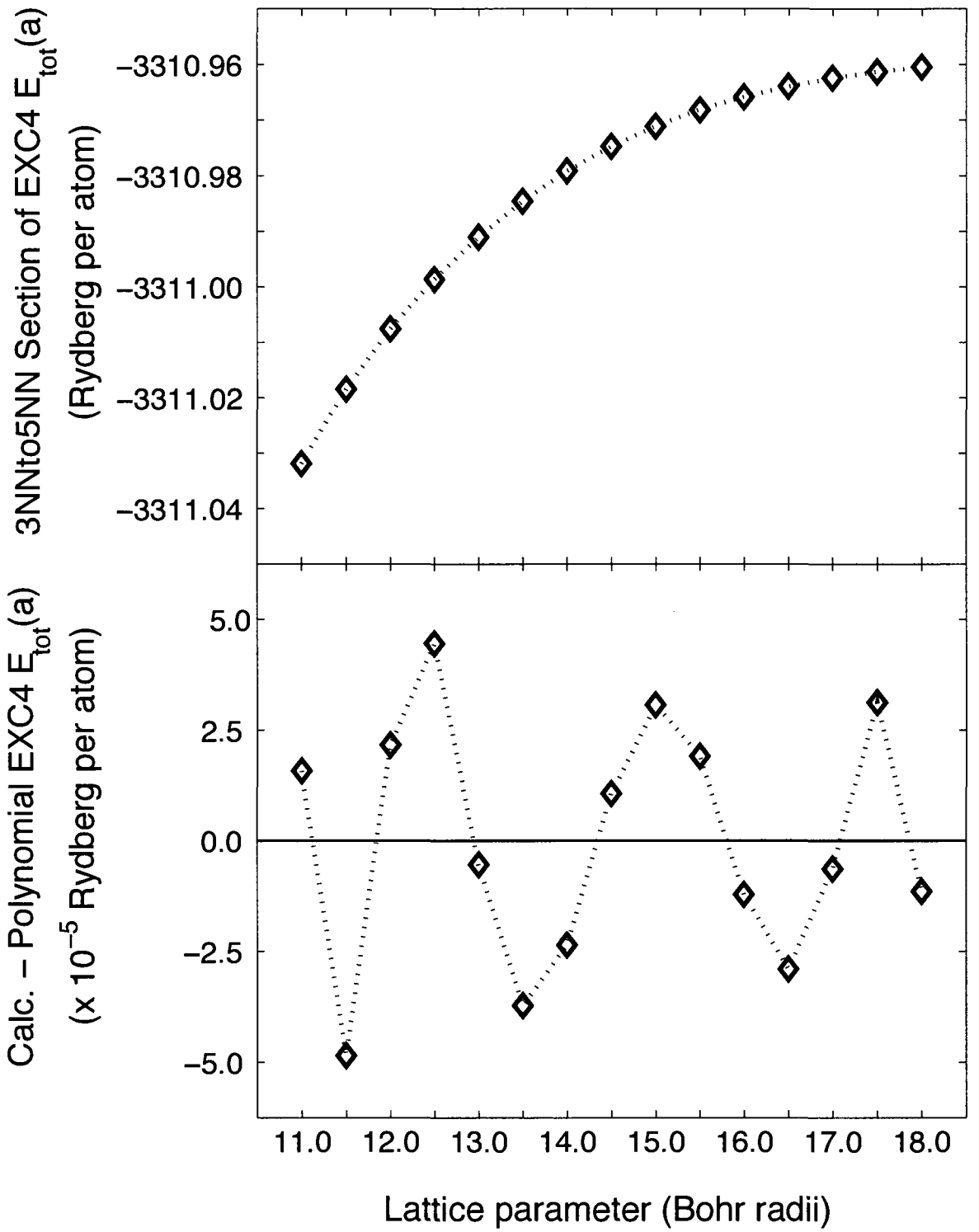

Figure B.12: 3NNto5NN section of the EXC4 $E_{tot}\,(a)$ curve of FCC Cu. Diamonds in the upper figure represent calculated values $E^{*}_{tot}\,(a)$ of the 3NNto5NN section of the EXC4 $E_{tot}\,(a)$ curve obtained using the TB-LMTO ESC program. The dotted line in the upper figure represents the optimal polynomial model of this section of the curve. The lower figure shows the function $\Delta E(a) = E^{*}_{tot}\,(a) - E_{tot}\,(a)$ in the 3NNto5NN section.

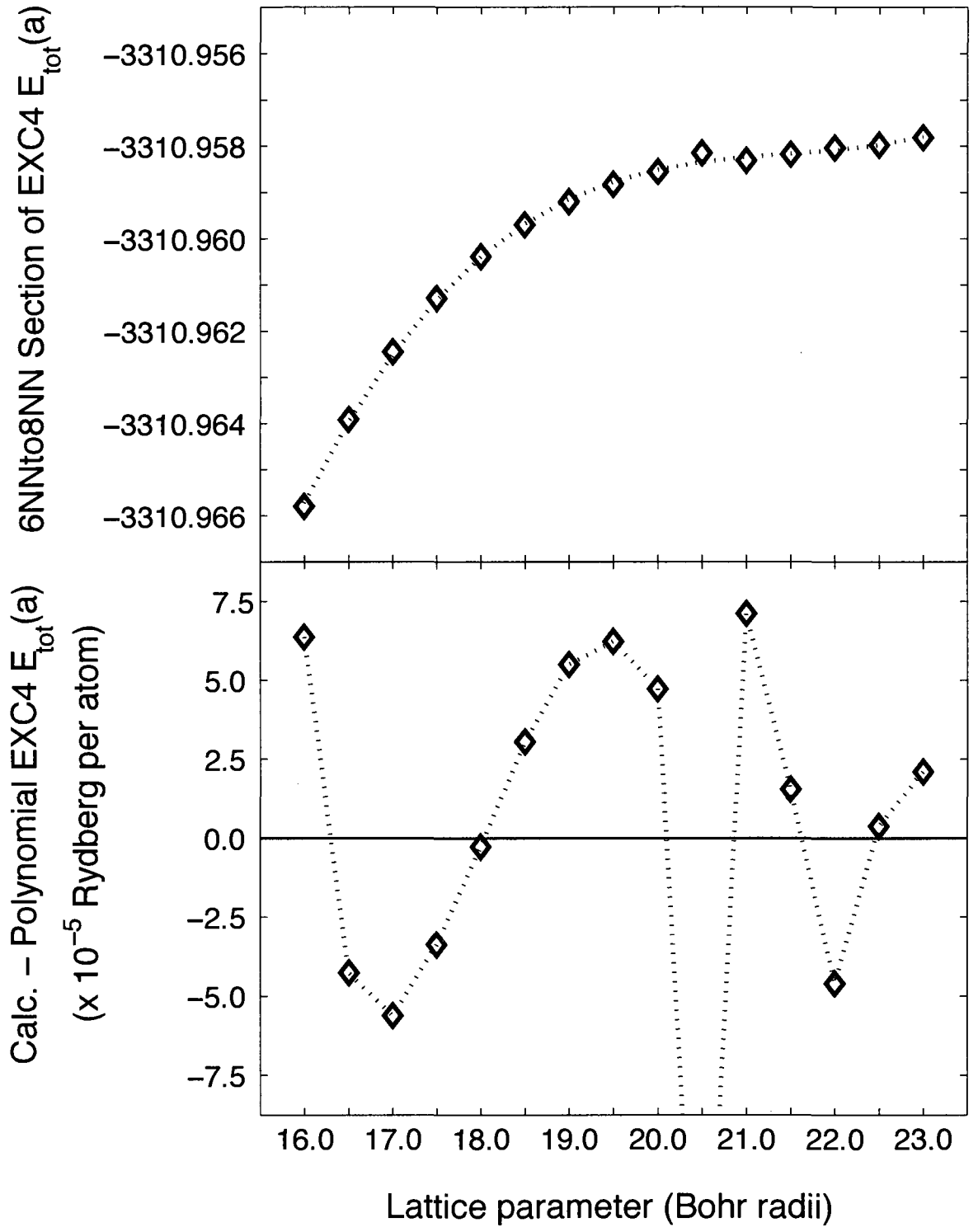

Figure B.13: 6NNto8NN section of the EXC4 $E_{tot}(a)$ curve of FCC Cu. Diamonds in the upper figure represent calculated values $E^{*}_{tot}(a)$ of the 6NNto8NN section of the EXC4 $E_{tot}(a)$ curve obtained using the TB-LMTO ESC program. The dotted line in the upper figure represents the optimal polynomial model of this section of the curve. The lower figure shows the function $\Delta E(a) = E^{*}_{tot}(a) - E_{tot}(a)$ in the 6NNto8NN section.

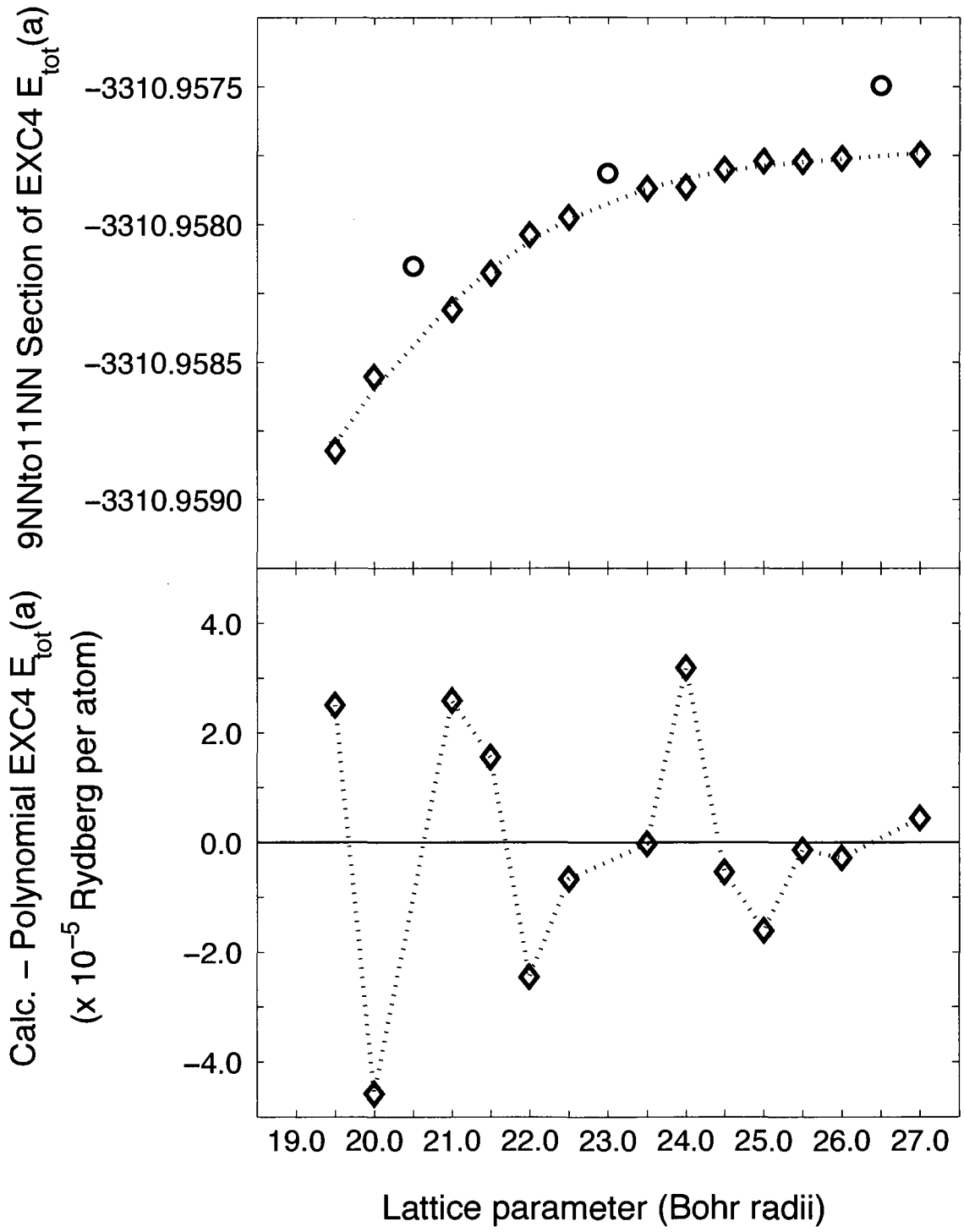

Figure B.14: 9NNto11NN section of the EXC4 $E_{tot}(a)$ curve of FCC Cu. Diamonds in the upper figure represent calculated values $E^{*}_{tot}(a)$ of the 9NNto11NN section of the EXC4 $E_{tot}(a)$ curve obtained using the TB-LMTO ESC program. Circles indicate calculated values that were omitted from the parametrization process. The dotted line in the upper figure represents the optimal polynomial model of this section of the curve. The lower figure shows the function $\Delta E(a) = E^{*}_{tot}(a) - E_{tot}(a)$ in the 9NNto11NN section.

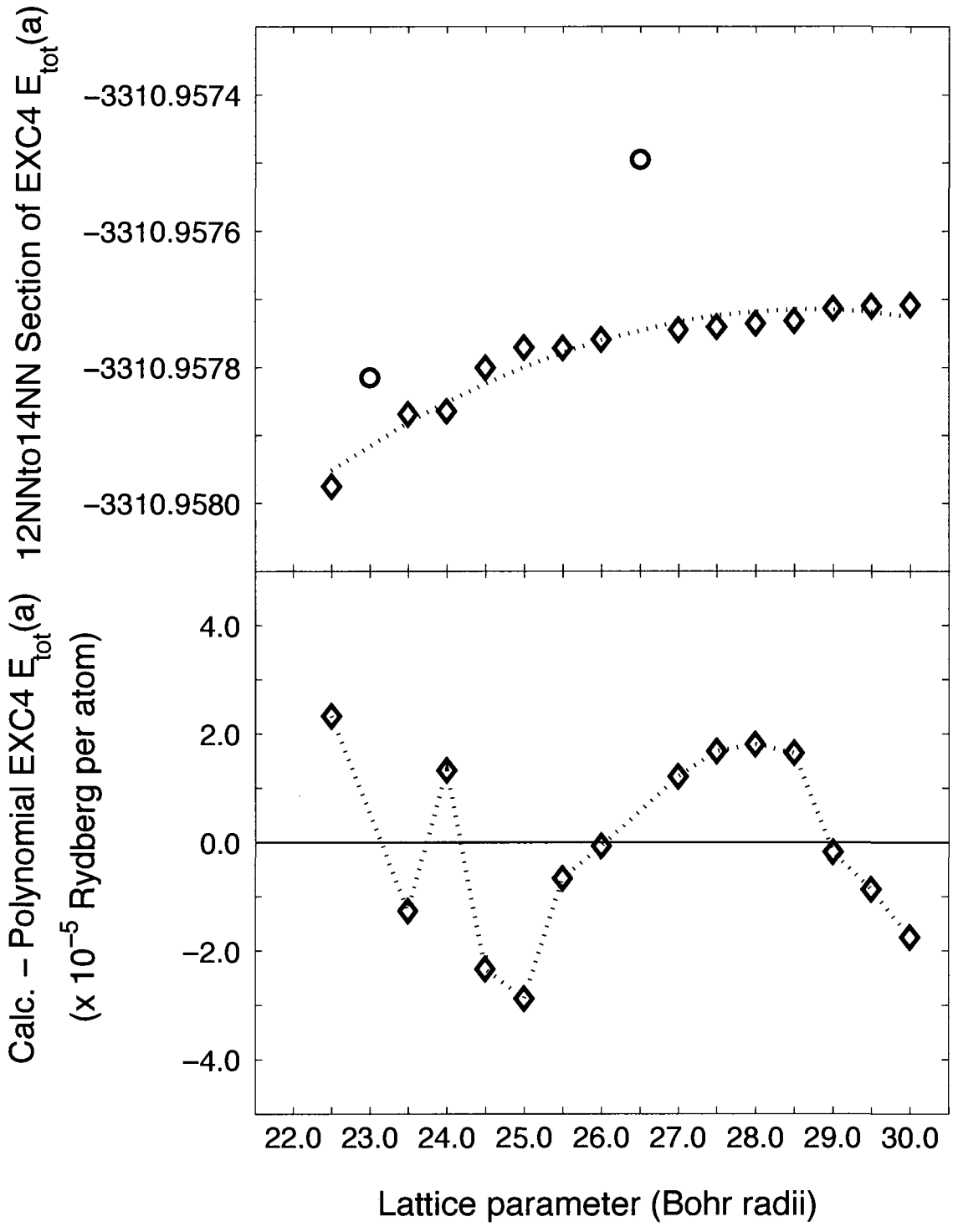

Figure B.15: 12NNto14NN section of the EXC4 $E_{tot}\,(a)$ curve of FCC Cu. Diamonds in the upper figure represent calculated values $E^{*}_{tot}\,(a)$ of the 12NNto14NN section of the EXC4 $E_{tot}\,(a)$ curve obtained using the TB-LMTO ESC program. Circles indicate calculated values that were omitted from the parametrization process. The dotted line in the upper figure represents the optimal polynomial model of this section of the curve. The lower figure shows the function $\Delta E(a) = E^{*}_{tot}\,(a) - E_{tot}\,(a)$ in the 12NNto14NN section.

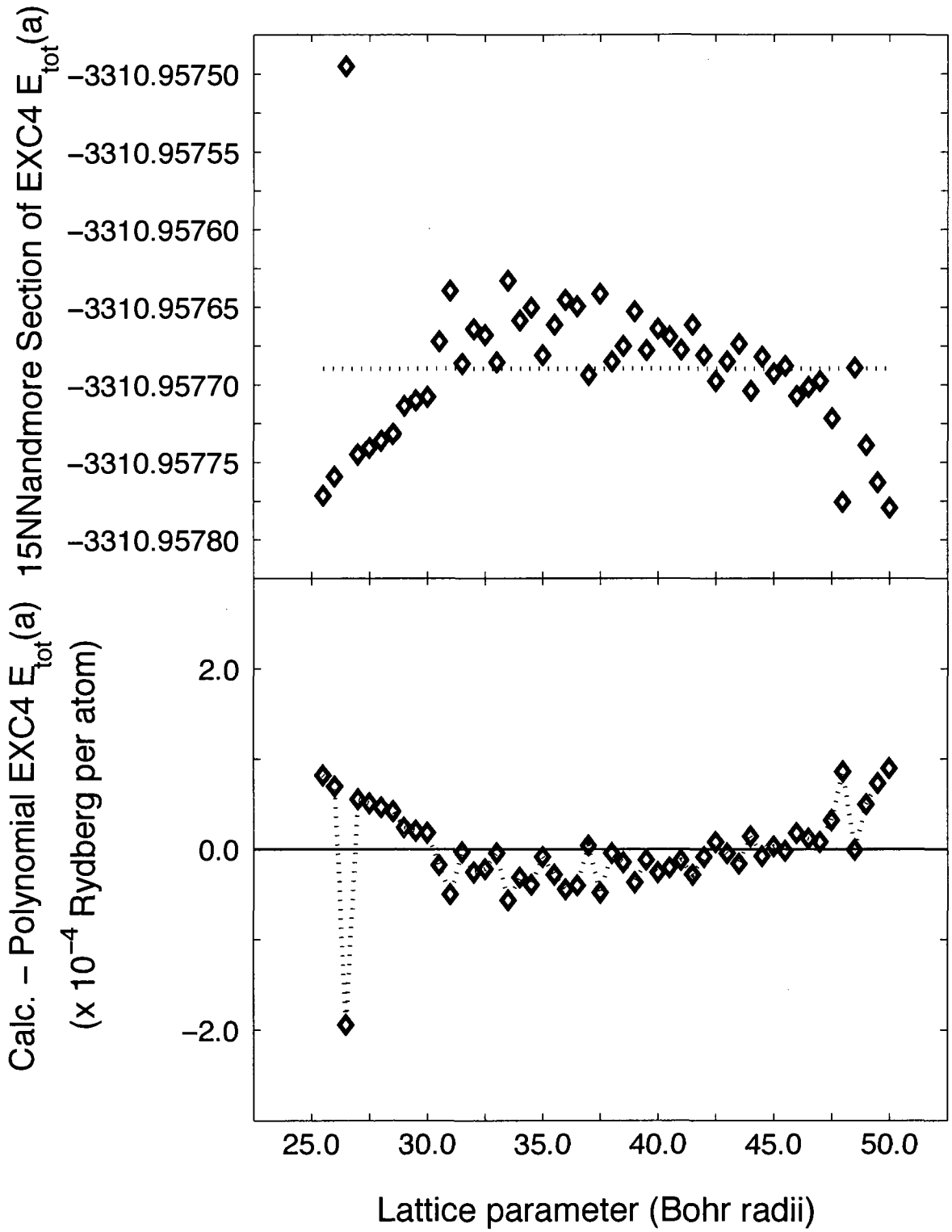

Figure B.16: 15NNandmore section of the EXC4 $E_{tot}\,(a)$ curve of FCC Cu. Diamonds in the upper figure represent calculated values $E^{*}_{tot}\,(a)$ of the 15NNandmore section of the EXC4 $E_{tot}\,(a)$ curve obtained using the TB-LMTO ESC program. The dotted line in the upper figure represents the optimal decaying exponential model of this section of the curve. The lower figure shows the function $\Delta E(a) = E^{*}_{tot}\,(a) - E_{tot}\,(a)$ in the 15NNandmore section.

B.2 Evaluation of the Numerical Precision of the Derivatives of the EXC2 and EXC4 E_{tot} (a) Curves

In order to calculate the $a\,(T)$ curve of metallic Cu using the theoretical method presented in chapter 6, knowledge of the first- and second-derivatives of the $E_{tot}\,(a)$ curve of FCC Cu is required. Now that the EXC2 and EXC4 $E_{tot}\,(a)$ curves have been parametrized, the evaluation of their first- and second-derivatives is a simple matter. However, the numerical precision of these derivatives must be evaluated.

B.2.1 Evaluation of the Numerical Precision of the Derivatives of the 1NN Section of the E_{tot} (a) Curve

To illustrate the evaluation of the numerical precision of the first- and second-derivatives of the calculated $E_{tot}\,(a)$ curves of FCC Cu, we here describe in detail the evaluation of the numerical precision of the derivatives of the 1NN section of the EXC2 $E_{tot}\,(a)$ curve. We do so using two approaches, one in which we simulate the calculation of the value of the 1NN section of the EXC2 $E_{tot}\,(a)$ curve, and one in which we make use of the confidence intervals provided in tables B.4 and B.7.

First Approach

In the first approach, we simulate the process of calculating values of the 1NN section of the EXC2 $E_{tot}\,(a)$ curve. We construct a simulated calculated value of this curve at some lattice parameter a by first calculating the value of the optimal polynomial description of the 1NN section of the EXC2 $E_{tot}\,(a)$ curve at the lattice parameter a. This polynomial has coefficients as given in table B.6. We then add to this calculated value a realization of a zero-mean Gaussian random variable with standard deviation of 4.5×10^{-6} Bohr radii. A realization of such a random variable can be calculated using a random number

generator [204]. Also, the standard deviation of this random variable is the estimated numerical precision of the calculated values of the 1NN section of the EXC2 $E_{tot}(a)$ curve, as given in table B.5. Therefore, the random variable in question simulates the process that produces the CPE's in the calculated values of the 1NN section of the EXC2 $E_{tot}(a)$ curve. In figure B.2, we illustrate 15 calculated values of the 1NN section of the EXC2 $E_{tot}(a)$ curve, each obtained at one of fifteen different lattice parameters. We simulate, as previously described, the calculation of 15 new values of the 1NN section of the EXC2 $E_{tot}(a)$ curve at the same fifteen lattice parameters.

Having simulated the calculation of the 1NN section of the EXC2 $E_{tot}(a)$ curve, we then use the Levenburg-Marquardt routine to find the optimal polynomial representation of this simulated curve. In section B.1.2, we modelled the 1NN section of the EXC2 $E_{tot}(a)$ curve using a fifth-order polynomial. We model the simulated calculated curve using a polynomial of the same order.

Having obtained the optimal polynomial representation of the simulated values of the 1NN section of the EXC2 $E_{tot}(a)$ curve, we evaluate the first- and second-derivatives of this new polynomial. We specifically calculate the value of these derivatives at the same lattice parameters at which a calculated value of the EXC2 $E_{tot}(a)$ curve is shown in figure B.2. We also evaluate the first- and second-derivatives of the original polynomial representation of the EXC2 $E_{tot}(a)$ curve at the same lattice parameters. We then define the value of two functions $\Delta E^{(1)}(a)$ and $\Delta E^{(2)}(a)$ at the same lattice parameters by subtracting the derivatives of the original polynomial representation of the 1NN section of the EXC2 $E_{tot}(a)$ curve from the derivatives of the polynomial representation of the simulated values of the curve. We note the values of the $\Delta E^{(1)}(a)$ and $\Delta E^{(2)}(a)$ functions for future analysis.

We then simulate the calculation of a new set of values of the 1NN section of the $E_{tot}(a)$ curve, and repeat the process of constructing functions $\Delta E^{(1)}(a)$ and $\Delta E^{(2)}(a)$ and of noting the value of these functions. We do so multiple times, and then evaluate the average, standard deviation, and maximum absolute value of the noted values of these

functions. We use this information to estimate the numerical precision of the first- and second-derivatives of the 1NN section of the EXC2 $E_{tot}(a)$ curve. Table B.10 shows the mean, standard deviation and maximum absolute value of 150000 calculated values of the $\Delta E^{(1)}(a)$ and $\Delta E^{(2)}(a)$ functions. These values were obtained by simulating the calculation of 10000 $E_{tot}(a)$ curves and by calculating 15 values of the functions $\Delta E^{(1)}(a)$ and $\Delta E^{(2)}(a)$ per simulated curve.

Table B.10: Mean, standard deviation, and maximum absolute value of the functions $\Delta E^{(1)}(a)$ and $\Delta E^{(2)}(a)$ obtained using approach 1

Function	Mean value	Standard deviation	Maximum absolute value
$\Delta E^{(1)}(a)$	1.5×10^{-7}	2.9×10^{-5}	3.0×10^{-4}
$\Delta E^{(2)}(a)$	-6.2×10^{-7}	2.9×10^{-4}	3.1×10^{-3}

Units of function $\Delta E^{(n)}(a)$: Rydberg per atom $\times$ (Bohr radii)$^{-n}$

Second Approach

In the second approach, we make use of the confidence intervals provided in tables B.4 and B.7. To evaluate the numerical precision of the first- and second-derivatives of the 1NN section of the EXC2 $E_{tot}(a)$ curve, we begin by choosing one of the coefficients of the optimal polynomial representation of this curve, say coefficient c_5, and add the magnitude of the confidence interval Δc_5 to its value. We then use the Levenburg-Marquardt routine to construct the best possible polynomial representation of the original calculated values of the 1NN section of the EXC2 $E_{tot}(a)$ curve, subject to the constraint that the value of c_5 is as just described.

Having obtained the optimal polynomial representation of the original calculated values of the 1NN section of the EXC2 $E_{tot}(a)$ curve with coefficient c_5 as defined in the previous paragraph, we evaluate the first- and second-derivatives of this new polynomial. We specifically calculate the value of these derivatives at the same lattice parameters at

which a calculated value of the 1NN section of the EXC2 $E_{tot}(a)$ curve is shown in figure B.2. We also evaluate the first- and second-derivatives of the original polynomial representation of the EXC2 $E_{tot}(a)$ curve at the same lattice parameters. We then define the value of two functions $\Delta E^{(1)}(a)$ and $\Delta E^{(2)}(a)$ at the same lattice parameters by subtracting the derivatives of the original polynomial representation of the 1NN section of the EXC2 $E_{tot}(a)$ curve from the derivatives of the polynomial with c_5 as defined in the previous paragraph. We note the calculated values of the functions $\Delta E^{(1)}(a)$ and $\Delta E^{(2)}(a)$ for future analysis.

We then construct another polynomial representation of the 1NN section of the EXC2 $E_{tot}(a)$ curve, this time after subtracting (instead of adding) the confidence interval Δc_5 from the coefficient c_5. Again, we evaluate the first- and second-derivatives of this new polynomial and define functions $\Delta E^{(1)}(a)$ and $\Delta E^{(2)}(a)$ as described in the previous paragraph. We again note the calculated values of the functions $\Delta E^{(1)}(a)$ and $\Delta E^{(2)}(a)$ for future analysis.

We repeat, once for each coefficient of the original polynomial representation of the 1NN section of the $E_{tot}(a)$ curve, the process of constructing new polynomial models of this curve as described in the previous paragraphs. For each new polynomial, we note the calculated values of the functions $\Delta E^{(1)}(a)$ and $\Delta E^{(2)}(a)$. We then evaluate the average, standard deviation, and maximum absolute value of the noted values of these functions. We use this information to estimate the numerical precision of the first- and second-derivatives of the 1NN section of the EXC2 $E_{tot}(a)$ curve. Table B.11 shows the mean, the standard deviation, and the maximum absolute value of 180 calculated values of the $\Delta E^{(1)}(a)$ and $\Delta E^{(2)}(a)$ functions. These values were obtained by constructing 12 new polynomial representations of the 1NN section of the EXC2 $E_{tot}(a)$ curve and by calculating 15 values of the functions $\Delta E^{(1)}(a)$ and $\Delta E^{(2)}(a)$ per new polynomial representation.

Table B.11: Mean, standard deviation, and maximum absolute value of the functions $\Delta E^{(1)}(a)$ and $\Delta E^{(2)}(a)$ obtained using approach 2

Function	Mean value	Standard deviation	Maximum absolute value
$\Delta E'^{(1)}(a)$	-1.4×10^{-9}	2.7×10^{-5}	7.0×10^{-5}
$\Delta E'^{(2)}(a)$	-7.2×10^{-10}	3.2×10^{-4}	7.9×10^{-4}

Units of function $\Delta E^{(n)}(a)$: Rydberg per atom $\times$ (Bohr radii)$^{-n}$

Comparison of First and Second Approach

In table B.12, we compare the standard deviation and absolute maximum value of the functions $\Delta E^{(1)}(a)$ and $\Delta E^{(2)}(a)$ obtained using the first and second approach. We observe that the standard deviation of the functions obtained using the two approaches are very similar. The maximum absolute values of the functions obtained using approach 2 are slightly larger but have the same order of magnitude as the standard deviations of the functions. In contrast, the maximum absolute values of the functions obtained with approach 1 are one order of magnitude larger than those obtained using approach 2.

We therefore take the maximum absolute value of the functions $\Delta E^{(1)}(a)$ and $\Delta E^{(2)}(a)$, obtained using the second approach, to be respectively the uncertainty in the first- and second-derivatives of the 1NN section of the EXC2 $E_{tot}(a)$ curve. These values are slightly more conservative estimates of the latter uncertainties than the standard deviations of the functions $\Delta E^{(1)}(a)$ and $\Delta E^{(2)}(a)$ obtained using the first or the second approach.

Table B.12: Comparison of the standard deviation and absolute maximum value of the functions $\Delta E^{(1)}(a)$ and $\Delta E^{(2)}(a)$ obtained using approach 1 and approach 2

	Standard deviation of $\Delta E^{(n)}(a)$		Maximum absolute value of $\Delta E^{(n)}(a)$	
n	As per approach 1	As per approach 2	As per approach 1	As per approach 2
1	2.9×10^{-5}	2.7×10^{-5}	3.0×10^{-4}	7.0×10^{-5}
2	2.9×10^{-4}	3.2×10^{-4}	3.1×10^{-3}	7.9×10^{-4}

Units of function $\Delta E^{(n)}(a)$: Rydberg per atom $\times$ (Bohr radii)$^{-n}$

B.2.2 Evaluation of the Numerical Precision of the Derivatives of All Sections of the EXC2 and EXC4 $E_{tot}(a)$ Curve

The numerical precision of the first- and second-derivatives of all sections of the two calculated $E_{tot}(a)$ curves is shown respectively in tables B.13 and B.14. The numerical precision of the derivatives is as estimated using the maximum absolute value of the functions $\Delta E^{(1)}(a)$ and $\Delta E^{(2)}(a)$ obtained using approach 2.

The reader should note that the numerical precision of the $a(T)$ curve of metallic Cu, as calculated in chapter 7, is estimated using the Levenburg-Marquardt routine and a method similar to approach 2.

Table B.13: Numerical precision of the first-derivative of the EXC2 and EXC4 $E_{tot}(a)$ curves

Curve section	Precision of EXC2 $E_{tot}^{(1)}(a)$ curve	Precision of EXC4 $E_{tot}^{(1)}(a)$ curve
1NN section	$\pm 7.0 \times 10^{-5}$	$\pm 6.4 \times 10^{-5}$
2NN section	$\pm 4.7 \times 10^{-6}$	$\pm 5.5 \times 10^{-5}$
3NNto5NN section	$\pm 1.3 \times 10^{-5}$	$\pm 1.9 \times 10^{-4}$
6NNto8NN section	$\pm 1.4 \times 10^{-4}$	$\pm 9.9 \times 10^{-5}$
9NNto11NN section	$\pm 2.7 \times 10^{-4}$	$\pm 2.7 \times 10^{-5}$
12NNto14NN section	$\pm 1.2 \times 10^{-4}$	$\pm 1.4 \times 10^{-5}$
15NNandmore section	$\pm 3.9 \times 10^{-5}$	± 0.0

All uncertainties have units: Rydberg per atom $\times$ (Bohr radii)$^{-1}$

Table B.14: Numerical precision of the second-derivative of the EXC2 and EXC4 $E_{tot}(a)$ curves

Curve section	Precision of EXC2 $E_{tot}^{(2)}(a)$ curve	Precision of EXC4 $E_{tot}^{(2)}(a)$ curve
1NN section	$\pm 7.9 \times 10^{-4}$	$\pm 7.2 \times 10^{-4}$
2NN section	$\pm 3.4 \times 10^{-5}$	$\pm 4.1 \times 10^{-4}$
3NNto5NN section	$\pm 4.4 \times 10^{-5}$	$\pm 6.3 \times 10^{-4}$
6NNto8NN section	$\pm 3.2 \times 10^{-4}$	$\pm 7.1 \times 10^{-5}$
9NNto11NN section	$\pm 1.8 \times 10^{-4}$	$\pm 1.8 \times 10^{-5}$
12NNto14NN section	$\pm 3.2 \times 10^{-5}$	$\pm 3.5 \times 10^{-6}$
15NNandmore section	$\pm 3.7 \times 10^{-5}$	± 0.0

All uncertainties have units: Rydberg per atom $\times$ (Bohr radii)$^{-2}$

Bibliography

[1] P. Eckerlin and H. Kandler. Table of the structures of the elements. In K.-H. Hellwege and J. L. Olsen, editors, *Structure Data of Elements and Intermetallic Phases*, volume 6 of *Landolt-Börnstein New Series, Group III*. Springer, 1971.

[2] K. Adachi, D. Bonnenberg, J. J. M. Franse, R. Gersdorf, Hempel K. A., K. Kanematsu, S. Misawa, M. Shiga, Stearns M. B., and H. P. J. Wijn. 3d, 4d and 5d Elements, Alloys and Compounds. In H. P. J. Wijn, editor, *Magnetic Properties of Metals*, volume 19a of *Landolt-Börnstein New Series, Group III*. Springer, 1986.

[3] C. E. Guillaume. Sur la dilatation des aciers au nickel. *Comptes Rendus de l'Académie des Sciences*, 124:176, 1897.

[4] C. H. Desch. Metals In The Use of Man. Broadcast lectures, British Broadcasting Corporation, March 1928.

[5] W. D. Jr. Callister. *Materials Science and Engineering - An Introduction*. John Wiley and Sons, Inc., third edition, 1994.

[6] C. C. Plummer, D. McGeary, and D. H. Carlson. *Physical Geology*. McGraw-Hill, 9th edition, 2003.

[7] D. J. Frost, C. Liebske, F. Langenhorst, C. A. McCammon, Trønnes R. G., and D. C. Rubie. Experimental evidence for the existence of iron-rich metal in the Earth's lower mantle. *Nature*, 428:409, 2004.

[8] R. Hutchinson, editor. *Meteorites: A Petrologic, Chemical and Isotopic Synthesis*. Cambridge University Press, 2004.

[9] K. Lagarec, D. G. Rancourt, S. K. Bose, B. Sanyal, and R. A. Dunlap. Observation of a composition-controlled high-moment / low-moment transiton in the face centered cubic Fe-Ni system: Invar effect is an expansion, not a contraction. *Journal of Magnetism and Magnetic Materials*, 236:107–130, 2001.

[10] K. Lagarec, D. G. Rancourt, S. K. Bose, and R. A. Dunlap. First observation of a composition-controlled low-moment / high-moment transition in the FCC Fe-Ni system: implications regarding Invar and anti-Invar behaviors. *Phase Transitions*, 75:211–219, 2002.

[11] H. Hasegawa and D. G. Pettifor. Microscopic theory of the temperature-pressure phase diagram of iron. *Physical Review Letters*, 50:130, 1983.

[12] D. Alfe, G. D. Price, and M. J. Gillan. Iron under Earth's core conditions: liquid-state thermodynamics and high-pressure melting curve from ab initio calculations. *Physical Review B*, 65:art. 165118, 2002.

[13] O. L. Anderson. Mineral physics of iron and of the core. *Reviews of Geophysics*, 33:429–441, 1995.

[14] A. B. Belonoshko, R. Ahuja, and B. Johansson. Stability of the body-centred-cubic phase of iron in the Earth's inner core. *Nature*, 424:1032–1034, 2003.

[15] A. B. Belonoshko, E. I. Isaev, N. V. Skorodumova, and B. Johansson. Stability of the body-centered-tetragonal phase of Fe at high pressure: Ground-state energies, phonon spectra, and molecular dynamics simulations. *Physical Review B*, 74:art. 214102, 2006.

[16] A. B. Belonoshko, N. V. Skorodumova, S. Davis, A. N. Osiptsov, A. Rosengren, and B. Johansson. Origin of the low rigidity of the Earth's inner core. *Science*, 316:1603–1605, 2007.

[17] A. B. Belonoshko, P. I. Dorogokupets, B. Johansson, S. K. Saxena, and L. Koči. ab initio equation of state for the body-centered-cubic phase of iron at high pressure and temperature. *Physical Review B*, 78:art. 104107, 2008.

[18] A. B. Belonoshko, N. V. Skorodumova, A. Rosengren, and B. Johansson. Elastic anisotropy of Earth's inner core. *Science*, 319:797–800, 2008.

[19] A. I. Funtikov. Phase diagram of iron: implications for the state of the Earth's core. *Izvestiya - Physics of the Solid Earth*, 36:958–964, 2000.

[20] A. Lioa, S. Bernard, G. L. Chiarotti, S. Scandolo, and E. Tosatti. Physics of iron at Earth's core conditions. *Science*, 287:1027–1030, 2000.

[21] J. F. Lin, D. L. Heinz, A. J. Campbell, J. M. Devine, W. L. Mao, and G. Y. Shen. Iron-nickel alloy in the Earth's core. *Geophysical Research Letters*, 29:art. 1471, 2002.

[22] M. Ross, D. A. Young, and R. Grover. Theory of the iron phase-diagram at Earth's core conditions. *Journal of Geophysical Research - Solid Earth and Planets*, 95(B13):21713–21716, 1990.

[23] P. Soderlind, J. A. Moriarty, and J. M. Willis. First-principles theory of iron up to Earth's core pressures: structural, vibrational and elastic properties. *Physical Review B*, 53:14063–14072, 1996.

[24] G. Steinle-Neumann, L. Stixrude, R. E. Cohen, and O. Gulseren. Elasticity of iron at high temperature and pressure. *Nature*, 413:57, 2001.

[25] L. Stixrude, R. E. Cohen, and D. J. Singh. Iron at high-pressure - linearized-augmented-plane-wave computations in the generalized gradient approximation. *Physical Review B*, 50:6442–6445, 1994.

[26] L. Vocadlo, J. Brodholt, D. Alfe, M. J. Gillan, and G. D. Price. Ab initio free energy calculations on the polymorphs of iron at core conditions. *Physics of the Earth and Planetary Interiors*, 117:123–137, 2000.

[27] L. Vocadlo, J. Brodholt, D. Alfe, G. D. Price, and M. J. Gillan. The structure of iron under the conditions of the Earth's inner core. *Geophysical Research Letters*, 26:1231–1234, 1999.

[28] G. Krier, M. van Schilfgaarde, A. T. Paxton, O. Jepsen, and O. K. Andersen. The TB-LMTO program, version 4.7. On-line at www.fkf.mpg.de/andersen/, 1994.

[29] O. K. Andersen. Linear methods in band theory. *Physical Review B*, 12:3060, 1975.

[30] O. K. Andersen and O. Jepsen. Explicit, first-principles tight-binding theory. *Physical Review Letters*, 53:2571, 1984.

[31] O. K. Andersen, Z. Pawlowska, and O. Jepsen. Illustration of the linear-muffin-tin-orbital tight-binding representation: Compact orbitals and charge density in Si. *Physical Review B*, 34:5253, 1986.

[32] H. L. Skriver. *The LMTO Method - Muffin-Tin Orbitals and Electronic Structure*, volume 41 of *Springer Series in Solid-State Sciences*. Springer-Verlag, 1983.

[33] P. Hohenberg and W. Kohn. Inhomogeneous electron gas. *Physical Review*, 136:B864, 1964.

[34] W. Kohn and L. J. Sham. Self-consistent equations including exchange and correlation effects. *Physical Review*, 140:A1133, 1965.

[35] O. Jepsen, G. Krier, A. Burkhardt, and O. K. Andersen. *The TB-LMTO-ASA program*. Max Planck Institut for Solid State Research, Heisenbergstr. 1, D-70569 Stuttgart, Federal Republic of Germany, 45 edition, September 2004.

[36] M. Born and J. R. Oppenheimer. Zur quantentheorie der moleküle. *Annalen der Physik*, 84, 1927.

[37] N. W. Ashcroft and N. D. Mermin. *Solid State Physics*. Harcourt, Inc., 1976.

[38] D. R. Hartree. The calculation of atomic structures. *Reports on Progress in Physics*, 11:113, 1947.

[39] J. C. Slater. A simplification of the Hartree-Fock method. *Physical Review*, 81(3):385, 1951.

[40] R. A. Serway, C. J. Moses, and C. A. Moyer. *Modern Physics*. Hartcourt Brace, 2nd edition, 1997.

[41] J. Chen, R. O. Esquivel, and M. J. Stott. Exchange-correlation potential for small atoms. *Philosophical Magazine B*, 69(5):1001–1009, 1994.

[42] L. Hedin and B. I. Lundqvist. Explicit local exchange-correlation potentials. *Journal of Physics C: Solid State Physics*, 4:2064, 1971.

[43] U. von Barth and L. Hedin. A local exchange-correlation potential for the spin polarized case: I. *Journal of Physics C: Solid State Physics*, 5:1629, 1972.

[44] D. Ceperley. Ground state of the fermion one-component plasma: a monte carlo study in two and three dimensions. *Physical Review B*, 18(7):3126, 1978.

[45] D. M. Ceperley and B. J. Alder. Ground state of the electron gas by stochastic method. *Physical Review Letters*, 45(7):566, 1980.

[46] S. H. Vosko, L. Wilk, and M. Nusair. Accurate spin-dependent electron liquid correlation energies for local spin density calculations: a critical analysis. *Canadian Journal of Physics*, 58:1200, 1980.

[47] D. C. Langreth and M. J. Mehl. Beyond the local-density approximation in calculations of ground-state electronic properties. *Physical Review B*, 28(4):1809, 1983.

[48] C. D. Hu and D. C. Langreth. A spin dependent version of the Langreth-Mehl exchange-correlation functional. *Physica Scripta*, 32:391–396, 1985.

[49] J. P. Perdew and W.. Yue. Accurate and simple density functional for the electronic exchange energy: generalized gradient approximation. *Physical Review B*, 33(12):8800, 1986.

[50] L. Vitos, B. Johansson, J. Kollár, and H. L. Skriver. Exchange energy in the local Airy gas approximation. *Physical Review B*, 62:10046, 2000.

[51] S. K. Bose, May 2009. Personal communication.

[52] S. K. Bose, May 2009. Personal communication.

[53] Y. Xie. Electronic-structure and properties of pure iron. *Acta Metallurgica Et Materialia*, 42:3705, 1994.

[54] A. Aguayo, G. Murrieta, and R. de Coss. Elastic stability and electronic structure of fcc Ti, Zr, and Hf: a first-principles study. *Physical Review B*, 65:art. 092106, 2002.

[55] P. Bagno, O. Jepsen, and O. Gunnarsson. Ground-state properties of third-row elements with nonlocal density functionals. *Physical Review B*, 40:1997, 1989.

[56] M. Cerny, J. Pokluda, M. Sob, M. Friak, and P. Sandera. Ab initio calculations of elastic and magnetic properties of Fe, Co, Ni and Cr crystals under isotropic deformation. *Physical Review B*, 67:art. 035116, 2003.

[57] J. H. J. Cho and M. Scheffler. Ab initio pseudopotential study of Fe, Co, and Ni employing the spin-polarized LAPW approach. *Physical Review B*, 53:10685, 1996.

[58] R. Hafner, D. Spisak, R. Lorenz, and J. Hafner. Magnetic ground state of Cr in density-functional theory. *Physical Review B*, 65:art. 184432, 2002.

[59] J. Izquierdo, A. Vega, L. C. Balbás, D. Sánchez-Portal, J. Junquera, E. Artacho, J. M. Soler, and P. Ordejón. Systematic ab initio study of the electronic and magnetic properties of different pure and mixed iron systems. *Physical Review B*, 61:13639, 2000.

[60] V. Ozolins and M. Korling. Full-potential calculations using the generalized gradient approximation - structural-properties of transition-metals. *Physical Review B*, 48:18304, 1993.

[61] D. J. Singh and J. Ashkenazi. Magnetism with generalized-gradient-approximation density functionals. *Physical Review B*, 46:11570, 1992.

[62] D. J. Singh, W. E. Pickett, and H. Krakauer. Gradient-corrected density functionals - full-potential calculations for iron. *Physical Review B*, 43:11628, 1991.

[63] J. X. Zheng-Johansson, O. Eriksson, and B. Johansson. Systematic behavior of the hexagonal axial ratio for the d transition metals. *Physical Review B*, 59:6131, 1999.

[64] C. Amador, W. R. L. Lambrecht, and B. Segall. Application of generalized gradient-corrected density functionals to iron. *Physical Review B*, 46:1870–1873, 1992.

[65] B. Barbiellini, E. G. Moroni, and T. Jarlborg. Effects of gradient corrections on electronic structure in metals. *Journal of Physics - Condensed Matter*, 2:7597, 1990.

[66] H. C. Hsueh, J. Crain, G. Y. Guo, H. Y. Chen, C. C. Lee, K. P. Chang, and H. L. Shih. Magnetism and mechanical stability of alpha-iron. *Physical Review B*, 66:art. 052420, 2002.

[67] H. J. F. Jansen, K. B. Hathaway, and A. J. Freeman. Structural properties of ferromagnetic BCC iron: a failure of the local-spin-density approximation. *Physical Review B*, 30:6177, 1984.

[68] T. C. Leung, C. T. Chan, and B. N. Harmon. Ground-state properties of Fe, Co, Ni and their monoxides: Results of the generalized gradient approximation. *Physical Review B*, 44:2923, 1991.

[69] P. H. T. Philipsen and E. J. Baerends. Cohesive energy of 3d transition metals: density functional theory atomic and bulk calculations. *Physical Review B*, 54:5326, 1996.

[70] T. Sasaki, A. M. Rappe, and S. G. Louie. Ab initio optimized pseudopotential calculations of magnetic systems. *Physical Review B*, 52:12760, 1995.

[71] M. Sigalas, D. A. Papaconstantopoulos, and N. C. Bacalis. Total energy and band-structure of the 3d, 4d, and 5d metals. *Physical Review B*, 45:5777, 1992.

[72] J. Zhu, X. W. Wang, and S. G. Louie. 1st-principles pseudopotential calculations of magnetic iron. *Physical Review B*, 45:8887–8893, 1992.

[73] Office québécois de la langue française. Le Grand dictionnaire terminologique. Online at www.granddictionnaire.com.

[74] R. H. Landau and M. J. Páez. *Computational Physics : Problem Solving with Computers*. Wiley Interscience, 1997.

[75] R. E. Walpole and R. H. Myers. *Probability and Statistics for Engineers and Scientists*. Prentice Hall, 5th edition, 1993.

[76] B. Diu, C. Guthmann, D. Lederer, and B. Roulet. *Physique Statistique*, volume 37 of *collection enseignement des sciences*. Hermann, 1989.

[77] V. Tsirelson, A. Stash, M. Kohout, H. Rosner, H. Mori, S. Sato, S. Lee, A. Yamamoto, and Yu. Grin. Features of the electron density in magnesium diboride: reconstruction from X-ray diffraction data and comparison with TB-LMTO and FPLO calculations. *Acta Crystallographica*, B59:575, 2003.

[78] Charles Kittel. *Introduction to Solid State Physics*. John Wiley and Sons, 6th edition, 1986.

[79] B. Farid and R. W. Godby. Cohesive energies of crystals. *Physical Review B*, 43:14248, 1991.

[80] Y. S. Touloukian, R. K. Kirby, R. E. Taylor, and P. D. Desai. Thermal expansion : Metallic elements and alloys. In *Thermophysical Properties of Matter*, volume 12 of *The TPRC Data Series*. IFI/Plenum, 1975.

[81] J. C. Slater. Statistical exchange-correlation in the self-consistent field. In Per-Olov Löwdin, editor, *Advances in Quantum Chemistry*, volume 6. Academic Press, 1972.

[82] R. Pauthenet. High field magnetization in magnetic materials. In M. Date, editor, *Conference on High Field Magnetism*, page 77. North-Holland Publishing Company, Amsterdam, 1983.

[83] V. L. Moruzzi. Singular volume dependence of transition-metal magnetism. *Physical Review Letters*, 57:2211, 1986.

[84] L. Fritsche and Y. M. Gu. Binding-properties of 3d transition metals in a generalized density-functional theory. *Physical Review B*, 48:4259, 1993.

[85] P. Söderlind, R. Ahuja, O. Eriksson, J. M. Wills, and B. Johansson. Crystal structure adn elastic-constant anomalies in the magnetic 3d transition metals. *Physical Review B*, 50:5918, 1994.

[86] F. Starrost, H. Kim, S. C. Watson, E. Kaxiras, and E. A. Carter. Density-functional theory modeling of bulk magnetism with spin-dependent pseudopotentials. *Physical Review B*, 64:art. 235105, 2001.

[87] P. James, O. Eriksson, B. Johansson, and I. A. Abrikosov. Calculated magnetic properties of binary alloys between Fe, Co, Ni, and Cu. *Physical Review B*, 59:419, 1999.

[88] O. K. Andersen, J. Madsen, U. K. Poulsen, O. Jepsen, and Kollar J. Magnetic ground state properties of transition metals. *Physica B*, 86-88:249–256, 1977.

[89] D. Bagayoko and J. Callaway. Lattice-parameter dependence of ferromagnetism in BCC and FCC iron. *Physical Review B*, 28:5419, 1983.

[90] P. Entel, H. Herper, E. Hoffman, G. Nepecks, E. Wassermann, M. Acet, V. Crisan, and H. Akai. Understanding iron and its alloys from first principles. *Philosophical Magazine B*, 80:141, 2000.

[91] H. C. Herper, E. Hoffmann, and P. Entel. Ab initio investigations of iron-based martensitic systems. *Journal de Physique IV*, 7(C5):71–76, 1997.

[92] H. Herper, E. Hoffman, and P. Entel. Ab initio full-potential study of the structural and magnetic phase stability of iron. *Physical Review B*, 60:3839, 1999.

[93] J. Kübler. Magnetic moments of ferromagnetic and antiferromagnetic BCC and FCC iron. *Physics Letters*, 81A:81, 1981.

[94] M. Marsman and J. Hafner. Broken symmetries in the crystalline and magnetic structures of gamma-iron. *Physical Review B*, 66:art. 224409, 2002.

[95] S. Mojmir and M. Friak. Electronic structure and magnetic properties of iron by ab initio calculations: recent advances. *Matellic Materials*, 38:159, 2000.

[96] V. L. Moruzzi, P. M. Marcus, and J. Kübler. Magnetovolume instabilities and ferromagnetism versus antiferromagnetism in bulk FCC iron and manganese. *Physical Review B*, 39:6957, 1989.

[97] V. L. Moruzzi and P. M. Marcus. Antiferromagnetism in 3d transition metals. *Physical Review B*, 43:8361, 1990.

[98] V. L. Moruzzi and P. M. Marcus. Antiferromagnetic-ferromagnetic transition in FeRh. *Physical Review B*, 46:2864, 1992.

[99] S. Mukherjee and R. E. Cohen. Tight-binding based non-collinear spin model and magnetic correlations in iron. *Journal of Computer-Aided Materials Design*, 8:107, 2002.

[100] F. J. Pinski, J. Staunton, B. L. Gyorffy, D. D. Johnson, and G. M. Stocks. Ferromagnetism versus antiferromagnetism in face-centered-cubic iron. *Physical Review Letters*, 56:2096, 1986.

[101] R. F. Sabiryanov, S. K. Bose, and O. N. Mryasov. Effect of topological disorder on the itinerant magnetism of Fe and Co. *Physical Review B*, 51:8958, 1995.

[102] B. Sanyal and S. K. Bose. Electronic structure and related thermal and magnetic properties of some ternary Invar alloys. *Physical Review B*, 62:12730, 2000.

[103] M. van Schilfgaarde, I. A. Abrikosov, and B. Johansson. Origin of the Invar effect in iron-nickel alloys. *Nature*, 400:46, 1999.

[104] C. S. Wang, B. M. Klein, and H. Krakauer. Theory of magnetic and structural ordering in iron. *Physical Review Letters*, 54:1852, 1985.

[105] E. F. Wassermann, M. Acet, P. Entel, and W. Pepperhoff. Basic understanding of the relations between Invar, anti-Invar and martensite in Fe-based alloys. *Journal of the Magnetics Society of Japan*, 23:385, 1999.

[106] N. E. Brener, G. Fuster, J. Callaway, J. L. Fry, and Y. Z. Zhao. Magnetic structure of bcc and fcc manganese. *Journal of Applied Physics*, 63:4057, 19988.

[107] V. M. Nadutov, Ye. O. Svystunov, T. V. Yefimova, and A. V. Gorbatov. Hyperfine magnetic structure and magnetic properties of Invar Fe-Ni-C alloys. In M. Mashlan, M. Miglierini, and P. Schaaf, editors, *Material Research in Atomic Scale by Mössbauer Spectroscopy*, pages 105 – 116. Kluwer Academic Publishers, 2003.

[108] R. E. Cohen, I. I. Mazin, and D. G. Isaak. Magnetic collapse in transition metal oxides at high pressure: Implications for the Earth. *Science*, 275:654, 1997.

[109] R. E. Cohen, S. Gramsch, G. Steinle-Neumann, and L. Stixrude. Importance of magnetism in phase stability, equations of state and elasticity. In R. J. Hemley, G. L. Chiarotti, M. Bernasconi, and L. Ulivi, editors, *High-Pressure Phenomena: Proceedings of the International School of Physics "Enrico Fermi", Course CXLVII*. IOS Press, 2002.

[110] S. A. McEnroe, F. Langenhorst, P. Robinson, G. D. Bromiley, and C. S. J. Shaw. What is magnetic in the lower crust? *Earth and Planetary Science Letters*, 226:175, 2004.

[111] E. C. Stoner. Collective electron specific heat and spin paramagnetism in metals. *Proceedings of the Royal Society of London A*, 165:372, 1938.

[112] E. C. Stoner. Collective electron ferromagnetism II. Energy and specific heat. *Proceedings of the Royal Society of London A*, 169:339, 1938.

[113] T. Jarlborg. Spin fluctuations, electron-phonon coupling and superconductivity in near-magnetic elementary metals - Fe, Co, Ni and Pd. *Physica C*, 385:513, 2003.

[114] A. M. Dziewonski and D. L. Anderson. Preliminary reference Earth model. *Physics of the Earth and Planetary Interiors*, 25:297, 1981.

[115] J. A. Jacobs. *The Earth's Core*, volume 37 of *International Geophysics Series*. Academic Press, 1987.

[116] J. A. Jacobs. *Deep Interior of the Earth*, volume 6 of *Topics in the Earth Sciences*. Chapman and Hall, 1992.

[117] J. F. Janak and A. R. Williams. Giant internal magnetic pressure and compressibility anomalies. *Physical Review B*, 14:4199, 1976.

[118] J. C. Slater. The ferromagnetism of nickel. *Physical Review*, 49:537, 1936.

[119] J. C. Slater. The ferromagnetism of nickel II. temperature effects. *Physical Review*, 49:931, 1936.

[120] J. C. Slater. The theory of ferromagnetism: Lowest energy levels. *Physical Review*, 52:198, 1937.

[121] R. M. White. *Quantum Theory of Magnetism*. Springer-Verlag, 2nd edition, 1983.

[122] P. W. Anderson. Localized magnetic states in metals. *Physical Review*, 124:41, 1961.

[123] W. E. Spicer. In F. Abelès, editor, *Proceedings of the International Colloquium on Optical Properties and Electronic Structure of Metals and Alloys*, page 294. North-Holland, Amsterdam, 1965.

[124] W. F. Krolikowski and W. E. Spicer. Photoemission studies of the nobel metals. I. Copper. *Physical Review*, 185:882, 1969.

[125] A. P. Cracknell. Band structures and Fermi surfaces of metallic elements. In K.-H. Hellwege and J. L. Olsen, editors, *Electron States and Fermi Surfaces of Metals*, volume 13c of *Landolt-Börnstein New Series, Group III*. Springer, 1984.

[126] H. Ibach and H. Lüth, editors. *Solid-State Physics*. Springer, 2nd edition, 1996.

[127] D. G. Rancourt and R. B. Scorzelli. Low spin γ-Fe-Ni (γLS) proposed as a new mineral in Fe-Ni-bearing meteorites: Epitaxial interrowth of γLS and tetrataenite as possible equilibrium state at 20-40 at % Ni. *Journal of Magnetism and Magnetic Materials*, 150:30–36, 1995.

[128] K. Knöpfle, L. M. Sandratskii, and J. Kübler. Spin spiral ground state of gamma-iron. *Physical Review B*, 62:5564, 2000.

[129] M. Uhl, L. M. Sandratskii, and J. Kübler. Electronic and magnetic states of gamma-Fe. *Journal of Magnetism and Magnetic Materials*, 103:314, 1992.

[130] H. Fruchtl and U. Krey. Itinerant magnetism of fcc iron and disordered iron-nickel-invar alloys. *Journal of Magnetism and Magnetic Materials*, 94:L20–L28, 1991.

[131] H. Hasegawa. An itinerant-electron theory of Invar effects. *Physica B*, 119:15, 1983.

[132] S. Lipinski. Magnetism of the disordered Ni-Fe alloy. *International Journal of Modern Physics B*, 7:965–967, 1993.

[133] D. G. Rancourt, P. Hargraves, and G. Lamarche. Microstructure and low temperature magnetism of Fe-Ni Invar alloys. *Journal of Magnetism and Magnetic Materials*, 87:71–82, 1990.

[134] M. Shiga. Invar alloys. *Current Opinion in Solid State and Materials Science*, 1:340–348, 1996.

[135] I. Takahashi. Volume dependence of the magnetic behavior in fcc Fe-Ni alloys. *Journal of Magnetism and Magnetic Materials*, 104-107:2057–2058, 1992.

[136] O. Yamada, F. Ono, I. Nakai, and H. Fujiwara. Explanation of Fe-Ni Invar anomalies by itinerant electron magnetism. *Journal of Magnetism and Magnetic Materials*, 15-18:1199–1200, 1980.

[137] Nan-xian Chen, Zhao-dou Chen, and Yu-chuan Wei. Multidimensional inverse lattice problem and a uniformly sampled arithmetic Fourier transform. *Physical Review E*, 55:R5, 1997.

[138] William D. Callister. *Materials Science and Engineering - An Introduction*. John Wiley and Sons, 3rd edition, 1994.

[139] Claude Cohen-Tannoudji, Bernard Diu, and Franck Laloë. *Quantum Mechanics*, volume 1 and 2. Wiley Interscience, 1977.

[140] James F. Shackelford. *Introduction to Materials Science for Engineers*. Prentice-Hall Inc., 4th edition, 1996.

[141] A. Debernardi, M. Alouani, and H. Dreyssé. Ab initio thermodyynamics of metals: Al and W. *Physical Review B*, 63:art. 064305–1, 2001.

[142] Xiaogang Lu and Yi Wang. Calculation of the Vibrational Contribution to the Gibbs Energy of Formation for Al_3Sc. *Calphad*, 26:555, 2002.

[143] Shobhana Narasimhan and Stefano de Gironcoli. Ab initio calculation of the thermal properties of Cu: Performance of the LDA and GGA. *Physical Review*, 64:art. 064302, 2002.

[144] Yi Wang. Classical mean-field approach for thermodynamics: Ab initio thermophysical properties of cerium. *Physical Review B*, 61:R11863, 2000.

[145] Yi Wang, Dongquan Chen, and Xinwei Zhang. Calculated Equation of State of Al, Cu, Ta, Mo, and W to 1000 GPa. *Physical Review Letters*, 84:3220, 2000.

[146] Yi Wang and Li Li. Mean-field potential approcah to thermodynamic properties of metal: Al as a prototype. *Physical Review B*, 62:196, 2000.

[147] Yi Wang and Yunfeng Sun. First-principles thermodynamic calculations for δ-Pu and ϵ-Pu. *Journal of Physics: Condensed Matter*, 12:L311, 2000.

[148] E. R. Cowley and R. C. Shukla. Comparison of theories of anharmonicity applied to a model of copper. *Physical Review B*, 9:1261, 1974.

[149] R. C. Shukla and E. R. Cowle. Helmholtz free energy of an anharmonic crystal to $o(\lambda^4)$ III. Equation of state for the Lennard-Jones solid. *Physical Review B*, 31:372, 1985.

[150] A. E. H. Love. *A Treatise on the Mathematical Theory of Elasticity*. Dover, 1944.

[151] S. M. Daw, S. M. Foiles, and M .I. Baskes. The embedded-atom method: a review of theory and applications. *Materials Science Reports*, 9:251–310, 1993.

[152] M. Manninen, R. M. Nieminen, and M. J. Puska. Introduction to Many-Atom Interactions in Solids. In M. Manninen, R. M. Nieminen, and M. J. Puska, editors, *Many-Atom Interactions in Solids*, page 2. Springer-Verlag, 50th edition, 1990.

[153] M. J. Stott. Interatomic Potential Energy. In P. Jena, R. Kalia, P. Vashishta, and M. P. Tosi, editors, *Correlations in Electronic and Atomic Fluids*, pages 139–153. World Scientific, 1990.

[154] A. E. Carlsson, G. D. Gelatt, and H. Ehrenreich. An ab initio pair potential applied to metals. *Philosophical Magazine A*, 41:241, 1980.

[155] E. Esposito, A. E. Carlsson, D. D. Ling, H. Ehrenreich, and C. D. Gelatt. First-principles calculations of the theoretical tensile strength of copper. *Philosophical Magazine A*, 41:251, 1980.

[156] N.-X. Chen and G.-B. Ren. Carlsson-Gelatt-Ehrenreich technique and the Möbius inversion theorem. *Physical Review B*, 45:8177, 1992.

[157] M. Li, S. J. Liu, N. X. Chen, Y. G. Teng, W. X. Zhang, and S. Z. Zhang. Modified Möbius inversion transform and interatomic pair potential in the bcc-metals Mo and Cr. *Physics Letters A*, 169:364, 1992.

[158] M. Li, S. J. Liu, and N. X. Chen. Modified Möbius inversion transform and phonon dispersion relations for copper. *Physics Letters A*, 177:134, 1993.

[159] S.-J. Liu, M. Li, and N.-X. Chen. Möbius transform and inversion from cohesion to elastic constants. *Journal of Physics - Condensed Matter*, 5:4381, 1993.

[160] A. Mookerjee, N.-X. Chen, V. Kumar, and M. Abdus Satter. Ab initio pair potentials for FCC metals: an application of the method of Möbius transformation. *Journal of Physics - Condensed Matter*, 4:2439, 1992.

[161] L. Z. Cao, J. Shen, and N. X. Chen. Theoretical study of the phase stability and site preference for R-3(Fe,T)(29) (R=Nd, Sm; T=V, Ti, Cr, Cu, Nb, Mo, Ag). *Journal of Alloys and Compounds*, 336:18, 2002.

[162] N. X. Chen, X. J. Ge, W. Q. Zhang, and F. W. Zhu. Atomistic analysis of the field-ion microscopy image of Fe3Al. *Physical Review B*, 57:14203, 1998.

[163] N. X. Chen, Y. Lu, J. Shen, and Y Wu. Atomistic simulation of rare earth-transition intermetallic compounds derived from CaCu5 type. *Progress in Natural Science*, 13:339, 2003.

[164] N. X. Chen, J. Shen, and X. P. Su. Theoretical study on the phase stability, site preference, and lattice parameters for Gd(Fe,T)(12). *Journal of Physics - Condensed Matter*, 13:2727, 2001.

[165] N. X. Chen, J. Shen, and X. L. Wang. Atomistic study of the phase stability and site preference for Gd-3(Fe,T)(29) (T=V, Ti, Cr, Mo, Cu, Ag). *Journal of Alloys and Compounds*, 46:356, 2003.

[166] S. Q. Hao and N. X. Chen. Atomistic simulation on the phase stability, site preference and lattice parameters for Nd(Fe, T)(12) with Nd(Fe, Ti)(12)N-x. *Physics Letters A*, 297:110, 2002.

[167] S. Q. Hao and N. X. Chen. Structure and Curie temperature of Y2Fe17-xCrx. *Science in China Series G - Physics Astronomy*, 46:356, 2003.

[168] S. Q. Hao, N. X. Chen, and J. Shen. Phase stability and site preference of Nd2Fe17-xTx (T=V, Ti, Nb) and Nd2-xZrxFe17. *Journal of Alloys and Compounds*, 343:53, 2002.

[169] S. Q. Hao, N. X. Chen, and J. Shen. Atomistic study of rare-earth compounds R2Fe17 (R=Y, Ce, Pr, Nd, Sm, Gd, Tb, Dy, Ho, Er, Tm, Lu) and Nd2Fe17Nx. *Modelling and Simulation in Materials Science and Engineering*, 10:425, 2002.

[170] S. Q. Hao, N. X. Chen, and J. Shen. Atomistic study on the structure and Curie temperature for Nd2Fe17-xCrx. *Journal of Magnetism and Magnetic Materials*, 246:115, 2002.

[171] Y. M. Kang and N. X. Chen. Site preference and vibrational properties of SccuxAl12-x. *Journal of Alloys and Compounds*, 349:41, 2003.

[172] T. M. Kang, N. X. Chen, and J. Shen. Site preference and vibrational properties of Ni3Al with ternary additions Pd and Ag. *Modern Physics Letters B*, 16:727, 2002.

[173] Y. M. Kang, N. X. Chen, and J. Shen. Atomistic simulation of the lattice constants and lattice vibrations in RT4Al8 (R=Nd, Sm; T=Cr, Mn, Cu, Fe). *Journal of Alloys and Compounds*, 352:26, 2003.

[174] Y. M. Kang, N. X. Chen, and J. Shen. Site preference and vibrational properties of ScFexAl12x. *Journal of Magnetism and Magnetic Materials*, 256:381, 2003.

[175] Y. M. Kang, N. X. Chen, and J. Shen. Lattice vibration of Ce1-xScxFe4Al8. *Journal of Physics and Chemistry of Solids*, 64:433, 2003.

[176] S. J. Liu, J. Cai, S. Q. Duan, and Ma. B. K. Application of a simple semi-empirical interatomic potential model to phonon density of states of Fe3Al. *Chinese Physics Letters*, 16:914, 1999.

[177] G. Liu, N. X. Chen, and Y. M. Kang. Atomistic simulation for the structural properties of Th-T and Th-T-in compounds (T = Fe, Co, Ni, Cu). *Journal of Alloys and Compounds*, 386:47, 2005.

[178] S. J. Liu, S. Q. Duan, and B. K. Ma. First-principles calculation of vibrational entropy for Fe-Al compounds. *Physical Review B*, 58:9705, 1998.

[179] Y. Liu, Y. M. Kang, and N. X. Chen. Ab initio interatomic potentials of cubic boron nitride. *Journal of Alloys and Compounds*, 349:17, 2003.

[180] X. D. Ni, N. X. Chen, J. Shen, Z. Q. Sun, and W. Y. Yang. Site preference of alloying elements in Fe3Al-based alloys. *Journal of Materials Research*, 16:344, 2001.

[181] P. Qian, J. Shen, and N. X. Chen. Theoretical study on the structural properties for (La1-xRx)(2)Co17-yTiy (R = Sm, Nd). *Journal of Alloys and Compounds*, 377:66, 2004.

[182] P. Qian, J. Shen, and N. X. Chen. Theoretical study of the rare-earth compounds Nd2Co17-xTx (T = Fe, Cr), and Nd-2(Co1-xFex)(17-y)Cr-y. *Journal of Alloys and Compounds*, 372:70, 2004.

[183] P. Qian, J. Shen, and N. X. Chen. Phase stability and site preference of the rare-earth intermetallic compound R(Co, T)(12) (R=Er or Dy, T=V, Ti, Cr, Mo, Mn, Nb, Ni, Cu). *Journal of Alloys and Compounds*, 366:41, 2004.

[184] P. Qian, N. X. Chen, and J. Shen. Atomistic simulation for the phase stability, site preference and thermal expansion of YFe12-xTx (T = TiV, Cr, Mn, Zr, Nb, Mo, W). *Solid State Communications*, 134:771, 2005.

[185] P. Qian, N. X. Chen, and J. Shen. Structural imitation and lattice vibration of R2CO17-xMnx (R = Dy, Ho). *Physics Letters A*, 335:464, 2005.

[186] J. Shen, P. Qian, and N. X. Chen. Quasi-ab initio study on the structure and Curie temperature for Nd2Co17-xVx and (Nd1-xErx)(2)Co15.5V1.5. *Modelling and Simulation in Materials Science and Engineering*, 12:871, 2004.

[187] Y. Wang, J. Shen, N. X. Chen, and J. L. Wang. Theoretical investigation on site preference of foreign atoms in rare-earth intermetallics. *Journal of Alloys and Compounds*, 319:62, 2001.

[188] S. Zhang and N. X. Chen. Ab initio interionic potentials for NaCl by multiple lattice inversion. *Physical Review B*, 66:art. 064106, 2002.

[189] S. Zhang and N. X. Chen. Atomistic simulations of B1-B2 phase transition in Kcl based on inversion pair potentials. *Acta Materialia*, 51:6151, 2003.

[190] S. Zhang and N. X. Chen. Study on the high-pressure properties of KCl crystal by inversion pair potentials. *Materials Science and Engineering B - Solid State Materials for Advanced Technology*, 99:588, 2003.

[191] S. Zhang and N. X. Chen. Determination of the B1-B2 transition path in RbCl by Mobius pair potentials. *Philosophical Magazine*, 83:1451, 2003.

[192] S. Zhang and N. X. Chen. Lattice inversion for interionic pair potentials. *Journal of Chemical Physics*, 118:3974, 2003.

[193] S. Zhang and N. X. Chen. Energies and stabilities of sodium chloride clusters based on inversion pair potentials. *Physica B - Condensed Matter*, 325:172, 2003.

[194] W. Q. Zhang, Q. Xie, X. J. Ge, and N. X. Chen. Interatomic potentials between distinct atoms from first-principles calculation and lattice-inversion method. *Journal of Applied Physics*, 82:578, 1997.

[195] H. Y. Geng, M. H. F. Sluiter, and N. X. Chen. Hybrid cluster expansions for local structural relaxations. *Physical Review B*, 73:art. 012202, 2006.

[196] J.-X. Sun. Equation of state and thermodynamic functions for the fcc soft-core multiple-Yukawa solid and application to fullerenes with compressible molecular radius. *Physical Review B*, 75:art. 035424, 2007.

[197] J.-X. Sun, L. C. Cai, Q. Wu, and F. Q. Jing. Analytic equation of state for solid fcc C-60 based on generalized free-volume theory. *Physical Review B*, 73:art. 155431, 2006.

[198] Q. Xie. Dynamics of adatom self-diffusion and island morphology evolution at a Cu(100) surface. *Physica Status Solidi B - Basic Research*, 207:153, 1998.

[199] L. Loomis and S. Sternberg. *Advanced Calculus*. Addison-Wesley, 1968.

[200] X. Gonze, G.-M. Rignanese, and R. Caracas. First-principle studies of the lattice dynamics of crystals, and related properties. *Zeitschrift für Kristallographie*, 220:458, 2005.

[201] National Institute of Standards and Technology. The NIST Reference on Constants, Units, and Uncertainty. Available at http://physics.nist.gov/constants, October 1994.

[202] M. Winter. WebElements^{TM} periodic table. Available at www.webelements.com, 1993-2007.

[203] C. J. Bradley and A. P. Cracknell. *The Mathematical Theory of Symmetry in Solids; representation theory for point groups and space groups*. Clarendon Press, 1972.

[204] W. H. Press, B. P. Flannery, S. A. Teukolsky, and W. T. Vetterling. *Numerical Recipes in C - The Art of Scientific Computing*. Cambridge University Press, 1st edition, 1988.

[205] J. R. Anderson, J. W. McCaffey, and D. A. Papaconstantopoulos. Band calculations for vanadium. *Solid State Communications*, 7:1439, 1969.

[206] F. Batallan, I. Rosenman, and C. B. Sommers. Band structure and Fermi surface of HCP ferromagnetic cobalt. *Physical Review B*, 11:545, 1975.

[207] G. A. Burdick. Energy band structure of copper. *Physical Review*, 129:138, 1963.

[208] N. A. Cade. A self-consistent bandstructure calculation for antiferromagnetic gamma manganese. *Journal of Physics F*, 10:L187, 1980.

[209] J. Callaway and C. S. Wang. Energy bands in ferromagnetic iron. *Physical Review B*, 16:2095, 1977.

[210] J. Callaway and C. S. Wang. Self-consistent calculation of energy bands in ferromagnetic nickel. *Physical Review B*, 7:1096, 1973.

[211] S. G. Das. Electronic structure and magnetic properties of scandium. *Physical Review B*, 13:3978, 1976.

[212] E. H. Hygh and R. M. Welch. Electronic structure of titanium. *Physical Review B*, 1:2424, 1970.

[213] G. E. Juras, B. Segall, and C. B. Sommers. Electronic structure of Zn. *Solid State Communications*, 10:427, 1972.

[214] A. C. Switendick. Self-consistent energy band calculations for chromium. I. charge and spin densities. *Journal of Applied Physics*, 37:1022, 1966.

[215] J. R. Anderson, D. A. Papaconstantopoulos, L. L. Boyer, and J. E. Schirber. Spin-polarized band-structure calculations for Ni. *Physical Review B*, 20:3172, 1979.

[216] H. L. Davis, J. S. Faulkner, and H. W. Joy. Calculation of the band structure for copper as a function of lattice spacing. *Physical Review*, 167:601, 1968.

[217] C. D. Gelatt, H. Ehrenreich, and R. E. Watson. Renormalized atoms: Cohesion in transition metals. *Physical Review B*, 15:1613, 1977.

[218] A. I. Gubanov and V. K. Nikulin. The theory of the cohesion of noble metals. *Physica Status Solidi*, 17:815, 1966.

[219] R. L. Jacobs. The electronic structure of the noble metals I. the energy bands. *Journal of Physics C: Solid State Physics*, 1:1296, 1968.

[220] W. J. O'Sullivan, A. C. Switendick, and J. E. Schirber. Volume dependence of the band structure of noble metals. *Physica Status Solidi (b)*, 68:K29, 1975.

[221] D. A. Papaconstantopoulos, J. R. Anderson, and J. W. McCaffrey. Self-consistent energy bands in vanadium at normal and reduced lattice spacings. *Physical Review B*, 5:1214, 1972.

[222] F. Perrot. An A.P.W.-Xalpha calculation of the cohesive energy of copper. *Physics Letters*, A44:15, 1973.

[223] E. C. Snow. Total energy as a function of lattice parameter for copper via the self-consistent augmented-plane-wave method. *Physical Review B*, 8(12):5391, 1973.

[224] N. W. Dalton. Approximate calculation of electronic band structures IV: Density of states for transition metals. *Journal of Physics C*, 3:1912, 1970.

[225] J. Hubbard and N. W. Dalton. The approximate calculation of electronic band structures II: Application to copper and iron. *Journal of Physics C: Solid State Physics*, 1:1637, 1968.

[226] H. Jones. The phase boundaries in binary alloys, part 2: The theory of the alpha, beta phase boundaries. *Proceedings of the Physical Society*, 39:250, 1937.

[227] M. Sen and S. Chatterjee. Electronic and optical properties of Sc. *Journal of Physics F*, 10:985, 1980.

[228] E. C. Snow and J. T. Waber. The APW energy bands for the body centered and face centered cubic modifications of the 3d transition metals. *Acta Metallurgica*, 17:623, 1969.

[229] J. H. Wood. Energy band in iron via the Augmented Plane Wave method. *Physical Review*, 126:517, 1962.

[230] L. F. Mattheiss. Energy bands for the iron transition series. *Physical Review*, 134:A970, 1964.

[231] S. L. Altmann and C. J. Bradley. The band structure of hexagonal close-packed metals II: Sc, Ti, Y and Zr. *Proceedings of the Physical Society*, 92:764, 1967.

[232] S. Asano and J. Yamashita. Band theory of antiferromagnetic chromium. *Journal of the Physical Society of Japan*, 23:714, 1967.

[233] G. C. Fletcher. Electron band structure of face-centred cubic manganese. *Journal of Physics C*, 2:1440, 1969.

[234] J. R. Anderson and J. W. McCaffrey. Band calculations for vanadium. *Solid State Communications*, 7:1439, 1969.

[235] R. A. Ballinger and C. A. W. Marshall. Study of potentials suitable for band structure calculations of the noble metals I. copper. *Proceedings of the Physical Society*, 91:201, 1967.

[236] G. Lebègue. Emploi de l'approximation des électrons presque libres dans l'étude du cuivre: détermination de la surface de Fermi et étude de la répartition spatiale des électrons. *Journal de Physique (Paris)*, 24:709, 1963.

[237] I. Mertig, E. Mrosan, U. Fleck, and H. Wonn. Calculation of Fermi surface orbit integrals using a tetrahedron method: I. Orientation dependence of cyclotron massed in Cu and Au. *Journal of Physics F*, 10:407, 1980.

[238] S. Wakoh and J. Yamashita. Band structure of cobalt by a self-consistent procedure. *Journal of the Physical Society of Japan*, 28:1151, 1970.

[239] C. C. Wan and S. Y. Tong. The 3D electronic band calculation of nickel by the extended Hückel method. *Surface Science*, 34:739, 1973.

[240] K. C. Wong. Calculation of transition metal band structures. II. *Journal of Physics C*, 3:378, 1970.

[241] R. F. Yegorov and V. P. Shirokovskii. The potential and electron density of crystalline copper. *Physics of Metals and Metallography (English translation)*, 40(3):41, 1975.

[242] J. Callaway. Electronic energy bands in iron. *Physical Review*, 99:500, 1955.

[243] J. F. Cornwell, D. M. Hum, and K. C. Wong. Density of states in iron. *Physics Letters*, A26:365, 1968.

[244] M. F. Manning. Electronic energy bands in body-centered iron. *Physical Review*, 63:190, 1943.

[245] J. H. Wood. Wave functions for iron d band. *Physical Review*, 117:714, 1960.

[246] J. Yamashita, M. Fukuchi, and S. Wakoh. Energy band structure of nickel. *Journal of the Physical Society of Japan*, 18:999, 1963.

[247] S. Asano and J. Yamashita. Band theory of antiferromagnetism in 3d f.c.c. transition metals. *Journal of the Physical Society of Japan*, 31:1000, 1971.

[248] E. Marschall and H. Bross. Ferromagnetic nickel: self-consistent calculation of energy bands. *Physica Status Solidi b*, 90:241, 1978.

[249] R. A. Tawil and J. Callaway. Energy bands in ferromagnetic iron. *Physical Review B*, 7:4242, 1973.

[250] S. Wakoh and Yamashita H. Band structure of ferromagnetic iron self-consistent procedure. *Journal of the Physical Society of Japan*, 21:1712, 1966.

[251] M. Yasui, E. Hayashi, and M. Shimizu. Self-consistent band calculations for iron in paramagnetic and ferromagnetic states. *Journal of the Physical Society of Japan*, 34:396, 1973.

[252] O. M. Mryasov, A. I. Liechtenstein, L. M. Sandratskii, and V. A. Gubanov. Magnetic structure of FCC iron. *Journal of Physics - Condensed Matter*, 3:7683, 1991.

[253] Y. Tsunoda. Spin-density wave in cubic gamma-Fe and gamma-Fe(100-x)Co(x) precipitates in Cu. *Journal of Physics - Condensed Matter*, 1:10427, 1989.

[254] The Thomson Corporation. ISI Web of Knowledge [on-line search engine for scientific publications]. Available at www.isiwebofknowledge.com.

[255] A. N. Andriotis, N. Lathiotakis, and M. Menon. Magnetic properties of Ni and Fe clusters: a tight binding molecular dynamics study. *Chemical Physics Letters*, 260:15–20, 1996.

[256] J. L. Chen, C. S. Wang, K. A. Jackson, and M. R. Pederson. Theory of magnetic and structural ordering in iron clusters. *Physical Review B*, 44:6558–6561, 1991.

[257] O. Dieguez, M. M. G. Alemany, C. Rey, P. Ordejon, and L. J. Gallego. Density-functional calculations of the structures, binding energies, and magnetic moment of Fe clusters with 2 to 17 atoms. *Physical Review B*, 63:5407, 2001.

[258] L. I. Kurkina and O. V. Farberovich. Ground-state electronic-structure and electronic excitations of small iron clusters. *Journal of Physics - Condensed Matter*, 4:6417–6428, 1992.

[259] K. Y. Lee, J. Callaway, and S. Dhar. Electronic-structure of small iron clusters. *Physical Review B*, 30:1724–1730, 1984.

[260] K. Y. Lee, J. Callaway, K. Kwong, R. Q. Tang, and A. Ziegler. Electronic-structure of small clusters of nickel and iron. *Physical Review B*, 31:1796–1803, 1985.

[261] J. M. Mouesca, L. Noodleman, and D. A. Case. Density-functional calculations of spin coupling in [Fe4S4](3+) clusters. *International Journal of Quantum Chemistry*, suppl. 22:95–102, 1995.

[262] T. Oda, A. Pasquarello, and R. Car. Fully unconstrained approach to noncollinear magnetism: application to small Fe clusters. *Physical Review Letters*, 80:3622–3625, 1998.

[263] C. Y. Yang, K. H. Johnson, D. R. Salahub, J. Kaspar, and R. P. Messmer. iron clusters - electronic-structure and magnetism. *Physical Review B*, 24:5673–5692, 1981.

[264] C. Becker and J. Hafner. Structural, electronic, and magnetic-properties of Fe-Y alloys. *Physical Review B*, 50:3913–3930, 1994.

[265] S. K. Bose, V. Drchal, J. Kudrnovsky, Jepsen O., and O. K. Andersen. Theoretical study of ordering in Fe-Al alloys based on a density-functional generalized-perturbation method. *Physical Review B*, 55:8184, 1997.

[266] J. W. Cai, H. L. Luo, Z. Zhi, and Q. Q. Zheng. 1st-principles calculations on the local magnetic-properties of face-centered-cubic disordered Fe-Pd alloys. *Journal of Physics - Condensed Matter*, 5:5343–5352, 1993.

[267] N. I. Kulikov and C. Demangeat. Spin polarization of disordered Fe-Cr and Fe-Mn alloys. *Physical Review B*, 55:3533–3542, 1997.

[268] C. Paduani and E. G. Dasilva. Electronic structure of disordered alpha-FeMn alloys. *Journal of Magnetism and Magnetic Materials*, 161:184–188, 1996.

[269] B. V. Reddy, P. Jena, and S. C. Deevi. Electronic structure and transport properties of Fe-Al alloys. *Intermetallics*, 8:1197–1207, 2000.

[270] P. Söderlind, B. Johansson, and O. Eriksson. Spin and orbital magnetism in Fe-Co and Co-ni alloys. *Journal of Magnetism and Magnetic Materials*, 104:2037–2039, 1992.

[271] A. N. Timoshevskii, V. A. Timoshevskii, and B. Z. Yanchitsky. The influence of carbon and nitrogen on the electronic structure and hyperfine interactions in face-centred-cubic iron-based alloys. *Journal of Physics - Condensed Matter*, 13:1051–1061, 2001.

[272] T. Asada and S. Blugel. Total energy spectra of complete sets of magnetic states for FCC-Fe films on Cu(100). *Physical Review Letters*, 79:507–510, 1997.

[273] J. A. Gomez and D. Guenzburger. Hyperfine fields and field gradients of thin films of face-centred-cubic Fe on Cu(001). *Journal of Physics - Condensed Matter*, 14:12311–12328, 2002.

[274] R. Lorenz and J. Hafner. Magnetic structure and anisotropy of thin Fe films on Cu(001) substrates. *Physical Review B*, 54:15937–15949, 1996.

[275] R. Lorenz and J. Hafner. Noncollinear magnetism in rough ultrathin gamma-Fe films. *Physical Review B*, 58:5197–5200, 1998.

[276] S. S. A. Razee, J. B. Staunton, L. Szunyogh, and B. L. Gyorffy. Onset of magnetic order in FCC-Fe films on Cu (100). *Physical Review Letters*, 88:art. 147201, 2002.

[277] D. Spisak and J. Hafner. Complex reconstructions and interdiffusion in gamma-iron films on Cu(100) - ab-initio study. *Journal of Magnetism and Magnetic Materials*, 226:1600–1601, 2001.

[278] S. K. Bose. Electronic structure and related properties of metallic glasses: linear muffin-tin orbital approach. *Metallurgical and Materials Transactions A*, 29A:1853, 1998.

[279] O. V. Kontsevoi, O. N. Mryasov, and V. A. Gubanov. Local magnetic-behavior of amorphous iron - real space self-consistent calculations in the screened LMTO basis in real space. *Fizika Tverdogo Tela*, 34:2624–2635, 1992.

[280] M. F. Acet, E. F. Wassermann, and W. Pepperhoff. Relevance of a magnetic instabilities to the phase stabilities of Fe alloys. *Philosophical Magazine B*, 80:127–139, 2000.

[281] A. Marini, G. Onida, and R. Del Sole. Plane-wave DFT-LDA calculation of the electronic structure and absorption spectrum of copper. *Physical Review B*, 64:art. 195125, 2001.

[282] V. L. Moruzzi, P. M. Marcus, K. Schwarz, and P. Mohn. Ferromagnetic phases of BCC and FCC Fe, Co, and Ni. *Physical Review B*, 34:1784, 1986.

[283] Y. Zhou, W. Lai, and J. Wang. Calculated electronic structure of metastable phases of Cu. *Physical Review B*, 49:4463, 1994.

[284] E. Blanca, C. Rodriguez, J. Shitu, and D. Novikov. Degree of localization of the exchange-correlation hole and its influence on the ground-state (structural and magnetic) properties of d metals. *Journal of Physics - Condensed Matter*, 2001.

[285] K. Kokko and M. P. Das. Some ground-state properties of 3d and 4d metals studied using the generalized gradient approximation. *Journal of Physics - Condensed Matter*, 10:1285, 1998.

[286] H. L. Skriver. Crystal structure from one-electron theory. *Physical Review B*, 31:1909, 1985.

[287] A. Bere, J. Chen, A. Hairie, G. Nouet, and E. Paumier. Determination of the high c/a ratio of hexagonal metals with a semi-empirical tight-binding method. *Computational Materials Science*, 17:249, 2000.

[288] V. A. Antropov, M. I. Katsnelson, M. van Schilfgaarde, and B. N. Harmon. Ab initio spin dynamics in magnets. *Physical Review Letters*, 75:729, 1995.

[289] V. A. Antropov, M. I. Katsnelson, B. N. Harmon, M. van Schilfgaarde, and D. Kusnezov. Spin dynamics in magnets: Equations of motion and finite temperature effects. *Physical Review B*, 54:1019, 1996.

[290] J. Hafner and R. Lorenz. Noncollinear magnetism in disordered alloys and intermetallic compounds. *Computational Materials Science*, 8:170, 1997.

[291] D. Hobbs, G. Kresse, and J. Hafner. Fully unconstrained noncollinear magnetism within the projector augmented-wave method. *Physical Review B*, 62:11556, 2000.

[292] Y. Kakehashi and T. Uchida. A simplified approach to non-collinear magnetism in amorphous transition metals. *Journal of Physics - Condensed Matter*, 12:8683, 2000.

[293] J. K. Kübler. *Theory of Itinerant Electron Magnetism*. Oxford University Press, 2000.

[294] J. Kübler, L. M. Sandratskii, and M. Uhl. Theory for itinerant electrons in non-collinear and incommensurate structured magnets. *Journal of Applied Physics*, 76:6694, 1994.

[295] R. Lorenz and J. Hafner. Disorder and noncollinear magnetism in permanent-magnet materials. *Journal of Applied Physics*, 79:5051, 1996.

[296] Y. Wang, G. M. Stocks, D. M. C. Nicholson, W. A. Shelton, V. P. Antropov, and B. N. Harmon. Noncollinear magnetic structure in Ni0.35Fe0.65. *Journal of Applied Physics*, 81:3873, 1997.

[297] J. C. Boettger. Strain-dependent band-structure effects in the magnetic moment of a hexagonal Fe monolayer. *Physical Review B*, 47:1138, 1993.